Search, synthesis and structural investigations of organic molecular ferroelectrics

LIU, HUIYU

LIU, HUIYU (2020) *Search, synthesis and structural investigations of organic molecular ferroelectrics* , Durham theses, Durham University. Available at Durham E-Theses Online: http://etheses.dur.ac.uk/13477/

Abstract

Search, synthesis and structural investigations of organic molecular ferroelectrics

PhD thesis Huiyu Liu December 2019

This thesis is inspired by the symmetry relationships frequently observed between paraelectric and ferroelectric phases. It aims to search for new molecular ferroelectrics, identify their structural phase transitions and understand how the behaviours of these materials are associated with phase transitions.

Chapter 1 is a literature review on two aspects of organic materials in the solid state which are closely related to structural phase transitions: ferroelectricity and unusual thermal expansion. It gives a brief introduction to ferroelectricity and uses a number of ferroelectric examples to illustrate the different phase transition types that can lead to ferroelectricity. An overview of unusual (negative) thermal expansion observed in inorganic, organic-inorganic and pure organic compounds is also included.

Chapter 2 introduces diffraction methods (single crystal and powder X-ray diffraction and neutron diffraction), complementary structural techniques (solid state nuclear magnetic resonance, thermal analysis, elemental analysis and second harmonic generation) and the theory behind them. It also introduces the concepts underlying the molecular symmetry-adapted distortion mode analysis, which are used in Chapter 3 and 4.

Chapter 3 describes a comprehensive study of chloranilic acid pyrazine (CA-Pyz) which undergoes a reversible phase transition at ~300 K and shows remarkable thermal expansion properties associated with the phase transition. We show that CA-Pyz has uniaxial negative thermal expansion over a wide temperature range with a linear contraction coefficient as negative as -1500×10^{-6} K^{-1} at 250 K. The concepts of symmetry-adapted rotational modes and strain modes are used to successfully understand the structural changes and the unusual thermal expansion behaviour of CA-Pyz.

Chapter 4 demonstrates the use of systematic and exhaustive symmetry-adapted distortion mode subgroup search methods to solve the high temperature structure of 5,6-dichloro-methylbenzimidazole (DC-MBI) successfully from powder diffraction data. It describes how different models can be automatically tested against powder diffraction data and how the best structural description can be chosen. This is the first example that uses exhaustive symmetry-adapted distortion mode subgroup search method to solve a molecular structure. DC-MBI has the unusual property of its high temperature structure being of lower symmetry than its low temperature structure.

Chapter 5 reports two new polymorphic forms of the 2:1 cocrystal of benzoic acid and ethylenediamine (2BA-ETD). Variable temperature PXRD measurements revealed two new forms of 2BA-ETDA (the *β*- and *γ*-forms). The structure of the *β*-form is solved successfully from powder diffraction data by using the symmetry descent subgroup search method. The structure of the *γ*-form has also been solved but is less clear cut. Three possible structure models for the *γ*-form are obtained from powder diffraction data using simulated annealing. Structural optimisation and ^{13}C solid state NMR study provide a result that is inconsistent with an SHG study. As a result, we present a structural model for the *γ*-form that we believe is most likely based on the data available.

Chapter 6 describes attempts to grow cocrystals of chloranilic acid (CA) with pyrazole (PYR) and benzimidazole (BEN) as potential hydrogen-bonded ferroelectric materials. It reports two previously-unknown structures of the monohydrate CA-PYR and CA-2BEN. The structure of monohydrated CA-PYR is solved using single crystal X-ray diffraction. The structural model helps rationalise why a dehydrated sample cannot be formed by gradually heating. The structure of CA-2BEN is solved from both powder and single crystal diffraction data. The structure solution from powder diffraction data is similar to that from single crystal diffraction data. This gives a confidence test on the methods we have used in other chapters.

Search, synthesis and structural investigations of organic molecular ferroelectrics

Huiyu Liu

Supervisors: Prof. Ivana Evans and Prof. John S.O. Evans

A thesis submitted in partial fulfilment of the requirements

for the degree of Doctor of Philosophy

Department of Chemistry

Durham University

December 2019

Table of Contents

Abbreviations

ADP	Atomic displacement parameter
2BA-EDT	Benzoic acid-ethylenediamine
CA-2BEN	Chloranilic acid-benzimidazole
CA-PYR	Chloranilic acid-pyrazole
CA-Pyz	Chloranilic acid-pyrazine
CSD	Cambridge structural database
DC-MBI	5,6-dichloro-2-methylbenzimidazole
DFT	Density functional theory
DSC	Differential scanning calorimetry
HT	High temperature
irrep	Irreducible representation
LT	Low temperature
PXRD	Powder X-ray diffraction
RT	Room temperature
SSNMR	Solid state nuclear magnetic resonance
TGA	Thermogravimetric

Declaration and statement of copyright

The work presented in chapter 3 has been previously published in collaboration with Dr Matthias J. Gutmann from Science and Technology Facilities Council (STFC) Rutherford Appleton Laboratory, Profs. Harold T. Stokes and Branton J. Campbell from Brigham Young University.

The work presented in chapter 4 has been previously published in collaboration with Dr Weiguo Zhang and Prof. P. Shiv Halasyamani from University of Houston, and Profs. Harold T. Stokes and Branton J. Campbell from Brigham Young University.

I declare that the work described in this thesis is my own, except where I have acknowledged help from, or collaboration with others. This PhD research was carried out in the Department of Chemistry, Durham University between October 2016 and December 2019. Preliminary work on chloranilic acid-pyrazine (identification of the phase transition) was carried out as part of my MRes degree. The results presented in this PhD thesis have not been submitted before for a degree in this or any other institution.

Acknowledgements

I would like to express my appreciation to all those who provided me the possibility to complete this thesis. I would first like to thank my parents for their unconditional love and support throughout my life. I would also like to give a special gratitude to my supervisors, Prof. John S.O. Evans and Prof. Ivana Evans who provided invaluable suggestions and encouragement throughout my research. I also want to say thank you to all the members in the Evans group: Melissa Rodriguez, Chloe Fuller, Josie Auckett, Bettina Schwaighofer, James Lewis, Luiza Rosa de Araujo and Matthew Chambers for being nice colleagues and friends.

My final thanks go to the staff of several services: Dr David Apperley of the Durham solid state NMR service, Dr Emily Unsworth of the Durham elemental analysis service and Mr William D Carswell of the Durham thermal analysis service.

Chapter 1 Introduction and literature review

Overview

This chapter reviews two important aspects of organic materials in the solid state which are closely related to structural phase transitions: molecular ferroelectrics and unusual thermal expansion properties. It gives brief overviews of the phase transition mechanisms and the types of phase transition that can lead to ferroelectric properties. It then discusses how phase transitions can give rise to exceptionally large negative thermal expansions observed in the metal-organic and pure organic compounds.

1.1 Introduction to ferroelectrics

1.1.1 Fundamentals of ferroelectricity

A ferroelectric is a polar material whose spontaneous polarisation can be modulated by an external electric field.[1-3] Crystalline materials must therefore crystallise in a non-centrosymmetric polar space group to be ferroelectrics. Ten possible polar classes of point group exist: 1, 2, *m*, *mm*2, 4, 4*mm*, 6, 6*mm*, 3, and 3*m*. The point groups of ferroelectric crystals must belong to one of these ten polar classes.[4] In order to be classed as a ferroelectric, a material has to exhibit a permanent spontaneous polarisation, and the orientation of its electric polarisation has to be reversible in response to an applied electric field. A polarisation-electric field (P-E) hysteresis loop can therefore validate the ferroelectricity in a material.[5] As shown in Figure 1.1, when a field is applied to a material from position zero, the dipoles are gradually directed in the same orientation as the external electric field. The summation of all dipoles, also known as the net polarisation, reaches its limit at position 1 under this high positive electric field. This maximum net polarisation is called the saturation polarisation, denotated as P_s. A decrease of the positive electric field decreases the magnitude of the net polarisation since a number of dipole moments no longer fully align with the applied electric field. However, the majority of dipole moments still align parallel to the positive electric field. At position 2, the net polarisation of a ferroelectric material is non-zero when the applied electric field is removed. This remaining polarisation at E=0 is known as remanent polarisation P_r. When a negative electric field is applied at this stage, the dipoles are gradually reorientated in the direction of the negative electric field as its magnitude increases. At position 3, the ferroelectric material possesses an equal number of oppositely directed dipole moments, resulting in a zero net polarisation. The applied negative electric field which leads to the disappearance of the net polarisation is called the coercive field E_c. When the maximum negative saturation polarisation, -P_s, is achieved, the dipoles are all aligned with the direction of the applied negative electric field at position 4. This switchable property of the polarisation (from 1 to 4) make ferroelectrics useful in a variety of technological applications.[5] The area enclosed by the *P-E* hysteresis loop gives a measure of the energy required to achieve switching.

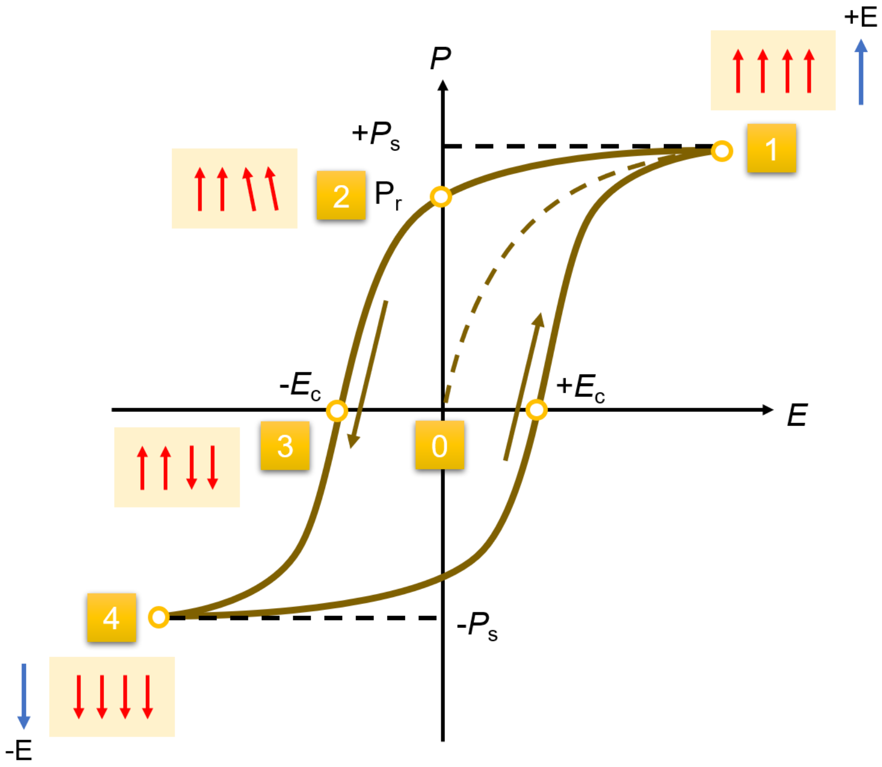

Figure 1.1: The hysteresis loop of polarisation (*P*) versus electric field (*E*). Dipole moments in a crystal are shown as red arrows.

1.1.2 Physical properties of ferroelectrics

Ferroelectrics have a wide range of technological application in optical and electric fields such as energy harvesting, data storage and memory devices.[6-7] Organic ferroelectrics have potential advantages over inorganic ferroelectrics materials because they are lightweight, environmentally friendly and easy to process. There are numerous potential applications of organic ferroelectrics as actuators, piezoelectric transducers and pyroelectric detectors as a result of the excellent pyro- and piezo-electric properties founded in ferroelectrics.[8-11] In this section, several physical properties of ferroelectric materials, including dielectric property, pyroelectricity and piezoelectricity, are introduced.

Dielectric properties

Dielectric properties refer to the ability of a material to be polarised in an applied electric field. Dielectric materials have important applications in capacitors. The dielectric constant (also known as the relative permittivity) is defined by Equation 1.1 as a ratio of the absolute permittivity of a material (ε_m) reletive to the vacuum permittivity (ε_o). It reflects how well a material will function in a parallel plate capacitor via the relationship expressed as Equation 1.2.

$$\varepsilon_r = \frac{\varepsilon_m}{\varepsilon_o}$$

Equation 1.1

$$C = \frac{Q}{V} = \frac{\varepsilon_r \varepsilon_0 A}{d}$$

Equation 1.2

In Equation 1.2, C is the capacitance of the parallel plate capactior, A is the area of plates overlapped and d is the distance between the two parallel plates.

The magnitude of the dielectric constant is strongly dependent on structure and temperature. In general, polar materials which possess permanent polarisation have larger dielectric constants than non-polar materials. Figure 1.2 shows the temperature dependence of the dielectric contant of a ferroelectric material. When a ferroelectric undergoes a paraelectric-to-ferroelectric phase transition, a peak or an anomaly in the dielectric constant can be detected. The Curie temperature, also known as the phase transition temperature T_c, can be identified from where this peak appears. In the paraelectric state, the dipole moments are disordered in terms of their orientations and thus cancel out each other. When the phase transition occurs on cooling, the material tranforms to a form (called the ferroelectric state) in which the dipoles within the structure are rearranged without cancelling out each other.

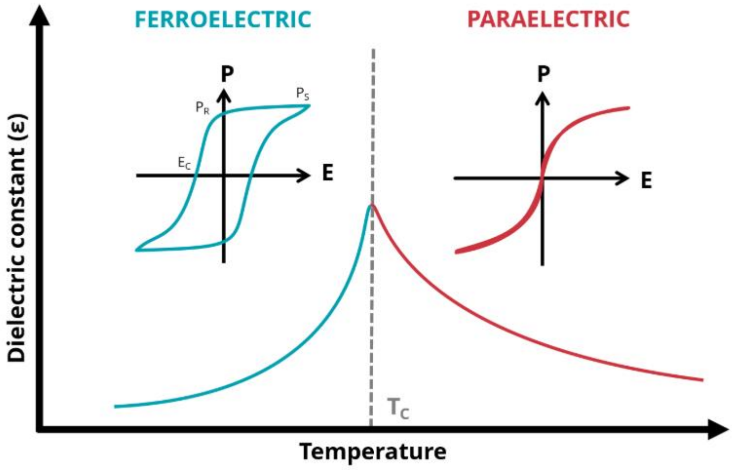

Figure 1.2: The temperature dependence of dielectric constant ε_r of a ferroelectric material. Figure is reproduced directly from https://www.chem.fsu.edu/~shatruk/molecular.html.

On the basis of the Curie-Weiss law, the temperature dependence of the dielectric constant above T_c is often described by Equation 1.3[12-13]:

$$\varepsilon_r = \frac{C}{T-\theta}$$

Equation 1.3

In the equation, C represents the Curie constant, and the θ is the Curie-Weiss temperature. The magnitude of dielectric constant decreases as the temperature increases.

Pyroelectric and piezoelectric properties

The relationship between ferroelectric, pyroelectric and piezoelectric materials in terms of their point group symmetry is shown in Figure 1.2. As seen from the figure, to be classed as piezoelectrics, the material must adopt a space group that lacks a centre of symmetry.[4, 20] Crystalline pyroelectric materials must crystallise in a polar space group, thus they are a sub-class of piezoelectric materials. The number of pyroelectrics is fewer than piezoelectrics in nature since only 10 of the 20 non-centrosymmetric point groups are polar. Ferroelectrics are inherently both pyroelectric and piezoelectric since they must adopt a polar space group.[14] However, the distinction between a ferroelectric and a pyroelectric is, as stated above, that a ferroelectric shows switching property under an applied electric field.

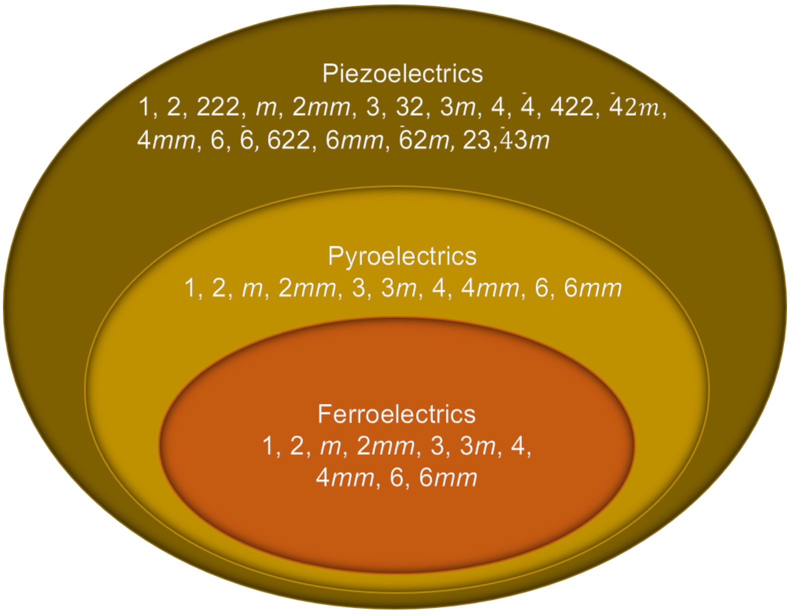

Figure 1.3: The relationship between piezo-, pyro- and ferroelectric materials. The possible point groups for each type of materials are given.[15-16]

Pyroelectricity is the ability of a material to change its electric polarisation in response to a uniform change in temperature.[17] The pyroelectric effect can be described mathematically by Equation 1.4.[18] In Equation 1.4, ΔP_i is the change in polarisation, p_i is the pyroelectric coefficient and ΔT is the change in temperature. The change in polarisation gives rise to a temporary voltage across the crystal. This property means pyroelectric materials are useful in heat sensors and power generation. Crystalline pyroelectric materials must exhibit a spontaneous polarisation even when an applied electric field is absent.[19]

$$\Delta P_i = p_i \Delta T$$

Equation 1.4

Piezoelectricity is a manifestation of the interaction between the electric field and mechanical stress in a material. Piezoelectric materials display the direct piezoelectric effect under which the material generates a temporary voltage between its surfaces in the presence of applied stress. Conversely, the internal strain of the material changes in response to an applied electric field; this is the so-called converse piezoelectric effect. This reversible process is a defining characteristic of piezoelectric materials. Ferroelectrics can be divided into two types in terms of their piezoelectricity.[21] In the first type, the ferroelectrics possess piezoelectricity in both the paraelectric and ferroelectric phases. KH_2PO_4 (KDP) is a well-known ferroelectric of this type. The ferroelectrics from the second type are piezoelectric only in their ferroelectric phase.

1.1.3 An example of organic ferroelectrics

Croconic acid is an organic species which exemplifies how molecular systems can give rise to ferroelectricity. A croconic acid molecule contains a five-membered carbon ring with two hydroxyl groups attached to two adjacent carbon atoms (Figure 1.4(c)). Due to the presence of both a proton-donor group (hydroxyl group) and a proton-acceptor group (ketone group) in the molecule, croconic acid can play a dual role of proton donor and acceptor.[22] The ferroelectric phase of the croconic acid belongs to orthorhombic space group $Pca2_1$. As depicted in Figure 1.4(a), the planar croconic acid molecules are linked by two crystallographically independent hydrogen bonds which are labelled as O_1H_1-O_5 and O_2H_2-O_4. O_1H_1-O_5 hydrogen bond connects croconic acid molecules along the c-axis forming a linear molecular sequence, while O_2H_2-O_4 hydrogen bond links croconic acid molecules forming a zigzag molecular sequence. The proton transfer between the two croconic acid molecules is believed to be responsible for the ferroelectricity.[23] Figure 1.4(c) and (d) illustrate the possible polarisation switching mechanism.

The ferroelectricity of croconic acid was confirmed by measuring the P-E hysteresis curves at room temperature (Figure 1.4(b)).[24-25] Croconic acid ($C_5H_2O_5$) shows a high saturation polarisation up to 21 μC/cm^2 and is the first example of a single-component organic ferroelectric with above-room-temperature ferroelectricity. Croconic acid thin films have recently been fabricated using solvent-free methods.[26] This new route may accelerate the development of flexible organic ferroelectric for electronic devices. One of the reasons why croconic acid was considered as a potential molecular ferroelectric was the presence of the pseudosymmetry in its polar structure.[24] However, there is no evidence for a structural phase transition to a paraelectric phase since the dielectric constant changes smoothly with temperature until the material decomposes at 450 K.[27-28]

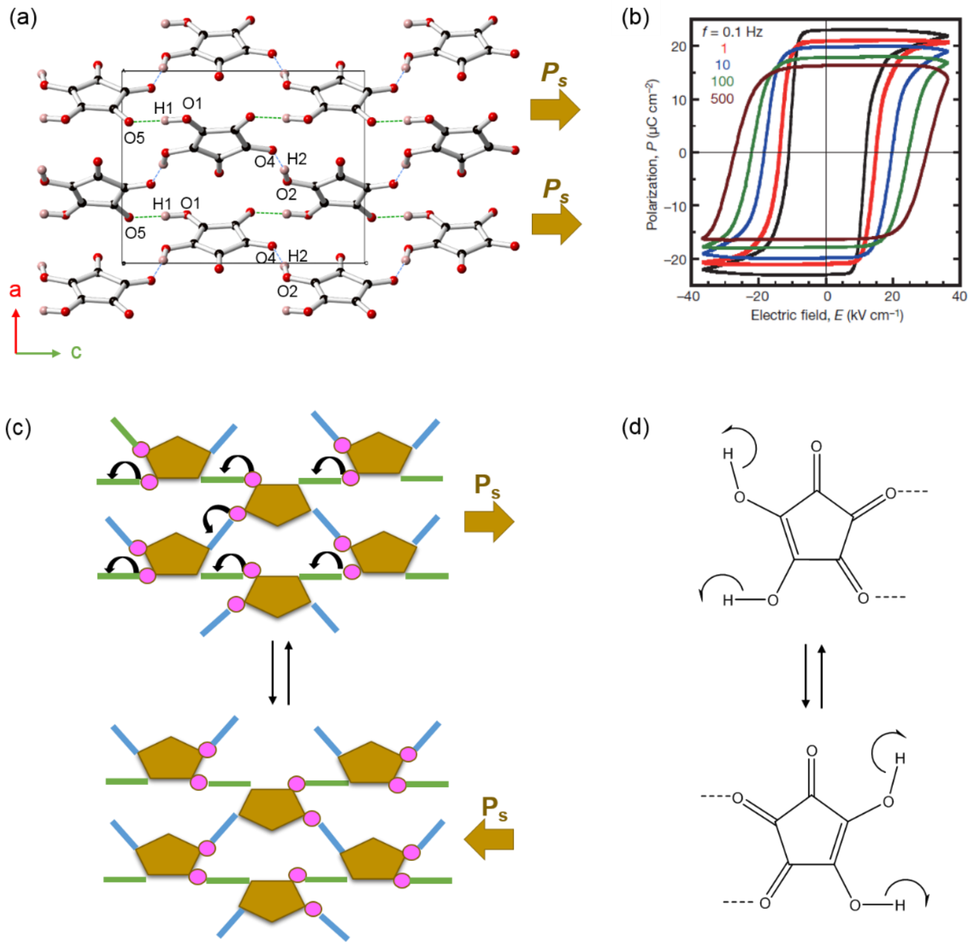

Figure 1.4: (a) The crystal structure of croconic acid in its ferroelectric state. (b) The *P-E* hysteresis loop measured by applying electric field with frequency *f* from 0.1 Hz to 500 Hz at 293 K. (c) Schematic representations of polarisation switching mechanism. (d) Molecular structure and proton tautomerism mechanism. Figure (b) is reproduced directly from reference 24.[24]

1.2 Phase transitions in the solid state

1.2.1 First-order and second-order phase transition

In general, phase transitions are often categorised as first-order or second-order, according to how the derivatives of the Gibbs free energy (G) vary at the Curie temperature.[29] In a first-order phase transition, the first derivatives of G, such as volume (V), entropy (S) and enthalpy (H), change discontinuously with respect to temperature. In contrast, in a second-order phase transition, the first derivatives of G change continuously, but second derivatives of G, e.g. heat capacity (C_p), thermal expansion (α) show discontinuous variations across the transition temperature. These two phase transition types can also be differentiated according to the Curie-Weiss law (Equation 1.3). The Curie-Weiss temperature θ can be derived from the linear relation of $\varepsilon_r{}^{-1}$ and

T when $T > T_c$. Only at a second-order phase transition, the Curie-Weiss temperature is approximately equal to the phase transition temperature, i.e. $\theta \sim T_c$.

1.2.2 Reconstructive and non-reconstructive phase transitions

The term phase transition in the solid state usually refers to a structural change. This structural phase transitions can be either reconstructive or non-reconstructive.[30] In a reconstructive phase transition, the structure changes significantly and the process involves the breaking and reforming of primary bonds. Therefore, the two structures before and after the phase transition need not to be directly related (e.g. by symmetry). In contrast, structure changes at a non-reconstructive transformation are more subtle and do not involve the breaking of primary bonds. Martensitic transformation is an illustration of non-reconstructive phase transition where concerted movements of atoms give rise to the phase transition. Atoms shift cooperatively by a small distance relative to their original position to form a new structure without any long range diffusion. Non-reconstructive phase transitions are often associated with symmetry lowering. The high-symmetry structure normally forms at high temperature and a lower-symmetry structure at low temperature. This relationship is not, however, thermodynamically necessary. For example, ferroelectricity is often associated with a nonpolar-to-polar structural phase transition.[2, 31] In most cases, this phase transition is symmetry lowering: the material in its ferroelectric phase retains some of the symmetry elements of its paraelectric phase. As a result, the paraelectric parent phase and the ferroelectric child phase of a material are related to each other through a group-subgroup relationship, i.e. the child has a subset of the symmetry of the parent.

1.2.3 Order parameters

An order parameter is a macroscopic and measurable quantity that can describe the main distinction between phases.[32] According to Landau theory[33], an order parameter must satisfy two fundamental requirements:

1) It should be non-zero and vary continuously with changing temperature in the low-symmetry phase.
2) It must disappear suddenly at the phase transition temperature T_c and remain zero in the high-symmetry phase even when surpassing T_c.

In general, an order parameter could be the magnitude of a polarisation, the magnitude of an atomic displacement, an electronic charge order, a spiral magnetic order or any other physical parameter that can break symmetry.[34] If an order parameter drives the phase transition (i.e. the order parameter is sufficient to cause the symmetry changes), it is called a primary order parameter. On the other hand, any other order parameters accompanying the primary order parameter are called secondary order parameters.[35] A secondary order parameter typically contributes less to the phase transition than primary order parameter and may not be sufficient to cause the symmetry change itself.[32] For example, ferroelectrics can be categorised as either proper or improper in terms of whether the primary order parameter is polarisation.[1] In a proper ferroelectric material, the phase transition is driven by the change in spontaneous polarisation, i.e. polarisation is the primary order parameter. By contrast, the change in polarisation is the secondary order parameter of a phase transition in an improper ferroelectric material[36], i.e.it appears as the side-effect of the primary order parameter.

1.2.4 Phase transitions in ferroelectric materials

Phase transitions in conventional organic ferroelectrics can be broadly divided into two types: order-disorder type and displacive type based on the primary order parameter of the phase transition.[1, 33] The leading driving force for a phase transition in an order-disorder ferroelectric is the ordering of dipole moments.[37] In the high temperature paraelectric phase, dipole moments are disordered and thus cancel out. In the low temperature ferroelectric phase, dipole moments undergo ordering, generating net polarisation. The transformation from ordered dipoles to disordered dipoles leads to the so-called order-disorder type transition. The phase transition in a displacive ferroelectric is characterised by an atomic or molecular displacement being the primary order parameter. The relative displacement of an atom or a molecule leads to symmetry breaking and a consequent change from paraelectric phase to ferroelectric phase. However, it needs to be noted that order-disorder and displacive phase transitions are not mutually exclusive. Another type of phase transition, electronic type, in molecular ferroelectrics that are distinct from the conventional phase transition types has also been reported. In the following section we use specific ferroelectric examples to discuss each phase transition type.

Potassium dihydrogen phosphate, $KH_2PO_4{\cdot}4H_2O$ (KDP)

The best-known hydrogen-bonded ferroelectric, KDP, is an example that undergoes order-disorder type phase transition.[38] Busch and Scherer[39] first reported the ferroelectricity of potassium dihydrogen phosphate ($KH_2PO_4{\cdot}4H_2O$) abbreviated as KDP (Figure 1.5). Historically, Slater[40] proposed a theory that the dynamics of the hydrogen bonds should account for the ferroelectric phase transition in KDP. The striking isotope effect by which the deuterated DKDP has a significantly higher Curie point (T_c=229 K) than the undeuterated KDP (T_c=122 K) confirmed the important roles of hydrogen bonds and supported Slater's theory.[41-43] At room temperature, the paraelectric phase adopts tetragonal space group $I\bar{4}2d$.[44] As shown in Figure 1.6(a), the protons can be located on two adjacent PO_4H_2 oxygen sites with equal probability, forming disordered non-polarised chains. At the Curie temperature (T_c=122 K), a second-order phase transition to a ferroelectric phase takes place.[41, 45] All hydrogen atoms undergo ordering, leading to a polar structure (space group *Fdd*2) in the ferroelectric phase (Figure 1.6(b)). Subsequent extensive structural studies[37, 46] revealed that the polarisation in the material mainly results from the displacements of phosphorus along the *c*-axis. As we can see from the right panels in Figure 1.6, all the P-O bonds of the undistorted tetrahedra have the same bond length in the disordered paraelectric phase. In the ordered ferroelectric phase, proton ordering leads to the formation of two P-(OH) and two P=O groups in each tetrahedron which in turn causes the phosphorus atom to shift from the centre of the tetrahedron along the *c*-axis. Although proton positional reordering triggers this paraelectric-to-ferroelectric phase transition, it only gives small contribution to the polarity. Thus, KDP is an example that shows mixed characteristics of order-disorder and displacive phase transitions. The atomic displacements observed in KDP are considered as the secondary order parameter. KDP is piezoelectric in both paraelectric and ferroelectric phases. Due to its good piezoelectricity, KDP is a promising alternative to quartz in terms of applications in piezoelectric transducers or sensors.[47]

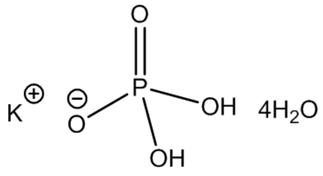

Figure 1.5: The molecular structure of potassium dihydrogen phosphate (KDP).

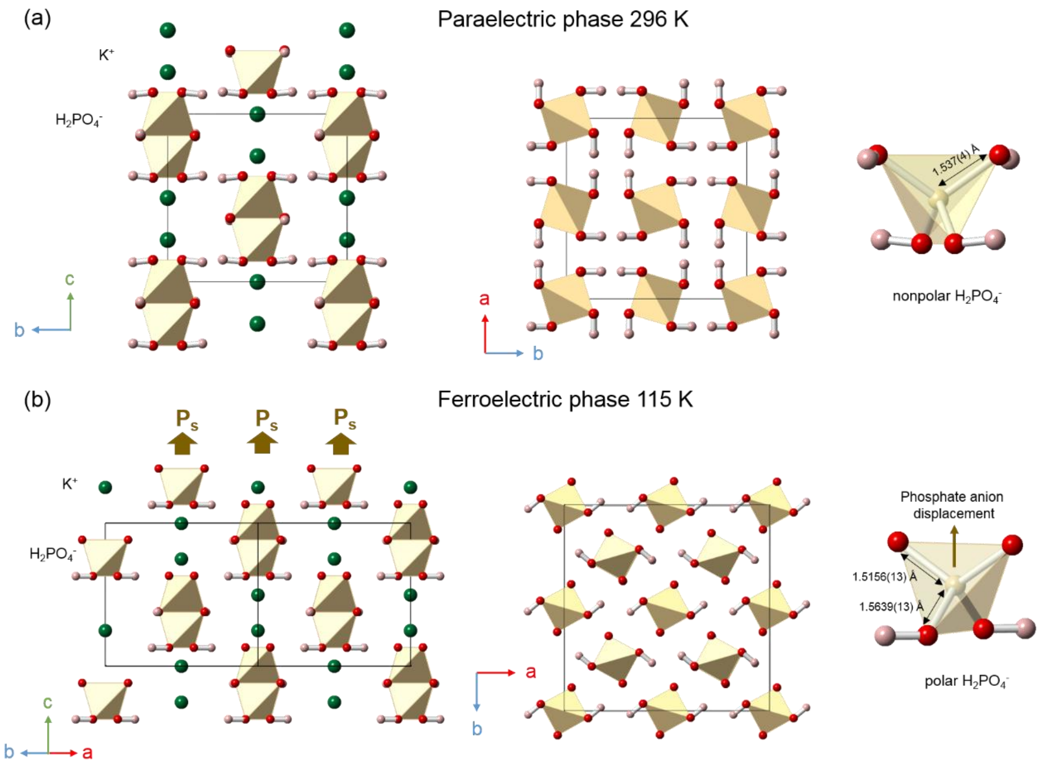

Figure 1.6: Crystal structures of KDP. (a) The crystal structure of KDP in the disordered paraelectric phase.[44] (b) The crystal structure of KDP in the ordered ferroelectric phase. Potassium ions are omitted in the middle panels for clarity. Individual $H_2PO_4^-$ tetrahedras are shown in the right panels. Colour legend: pink-H; red-O; yellow-P; dark green-K.[45]

(3-Pyrrolinium)($CdCl_3$), $C_4H_8NCdCl_3$

Another material that undergoes a order-disorder phase transition is the hybrid organic-inorganic material (3-Pyrrolinium)($CdCl_3$). The crystal structures of both paraelectric and ferroelectric forms were determined by single crystal X-ray diffraction.[48] As shown in Figure 1.7(b) and (c), the structures of both forms are related to hexagonal perovskites and contain infinite face-sharing $CdCl_6$ octahedra which run along the *c*-axis. At 346 K, paraelectric (3-Pyrrolinium)($CdCl_3$) crystallises in the centrosymmetric orthorhombic space group *Cmcm*. The organic cations are disordered in the paraelectric phase as the N1 and C3 sites are equally occupied by C and N atoms. (3-Pyrrolinium)($CdCl_3$) undergoes a phase transition to a ferroelectric phase at T_c = 316 K. The ferroelectric (3-Pyrrolinium)($CdCl_3$) adopts polar space group $Cmc2_1$. The ordering of the organic cations leads to the ferroelectric-to-paraelectric phase transition, and gives rise to a high saturation polarisation with magnitude of P_s = 5.1 μC/cm^2. It is almost certainly related to dynamics of the pyrrolinium molecule.

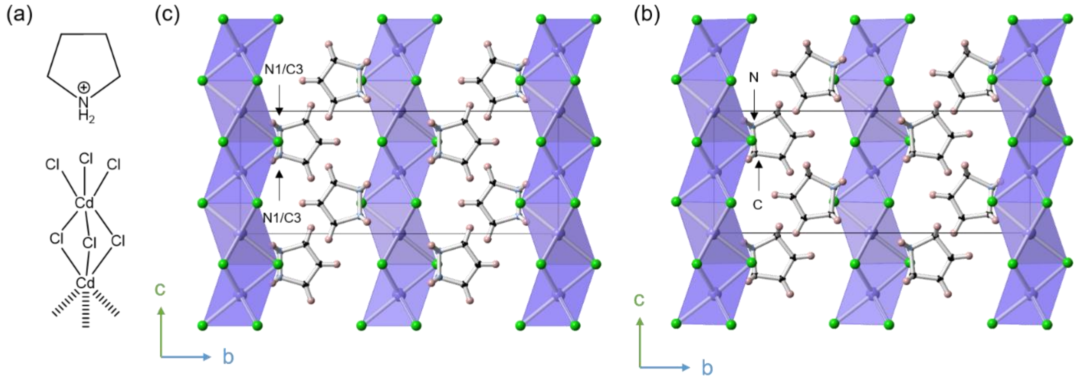

Figure 1.7: (a) Molecular structure of (3-Pyrrolinium)($CdCl_3$) and crystal structures of (3-Pyrrolinium)(CdCl3) in its (a) paraelectric state and (b) ferroelectric state. Colour legend: pink-H; black-C; blue-N; green-Cl; purple-Cd

Chloranilic acid phenazine, $C_6H_2Cl_2O_4{\cdot}C_{12}H_8N_2$ (CA-Phz)

The organic ferroelectric chloraniliac acid phenazine (CA-Phz) undergoes several phase transitions. Hydrogen bonds in CA-Phz make crucial contributions to these ferroelectric phase transitions. The 1:1 co-crystal (Figure 1.8(a)) consisting of neutral chloranilic acid and phenazine is abbreviated as CA-Phz ($C_6H_2Cl_2O_4{\cdot}C_{12}H_8N_2$). It undergoes three phase transitions upon cooling, evidenced by increases in dielectric constants at the Curie temperatures. Detailed information on the phase transitions is summarised in Table 1.1.

Table 1.1: Phase transitions of chloranilic acid phenazine.

Phase	Temperature	Space group	Polymorph
I	>253 K	$P2_1/n$	Paraelectric
II	253 – 147 K	$P2_1$	Ferroelectric
III	147 – 137 K	$P2_1(\frac{1}{2}\sigma_2\frac{1}{2})0$, $\sigma_2 = 0.5139$	Ferroelectric incommensurate
IV	< 137 K	$P2_1(\frac{1}{2}\sigma_2\frac{1}{2})0$, $\sigma_2 = 0.5$ or $F1$	Ferroelectric

The paraelectric structure (Figure 1.8(b)) of CA-Phz is monoclinic (space group $P2_1/n$) as determined by single crystal neutron diffraction.[49-50] The CA and Phz molecules connect alternatively via O-H⋯N hydrogen-bonding interactions forming one dimensional molecular chains. However, no acid-base interactions (i.e. proton transfer) are observed in this paraelectric phase. The second phase (phase II) of CA-Phz is ferroelectric, stable between 253 K and 147 K, and belongs to non-centrosymmetric polar space group $P2_1$. The hydrogen positions were determined precisely from single crystal neutron diffraction at 160 K by Kumai *et.al*.[51] As shown in Figure 1.8(c), all the hydrogens are involved in O-H⋯N interactions, but one of the two hydrogens of CA moves towards the nitrogen atoms of Phz, leading to a longer O-H bond (1.32(6) Å). Unusually large anisotropic displacement parameters (ADP) on hydrogen atoms were observed. The ADP ellipsoids elongate along the hydrogen-bonding direction, which is indicative of prominent proton motion towards the proton acceptors.[52] The involvement of proton displacements in the paraelectric-to-ferroelectric phase transition was also reflected by the increase in the Curie temperature of deuterated CA-Phz (T_c=304 K) by 51 K.[1, 53-54]. Even though the polarisation vector due to proton movements has a large component in the *ac* plane, the total polarisation in the *ac* plane is zero since the polarisation components in the *ac* plane cancel out each other. Thus, the resultant saturation polarisation is approximately along the *b*-axis with a magnitude of 1.8 μC/cm^2.

Between 147 K and 137 K, a incommensurate ferroelectric phase (IC phase III) exists. The structure of this IC phase belongs to polar space group $P2_1$ and has the same basic molecular connectivity as phase II.[55] However, the hydrogen bond geometry of the CA-Phz IC phase is slightly different from CA-Phz phase II. Figure 1.8(d) shows the average structure of the IC phase. One of the two hydrogen atoms in CA molecule is closer towards the nitrogen atom in Phz, leading to a longer O-H bond (1.435(16) Å) and a shorter N···H bond (1.320(15) Å). However, the bond length of N···H bond is still much longer than expected for a N-H bond (~1.03 Å).[56] This suggests that the ferroelectricity of the incommensurate CA-Phz also results from the proton displacements.

On further cooling through 137 K, the second ferroelectric phase of CA-Phz (phase IV) forms. The structure of CA-Phz phase IV was determined at 100 K by synchrotron X-ray diffraction.[57] It adopts a triclinic space group (*F*1) with a $2a \times 2b \times 2c$ supercell relative to the CA-Phz phase II. As shown in Figure 1.8(e), the structure of CA-Phz phase IV consists of two "planes" (planes I and II) which contain molecules running along [1 -1 0] and [1 1 0], respectively. Hydrogens in chains B and C are not involved in any proton transfer. As a result, CA and Phz molecules in these two chains remain in their neutral forms. Meanwhile, half of the hydrogens in chains A and D migrate to the nitrogen atoms, resulting in the negatively charged CA and positively charged Phz. The ferroelectricity in CA-Phz phase IV arises from proton transfer which involves 25% of the hydrogen atoms present. The direction of the resultant spontaneous polarisation is close to the *b*-axis with a magnitude of 2.54 μC/cm^2.

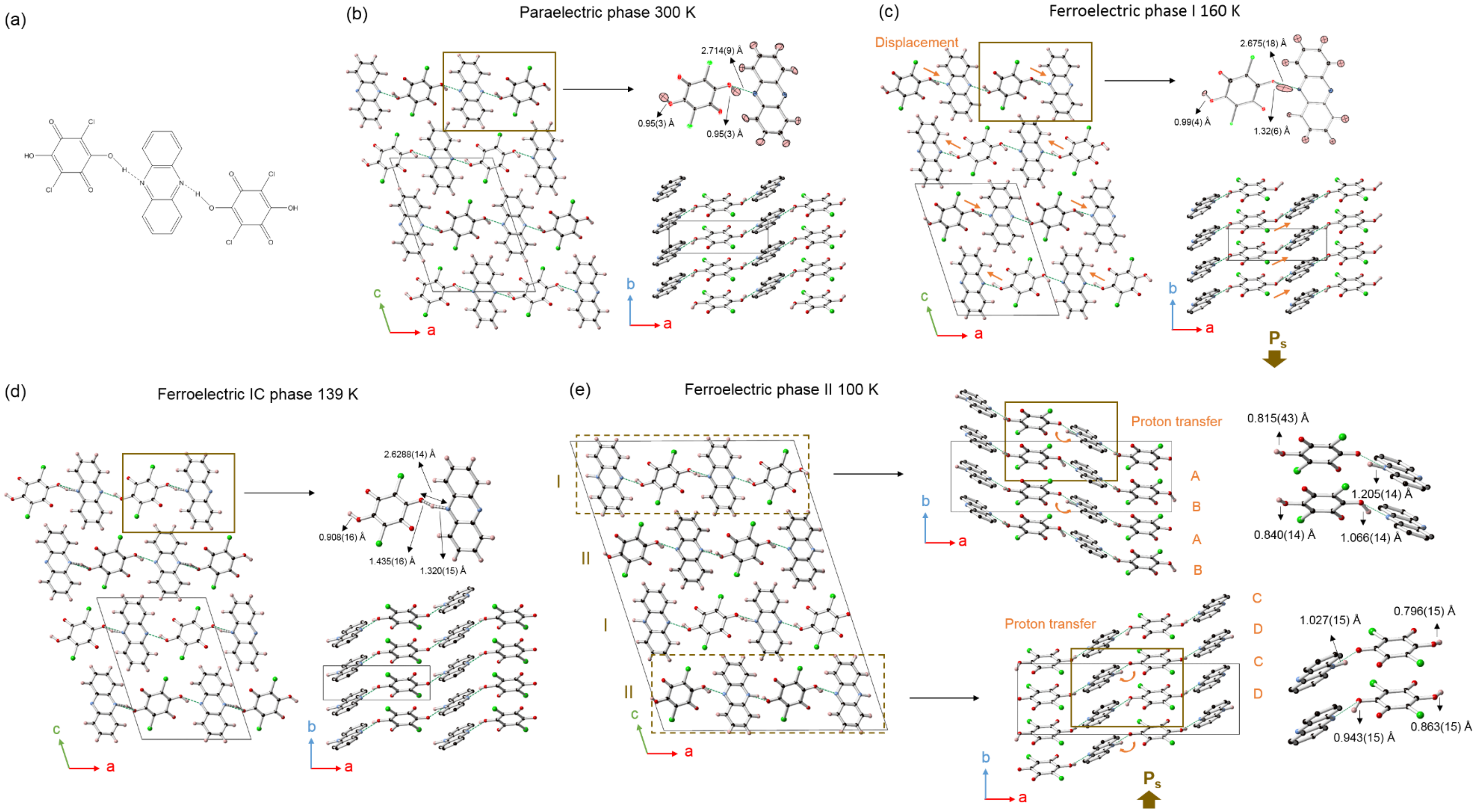

Figure 1.8: Molecular and crystal structures of chloranilic acid phenzaine (CA-Phz). (a) Molecular structure of CA-Phz. (b) Paraelectric structure of CA-Phz phase I determined at 300 K. (c) Ferroelectric structure of CA-Phz phase II determined at 160 K. (d) Ferroelectric incommensurate structure of CA-Phz phase III determined at 139 K. (e) Ferroelectric structure of CA-Phz phase IV determined at 100 K. Thermal ellipsoids are drawn at 50% probability. Colour legend: black-C; grey-H; red-O; blue-N; green-Cl.

Forms II/III and form IV therefore all have ferroelectric structures that result from proton movements but differ in being either proton displacement or proton transfer. In forms II/III 50% of the hydrogen atoms shift towards the nitrogen atoms but are not fully transferred, while in the form IV 25% of the hydrogen atoms are transferred. The CA-Phz system shows the complexity of ferroelectric phase transition that is possible in molecular systems.

Tetrathiafulvalene-ρ-chloranil, $C_6H_4S_4{\cdot}C_6Cl_4O_2$ (TTF-QCl_4)

A final important type of phase transition in organic ferroelectrics is "electronic type" where an electronic order parameter, such as magnetic ordering or electronic charge ordering, is responsible for the polarisation switching and the phase transition. This phenomenon was first discovered in the inorganic ferroelectric $TbMnO_3$[58] in which magnetism controls the polarisation ordering. Electronic ferroelectrics are good examples of improper ferroelectrics since changes in polarisation are the by-product of the electronic order parameter.

Charge transfer (CT) type molecular ferroelectrics containing electron donor (D) and electron acceptor (A) species belong to this class of ferroelectrics[1], and typically contain a mixed-stack of D and A species. Tetrathiafulvalene-*ρ*-chloranil (TTF-QCl_4)[59-60] and tetrathiafulvalene-ρ-bromanil (TTF-QBr_4)[61-62] (Figure 1.9 and 1.10(a)) are the best-known examples of mixed-stack electronic organic ferroelectrics. The transformation from a neutral structure into a more ionic structure is termed a "neutral-to-ionic" (N-I) phase transition.[63]

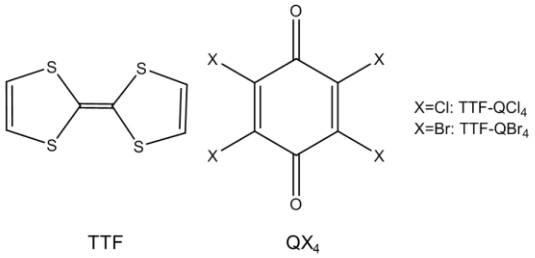

Figure 1.9: The molecular structures of tetrathiafulvalene-ρ-chloranil (TTF-QCl_4) and tetrathiafulvalene-ρ-bromanil (TTF-QBr_4).

The investigation of TTF-QCl_4 can be traced back to 1991 when the dielectric response induced by temperature and pressure was measured and used to identify the phase transition temperature (T_c=81 K).[60] TTF-QCl_4 was originally regarded as a displacive-type ferroelectric since molecular displacements were considered to account for the ferroelectric phase transition.[1] However, subsequent studies on phase transitions in terms of the macroscopic and microscopic mechanism have revealed a slightly different phase transition mechanism.[64-67] The neutral paraelectric phase of TTF-QCl_4 crystallises in centrosymmetric monoclinic space group ($P2_1/n$) where alternating neutral D and A molecules are equally spaced apart (Figure 1.10(a) and (b)). A small amount of charge transfer from TTF to QCl_4 (ionicity ~0.2) suggests that the TTF and QCl_4 molecules are not exactly neutral even in this nominally “neutral” phase. As illustrated in Figure 1.10(a), TTF-QCl_4 undergoes a first-order N-I phase transition to a polar structure (space group *Pn*) at the critical temperature 81 K. The huge jump in ionicity at T_c provides evidence of the phase transition.[67]

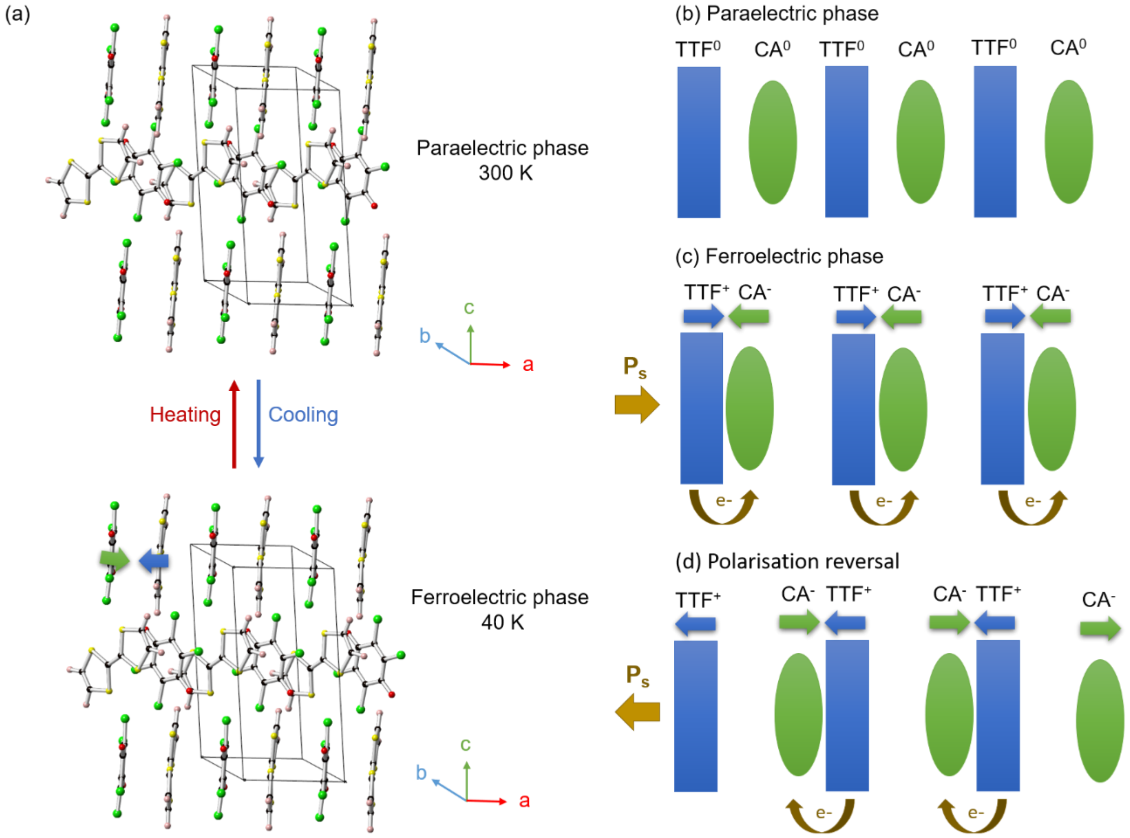

Figure 1.10: Illustration of neutral-to-ionic phase transition in TTF- QCl_4. (a) Crystal structures of paraelectric and ferroelectric phases. (b) Schematic representation of paraelectric phase. (c) Schematic representation of N-I phase transition to the ferroelectricity. (d) Schematic representation of the possible polarisation switching mechanism. Colour legend: black-C; pink-H; red-O; light yellow-S; green-Cl.

As shown in Figure 1.10(c), charge transfer and molecular dimerisation take place simultaneously at the phase transition. The leading driving force of this transition is charge transfer between electron donor and acceptor due to the valence instability.[68-69] An inherent structural instability (also known as the Peierls instability) turns the equally spaced $D^+ A^- D^+ A^- D^+ A^-$ chain into the dimerised D^+A^--D^+A^--D^+A^- chain. The structural instability involves the displacements of charged species as the oppositely charged D^+ and A^- move towards each other when forming polarised dimers. As shown in Figure 1.10(d), the polarisation direction can be switched by forming A^-D^+-A^-D^+-A^-D^+ chains.[70] Electronic effects therefore give rise to the macroscopic polarisation and drive the ferroelectric phase transition in TTF-QCl_4.[34] Therefore, TTF-QCl_4 is essentially an electronic type ferroelectric rather than a displacive type ferroelectric. Even though molecular displacements do accompany the phase transition, they are a consequence of the electronic charge redistributions, but not vice versa. This means the molecular displacements are not the primary order parameter and thus the phase transition in TTF-QCl_4 is clearly not of the displacive type.

1.3 Positive and negative thermal expansion

Most materials undergo positive thermal expansion (PTE) upon heating, which means their unit cells expand in response to increasing temperature. However, some materials exhibit a contraction upon heating, which is known as negative thermal expansion (NTE). We will encounter this phenomenon in chapter 3 and 4.

The coefficient of thermal expansion (CTE) over a certain temperature range can be calculated by Equation 1.5 where α_l is the linear CTE, Δl is the change in the length in a certain direction, l_0 is the initial length and ΔT is the change in temperature.

$$\alpha_l = \frac{\Delta l}{l_0 \times \Delta T}$$

Equation 1.5

The interest of research into NTE arises from the potential applications of NTE materials in controlling the overall thermal expansion in a system. For example they can be used to compensate for the positive thermal expansion (PTE) of other components. Therefore, tunable thermal expansion by chemical modification has attracted significant attention.[71]

A large number of NTE studies have been performed on inorganic materials. For instance, ZrW_2O_8[72] was found to show NTE with α_l = -9×10^{-6} K^{-1} over the temperature range of 2-300 K corresponding to a contraction of $\Delta l/l \sim -0.1\%$ over a 100 K range. The negative thermal expansion of ZrW_2O_8 is inherently isotropic due to its cubic structure, leading to an overall contraction in unit cell volume with α_V of -27.3×10^{-6} K^{-1}. The NTE phenomenon found in zirconium tungstate is induced by the transverse vibrational motion of central oxygen atoms in the Zr-O-W linkages. Similar transverse vibrational motion was also reported to give rise to NTE in other materials such as ReO_3[73] and ScF_3[74].

The term “colossal negative thermal expansion” was introduced to define materials with α_l more negative than -100×10^{-6} K^{-1} and hence a $\Delta l/l$ contraction larger than 1% over 100 K. $Ag_3[Co(CN)_6]$[75] was the first such material and exhibits a uniaxial NTE of $\Delta c/c \sim -1.3\%$ over 100 K and $\alpha_c = -130\times10^{-6}$ K^{-1} in a wide temperature range of 20-500 K. The magnitude of the change in unit cell parameter c is approximately 13 times bigger than the one for ZrW_2O_8. The large NTE in $Ag_3[Co(CN)_6]$ is related to its inherent geometric flexibility, which means that weak Ag-Ag argentophilic interaction make a significant contribution to determining the cell volume. Subsequently, colossal isotropic NTE was reported in other framework systems such as the UiO-66 MOF[76] and $[Fe(bpac)(Au(CN)_2)_2]\cdot 2EtOH$[77].

Unit cell changes associated with various electronically-driven phase transitions have also been found to give rise to NTE in several materials. When this occurs over a narrow temperature range it can lead to very negative expansion coefficients, though the practical use may be limited. For example $Sm_{2.75}C_{60}$[78] was reported to have linear expansion coefficients of with $\alpha_l \sim -80\times10^{-6}$ K^{-1} over a temperature range from 5–32 K, though the overall contraction $\Delta l/l$ is only ~ -0.24% over a 100 K range. In $Yb_8Ge_3Sb_5$[79], charge transfer gives rise to an anisotropic NTE with $\alpha_a = -400\times10^{-6}$ K^{-1}, $\alpha_c = -750\times10^{-6}$ K^{-1} and a very large tremendous α_v value of -1550×10^{-6} K^{-1} but only over a narrow temperature range of 5–15 K. The overall $\Delta l/l$ is ~ -0.44% over 100 K. Materials with significant contraction over wider temperature ranges include the ferroelectric $PbTiO_3$ with $\alpha_c \sim -70\times10^{-6}$ K^{-1} over the temperature range of 298–763 K and the largest contraction in cell dimension $\Delta c/c$ has a value of $\sim -0.72\%$ over a 100 K range.[80] In $Bi_{0.95}La_{0.05}NiO_3$[81], a charge transfer effect drives an intrinsic NTE of -137×10^{-6} K^{-1} over a 300–370 K temperature range. In reduced Ca_2RuO_4[82] dilatometry has shown $\alpha_l = -115\times10^{-6}$ K^{-1} from 135–345 K, through the diffraction-derived intrinsic contraction is much lower ($\alpha_l = -17\times10^{-6}$ K^{-1}).

NTE facilitated by weaker intermolecular interactions such as hydrogen bond have also been reported in pure organic molecular systems. An illustration of this is N’-2-propylydene-4-hydroxybenzohydrazide (IMACET)[83] which is a so-called thermosalient or “jumping crystal”, with $\alpha_c \approx -290\times10^{-6}$ K^{-1} over the temperature range 298–373 K. (S,S)-octa-3,5-diyn-2,7-diol[84] and 1,4-Bis(1’-hydroxycyclopentyl)-1,3-butadiyne[85] were also observed to exhibit colossal NTE with biaxial CTEs of $\alpha_b = -130\times10^{-6}$ K and $\alpha_c = -250\times10^{-6}$ K^{-1} over the temperature range 225–330 K and uniaxial NTE with α_l =

-116×10^{-6} K^{-1} over the temperature range 100-340 K, respectively. The extreme NTE behaviour in both materials is associated with the packing rearrangement triggered by collective tilting of molecules. Methanol monohydrate in contrast has a large volume expansion α_V = +500×10^{-6} K^{-1} that causes more modest contraction in one dimension α_a = −60×10^{-6} K^{-1} (both at 155 K) along with negative linear compressibility.[86] More examples[87-92] exemplifying unusual NTE behaviour in organic molecular materials are summarised in Table 1.1.

Table 1.1: Coefficients of thermal expansion of some inorganic, metal-organic framework and organic compounds.

Materials	α_l **(× 10^{-6} K^{-1})**	α_V **(× 10^{-6} K^{-1})**	**T range (K)**	**Ref.**
Inorganic compounds				
ZrW_2O_8	α_l = -9	-27.3	2-300	72
$Ag_3[Co(CN)_6]$	α_a = 150 α_c = -130	132	20-500	75
$Sm_{2.75}C_{60}$	α_l ~ -80	-400	5-32	78
$Yb_8Ge_3Sb_5$	α_a = -400 α_c = -750	-1550	5-15	79
$PbTiO_3$	α_c = -70	-19.9	348-763	80
$Bi_{0.95}La_{0.05}NiO_3$	α_l = -137	-414	300-370	81
$Ca_2RuO_{3.74}$	α_l = -115		135-345	82
Metal-organic frameworks				
UiO-66 (Hf)	α_l = -31	97	433-613	76
$[Fe(bpac)(Au(CN)_2)_2]\cdot 2EtOH$	α_a = -1360		190-240	77
Organic compounds				
IMACET	$\alpha_{a/b}$ = 230 α_c = -290		298-373	83
(S,S)-octa-3,5-diyn-2,7-diol	α_a = 515 α_b = -85 α_c = -204	60	240-330	84
1,4-Bis(1′-hydroxycyclopentyl)-1,3-butadiyne	α_a = -116 α_b = 118 α_c = 184		100-340	85
$MeOH\cdot H_2O$	α_a = -60	500		86
(Phenylazophenyl)palladium hexafluoroacetonate	α_a = 260 α_b = 39 α_c = -79	247	223-348	87
$(NH_4)_2SO_4$	α_a ~ -170	-150	170-223	89
$C_6H_{13}N_2Cl\cdot 3H_2O$	α_a = -213 α_b = 38 α_c = -459	-628	270-295	90

1.4 Aims and objectives of the project

Inspired by the group-subgroup relationships commonly observed between paraelectric and ferroelectric phases, this project aims at searching for new molecular ferroelectrics by identifying materials that might show this type of possible phase transitions. Syntheses of various potential molecular ferroelectric materials were attempted, and methods such as variable temperature single crystal and powder X-ray diffraction, solid state NMR and thermal analysis were used to examine the crystal structures and phase transitions.

The thesis is outline as follow. Chapter 2 describes experimental methods and outlines some of the theory behind different techniques. Chapter 3 will describe the structural changes and associated unusual thermal expansion associated with the phase transition in chloranilic acid pyrazine (CA-Pyz) by using variable temperature single crystal and powder X-ray diffraction and solid state NMR. It will also demonstrate the use of symmetry-adapted molecular distortion modes to help understand the unusual structure and unit cell parameter changes through the phase transition. This was the first application of rotational symmetry modes to understand a molecular phase transition. Chapter 4 will focus on the phase transition study and HT phase identification of ferroelectric 5,6-dichloro-2-methylbenzimidazole (DC-MBI). An exhaustive subgroup search method is developed to help solve the crystal structure from powder diffraction data. Chapter 5 will report the structural investigations of benzoic acid ethylenediamine (2BA-ETD) by using powder X-ray diffraction, density functional theory (DFT) calculations and solid state NMR. We identify several new polymorphs of this composition. Chapter 6 will describe our attempts to grow cocrystals using chloranilic acid as the acidic component for designing potential ferroelectric materials.

References

1. Horiuchi, S.; Tokura, Y., Organic ferroelectrics. *Nature Materials* **2008,** *7* (5), 357-366.
2. Keppens, V., Structural transitions: 'Ferroelectricity' in a metal. *Nature Materials* **2013,** *12* (11), 952-953.
3. Horiuchi, S.; Kumai, R.; Fujioka, J.; Tokura, Y., Supramolecular approach to organic ferroelectrics. *Physica B: Condensed Matter* **2010,** *405* (11, Supplement), S334-S337.
4. Giacovazzo, C., Symmetry in crystals. In *Fundamentals of Crystallography*, 3 ed.; Oxford University Press: Oxford, 2011.
5. Damjanovic, D., Chapter 4 - Hysteresis in Piezoelectric and Ferroelectric Materials A2 - Bertotti, Giorgio. In *The Science of Hysteresis*, Mayergoyz, I. D., Ed. Academic Press: Oxford, 2006; pp 337-465.
6. Scott, J. F.; Carlos, A. P. D. A., Ferroelectric Memories. *Science* **1989,** *246* (4936), 1400-1405.
7. Dawber, M.; Rabe, K. M.; Scott, J. F., Physics of thin-film ferroelectric oxides. *Reviews of Modern Physics* **2005,** *77* (4), 1083-1130.

8. Owczarek, M.; Hujsak, K. A.; Ferris, D. P.; Prokofjevs, A.; Majerz, I.; Szklarz, P.; Zhang, H.; Sarjeant, A. A.; Stern, C. L.; Jakubas, R.; Hong, S.; Dravid, V. P.; Stoddart, J. F., Flexible ferroelectric organic crystals. *Nature Communications* **2016,** *7*, 13108.
9. Ryo, S.; Yoshinori, H.; Tomoya, T.; Tomohito, S.; Kenjiro, F.; Daisuke, K.; Fabrice Domingues dos, S.; Atsushi, M.; Shizuo, T., Ultrathin flexible memory devices based on organic ferroelectric transistors. *Japanese Journal of Applied Physics* **2016,** *55* (10S), 10TA04.
10. Gao, W.; Chang, L.; Ma, H.; You, L.; Yin, J.; Liu, J.; Liu, Z.; Wang, J.; Yuan, G., Flexible organic ferroelectric films with a large piezoelectric response. *NPG Asia Mater* **2015,** *7*, e189.
11. Yuan, Y.; Xiao, Z.; Yang, B.; Huang, J., Arising applications of ferroelectric materials in photovoltaic devices. *Journal of Materials Chemistry A* **2014,** *2* (17), 6027-6041.
12. Horiuchi, S.; Ishii, F.; Kumai, R.; Okimoto, Y.; Tachibana, H.; Nagaosa, N.; Tokura, Y., Ferroelectricity near room temperature in co-crystals of nonpolar organic molecules. *Nature Materials* **2005,** *4* (2), 163-166.
13. Lines, M. E.; Glass, A. M., Basic Concepts. In *Principles and Applications of Ferroelectrics and Related Materials*, Oxford University Press: Oxford, 2001.
14. Bowen, C. R.; Kim, H. A.; Weaver, P. M.; Dunn, S., Piezoelectric and ferroelectric materials and structures for energy harvesting applications. *Energy & Environmental Science* **2014,** *7* (1), 25-44.
15. Whatmore, R., Ferroelectric Materials. In *Springer Handbook of Electronic and Photonic Materials*, Kasap, S.; Capper, P., Eds. Springer International Publishing: Cham, 2017; pp 1-1.
16. Ok, K. M.; Chi, E. O.; Halasyamani, P. S., Bulk characterization methods for non-centrosymmetric materials: second-harmonic generation, piezoelectricity, pyroelectricity, and ferroelectricity. *Chemical Society Reviews* **2006,** *35* (8), 710-717.
17. Srinivasan, M. R., Pyroelectric materials. *Bulletin of Materials Science* **1984,** *6* (2), 317-325.
18. Kepler, R. G., Piezoelectricity, Pyroelectricity, and Ferroelectricity in Organic Materials. *Annual Review of Physical Chemistry* **1978,** *29*, 497-518.
19. Gränicher, H.; Hadni, A. Pyroelectricity. https://www.accessscience.com/content/pyroelectricity/559200.
20. Gränicher, H. Piezoelectricity. https://www.accessscience.com/content/piezoelectricity/516200.

21. Känzig, W. Ferroelectrics. https://www.accessscience.com/content/ferroelectrics/254500.

22. Cai, Y.; Luo, S.; Zhu, Z.; Gu, H., Ferroelectric mechanism of croconic acid: A first-principles and Monte Carlo study. *The Journal of Chemical Physics* **2013,** *139* (4), 044702.

23. Horiuchi, S.; Kobayashi, K.; Kumai, R.; Ishibashi, S., Proton tautomerism for strong polarization switching. *Nature Communications* **2017,** *8* (1), 14426.

24. Horiuchi, S.; Tokunaga, Y.; Giovannetti, G.; Picozzi, S.; Itoh, H.; Shimano, R.; Kumai, R.; Tokura, Y., Above-room-temperature ferroelectricity in a single-component molecular crystal. *Nature* **2010,** *463* (7282), 789-792.

25. Day, C., A single-component organic crystal is ferroelectric at room temperature. *Physics Today* **2010,** *63* (4), 16-17.

26. Jiang, X.; Lu, H.; Yin, Y.; Zhang, X.; Wang, X.; Yu, L.; Ahmadi, Z.; Costa, P. S.; DiChiara, A. D.; Cheng, X.; Gruverman, A.; Enders, A.; Xu, X., Room temperature ferroelectricity in continuous croconic acid thin films. *Applied Physics Letters* **2016,** *109* (10), 102902.

27. Hydrogen Bonding in the Organic Ferroelectric Croconic Acid: Insights from Experiment and First-Principles Modelling. *Journal of the Physical Society of Japan* **2013,** *82* (Suppl.A), SA001.

28. Sikora, M.; Pojawis, P.; Katrusiak, A., Damping and Resonance Correlations in OH···O Bonded Ferroelectrics. *The Journal of Physical Chemistry C* **2013,** *117* (27), 14213-14217.

29. Roos, Y. H.; Drusch, S., Chapter 1 - Introduction to phase transitions. In *Phase Transitions in Foods (Second Edition)*, Academic Press: San Diego, 2016; pp 1-17.

30. Dinnebier Robert, E.; Leineweber, A.; Evans John, S. O., *Rietveld Refinement, Practical Powder Diffraction Pattern Analysis using TOPAS*. 2018.

31. Catti, M., Physical properties of crystals: Phenomenology and modelling. In *Fundamentals of Crystallography*, 3 ed.; Oxford University Press: Oxford, 2011.

32. Perez-Mato, J. M.; Orobengoa, D.; Aroyo, M. I., Mode crystallography of distorted structures. *Acta Crystallographica Section A* **2010,** *66*, 558-590.

33. Muller, U., *Symmetry Relations between Crystal Structures*. Oxford University Press New York: 2013.

34. Sumio, I., Electronic ferroelectricity in molecular organic crystals. *Journal of Physics: Condensed Matter* **2014,** *26* (49), 493201.

35. Campbell, B. J.; Stokes, H. T.; Tanner, D. E.; Hatch, D. M., ISODISPLACE: a web-based tool for exploring structural distortions. *Journal of Applied Crystallography* **2006,** *39*, 607-614.

36. Cheong, S.-W.; Mostovoy, M., Multiferroics: a magnetic twist for ferroelectricity. *Nature Materials* **2007,** *6* (1), 13-20.

37. Lines, M. E.; Glass, A. M., Order-Disorder Ferroelectrics. In *Principles and Applications of Ferroelectrics and Related Materials*, Oxford University Press: Oxford, 2001.

38. Koval, S.; Kohanoff, J.; Lasave, J.; Colizzi, G.; Migoni, R. L., First-principles study of ferroelectricity and isotope effects in H-bonded KH_2PO_4 crystals. *Physical Review B* **2005,** *71* (18), 184102.

39. Busch, G.; Scherrer, P., Eine neue seignette-elektrische Substanz. *Naturwissenschaften* **1935,** *23* (43), 737-737.

40. Slater, J. C., Theory of the Transition in KH2PO4. *The Journal of Chemical Physics* **1941,** *9* (1), 16-33.

41. Koval, S.; Kohanoff, J.; Migoni, R. L.; Tosatti, E., Ferroelectricity and Isotope Effects in Hydrogen-Bonded KDP Crystals. *Physical Review Letters* **2002,** *89* (18), 187602.

42. Koval, S.; Kohanoff, J.; Lasave, J.; Colizzi, G.; Migoni, R. L., First-principles study of ferroelectricity and isotope effects in H-bonded KH_2PO_4 crystals. *Physical Review B* **2005,** *71* (18), 184102.

43. Horiuchi, S.; Kumai, R.; Tokura, Y., Room-Temperature Ferroelectricity and Gigantic Dielectric Susceptibility on a Supramolecular Architecture of Phenazine and Deuterated Chloranilic Acid. *Journal of the American Chemical Society* **2005,** *127* (14), 5010-5011.

44. Cai, W.; Katrusiak, A., Structure of the high-pressure phase IV of KH_2PO_4 (KDP). *Dalton Transactions* **2013,** *42* (4), 863-866.

45. Fukami, T., Refinement of the Crystal Structure of KH_2PO_4 in the Ferroelectric Phase. *Physica Status Solidi (a)* **1990,** *117* (2), K93-K96.

46. Shi, P.-P.; Tang, Y.-Y.; Li, P.-F.; Liao, W.-Q.; Wang, Z.-X.; Ye, Q.; Xiong, R.-G., Symmetry breaking in molecular ferroelectrics. *Chemical Society Reviews* **2016,** *45* (14), 3811-3827.

47. Tichý*, J.; Erhart, J.; Kittinger*, E.; Přívratská, J., Principles of Piezoelectricity. In *Fundamentals of Piezoelectric Sensorics: Mechanical, Dielectric, and Thermodynamical Properties of Piezoelectric Materials*, Springer Berlin Heidelberg: Berlin, Heidelberg, 2010; pp 1-14.

48. Ye, H.-Y.; Zhang, Y.; Fu, D.-W.; Xiong, R.-G., An Above-Room-Temperature Ferroelectric Organo–Metal Halide Perovskite: (3-Pyrrolinium)($CdCl_3$). *Angewandte Chemie* **2014,** *126* (42), 11424-11429.

49. Horiuchi, S.; Kumai, R.; Tokura, Y., Hydrogen-bonded donor-acceptor compounds for organic ferroelectric materials. *Chemical Communications* **2007,** (23), 2321-2329.
50. Kumai, R.; Horiuchi, S.; Sagayama, H.; Arima, T.-h.; Watanabe, M.; Noda, Y.; Tokura, Y., Structural Assignment of Polarization in Hydrogen-Bonded Supramolecular Ferroelectrics. *Journal of the American Chemical Society* **2007,** *129* (43), 12920-12921.
51. Gotoh, K.; Asaji, T.; Ishida, H., Hydrogen bonding in two solid phases of phenazine-chloranilic acid (1/1) determined at 170 and 93 K. *Acta Crystallographica Section C* **2007,** *63* (1), o17-o20.
52. Lee, K.; Kolb, B.; Thonhauser, T.; Vanderbilt, D.; Langreth, D. C., Structure and energetics of a ferroelectric organic crystal of phenazine and chloranilic acid. *Physical Review B* **2012,** *86* (10), 104102.
53. Horiuchi, S.; Kumai, R.; Tokura, Y., Room-temperature ferroelectricity and gigantic dielectric susceptibility on a supramolecular architecture of phenazine and deuterated chloranilic acid. *Journal of the American Chemical Society* **2005,** *127*, 5010-5011.
54. Asaji, T.; Seliger, J.; Žagar, V.; Sekiguchi, M.; Watanabe, J.; Gotoh, K.; Ishida, H.; Vrtnik, S.; Dolinšek, J., Phase transition and temperature dependent electronic state of an organic ferroelectric, phenazine–chloranilic acid (1:1). *Journal of Physics: Condensed Matter* **2007,** *19* (22), 226203.
55. Noohinejad, L.; Mondal, S.; Ali, S. I.; Dey, S.; van Smaalen, S.; Schonleber, A., Resonance-stabilized partial proton transfer in hydrogen bonds of incommensurate phenazine-chloranilic acid. *Acta Crystallographica Section B* **2015,** *71* (2), 228-234.
56. Allen, F. H.; Kennard, O.; Watson, D. G.; Brammer, L.; Orpen, A. G.; Taylor, R., Tables of bond lengths determined by X-ray and neutron diffraction. Part 1. Bond lengths in organic compounds. *Journal of the Chemical Society, Perkin Transactions 2* **1987,** (12), S1-S19.
57. Noohinejad, L.; Mondal, S.; Wölfel, A.; Ali, S. I.; Schönleber, A.; van Smaalen, S., Ferroelectricity of Phenazine–Chloranilic Acid at T = 100 K. *Journal of Chemical Crystallography* **2014,** *44* (8), 387-393.
58. Kimura, T.; Goto, T.; Shintani, H.; Ishizaka, K.; Arima, T.; Tokura, Y., Magnetic control of ferroelectric polarization. *Nature* **2003,** *426* (6962), 55-58.
59. Giovannetti, G.; Kumar, S.; Stroppa, A.; van den Brink, J.; Picozzi, S., Multiferroicity in TTF-CA Organic Molecular Crystals Predicted through *Ab*-Initio Calculations. *Physical Review Letters* **2009,** *103* (26), 266401.

60. Okamoto, H.; Mitani, T.; Tokura, Y.; Koshihara, S.; Komatsu, T.; Iwasa, Y.; Koda, T.; Saito, G., Anomalous dielectric response in tetrathiafulvalene-*p*-chloranil as observed in temperature- and pressure-induced neutral-to-ionic phase transition. *Physical Review B* **1991,** *43* (10), 8224-8232.
61. Tokura, Y.; Koshihara, S.; Iwasa, Y.; Okamoto, H.; Komatsu, T.; Koda, T.; Iwasawa, N.; Saito, G., Domain-wall dynamics in organic charge-transfer compounds with one-dimensional ferroelectricity. *Physical Review Letters* **1989,** *63* (21), 2405-2408.
62. Girlando, A.; Pecile, C.; Torrance, J. B., A key to understanding ionic mixed stacked organic solids: tetrathiafulvalene-bromanil (TTF-BA). *Solid State Commun.* **1985,** *54*, 753-759.
63. Horiuchi, S.; Kumai, R.; Okimoto, Y.; Tokura, Y., Chemical approach to neutral–ionic valence instability, quantum phase transition, and relaxor ferroelectricity in organic charge-transfer complexes. *Chemical Physics* **2006,** *325* (1), 78-91.
64. Ishibashi, S.; Terakura, K., First-principles study of spontaneous polarization in tetrathiafulvalene-p-chloranil (TTF-CA). *Physica B: Condensed Matter* **2010,** *405* (11, Supplement), S338-S340.
65. Giovannetti, G.; Kumar, S.; Stroppa, A.; van den Brink, J.; Picozzi, S., Multiferroicity in TTF-CA Organic Molecular Crystals Predicted through Ab Initio Calculations. *Physical Review Letters* **2009,** *103* (26), 266401.
66. Girlando, A.; Painelli, A.; Bewick, S. A.; Soos, Z. G., Charge fluctuations and electron–phonon coupling in organic charge-transfer salts with neutral–ionic and Peierls transitions. *Synthetic Metals* **2004,** *141* (1–2), 129-138.
67. Kobayashi, K.; Horiuchi, S.; Kumai, R.; Kagawa, F.; Murakami, Y.; Tokura, Y., Electronic Ferroelectricity in a Molecular Crystal with Large Polarization Directing Antiparallel to Ionic Displacement. *Physical Review Letters* **2012,** *108* (23), 237601.
68. Torrance, J. B., Anomalous nature of neutral-to-ionic phase transition in tetrathiafulvalene-chloranil. *Physical Review Letters* **1981,** *47*, 1747-1750.
69. Torrance, J. B.; Vazquez, J. E.; Mayerle, J. J.; Lee, V. Y., Discovery of a neutral-to-ionic phase transition in organic materials. *Physical Review Letters* **1981,** *46*, 253-257.
70. Kirova, N.; Brazovskii, S., Electronic ferroelectricity in carbon based materials. *Synthetic Metals* **2016,** *216*, 11-22.
71. Chen, J.; Hu, L.; Deng, J.; Xing, X., Negative thermal expansion in functional materials: controllable thermal expansion by chemical modifications. *Chemical Society Reviews* **2015,** *44* (11), 3522-3567.

72. Mary, T. A.; Evans, J. S. O.; Vogt, T.; Sleight, A. W., Negative Thermal Expansion from 0.3 to 1050 Kelvin in ZrW_2O_8. *Science* **1996,** *272* (5258), 90-92.
73. Rodriguez, E. E.; Llobet, A.; Proffen, T.; Melot, B. C.; Seshadri, R.; Littlewood, P. B.; Cheetham, A. K., The role of static disorder in negative thermal expansion in ReO_3. *Journal of Applied Physics* **2009,** *105* (11), 114901.
74. Greve, B. K.; Martin, K. L.; Lee, P. L.; Chupas, P. J.; Chapman, K. W.; Wilkinson, A. P., Pronounced Negative Thermal Expansion from a Simple Structure: Cubic ScF_3. *Journal of the American Chemical Society* **2010,** *132* (44), 15496-15498.
75. Goodwin, A. L.; Calleja, M.; Conterio, M. J.; Dove, M. T.; Evans, J. S. O.; Keen, D. A.; Peters, L.; Tucker, M. G., Colossal Positive and Negative Thermal Expansion in the Framework Material $Ag_3[Co(CN)_6]$. *Science* **2008,** *319* (5864), 794-797.
76. Cliffe, M. J.; Hill, J. A.; Murray, C. A.; Coudert, F.-X.; Goodwin, A. L., Defect-dependent colossal negative thermal expansion in UiO-66(Hf) metal-organic framework. *Physical Chemistry Chemical Physics* **2015,** *17* (17), 11586-11592.
77. Mullaney, B. R.; Goux-Capes, L.; Price, D. J.; Chastanet, G.; Létard, J.-F.; Kepert, C. J., Spin crossover-induced colossal positive and negative thermal expansion in a nanoporous coordination framework material. *Nature Communications* **2017,** *8* (1), 1053.
78. Arvanitidis, J.; Papagelis, K.; Margadonna, S.; Prassides, K.; Fitch, A. N., Temperature-induced valence transition and associated lattice collapse in samarium fulleride. *Nature* **2003,** *425* (6958), 599-602.
79. Margadonna, S.; Prassides, K.; Chondroudi, M.; Salvador, J. R.; Kanatzidis, M. G., Temperature-induced abrupt volume inflation in the mixed-valence ternary Zintl phase $Yb_8Ge_3Sb_5$. *Chemical Communications* **2005,** (46), 5754-5756.
80. Mukhopadhyay, S.; Gutmann, M. J.; Jura, M.; Jochym, D. B.; Jimenez-Ruiz, M.; Sturniolo, S.; Refson, K.; Fernandez-Alonso, F., Ferroelectric behaviour in solid croconic acid using neutron scattering and first-principles density functional theory. *Chemical Physics* **2013,** *427*, 95-100.
81. Azuma, M.; Chen, W.-t.; Seki, H.; Czapski, M.; Olga, S.; Oka, K.; Mizumaki, M.; Watanuki, T.; Ishimatsu, N.; Kawamura, N.; Ishiwata, S.; Tucker, M. G.; Shimakawa, Y.; Attfield, J. P., Colossal negative thermal expansion in $BiNiO_3$ induced by intermetallic charge transfer. *Nature Communications* **2011,** *2*, 347.
82. Takenaka, K.; Okamoto, Y.; Shinoda, T.; Katayama, N.; Sakai, Y., Colossal negative thermal expansion in reduced layered ruthenate. *Nature Communications* **2017,** *8*, 14102.
83. Panda, M. K.; Centore, R.; Causà, M.; Tuzi, A.; Borbone, F.; Naumov, P., Strong and Anomalous Thermal Expansion Precedes the Thermosalient Effect in Dynamic Molecular Crystals. *Scientific Reports* **2016,** *6*, 29610.

84. Das, D.; Jacobs, T.; Barbour, L. J., Exceptionally large positive and negative anisotropic thermal expansion of an organic crystalline material. *Nature Materials* **2010,** *9* (1), 36-39.

85. Das, D.; Barbour, L. J., Uniaxial negative thermal expansion induced by moiety twisting in an organic crystal. *CrystEngComm* **2018,** *20* (35), 5123-5126.

86. Fortes, A. D.; Suard, E.; Knight, K. S., Negative linear compressibility and massive anisotropic thermal expansion in methanol monohydrate. *Science* **2011,** *331* (6018), 742-746.

87. Panda, M. K.; Runčevski, T.; Chandra Sahoo, S.; Belik, A. A.; Nath, N. K.; Dinnebier, R. E.; Naumov, P., Colossal positive and negative thermal expansion and thermosalient effect in a pentamorphic organometallic martensite. *Nature Communications* **2014,** *5*, 4811.

88. Haas, S.; Batlogg, B.; Besnard, C.; Schiltz, M.; Kloc, C.; Siegrist, T., Large uniaxial negative thermal expansion in pentacene due to steric hindrance. *Physical Review B* **2007,** *76* (20), 205203.

89. Shmyt'ko, I. M.; Afonikova, N. S.; Torgashev, V. I., Anomalous states of the structure of $(NH_4)_2SO_4$ crystals in the temperature range 4.2–300 K. *Physics of the Solid State* **2002,** *44* (12), 2309-2317.

90. Szafranski, M., Strong negative thermal expansion and relaxor ferroelectricity driven by supramolecular patterns. *Journal of Materials Chemistry C* **2013,** *1* (47), 7904-7913.

91. Liu, Z.; Gao, Q.; Chen, J.; Deng, J.; Lin, K.; Xing, X., Negative thermal expansion in molecular materials. *Chemical Communications* **2018,** *54* (41), 5164-5176.

92. Saha, B. K., Thermal Expansion in Organic Crystals. *Journal of the Indian Institute of Science* **2017,** *97* (2), 177-191.

Chapter 2 Experimental and data analysis methods

Overview

This chapter will discuss the experimental details and methods used in the analysis of the materials reported in this thesis: diffraction methods (single crystal and powder X-ray and neutron) and the complementary techniques used (solid state nuclear magnetic resonance, thermal analysis and second harmonic generation). The concepts underlying the symmetry mode analysis (used in Chapter 3 and 4) are also introduced.

2.1 X-ray diffraction

2.1.1 The diffraction of X-rays by crystalline solids

Diffraction is an interference phenomenon which occurs when an electromagnetic wave bends around obstacles or slits. A crystalline material can be regarded as periodically repeating planes of atoms and each set of the parallel planes can be characterised by an interplanar spacing d_{hkl}. It can be likened to an optical grating, and thus should be able to diffract X-ray radiation. When the necessary geometrical condition is fulfilled the diffraction maxima occur due to constructive interference between neighbouring reflected X-ray beams. This geometrical condition (the so-called Bragg's law) is given in Equation 2.1 and depicted in Figure 2.1. As shown in Figure 2.1, beam 22' travels an extra distance XYZ (highlighted in red) compared to beam 11'. In order for the two to be "in phase" and interfere constructively, the difference in path lengths XYZ must equal an integer multiple (n) of the wavelength.

$$n\lambda = 2d_{hkl}sin\theta$$

Equation 2.1

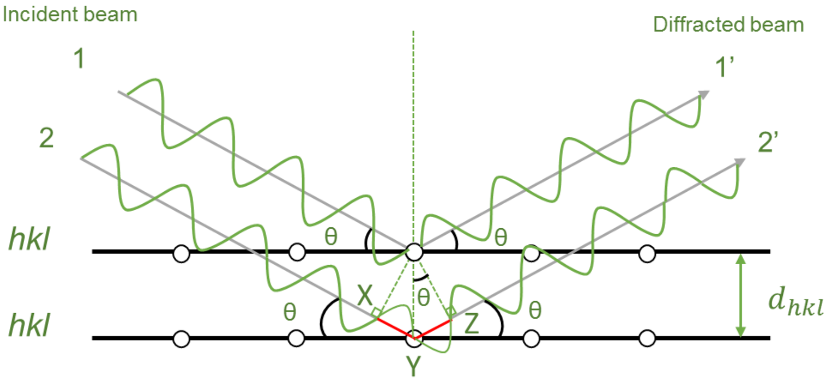

Figure 2.1: The schematic representation of Bragg's law.

θ is the incident and reflected angle and λ is the wavelength of the radiation. One important application of Bragg's law is in the determination of the unit cell parameters of crystalline materials. The distance d_{hkl} between adjacent *hkl* planes is closely related to the unit cell parameters. For example, this relationship is expressed in Equation 2.2 for a monoclinic crystal system. Similar equations exist for other crystal systems Once we use Bragg's law to calculate the value of d_{hkl} from the positions of the observed peaks, we can determine the unit cell parameters.

$$\frac{1}{{d_{hkl}}^2} = \left(\frac{h^2}{a^2} + \frac{k^2 \sin^2\beta}{b^2} + \frac{l^2}{c^2} - \frac{2hl\cos\beta}{ac}\right)\cos\beta$$

Equation 2.2

Though Bragg's law gives a simple and convenient geometric expression for the diffraction condition, it should be noted that "reflection off planes" is not a correct physical picture of this phenomenon.

X-rays are scattered coherently by the electrons in an atom. The scattering power of an atom is the resultant of the individual scattering by its electrons. The atomic scattering factor, f_n, is a term used to describe the X-ray scattering power of an atom. In order to calculate the total scattering power from a crystal, the scattering from all individual atoms in the unit cell is added together, resulting in a quantity called the structure factor F_{hkl}. The calculated structure factor (F_{hkl}) depends on the fractional atomic coordinates (x_n, y_n, z_n) and the scattering factor (f_n) of each atom in the unit cell. The mathematical relationship for this is expressed as:

$$F_{hkl} = \sum_n f_n e^{2\pi i(hx_n + ky_n + lz_n)}$$

Equation 2.3

For each individual *hkl* reflection, the intensities (I_{hkl}) of the X-ray scattered are proportional to the square modulus of the structure factor ($|F_{hkl}|^2$). Equation 2.4 is used to work out the intensity of a reflection:

$$I_{hkl} = cL(2\theta)P(2\theta)A(2\theta)j_{hkl}|F_{hkl}|^2$$

Equation 2.4

where c, L, P and A are the scale, Lorentz, polarisation and absorption factors respectively; j_{hkl} is the multiplicity which stands for the number of symmetry equivalent reflections.

2.1.2 Laboratory X-ray source

In the laboratory, X-ray radiation is commonly generated in an X-ray tube (Figure 2.2(a)) by accelerating a beam of electrons and shooting them onto a metal target, such as copper or molybdenum. An X-ray tube comprises a cathode fitted with a filament and a metal anode. The heated filament produces electrons that are accelerated under vacuum by high voltage. The energetic beam of electrons is directed to hit the anode metal. The wavelength of the emitted energy caused by the collision between the high-speed electrons and the metal lies in the X-ray wavelength range. For instance, the resulting X-ray spectrum of copper is shown in Figure 2.2(b). It consists of a broad continuous spectrum of X-rays known as white radiation (bremsstrahlung radiation) and a second discontinuous spectrum of X-rays called characteristic radiation. White radiation results from the rapid deceleration of high-speed electrons when they strike a metal atom. When the energy of the accelerated electrons is higher than a certain value, the characteristic spectrum of X-rays is observed. Figure 2.2(c) illustrates the process of generating characteristic X-ray radiation in the copper atom. The incoming electron has sufficient energy to ionise an electron in the inner 1s orbital or K shell. An electron from other orbitals, typically outer 2p (L shell) or 3p (M shell) levels, will rapidly drop down to occupy the vacancy in the 1s level. A characteristic X-ray arising from 2p→1s transition is called Kα radiation which is a mixed radiation of $K\alpha_1$ and $K\alpha_2$ with an average wavelength of 1.5418 Å. The radiation produced by 3p→1s transition is called K_β radiation with a wavelength of 1.3922 Å.

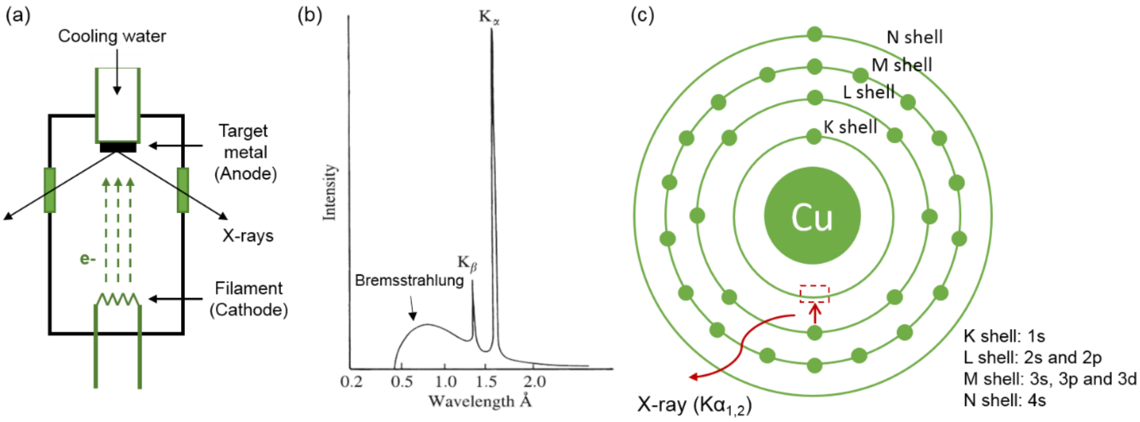

Figure 2.2: (a) A sketch of a sealed X-ray tube. (b) The characteristic spectrum of copper superimposed on the white radiation spectrum. (c) The generation of $K\alpha_{1,2}$ radiation by 2p→1s transition in copper. Figure (b) is reproduced directly from reference 1.[1]

2.1.3 Synchrotron X-ray source

A synchrotron is a particle accelerator in which high-energy charged particles are accelerated to reach nearly the speed of light in a circular orbit. As shown in Figure 2.3, it comprises an electron gun, linear accelerator, booster synchrotron, storage ring and several beamlines distributed tangentially to the ring. When an electron beam is produced by the electron gun, it enters the linear accelerator, gaining extremely high energy. Then, the accelerated electrons are injected into the second accelerator, booster ring, in which electrons reach their maximum speed. These high energy electrons finally move to the storage ring and generate intense synchrotron radiation as they move in an approximately circular path. The resulting radiation can then be directed into each experimental working area via a beamline. In this PhD project, data were collected on beamline I11, which is designed for high-resolution powder diffraction measurements, at the Diamond Light Source. The diffractometer is equipped with multi-analysing crystals (MAC) and photomultiplier detectors. An Oxford Cryosystems Cryostream device was used to control temperature for variable temperature measurements.

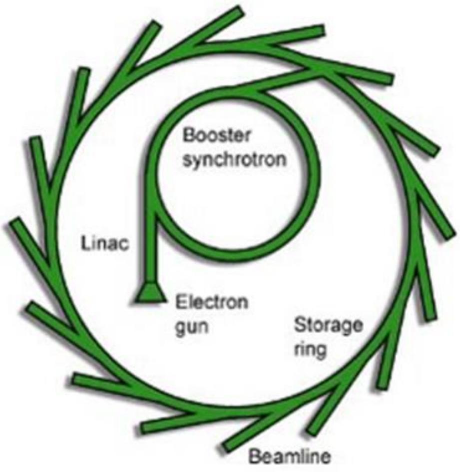

Figure 2.3: The design of the Diamond Light Source synchrotron. This figure is reproduced directly from reference 2.[2]

2.2 Single crystal X-ray diffraction

Single crystal X-ray diffraction is a powerful technique to solve the structures of crystalline materials. It can not only determine the unit cell parameter and space group but also provide accurate and precise information about atomic coordinates, and from these bond lengths and bond angles.

2.2.1 Crystal growth and selection

All crystals suitable for single crystal X-ray diffraction were grown using solution evaporation methods in 10 mL vials loosely capped with lids. An adequate amount of each material was dissolved in a minimal volume of solvent in order to prepare the nearly saturated solution. Specific masses and volumes are detailed in each chapter. Two ways were attempted to induce crystallisation from solution, either leaving the solution to cool slowly to room temperature or placing the solution in a 5°C fridge. Single crystals were visually assessed by using a polarizing microscope. When rotating the polarizer under the microscope, a single crystal will extinguish light uniformly.

2.2.2 Crystal mounting and centring

The crystal is mounted on a Kapton loop using perfluoropolyether oil if the measurement is carried out below 240 K. Since the oil is liquid above 240 K, the crystal needs to be attached to a glass fibre using a small drop of epoxy resin if the experimental temperature is higher than 240 K. After mounting a single crystal on the diffractometer, the centring of the crystal within the X-ray beam was carried out by adjusting the crystal position in two orthogonal directions until no translation occurred on rotation.

2.2.3 Instrumentation

Three laboratory diffractometers were used to examine the selected single crystals and collect the data from the most suitable single crystal. Information for each single crystal diffractometer is summarised in Table 2.1

Table 2.1: Information on single crystal diffractometers used.

	Oxford Gemini S Ultra diffractometer	**Bruker D8 Venture diffractometer**	**Bruker SMART 6000 diffractometer**
Abbr.	OD	D8V	6K
Power	50 kV, 35 mA	50 kV, 1.0 mA	50 kV, 35 mA
Radiation	Mo Kα	Mo Kα or Cu Kα	Mo Kα
Wavelength	0.7107 Å	0.7107 Å or 1.5418 Å	0.7107 Å
Detector	Charge-coupled device (CCD) area detector	Photon100 CMOS detector	Charge-coupled device (CCD) area detector

The “OD” was the most frequently used diffractometer for crystal screening and full data collection in this work. It is fitted with a CCD area detector, a Mo tube and graphite monochromator. A Cryostream Plus Controller was used to control the experimental temperature over the range of 120 K to 350 K. The raw data sets collected on “OD” were processed using the CrysAlisPro software[3].

The “D8V” was used to examine small needle-like single crystals in this work. Only low-temperature data sets (120 K) were collected on the “D8V”. It is equipped with an IμS-microsource, focusing mirrors and a Photon100 CMOS detector. It can be switched between Mo Kα and Cu Kα radiation. The APEX3 software[4] was used for data collection, data reduction and unit cell determination.

The “6K” with a CCD area detector and a Mo tube is controlled using Bruker’s SMART software suite[4]. It is also fitted with an Oxford Cryosystems Nitrogen Cryostream 600® cryostat. Crystal screening and data collection were attempted at high-temperature (450 K and above) on the “6K”.

2.2.4 Structure solution from single crystal data

The crystal structure, expressed as electron density, is the Fourier transform of the structure factor. If both the amplitude and phase of the structure factor for each reflection are known, the electron density can then be derived based on Equation 2.5, and thus the positions of individual atoms in a unit cell can be determined.

$$\rho(x,y,z) = \frac{1}{V}\sum_{h}\sum_{k}\sum_{l} F_{hkl}\, e^{-2\pi i(hx+ky+lz)}$$

Equation 2.5

However, a phase problem is encountered during the experiment due to the fact that we cannot determine the phase of the structure factor from Equation 2.4. In order to overcome the phase problem, crystal structures are typically determined by direct methods when single crystal diffraction data is available. The term “direct methods (DM)” refers to a method that attempts to estimate the phase of structure factor directly from their amplitudes.[5] In this work the SIR92[6] package interfaced with the CRYSTALS[7] software was used for structure solution. Once a suitable model was found, crystal structure refinement was carried out. In a crystal structure refinement, either $\sum w(F_o - F_c)^2$ or $\sum w(F_o^2 - F_c^2)^2$ is minimized in order to obtain an optimized crystal structure (F_o is the amplitude of the observed structure factor from experiment, F_c is the amplitude of the calculated structure factor from the constructed model and w is weight). We used F^2 refinements against the single crystal data in our work. All non-hydrogens were refined anisotropically. Missing hydrogens were located using Fourier difference maps and either refined with isotropic temperature factors or fixed geometrically (strategies used for refining hydrogen atoms are given in experimental section in each chapter). A three parameter Chebyshev weighting scheme[8] was then applied to enhance the precision of the refinement. The conventional R-value (R) and the weighted R-value (R_w) given in Equation 2.6 and 2.7 are used to reflect the quality of the structure refinement.

$$R = \frac{\sum \left| |F_{obs}| - |F_{calc}| \right|}{\sum |F_{obs}|}$$

Equation 2.6

$$R_w = \sqrt{\frac{\sum w_i ({F_{obs}}^2 - {F_{calc}}^2)^2}{\sum w_i ({F_{obs}}^2)^2}}$$

Equation 2.7

2.3 Powder X-ray diffraction

Powder X-ray diffraction (PXRD) is an analytical technique that is used routinely for qualitative analysis, phase identification and purity assessment of polycrystalline materials. Moreover, it provides precise information on unit cell parameters and their temperature dependence, which can reveal phase transitions and the structural changes in a system. Powder diffraction can also be used to refine crystal structures or, in favourable cases, determine structures *ab-initio*.

Ideally, in a powder diffraction experiment, the crystallites should be randomly orientated in all directions. However preferred orientation, a phenomenon that occurs when there is a strong tendency for the crystallites to arrange in a particular direction is often observed, particularly when a sample is mounted on a flat plate. For some samples, the intensity pattern of reflections can be influenced severely by preferred orientation. Problems caused by preferred orientation can be alleviated by collecting data on samples in capillaries or by applying a preferred orientation correction (March-Dollase or spherical harmonics functions).

2.3.1 Sample preparation

Polycrystalline samples of single-component compounds were used as purchased. Two methods were used to produce a polycrystalline sample of a two-component compound: 1) gentle grinding of single crystals, 2) co-grinding of two components when single crystals do not form. For flat plate measurements, samples were evenly sprinkled onto a silicon plate by passing through a sieve (150 or 200 mesh). For laboratory capillary measurements, as shown in Figure 2.4, samples were loaded into 0.7 mm external diameter borosilicate glass capillaries to a length of 38 mm. The capillary was sealed to a glass holder using superglue and then attached to the goniometer head.

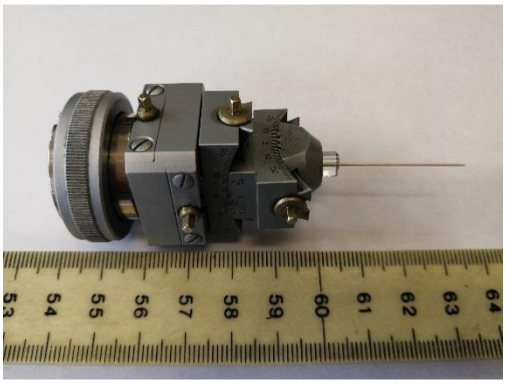

Figure 2.4: A prepared sample for laboratory capillary measurements.

2.3.2 Instrumentation

Three Bruker d8 Advanced diffractometers were used to collect powder diffraction data in this work. Information for each diffractometer is summarised in Table 2.2.

Table 2.2: Information of Bruker d8 Advanced diffractometers

	Bruker d8 Advanced diffractometers		
Abbr.	d6	d7	d9
Configuration	Transmission	Reflection or transmission	Reflection
Power	50 kV, 50 mA	40 kV, 40 mA	40 kV, 40 mA
Radiation	Mo Kα	Cu Kα	Cu Kα
Wavelength	0.7093 Å	1.5418 Å	1.5418 Å
Detector	LYNXEYE_XE	LYNXEYE	LYNXEYE

The “d6” is equipped with an LYNXEYE_XE detector and uses a Mo tube and Ge(III) monchromator to produce Mo Kα (λ = 0.7093 Å) radiation which is conditioned using a 1 mm exit slit off the monochromator. High-quality room temperature data for the purpose of structure solution were acquired in capillary mode. Variable temperature measurements were also performed over temperatures between 100 K and 500 K. An

Oxford Cryosystems Crystream Plus device was used to set the experimental temperature.

The “d7” is equipped with an LYNXEYE detector and uses a Cu tube to generate Cu $K\alpha_{1,2}$ radiation (λ = 1.5418 Å). It can be switched between flat-plate mode and capillary mode. It was used for a routine scan and rapid phase identification in flat-plate mode with a variable divergence slit set to illuminate a 6 × 12 mm sample area (v6). In capillary mode, a Goebel mirror produces a parallel incident beam and variable temperature measurements can be carried out. An Oxford Cryosystems Cryostream Plus device was used to set the experimental temperature for variable temperature measurements.

The “d9” is also equipped with an LYNXEYE detector and a Cu tube to produce Cu $K\alpha_{1,2}$ radiation (λ = 1.5418 Å) which is conditioned using a v6 variable divergence slit. All the data collections were performed in flat-plate mode on the “d9”. When collecting data over a temperature range between 12 K and 300 K, the “d9” is configured with an Oxford Cryosystems PheniX cryostat. Data can also be collected between 300 K and 1500 K when the “d9” is configured with an Anton Paar HTK1200 furnace.

2.3.3 The Rietveld method

Powder diffraction data were analysed by the Rietveld method using TOPAS Academic software.[9-10] The Rietveld method is a structure refinement method in which powder diffraction patterns are calculated and fitted to the observed data by varying a number of adjustable parameters.[11-12] The parameters can be generally divided into two categories: those from the structural model and instrumental parameters. Rietveld refinement for analysing powder data is based on non-linear least squares. The least-squares residual (S_y) is expressed as the weighted difference between the experimental pattern and the simulated pattern in terms of the peak intensity at each experimentally measured point. Equation 2.8 defines the quantity minimised in a refinement.

$$S_y = \sum_i w_i[y_i(obs) - y_i(calc)]^2$$

Equation 2.8

Here, $y_i(obs)$ is the observed intensity at each step and $y_i(calc)$ is the calculated intensity at each step. The weight, w_i, is equal to the reciprocal of the experimental variance ($1 / \sigma^2$). In order to judge when the best fit is attained, several criteria of fit are introduced. The R-weighted pattern (R_{wp}), the statistically expected R value (R_{exp}) and the goodness-of-fit (GOOF, $\sqrt{\chi^2}$) are defined in Equation 2.9, Equation 2.10 and Equation 2.11, respectively.[12]

$$R_{wp} = \sqrt{\frac{\sum w_i (y_i - y_{ci})^2}{\sum w_i (y_i)^2}}$$

Equation 2.9

$$R_{exp} = \sqrt{\frac{(N - P)}{\sum W_i (y^i)^2}}$$

Equation 2.10

$$GOOF = \sqrt{\chi^2} = \frac{R_{wp}}{R_{exp}}$$

Equation 2.11

In Equation 2.10, N represents the number of observations while P is the number of parameters.

2.3.4 Structure solution from powder data

Even though structure determination from single crystal diffraction is a routine method, solving crystal structures from powder diffraction is needed when materials can only be prepared as polycrystalline samples. Structure determination from powder diffraction data is much more challenging and in this work involved six steps:

1) Extraction of peak positions,
2) Peak indexing for unit cell parameter determination,
3) Pawley fitting to confirm the unit cell and extract intensities,
4) Inspection of the systematic absences following the Pawley fitting,
5) Structure solution attempted in all possible space groups by simulated annealing or by local Rietveld minimisation,
6) Final structural refinement.

The method for solving structures from powder diffraction used here is distinct from the one adopted by single crystal diffraction. In contrast to the reciprocal space method used in single crystal work, our adopted approach for powder diffraction data aims to explore all the possibilities in real space. Therefore, in step 5), efforts are devoted to generating an enormous number of possible structural arrangements to test. A structure-solving program, such as DASH[13], implement the global optimization method of simulated annealing (SA) in order to search for the global minimum among all the local minima in direct space. In SA, a procedure similar to the Monte-Carlo method is involved in generating trial structural models by randomising the structural parameters. For an organic molecular compound, rigid bodies or z-matrixes are used to describe molecules. The use of rigid bodies reduces the number of adjustable parameters. We only need to determine the rotations of the rigid body around three orthogonal coordinates, the shifts of the rigid body in *xyz* directions and the torsion angles between certain bonds if needed. The agreement between the calculated intensities of reflections from the structural models and the experimental intensities is assessed by χ^2. In each step χ^2 is calculated from a new structure model by changing the parameters slightly. If the new ${\chi_j}^2$ is smaller than the old one ${\chi_i}^2$, the new set of structure parameters will always be adopted since it yields an improved fit, and it will be a better structure solution than the old one. If the new ${\chi_j}^2$ is larger than the old one, the new set of parameters will be either accepted or rejected according to the Boltzmann distribution:

$$e^{\left(-\frac{{\chi_j}^2-{\chi_i}^2}{kT}\right)}$$

The temperature T in the expression does not refer to a real temperature. It was chosen to have a high value at the beginning to give a high probability to accept a parameter set which lead to worse χ^2. This uphill move is crucial as it allows escape from a local minimum. The probability of accepting a worse parameter set decreases with decreasing temperature. After several runs each involving millions of iterations, the algorithm terminates when the user-set maximum number of moves is reached.

The SA algorithm used in TOPAS slightly differs from the conventional SA discussed above.[14] When solving crystal structure from powder diffraction data in TOPAS, Rietveld refinement is performed for each trial structure. In our work, both methods always led to similar models.

2.4 Neutron single crystal diffraction

Single crystal neutron diffraction data were collected on the SXD instrument of the ISIS Neutron and Muon Source at the Rutherford Appleton laboratory. The crystal was attached to a goniometer head using adhesive Al foil and placed in a rotating bottom-loading CCR. Data were collected for several crystal orientations, typically for 3 hours each. Initial data reduction was done using SXD2001[15] software within the IDL virtual machine, and refinement of the structural model was carried out in Jana2006[16]. The fractional coordinates and anisotropic atomic displacement factors were refined for all atoms against F_{hkl}^2.

2.5 Solid state nuclear magnetic resonance (SSNMR)

Solid state NMR studies magnetic nuclei under an external magnetic field by observing their responses to radiofrequency radiation. In this thesis, we used ^{1}H or ^{13}C solid state NMR spectra in support of X-ray diffraction data. In the presence of an external magnetic field, the nucleus of an atom possesses two spin states that differ in energy. The orientation of the high energy spin state is parallel to the external magnetic field; while the orientation of the low energy spin state is antiparallel to the applied magnetic field. The difference in populations of high energy and low energy spin states gives rise to the NMR signals. Samples are loaded into a probe and spun at high speed at the magic angle of 54.74° to the applied magnetic field in order to average all dipolar interactions and anisotropies to zero and obtain relatively narrow linewidths.

Solid state NMR spectra can provide information on the contents of the unit cell. It is a powerful auxiliary technique for determining the local environment and dynamics at the molecular level. When an organic material undergoes a structural transformation, the symmetry is broken, which leads to changes in the environment of atoms in the molecule. As a result, ^{1}H or ^{13}C spectra can help us probe the changes in arrangements of hydrogens or carbons. Solid state NMR spectra were acquired by Dr David Apperley of the Durham Solid State NMR service.

2.6 Second harmonic generation (SHG)

Second harmonic generation is a nonlinear optical phenomenon involving the halving of the wavelength of incident light. SHG does not occur in a material when a centre of inversion exists. As a result, the nonlinear coefficient vanishes in the 11 centrosymmetric point groups. In addition, the three noncentrosymmetric-nonpolar point groups 422, 622 and 432 also do not show SHG signals. This makes the second harmonic generation technique a powerful tool to acquire symmetry information on a material. Any crystal system that belongs to the above 14 point groups will not display SHG; on the other hand, crystals that adopt the other 18 point groups can be SHG active. One of the widely used applications of SHG is to detect ferroelectric phase transitions. Since ferroelectric materials usually undergo a polar-to-nonpolar phase transition, the appearance of the SHG signal at low temperature proves the lack of a centre of inversion and in turn indicates the emergence of potential ferroelectricity. The vanishing of the SHG signals at higher temperature is strong evidence for the formation of a nonpolar phase. SHG measurements were performed by Dr Weiguo Zhang from University of Houston using equipment described in the literature.[17]

2.7 CHN elemental analysis

The CHN elemental analysis (or CHN microanalysis) is an analytic method to determine the weight percentage of carbon, hydrogen and nitrogen in a sample. The sample is weighed accurately to one millionth of a gram and combusted completely at a temperature above 1800°C to form CO_2, N_2, N_xO_y, H_2O and other by-products. The quantity of each gas is recorded by the detector, and therefore the weight percentages can be calculated. The CHN elemental analysis was performed by Dr Emily Unsworth of the Durham elemental analysis service on an Exeter CE-440 elemental analyser.

2.8 Thermal analysis

Differential scanning calorimetry (DSC) analysis

Differential scanning calorimetry is a thermoanalytical technique that monitors the difference in the amount of heat required to increase the temperature of a sample and a reference in order to maintain the sample at the same temperature as the reference. The result of a DSC is presented in a curve of heat flux versus temperature. DSC can reveal phase transitions in a material. DSC analysis was performed by Mr William D Carswell of the Durham thermal analysis service on a Perkin Elmer Pyris 1 DSC instrument.

Thermogravimetric (TGA) analysis

Thermogravimetric analysis is a thermoanalytical technique that continuously measures the mass of a sample with respect to its initial mass with increasing temperature. From this analysis, we can obtain information on the thermal decomposition of a sample. TGA analysis was performed by Mr William D Carswell of the Durham thermal analysis service on a Perkin Elmer Pyris 1 TGA instrument.

2.9 Distortion mode analysis

Distortion mode analysis is a powerful technique for understanding materials that undergo phase transitions when analysing both single crystal and powder diffraction data. Structures before and after symmetry-lowering phase transitions always possess a group-subgroup relationship (as discussed in section 1.2.2), and distortion mode analysis is motivated by this relationship.

To understand the subtle change associated with symmetry-lowering phase transitions, we can employ three approaches to construct the parameter set when conducting the lower symmetry refinement:

1) Traditional fractional atomic coordinates *xyz* approach,
2) Traditional rigid body approach,
3) Symmetry-motivated distortion mode approach using either atomic coordinates or rigid bodies.

The first approach needs one to define three displacive parameters along three axes for each atom. However, it is often not feasible to independently refine individual atomic coordinates for a complex organic material when only powder diffraction data are available. We therefore did not apply the application of traditional atomic *xyz* coordinates in most of our work. Option 2, the use of rigid bodies, allows us to minimise the number of necessary parameters. The term “rigid body” refers to a group of atoms that rotates and translates as an entirety with invariant internal coordinates in the refinement. Rigid bodies are typically defined in terms of Cartesian coordinates or as a z-matrix and each rigid body normally needs three rotational parameters and three translational parameters to describe its movements. Even though the rigid body approach is more promising than the conventional *xyz* atomic coordinates approach due to the fact that it substantially decreases the number of adjustable parameters, it is often not the most helpful way to understand the nature of a phase transition.

The symmetry-adapted distortion modes approach involving rigid bodies turns out to be the most effective way to investigate molecular phase transitions. The term “distortion” here describes the symmetry-lowering structural change induced by physical order parameters such as rotations, atomic displacements, strain and occupancies. In this method, we view the lower symmetry structure as the distorted “child” and the higher symmetry structure as the “parent”. The distorted structures are described by the parent high symmetry structure plus the amplitudes of symmetry-breaking distortion modes. The advantages of using symmetry distortion modes are striking:

1) We often only need a small number of important parameters to describe the phase transition.
2) We can easily quantify the structural distortion that breaks the parent symmetry.
3) The amplitude of each distortion mode is defined to be zero in the parent phase. Once we know the amplitude for each distortion mode in the child phase, we can reveal the importance of individual distortions.
4) We can easily and graphically understand the relationship between the parent and the distorted child structures.

Because of the power of symmetry-adapted distortion modes, Rietveld refinement including a distortion-mode description can help understand the essence of a phase transition. This has been done for a number of structural transitions[18-20] and more recently extended to investigate magnetic transitions[10, 21-22], where axial vectors are set up to describe magnetic spins. The same "language" used to describe magnetic spins can be applied to describe the motion of rigid molecules (see next section). In this work, Rietveld refinements based on rigid-body rotational distortion modes or strain modes were exploited to elucidate phase transitions. All symmetry-mode calculations were performed using the ISODISTORT software.[23] The label for each mode in ISODISTORT language contains the irreducible representation (irrep)[24-25] of the parent point group symmetry followed by the Wyckoff site using the conventional molecular spectroscopy notations. Additional subscripts (_1 and _2) are used to differentiate two distinct modes belonging to the same point group irrep.

2.9.1 Rotational mode analysis

In a rotational mode analysis of a molecular system, each rotation mode corresponds to a symmetry-allowed rotational moment and is described with a unique axial vector. We introduced a dummy site (a pivot point) at the centre of each molecule in the asymmetric unit. An axial-vector for a rotational mode is replaced through this pivot point. The direction of the axial-vector indicates the rotational moment direction, while the length of the vector defines the magnitude of the rotation mode in radians. It is easy to see from the rotational mode amplitude which mode is playing a leading role in breaking the parent symmetry and what molecular rotation related to the mode is important. Muller *et al.*[22] demonstrated the benefits of using rotational distortion modes to understand the octahedral rotations in $Mg(H_2O)RbBr_3$ against the traditional analytical methods. The parameter set constructed by rotational modes produces a comparable Rietveld fit to more involved methods, and it was more easily interpreted. Details and examples of these methods are included in Chapters 3 and 4.

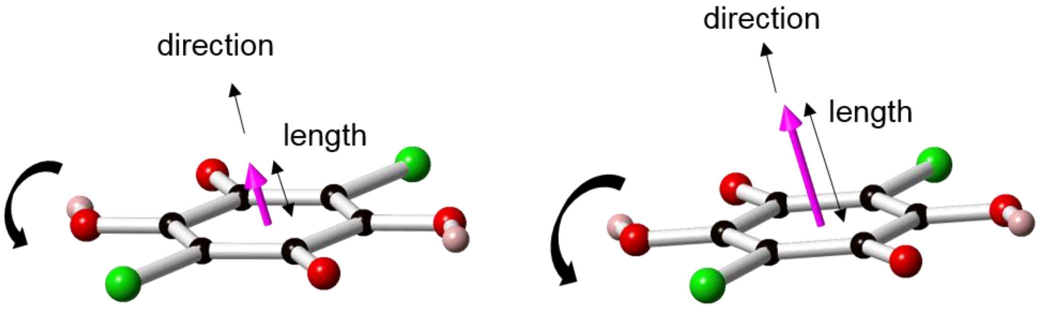

Figure 2.5: Illustration of an axial-vector for a rotational mode.

2.9.2 Strain mode analysis

Strain mode analysis is slightly different from rotational modes analysis since lattice strain is a macroscopic response to external stimuli. Strain mode amplitudes indicate the unit cell change in a child cell relative to the parent cell. It is a useful analytical method to understand unit cell distortions at phase transitions.

References

1. Hugo L, M.; Artioli, G., Experimental methods in X-ray and neutron crystallography. In *Fundamentals of Crystallography*, 3 ed.; Oxford University Press: Oxford, 2011.
2. Source, D. L. http://www.diamond.ac.uk/Home/About/How-Diamond-Works.html (accessed 10/07).
3. CrysAlis, P., Agilent technologies. *Yarnton, Oxfordshire, England* **2011**.
4. APEX, B., SAINT and SADABS. Bruker AXS Inc. Madison: 2010.
5. Main, P., Crystal Structure Analysis: Principles and Practice. In *Direct methods of crystal-structure determination*, Oxford University Press: 2009.
6. Altomare, A. C., G.; Giacovazzo, C.; Guagliardi, A.; Burla, M.C.; Polidori, G.; Camalli, M, SIR92. *Journal of Applied Crystallography* **1994,** *27*, 437.
7. Betteridge, P. W., Carruthers, J.R., Cooper, R.I., Prout, K., Watkin, D.J, CRYSTALS. *Journal of Applied Crystallography* **2003,** *36*, 1487.
8. Carruthers, J. R.; Watkin, D. J., A weighting scheme for least-squares structure refinement. *Acta Crystallographica Section A* **1979,** *35* (4), 698-699.
9. Coelho, A. A.; Evans, J. S. O.; Evans, I. R.; Kern, A.; Parsons, S., The TOPAS symbolic computation system. *Powder Diffraction* **2011,** *26* (4), S22.
10. Dinnebier Robert, E.; Leineweber, A.; Evans John, S. O., *Rietveld Refinement, Practical Powder Diffraction Pattern Analysis using TOPAS*. 2018.

11. Young, R. A., *Rietveld method*. New ed. ed.; Oxford University Press: Oxford, 1995; p [308]p : 87ill ; 24cm.
12. McCusker, L. B.; Von Dreele, R. B.; Cox, D. E.; Louer, D.; Scardi, P., Rietveld refinement guidelines. *Journal of Applied Crystallography* **1999,** *32* (1), 36-50.
13. David, W. I. F.; Shankland, K.; van de Streek, J.; Pidcock, E.; Motherwell, W. D. S.; Cole, J. C., DASH: a program for crystal structure determination from powder diffraction data. *Journal of Applied Crystallography* **2006,** *39* (6), 910-915.
14. Coelho, A., Whole-profile structure solution from powder diffraction data using simulated annealing. *Journal of Applied Crystallography* **2000,** *33* (3 Part 2), 899-908.
15. Gutmann, M., SXD2001 - a program for treating data from TOF neutron single-crystal diffraction. *Acta Crystallographica Section A* **2005,** *61* (a1), c164.
16. Petříček, V.; Dušek, M.; Palatinus, L., Crystallographic Computing System JANA2006: General features. In *Zeitschrift für Kristallographie - Crystalline Materials*, 2014; Vol. 229, p 345.
17. Ok, K. M.; Chi, E. O.; Halasyamani, P. S., Bulk characterization methods for non-centrosymmetric materials: second-harmonic generation, piezoelectricity, pyroelectricity, and ferroelectricity. *Chemical Society Reviews* **2006,** *35* (8), 710-717.
18. Kerman, S.; Campbell, B. J.; Satyavarapu, K. K.; Stokes, H. T.; Perselli, F.; Evans, J. S., The superstructure determination of displacive distortions via symmetry-mode analysis. *Acta Crystallographica Section A: Foundations of Crystallography* **2012,** *68* (2), 222-234.
19. Hatch, D. M.; Stokes, H. T.; Aleksandrov, K.; Misyul, S., Phase transitions in the perovskitelike A 2 BX 4 structure. *Physical Review B* **1989,** *39* (13), 9282.
20. Stokes, H. T.; Kisi, E. H.; Hatch, D. M.; Howard, C. J., Group-theoretical analysis of octahedral tilting in ferroelectric perovskites. *Acta Crystallographica Section B: Structural Science* **2002,** *58* (6), 934-938.
21. Senn, M. S.; Wright, J. P.; Attfield, J. P., Charge order and three-site distortions in the Verwey structure of magnetite. *Nature* **2012,** *481* (7380), 173-176.
22. Muller, M.; Dinnebier, R. E.; Dippel, A.-C.; Stokes, H. T.; Campbell, B. J., A symmetry-mode description of rigid-body rotations in crystalline solids: a case study of $Mg(H_2O)_6RbBr_3$. *Journal of Applied Crystallography* **2014,** *47* (2), 532-538.
23. Campbell, B. J.; Stokes, H. T.; Tanner, D. E.; Hatch, D. M., ISODISPLACE: a web-based tool for exploring structural distortions. *Journal of Applied Crystallography* **2006,** *39* (4), 607-614.

24. Stokes, H. T.; Hatch, D. M.; Kim, J., Images of physically irreducible representations of the 230 space groups. *Acta Crystallographica Section A: Foundations of Crystallography* **1987,** *43* (1), 81-84.

25. Stokes, H. T.; Campbell, B. J.; Cordes, R., Tabulation of irreducible representations of the crystallographic space groups and their superspace extensions. *Acta Crystallographica Section A* **2013,** *69* (4), 388-395.

Chapter 3 Unusual uniaxial negative thermal expansion behaviour associated with phase transition of chloranilic acid pyrazine (CA-Pyz)

Overview

Chloranilic acid pyrazine (CA-Pyz) undergoes a newly discovered phase transition close to 300 K. Unusual thermal expansion behaviours associated with the phase transition are also observed. In this chapter, we discuss the application of symmetry adapted distortion modes to this organic molecular compound to help understand its structural changes and the unusual temperature dependence of cell parameters during the phase transition.

3.1 Introduction

An acid-base combination is a conventional strategy to produce organic ferroelectrics via intermolecular hydrogen bonds. Anilic acid always acts as an acid component in this type of binary compound. As shown in Scheme 3.1, it can undergo a series of deprotonation processes forming monovalent or divalent species with $pK_1=0.73$ and $pK_2=3.08$.[1] It has comparable acid dissociation constants to those of carboxylic acids, indicating the relatively strong proton donating ability. This unit is also able to yield strong intra- or intermolecular hydrogen-bonding interactions through keto-enol tautomerisation (Scheme 3.2).[2] This interaction could be of use for collective proton migration and thus could be responsible for the polarity reversal in an organic ferroelectric material. Chloranilic acid phenazine[3-6] is a well-known pure organic ferroelectric containing chloranilic acid as the acidic component (as discussed in section 1.2.4). It undergoes a phase transition on cooling to 253 K, where its paraelectric phase (monoclinic $P2_1/n$) transforms to a ferroelectric phase (monoclinic $P2_1$). Hydrogen bonds play an important role in its phase transition, evidenced by the significant change in the Curie temperature of the deuterated compound.[7]

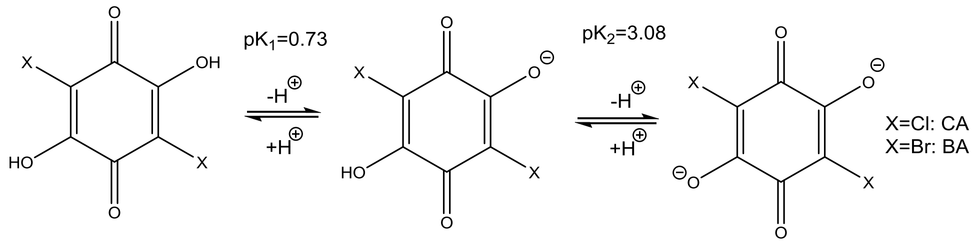

Scheme 3.1: Deprotonation and protonation process of anilic acid.

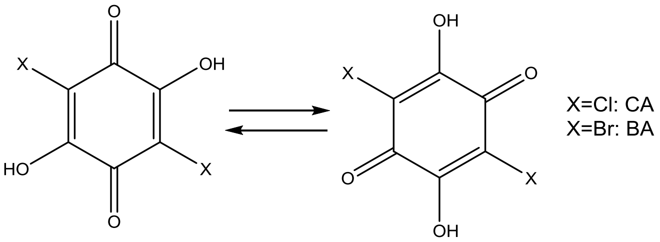

Scheme 3.2: Proton tautomerism of anilic acid.

Chloranilic acid pyrazine, abbreviated as CA-Pyz, displays a similar hydrogen bonding geometry to that found in chloranilic acid phenazine.[8] As shown in Figure 3.1, alternating chloranilic acid and pyrazine molecules are linked by intermolecular O-H…N hydrogen bonds forming a hydrogen-bonded chain along the [101] direction. The chloranilic acid and pyrazine molecular planes are perpendicular to each other, leading to a dihedral angle between these two molecular planes of 90°. The hydrogen-bonded chains stack along the *b*-axis without remarkable interactions between chains. There is no evidence for proton transfer, which indicates the formation of a neutral hydrogen bond in CA-Pyz at room temperature.[9] The donor-acceptor distance is 2.719(3) Å, and the O-H…N angle is 151(3)°. The crystal structure of CA-Pyz belongs to the monoclinic *C*2/*m* space group at room temperature with unit cell parameters of a = 8.296(5) Å, b = 6.654(2) Å, c = 10.993(2) Å, β = 101.60(3)° and V = 594.44(11) $Å^3$. If CA-Pyz exhibits ferroelectricity at low temperature, it would have to undergo a phase transition to a polar space group, presumably via proton migration in the O-H···N hydrogen bond.

This work aimed to determine the low-temperature structure and understand the behaviour of CA-Pyz. Herein, we solved the low-temperature crystal structure of CA-Pyz from single crystal diffraction and identified a phase transition by both variable temperature single crystal and powder X-ray diffraction. Whilst it does not lead to ferroelectricity, the phase transition is accompanied by remarkable changes in the structure. We have used a variety of approaches for understanding and interpreting the X-ray diffraction data. These approaches include the application of rotational symmetry-adapted distortion modes to describe the phase transition and the application of strain modes to quantify and explain the thermal expansion behaviour. Both approaches allowed us to have a comprehensive understanding of the phase transition and accompanied thermal expansion in CA-Pyz. The work has been published in Chemistry of Material.[10]

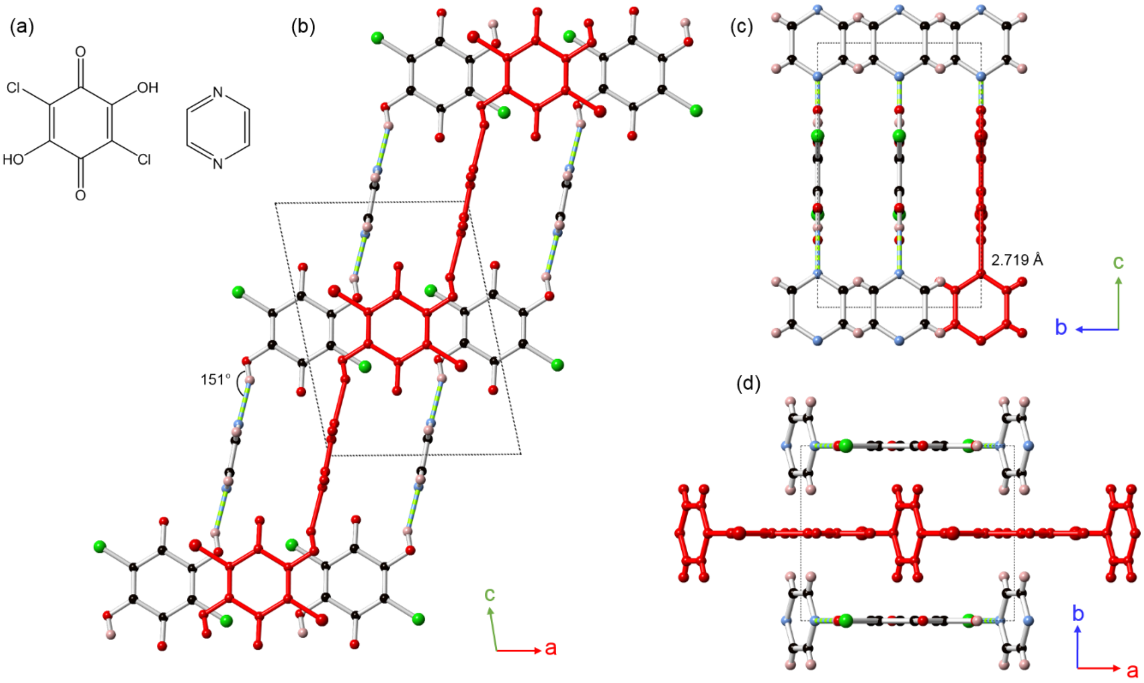

Figure 3.1: Molecular structure and crystal structure of chloranilic acid pyrazine (CA-Pyz). (a) Molecular structure of CA-Pyz. (b)-(d) Crystal structure of CA-Pyz obtained at 295 K from single crystal diffraction viewed down crystallographic *b*-, *a*- and *c*-axis, respectively. Colour legend: black-C; grey-H; blue-N; red-O; green-Cl. Hydrogen bonds are indicated by the light green-grey dashed line. A hydrogen-bonded chain is highlighted in red.

3.2 Experimental details

3.2.1 Sample preparation

Single crystals of CA-Pyz were obtained from the slow evaporation of an acetonitrile solution of chloranilic acid (Aldrich) and pyrazine (Aldrich, 99%) in a 1:1 molar ratio. Chloranilic acid (0.0627g, 0.3mmol) and pyrazine (0.0240g, 0.3 mmol) were dissolved separately in a minimum volume of acetonitrile (typically 6 mL and 1 mL respectively) with gentle heating for 30 minutes. Then, the solutions were combined in a 10 mL sample vial. Two batches of samples were prepared. One was left to crystallise at room temperature while another was left to grow crystals in the fridge. Orange-red crystals appeared after two days in the vial which was in the fridge. Five days later, orange-red rhombus-shaped crystals also appeared in the vial left at room temperature. Polycrystalline samples were produced by gentle grinding.

3.2.2 Single crystal X-ray diffraction (SCXRD) experiments

Single crystals from both batches were screened, and a crystal grown in the fridge was selected for data collections. Variable temperature laboratory SCXRD measurements were carried out at 300 K, 275 K, 250 K, 230 K, 200 K and 150 K on both cooling and warming. All data collections were acquired on the diffractometer “OD”. Crystal structures were all solved by a default SIR92[11] structure solution routine incorporated in the CRYSTALS[12] software. The hydrogen atoms were located by difference Fourier maps and refined isotropically without restraints. Single crystal neutron diffraction data were collected at 295 K on the SXD diffractometer at the ISIS Neutron and Muon Source at the Rutherford Appleton laboratory.

3.2.3 Variable temperature powder x-ray diffraction (PXRD)

Variable temperature capillary PXRD experiments were performed on the diffractometer “d6” using Mo radiation, for investigating the phase transition. A 0.7 mm external-diameter borosilicate glass capillary was filled to a length of 30 mm by gently tapping small amounts of sample down the tube. Experimental details are summarised in Table 3.1. The sample was cooled and warmed at a rate of 15 K h^{-1}. Each PXRD pattern was recorded for 20 mins over a 2θ range of 1°-30° using a step size 0.01°. All PXRD data were analysed using Topas Academic software.[13-15]

Table 3.1: Experimental details for variable temperature powder X-ray diffraction.

Experiment	**Process**	**T_{min} (K)**	**T_{max} (K)**	**Rate (K/hour)**	**T_c (K)**	**No. of runs**	**Total time (hour)**
d6b_00802	cooling	100	310	15	307	50	17
d6b_00803	warming	150	400	15	300	62	20

3.2.4 Variable temperature synchrotron X-ray diffraction

Synchrotron X-ray diffraction data were collected at beamline I11 at the Diamond Light Source. Ground samples were loaded into a 0.7 mm external-diameter quartz capillary to a length of 30 mm. The capillary was then sealed by superglue and attached to a metal brass holder which span during the experiment. Four different data collections were performed and experimental details are summarised in Table 3.2. Experiment 3 and 4 are the most optimal experiments, where a series of 4 mins scan was collected every 4 K between 180 and 360 K.

Table 3.2: Experimental details for variable temperature synchrotron X-ray diffraction.

Experiment	**Process**	**Tmin (K)**	**Tmax (K)**	**Temperature step (K)**	**Tc (K)**	**No. of runs**	**Total time (hour)**
1	Warming	100	440	20	320	18	7.5
2	Cooling	100	440	20	280	18	7.5
3	Warming	180	360	4	308	46	5.4
4	Cooling	180	360	4	268	46	5.4

3.2.5 Symmetry mode analysis

All symmetry-mode calculations were performed using the ISODISTORT software.[16] The symmetry-allowed degrees of freedom of axial vectors at the centre of inversion of chloranilic acid and pyrazine molecules were calculated with ISODISTORT. Command files containing both a rotational symmetry-mode description and a more familiar displacive symmetry-mode description were generated in a format suitable for TOPAS Academic.

3.2.6 Solid state NMR and thermal analysis

^{1}H solid state NMR were recorded at 205 K and 308 K with a 15 kHz spinning rate with neat tetramethylsilane as reference on a Bruker Advance III HD instrument. Differential scanning calorimetry (DSC) experiments were performed on a Perkin Elmer Pyris 1 DSC instrument. The sample (2.831 mg) was heated from 120 K to 520 K at a rate of 10 K min^{-1}.

3.3 VT PXRD: Observation of the phase transition

The variable temperature (VT) PXRD patterns obtained from both synchrotron and laboratory experiments are shown in Figure 3.2. It is apparent from these data that CA-Pyz undergoes a reversible phase transition close to 300 K, and the extreme *hkl* reflection splitting (indicated in Figure 3.2 and summarised in Table 3.3) suggests that there is a significant change in unit cell parameters associated with the phase transition. We call the *hkl* reflections that show extreme splitting behaviours “tuning-fork” reflections. For example, reflections such as the (11-1) at ~9.6° 2θ at high-temperature in Figure 3.2(a) undergoes notable splitting, resulting in the reflections (011) and (101), that are equivalent at high-temperature, being separated by several degrees in 2θ at low-temperature. Sharp peaks are always observed at low temperature which is consistent with a highly crystalline sample. However, we see some peak broadening just below the phase transition temperature that accompanies the dramatic changes in peak positions in both VT PXRD patterns. The peak broadening implies that we would need to take the effects of crystallite size or strain into consideration; this is discussed in section 3.7.2. It is also worth noting that peaks show subtly different behaviour in the synchrotron cooling data. On cooling, it is clear that some “tuning-fork” reflections appearing at approximately 2θ 9.6°, 10.6°, 11.9° and 18.6° start to diverge at two distinct temperatures. We name this phenomenon thermal-history-dependent reflection splitting. It happens presumably because crystallites did not respond uniformly to the temperature change. It seems that some crystallites in the capillary retain the high-temperature form while others start undergoing the phase transition to a low-temperature form. This could be caused by inter-crystallites interactions in the polycrystalline samples. The appearance of the thermal-history-dependent reflection splitting tells us how we need to analyse cooling data. A single-phase model is probably not sufficient and we would need to use multiple phases for fitting the cooling data. By multiple phases, we mean closely related phases that adopt the same space group but have slightly different unit cell parameters. This analysis is discussed in section 3.7.3 after determination of the low temperature from single crystal experiments is described.

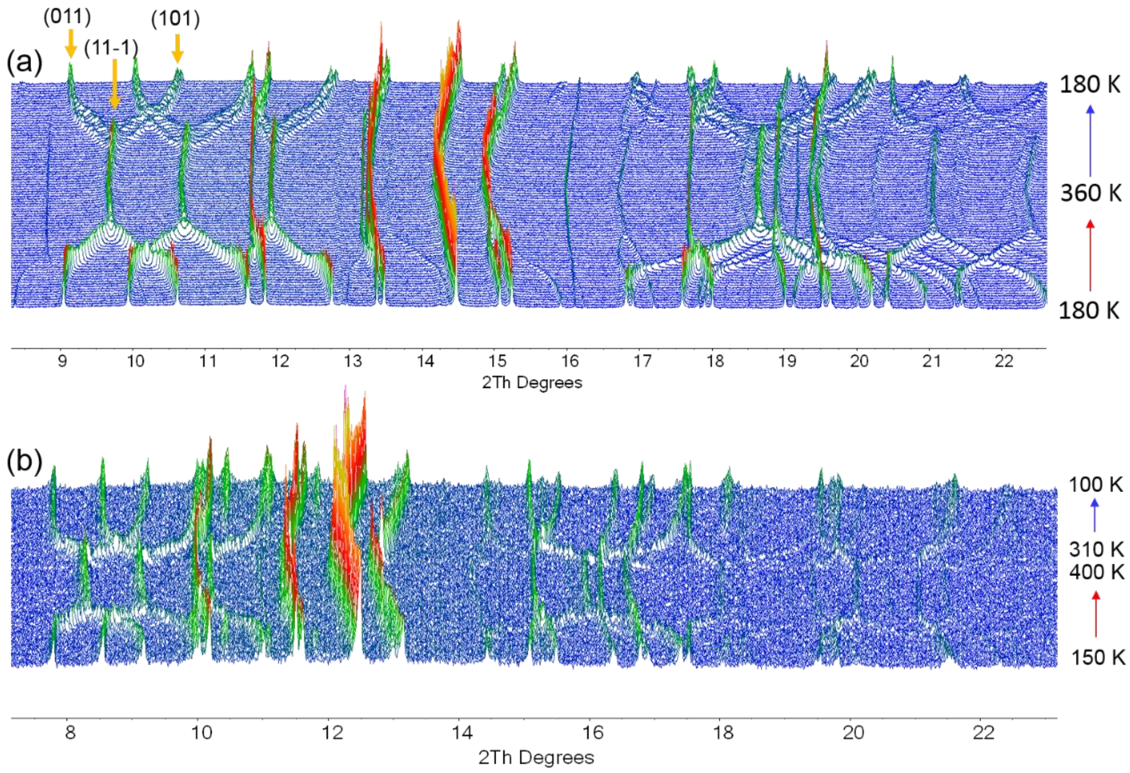

Figure 3.2: Variable temperature powder diffraction patterns obtained from (a) synchrotron and (b) laboratory experiments.

Table 3.3: Positions of selected “tuning-fork” reflections at high-temperature and resulting reflections at low-temperature in synchrotron data.

HT (T = 360 K)			LT (T = 180 K)		
***hkl* Reflection**	**2*θ*/°**	***d*-spacing**	***hkl* Reflection**	**2*θ*/°**	***d*-spacing**
(11-1)	9.6	4.9	(011) (101)	9.1 10.7	5.2 4.4
(111)	10.6	4.5	(01-1) (10-1)	9.9 11.7	4.8 4.1
(11-2)	11.9	4.0	(012) (102)	11.6 12.8	4.1 3.7
(31-1)	18.6	2.6	(121) (211)	17.6 20.2	2.7 2.4
(311)	20.2	2.4	(12-1) (21-1)	19.1 21.7	2.5 2.2
(31-3)	21.0	2.3	(123) (213)	20.5 22.8	2.3 2.1

3.4 Single crystal X-ray diffraction studies

A laboratory single crystal data collection was performed at 150 K, which revealed CA-Pyz has a different structure from the one reported by Ishida and Kashino[9]. This low-temperature (150 K) structure was found to adopt a triclinic space group *P*-1, with unit cell parameters of a = 4.7684(2) Å, b = 5.8402(3) Å, c = 10.6897(5) Å, α = 82.038(4)°, β = 81.568(4)°, γ= 76.938(4)° and V = 285.134(12) Å^3. In the 150 K structure, chloranilic acid and pyrazine molecules show the same connectivity as at room temperature. Since the low-temperature structure has a centrosymmetric space group, the phase transition of CA-Pyz is obviously not of a ferroelectric-type. However, what is happening in the system during the phase transition remains interesting. Figure 3.3 shows equivalent views of the low-temperature structure to those shown in Figure 3.1 for the room-temperature structure. The hydrogen-bonding geometry for the low-temperature structure remains almost unchanged compared to the room-temperature structure. Chloranilic acid and pyrazine molecules are linked by medium-length O-H····N hydrogen bonds, with the donor-acceptor distance of 2.709(7) Å and the O-H…N angle of 157(6)°, forming a one-dimensional network along [-1-11] direction. However, the dihedral angle (64.5°) between molecular planes of chloranilic acid and pyrazine has changed significantly, decreasing by 25.5° in contrast to the dihedral angle observed in the room-temperature structure. The chains of hydrogen-bonded chloranilic acid and pyrazine molecules stack along [-110].

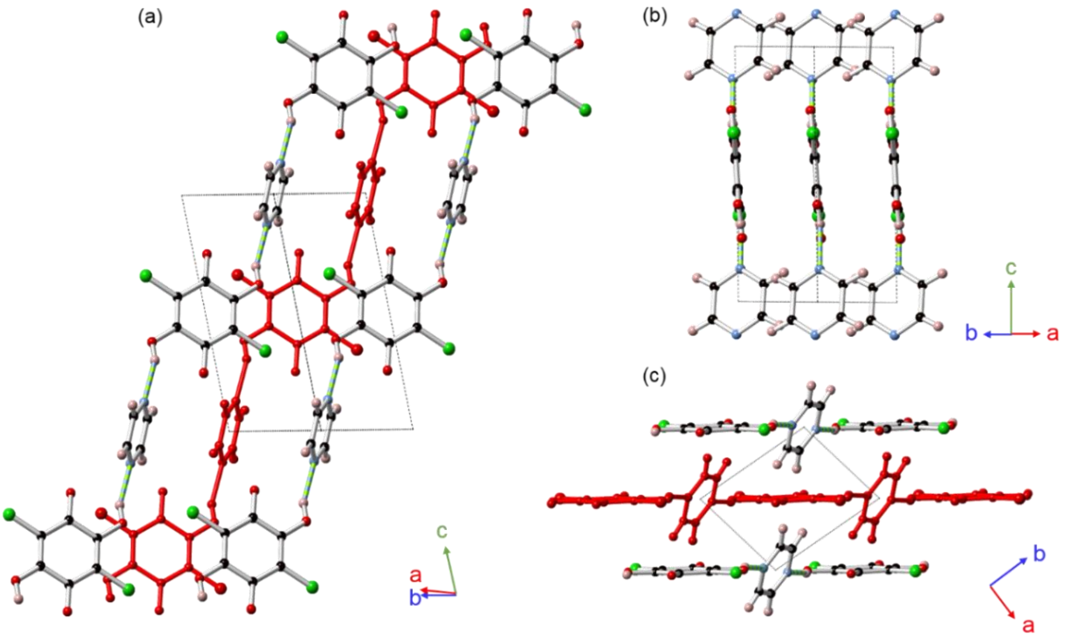

Figure 3.3: Crystal structure of CA-Pyz obtained at 150 K from single crystal X-ray diffraction. Crystal structure viewed down (a) [1-10] direction, (b) [-1-10] direction and (c) crystallographic c-axis. Colour legend: black-C; grey-H; blue-N; red-O; green-Cl. Hydrogen bonds are indicated by the light green-grey dashed line. A hydrogen-bonded chain is highlighted in red.

A more comprehensive set of variable temperature measurements was therefore carried out in order to gain insight into the structural changes associated with the phase transition. Single crystal diffraction measurement were performed at 300 K, 275 K, 250 K, 230 K, 200 K and 150 K upon both warming and cooling. Crystallographic data and experimental details are summarised in Table 3.4. At 300 K, CA-Pyz adopts the previously reported monoclinic structure in space group *C*2/*m*.[9] We refer to this as the high temperature (HT) form of CA-Pyz. Below this temperature, CA-Pyz adopts the new triclinic form (LT form, space group $P\bar{1}$) and appears twinned. The twin fraction is equal to 0.5:0.5 and the twin law is (0 -1 0, -1 0 0, 0 0 -1). Since hydrogen atoms diffract X-ray weakly, it is not reliable to determine the hydrogen position from powder X-ray diffraction data. Instead of measuring the O-H or N···H bond lengths, we use the C-O single bond lengths as a proxy for detecting potential temperature-induced proton migration. The molecular structure with atomic labelling is shown in Figure 3.4. In Figure 3.5, we show the donor-acceptor N7···O5 and C4-O5 single bond distances at each temperature. The donor-acceptor bond ($d_{N\cdots O}$ ~2.70 Å) and the C-O single bond (~1.31 Å) lengths remain unchanged between 150 and 300 K, suggesting that the latter retains single bond character throughout this temperature region.[17] Therefore we conclude that there is no proton migration involved during the phase transition.

Table 3.4: Crystallographic data for chloranilic acid pyrazine (a) From X-ray diffraction warming measurements. (b) From X-ray diffraction cooling measurements.

(a)	**300 K**	**275 K**	**250 K**	**230 K**	**200 K**	**150 K**
Chemical formula	$C_{10}H_6N_2O_4Cl_2$					
M_r	289.08					
Crystal system	Monoclinic	Triclinic	Triclinic	Triclinic	Triclinic	Triclinic
Space group	C2/m	P-1	P-1	P-1	P-1	P-1
Z	2	1		1	1	1
***a* (Å)**	8.2963(4)	5.1258(6)	4.9490 (5)	4.8687(6)	4.8199(3)	4.7808(4)
***b* (Å)**	6.6614(4)	5.5026(5)	5.6902(5)	5.7745(5)	5.8151(5)	5.8339(4)
***c* (Å)**	10.9963(5)	10.9695(9)	10.8820(8)	10.8024(10)	10.7532(5)	10.7057(9)
***α* (°)**	90	81.354(7)	81.686(6)	81.774(7)	81.892(5)	82.004(7)
***β* (°)**	101.590(4)	80.725(9)	80.986(7)	81.355(9)	81.517(4)	81.543(8)
***γ* (°)**	90	77.473(9)	77.572(7)	77.524(9)	77.366(6)	77.018(7)
Volume ($Å^3$)	595.32(2)	295.94(3)	293.61(2)	291.23(3)	289.026(12)	286.04(3)
No. of measured reflections	9098	5526	7606	6665	6031	7004
I/Sigma cutoff	2	2	2	2	2	2
No. of observed reflections	609	747	2440	2239	2972	3036
No. of parameters	59	95	95	95	95	95
R, Rw	0.0537, 0.0729	0.0605, 0.0519	0.0682, 0.0483	0.0652, 0.0959	0.0728, 0.0732	0.0923, 0.0693
Twin fractions		0.490(3) 0.510(3)	0.4988(8) 0.5012(8)	0.4997(12) 0.5003(12)	0.5048(8) 0.4952(8)	0.5042(8) 0.4958(8)

(b)	**300 K**	**275 K**	**250 K**	**230 K**	**200 K**	**150 K**
Chemical formula	$C_{10}H_6N_2O_4Cl_2$					
M_r	289.08					
Crystal system	Monoclinic	Triclinic	Triclinic	Triclinic	Triclinic	Triclinic
Space group	C2/m	P-1	P-1	P-1	P-1	P-1
Z	2	1	1	1	1	1
***a* (Å)**	8.2924(5)	5.1316(7)	4.9887(4)	4.8906(5)	4.8242(3)	4.7821(5)
***b* (Å)**	6.6543(5)	5.4889(8)	5.6350(5)	5.7517(5)	5.8096(3)	5.8258(6)
***c* (Å)**	10.9934(6)	10.9666(12)	10.9175(8)	10.8475(9)	10.7703(6)	10.7018(10)
***α* (°)**	90	81.345(11)	81.612(6)	81.785(7)	81.848(5)	81.926(8)
***β* (°)**	101.594(6)	80.683(10)	80.726(6)	81.137(8)	81.421(5)	81.568(8)
***γ* (°)**	90	77.455(12)	77.499(7)	77.490(8)	77.317(5)	76.993(8)
Volume ($Å^3$)	594.24(3)	295.40(3)	293.74(2)	292.42 (2)	289.330(16)	285.57(3)
No. of measured reflections	3309	5115	9056	6783	4125	3060
I/Sigma cutoff	2	2	2	2	2	2
No. of observed reflections	666	1060	1269	3094	2431	1949
No. of parameters	59	95	95	95	95	95
R, Rw（%）	0.0511, 0.0158	0.0556, 0.0248	0.0549, 0.0516	0.0645, 0.1249	0.0758, 0.1710	0.0760, 0.1836
Twin fractions		0.5123(16) 0.4877(16)	0.501(2) 0.499(2)	0.4969(13) 0.5031(13)	0.499(2) 0.501(2)	0.509(3) 0.491(3)

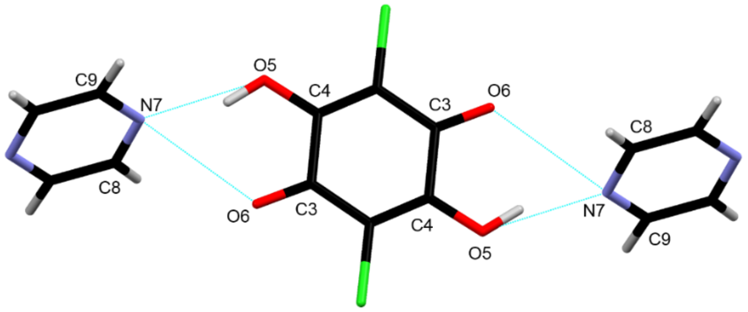

Figure 3.4: The molecular structure of CA-Pyz with atomic numbering scheme.

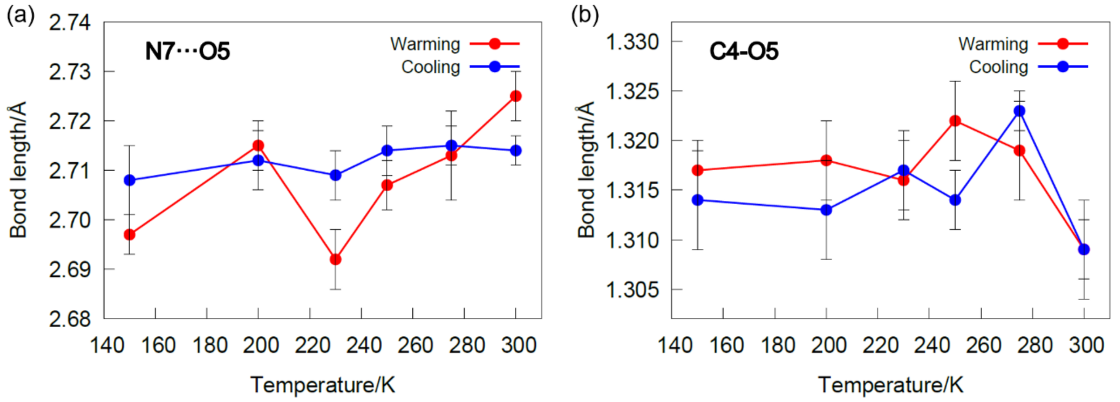

Figure 3.5: The temperature dependence of (a) N7···O5 distance and (b) C4-O5 bond distances obtained from single crystal X-ray diffraction.

From the crystal structure solved from single crystal X-ray diffraction, we are able to work out the relationship between the HT structure and LT structure of CA-Pyz. The transformation can be expressed mathematically by a matrix (0.5 0.5 0, 0.5 -0.5 0, 0 0 -1). As demonstrated in Figure 3.6, we can convert the HT structure to the LT (*P*-1 cell setting) by applying the matrix to the HT structure. This helps us interpret our X-ray diffraction data more conveniently by using a single structural model at all temperatures. The HT structure in the LT setting has unit cell parameters of *a*= 5.3161 Å, *b*= 5.3161 Å, *c*= 10.9934 Å, *α*= 80.98°, *β*= 80.98°, *γ*= 77.49° and V=297.11 $Å^3$. This shows that we would expect the cell edges *a* and *b* and the cell angles *α* and *β* of the LT phase become equal at the phase transition when we analyse the data using a single structural model based on the *P*-1 cell. A schematic representation of the structural distortion that occurs when we analyse this is shown in Figure 3.7(a). We observe a shift in pyrazine position (Figure 3.7(b)) arising from the sliding of planes of chloranilic acid molecules and the change in molecular position of Pyz increases with decreasing temperature. By 150 K, a significant shift in pyrazine molecule position has occured with each layer moving laterally from its high-temperature position by ~1.34 Å. We also see a marked shrinkage of distance between adjacent CA planes (Figure 3.7(c)) on cooling.

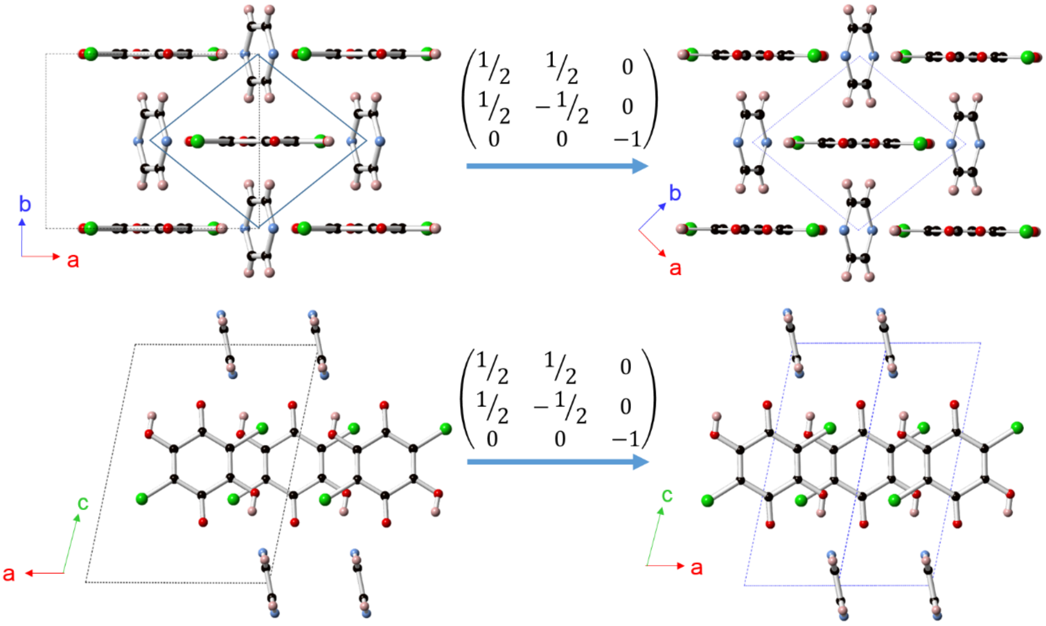

Figure 3.6: Parent structure transformed to the child P-1 setting. The blue diamond shown in top left figure represents the LT cell and the grey the HT cell.

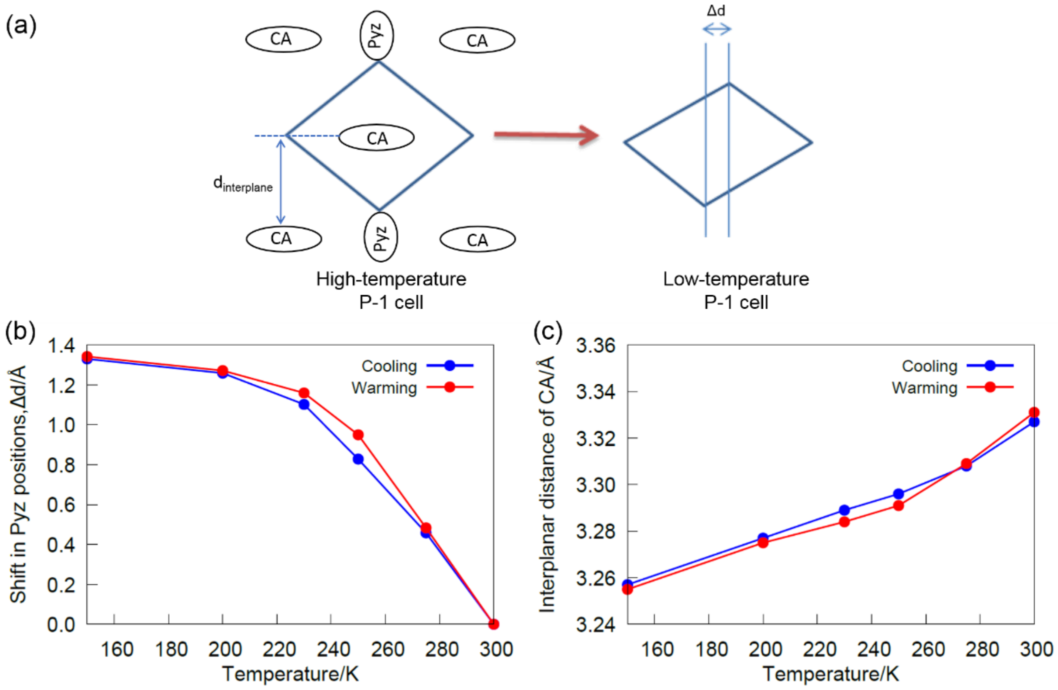

Figure 3.7: (a) A schematic representation of the CA-Pyz unit cell distortion. (b) The temperature dependence of lateral shift in pyrazine molecule position with a sliding of adjacent planes of chloranilic acid molecules. (c) The temperature dependence of minimum distance change between adjacent layers of chloranilic acid molecules.

3.5 Single crystal neutron diffraction study

Single crystal neutron diffraction data recorded at 300 K allowed us to determine the hydrogen atom positions and anisotropic atomic displacement parameters (ADPs) of the HT structure more accurately. ADPs indicates the magnitude and direction of the thermal motion of an atom. Crystallographic data and experimental details are summarised in Table 3.5. Figure 3.8(a) displays the crystal structure with ADPs determined from neutron diffraction and 3.8(b) shows the evolution of ADPs on non-hydrogen atoms determined from variable temperature single crystal X-ray diffraction and room-temperature neutron diffraction. In Figure 3.8(b), the magnitude of the ADPs on atoms of the pyrazine molecules, especially all the carbon atoms, shows the most significant change. As Ishida and Kashino reported, one of the carbon atoms in the pyrazine molecule shows remarkable anisotropic displacement perpendicular to the pyrazine ring. However, their attempts to resolve this by disordering the carbon atom around a pseudo two-fold axis failed. Their observation together with our observation of large ADPs on H atoms suggest large librational motion perpendicular to the pyrazine ring at room temperature.

Table 3.5 Crystallographic data for the chloranilic acid pyrazine co-crystal from neutron diffraction measurement at 295 K.

Temperature/K	295
Chemical formula	$C_{10}H_6N_2O_4Cl_2$
M_r	289.08
Crystal system	Monoclinic
Space group	*C2/m*
Z	2
***a* (Å)**	8.3163(5)
***b* (Å)**	6.5702(5)
***c* (Å)**	10.9769(6)
***α* (°)**	90
***β* (°)**	101.494(6)
***γ* (°)**	90
Volume (Å^3)	587.75(7)
No. of measured reflections	449
No. of observed reflections	445
No. of parameters	70
R, Rw (%)	8.97, 19.64

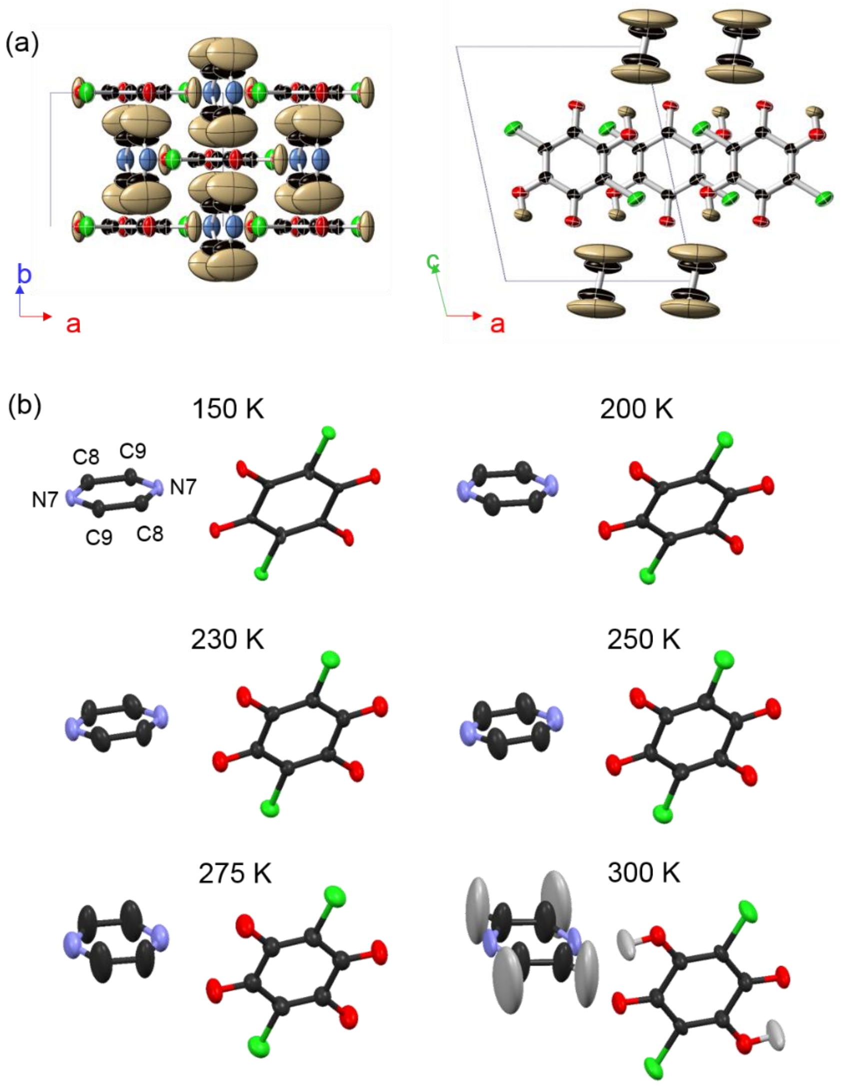

Figure 3.8: (a) The atomic displacement parameters determined from 300 K neutron diffraction refinements using the monoclinic cell. ADPs drawn at a 20% probability level. (b) The evolution of anisotropic atomic displacement parameters with changing temperature. 150 K – 275 K obtained from single crystal X-ray diffraction and 300 K from single crystal neutron diffraction.

The temperature dependences of N7-C9, N7-C8 and C8-C9 bond lengths within the Pyz ring obtained from X-ray diffraction are shown in Figure 3.9. Since the Pyz librational motion appears to be around the N···N axis, C8-C9 bond lengths remain almost unchanged. However, we observe an apparent reduction in N7-C8 and N7-C9 bond lengths at high temperature from both single crystal neutron and X-ray diffraction data. For example, the observed bond lengths of N7-C8 are ~1.33 Å and ~1.25 Å at 150 K and 300 K respectively from X-ray diffraction data. The differences arise from the fact that at high temperatures the relatively rigid molecules undergo correlated atomic motion leading to the well-known underestimation of bond lengths when using harmonic displacement parameters.[18] A schematic diagram to explain this reduction of bond length caused by thermal motion is given in Figure 3.10. As an approximation, a TLS (translation, libration, screw) analysis of the experimental 295 K neutron ADPs[19] gives eigenvalues of the librational tensor of the Pyz molecule of ~22, 8 and 6° and translations of 0.36, 0.23 and 0.1 Å^2. Our TLS analysis gives observed and corrected N7-C8 distances of 1.275 and 1.360 Å, respectively. These are similar to bond lengths obtained from single crystal X-ray data at 300 K and 150, confirming the librational origin of the shortening.

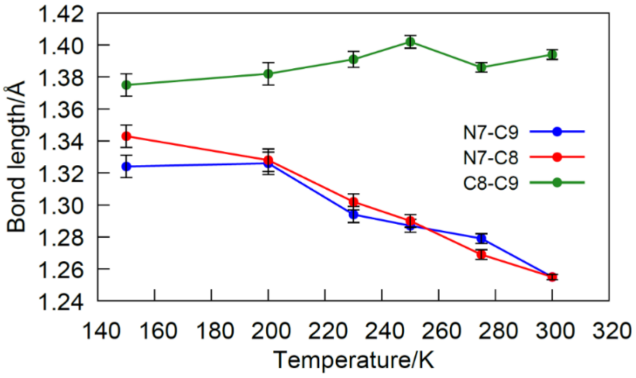

Figure 3.9: The temperature dependence of N7-C9, N7-C8 and C8-C9 bond lengths in the pyrazine molecule.

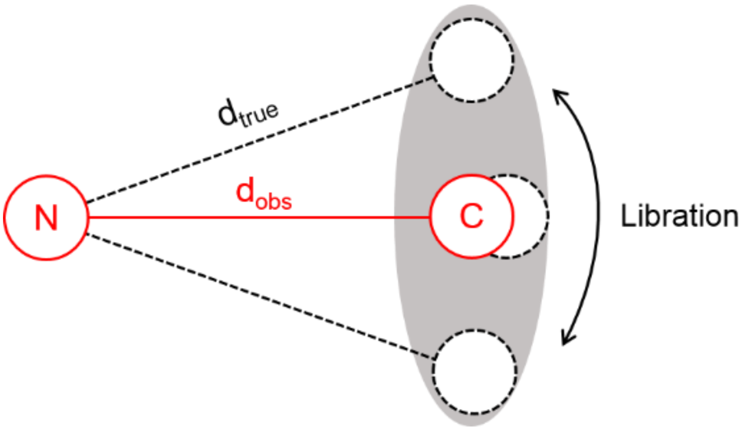

Figure 3.10: Schematic representation of how thermal motion leads to an apparent reduction in bond length. The observed N-C bond is drawn using a red solid line. The true N-C bond is represented by the black dashed line. The grey shadow shows the anisotropic atomic displacement on carbon atom that approximates the overall atomic distribution.

3.6 Solid state NMR study

1H solid state NMR spectra were recorded at 205 K and 308 K at a spinning rate of 15 KHz (Figure 3.11). The high-frequency (13.1 and 13.5 ppm) signal is assigned to hydrogen (involved in the moderate hydrogen bond) in CA molecule while the low-frequency (8.5 and 8.6 ppm) signal is assigned to aromatic hydrogens on Pyz. The CA OH proton signal shifts by ~ 0.5 ppm indicating a small change in the proton environment and hydrogen bond network in the two phases. This observation supports our observation from X-ray diffraction data that only a subtle change in this part of the structure occurs at the phase transition. The dynamics in the HT structure are evidenced by the ^{1}H solid state NMR signal narrowing. Both CA OH and Pyz proton signals narrow on warming, 950/550 Hz and 1490/600 Hz respectively. This is consistent with the high ADPs observed in neutron diffraction data.

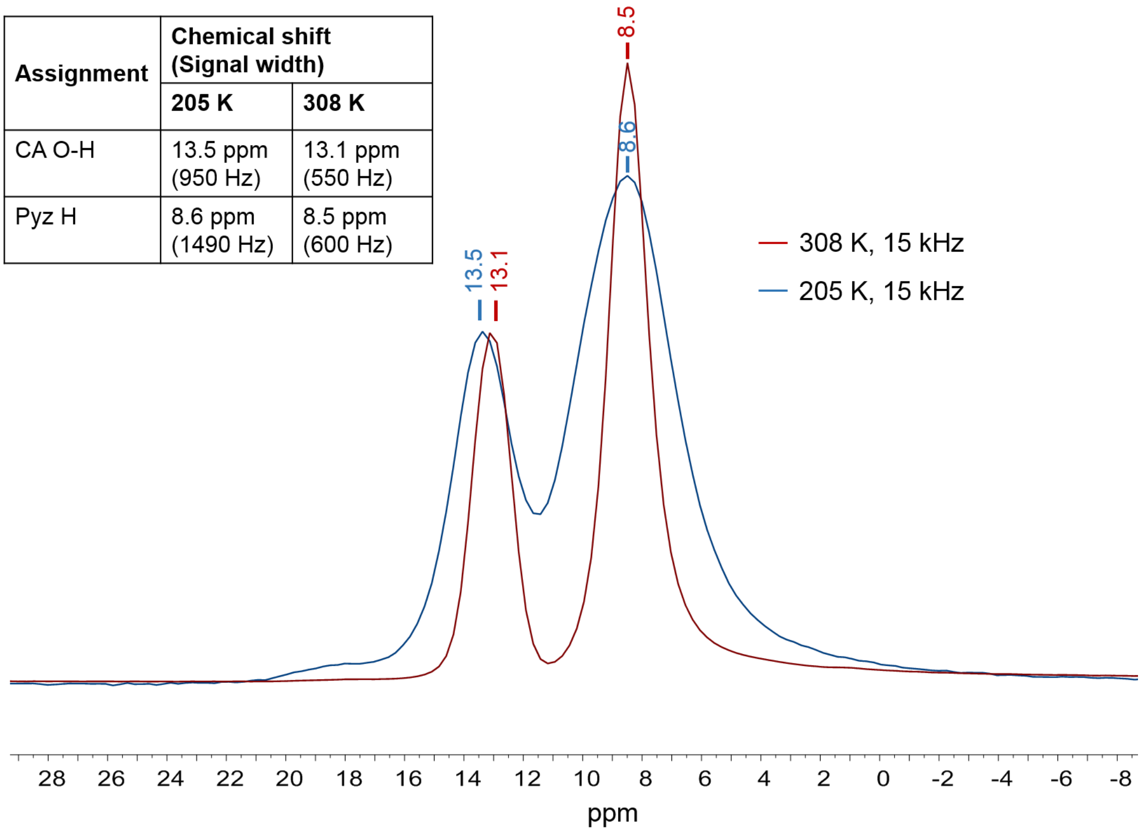

Assignment	Chemical shift (Signal width)	
	205 K	**308 K**
CA O-H	13.5 ppm (950 Hz)	13.1 ppm (550 Hz)
Pyz H	8.6 ppm (1490 Hz)	8.5 ppm (600 Hz)

Figure 3.11: ^{1}H solid state NMR spectra. The red spectrum was recorded with 15 kHz spinning at 308 K. The blue spectrum was recorded with 15 kHz spinning at 205 K. The table inserted to the top left summarises peak positions and widths (given in brackets).

3.7 Rietveld refinement and determination of cell parameters

The variable temperature single crystal experiments showed significant changes in atomic coordinates and unit cell parameters occuring at the HT to LT phase transition. In this section we describe details of the Rietveld analysis that was used to gain more information on these changes. The refinements described were done using a symmetry-adapted rotational mode description. We give details of this in the structural discussion of section 3.8, which integrates single crystal and powder observations.

3.7.1 Peak broadening

If a lattice is strained, the *d*-spacings of *hkl* reflection will change. According to Bragg's law (Equation 2.1), a change in *d*-spacing will give rise to a shift in 2θ. When the sample undergoes inhomogeneous strain (microstrain), changes in *d*-spacing will not be uniform and the shifts in 2θ will lead to peak broadening. When this is anisotropic, different *hkl* reflections show different broadenings. As we observe peak broadening in PXRD patterns just below the phase transition temperature, we introduced a simple anisotropic peak shape to describe the peak broadening. A 4th order spherical harmonic function in *P*-1 symmetry for the correction of anisotropic peak broadening gives rise to 15 refinable parameters.[20] Detailed information of the spherical harmonics is given in Appendix IX. If we included all of the 15 parameters, the majority of the terms (apart from y00, y20, y44p and y55m) refined close to zero at all temperatures. If only 4 spherical harmonic terms (y00, y20, y44p and y44m) were refined, the average R_{wp} (19.05% over 46 different temperature) for all refinements remained almost unchanged compared to using all 15 terms. As a result, four spherical harmonics parameters of the 15 possible terms for anisotropic microstrain correction were judged sufficient. Peak broadening could also result from the crystallite size and thus we also tested for crystallite size broadening by using the Topas CS_G parameter to model peak widths. This correction did not improve the fits, as judged by the R_{wp} almost not changing. So, we can conclude that crystallite size-related broadening is not an important factor here, and the most significant contribution to peak broadening arises from sample strain.

3.7.2 "Single-phase" model vs "Three-phase" model

Due to the thermal-history-dependent peak splitting observed in the PXRD patterns discussed above (Figure 3.2(a)), models used for the refinements against cooling and warming data slightly differ. As shown in Figure 3.12(a), it is not surprising that a single-phase refinement against 240 K data collected on cooling is not sufficient for getting a good fit because of the marked thermal-history-dependent reflection splitting. As we can see in the inset, a number of peaks are not modelled by using the "single-phase" model. We then attempted to perform a refinement using three closely related phases and it turned out that this "three-phase" model significantly decreased the R_{wp} (by ~9%) and gave a visually better Rietveld fit. The three phases coexisting just below T=296 K all belong to triclinic space group *P*-1 but are allowed to have slightly different unit cell parameters. On the other hand, since we did not see thermal-history-dependent peak splitting on warming, we performed Rietveld refinements using the "single-phase" model throughout for powder diffraction data collected on warming. For structural refinements against laboratory data, a single phase is sufficient to get good fits at all temperatures since there is no observation of thermal-history-dependent reflection splitting at the experimental resolution in Figure 3.2(b).

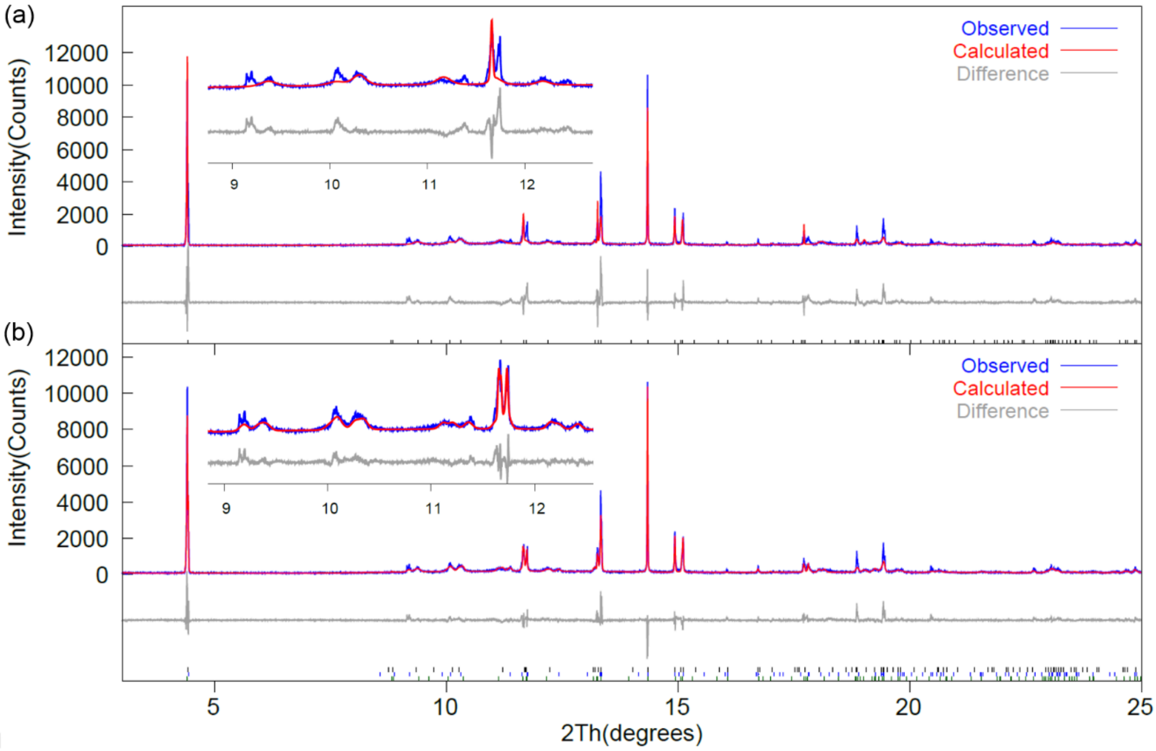

Figure 3.12: The Rietveld fits (a) using "single-phase" model with R_{wp} = 27.37% and (b) using "three-phase" model with R_{wp} = 18.87% against synchrotron data collected at 240 K upon cooling.

3.7.3 Results from variable temperature Rietveld refinements

Final Rietveld refinements were carried out using a rotational symmetry mode description and *P*-1 cell setting at all temperatures. All parameters refined are summarised in Table 3.6. Instrumental peak shape (TCHZ peak shape) and axial divergence were determined with silicon standard 640c NIST, then fixed in our X-ray powder diffraction refinements. The variable temperature Rietveld fits to the synchrotron experiments 3 and 4 (Table 3.2) are given in Figure 3.14. Rietveld refinement confirms that the sample adopts the *P*-1 structure identified by single crystal experiment at low temperature. Our refinements give good agreement between the calculated patterns and the observed patterns at all temperatures.

Table 3.6: Summary of parameters refined in the final refinements

Parameters	**Number of parameters refined**	
	Warming data	**Cooling data**
Unit cell parameters	6	18 (6 for each phase)
Scale factor	1	3 (1 for each phase)
Isotropic thermal parameters	2 (1 for each molecule)	2 (1 for each molecule)
Rotational symmetry modes	6	6
Internal symmetry modes	36	36
Spherical harmonic peak shape	4	4
Background	12	12
Zero point correction	1	1

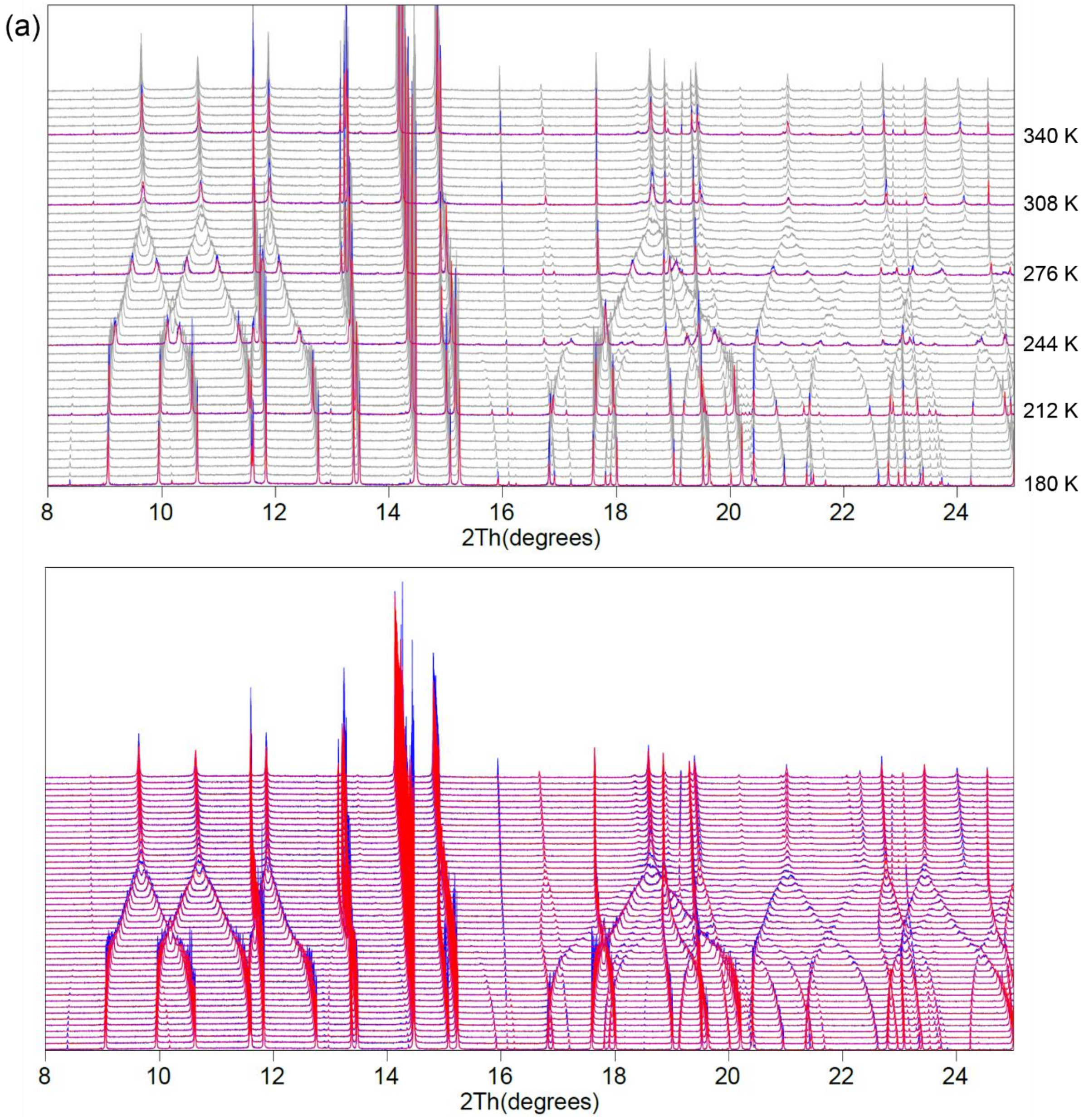
(a)
340 K
308 K
276 K
244 K
212 K
180 K
8
10
12
14
16
18
20
22
24
2Th(degrees)
8
10
12
14
16
18
20
22
24
2Th(degrees)

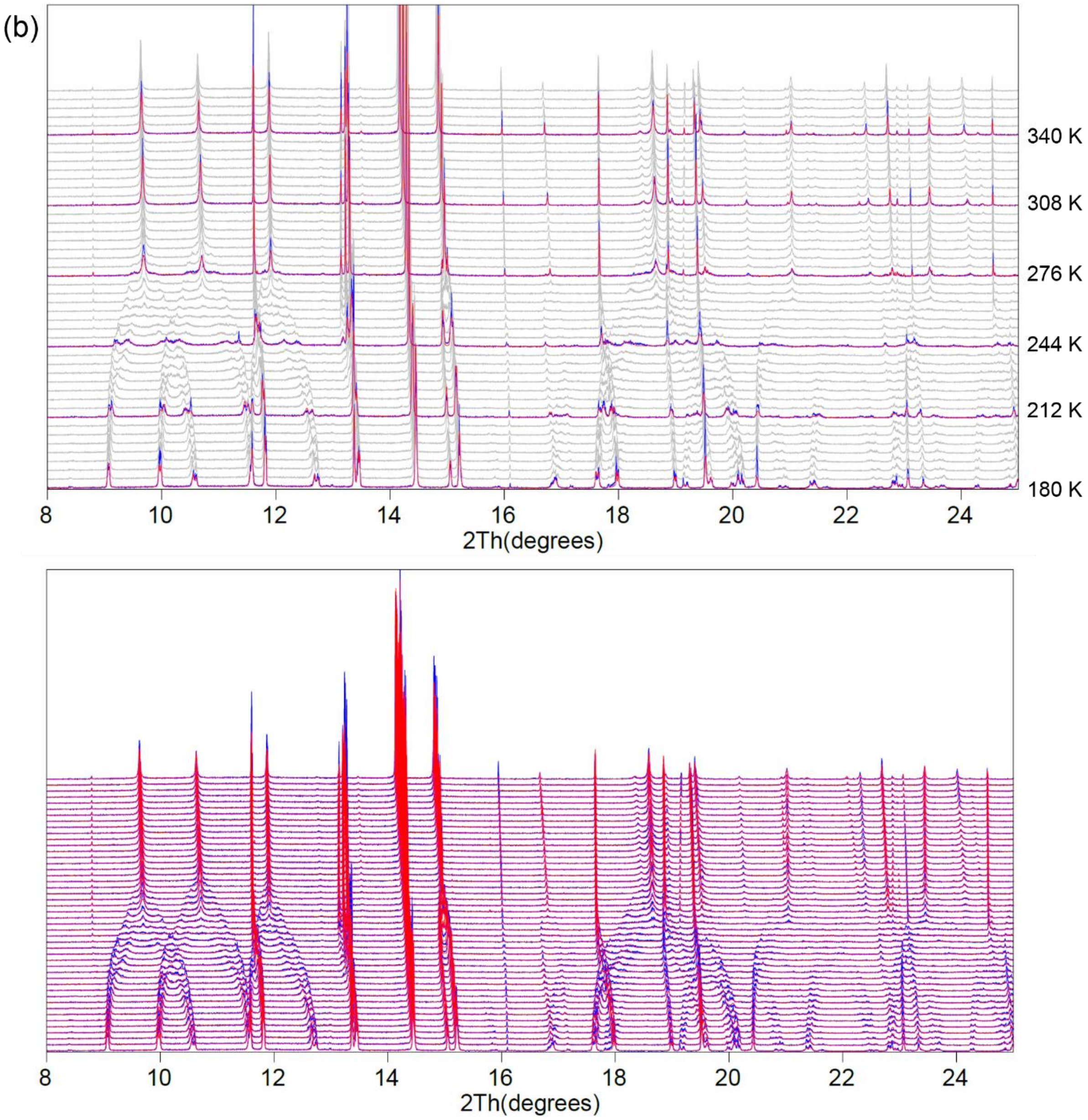

Figure 3.13: The best Rietveld fits to (a) synchrotron experiment 3 collected on warming and (b) synchrotron experiment 4 collected on cooling.

The magnitude of the peak shape spherical harmonics coefficients obtained from synchrotron experiments 3 and 4 is shown in Figure 3.14. These coefficients help us understand the microstructural strain. As shown in Figure 3.14(a), the structure is unstrained between 180 K and 212 K and the coefficients remain extremely small. All coefficients change noticeably between 212 K and 324 K and retain small magnitudes above 324 K. This indicates that the lattice is significantly strained over the temperature range of 212–324 K but become less strained at the end of the heating experiment. On cooling (Figure 3.14(b)), the sample initially retains the small strain broadening observed at the end of the heating experiment. All the coefficients stay almost unchanged between

360 K and 280 K. However, all coefficients show prominent changes over the temperature range of 280–220 K on cooling which is narrower than we see on warming. However, values of the spherical harmonics coefficients are bigger than we obtained from warming data. This is reflected in the PXRD patterns in Figure 3.2(b) in which visibly broader peaks are displayed on cooling. The insets in Figure 3.15 are visual representations of the spherical harmonics function for sample strains plotted on the same scale. We could observe severe sample strain occurring along [100] and [010] directions that are major direction changes occurring in the crystal structure during the phase transition.

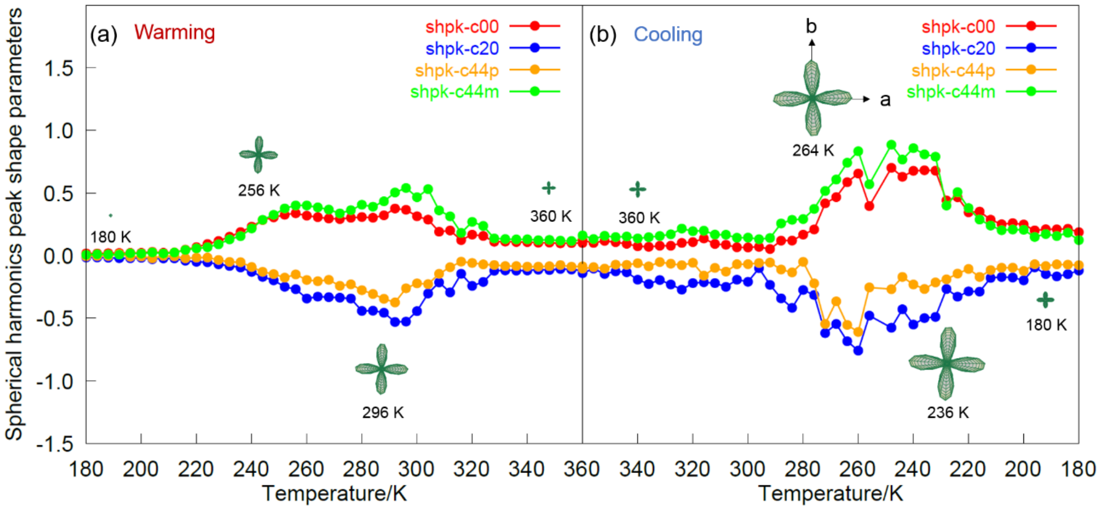

Figure 3.14 Values of *hkl*-dependent spherical harmonics peak shape parameters obtained from (a) warming data and (b) cooling data. Visual representations of spherical harmonics shown as insets.

Figure 3.15 displays the unit cell parameters in *P*-1 cell setting extracted from these refinements. Warming values are closed points and cooling are open points. The phase transition temperature, $T_c = 300$ K, is defined by the temperature where cell parameters *a* and *b* converge. On warming, between 180 K and 300 K, the unit cell parameter *a* elongates by +7.1% corresponding to an expansion of $\Delta l/l \sim 5.9\%$ over 100 K while the unit cell parameter *b* decreases by -6.3% over the same temperature range corresponding to a contraction of $\Delta l/l \sim$ -5.4% over 100 K. Unit cell parameter *c* increases by +2% between 180 K and 300 K. The cell angle β shows a more unusual temperature dependency. It initially decreases on warming but then increases at $T \approx 260$ K, whereas α decreases monotonically on warming. This suggests that two processes might be occurring during the overall phase transition. Since the sample shows multiphase behaviour on cooling, we include the unit cell parameters of the three closely related phases (shown as boxes, circles and triangles) in Figure 3.15. The phase transition temperatures, where the cell parameters *a* and *b* diverge, are slightly different for each phase (~300 K, 276 K and 264 K respectively) as expected. However, the overall temperature dependence of each cell parameter is very similar to the one observed from warming data.

A marked discontinuity at 260 K and a smaller discontinuity at 300 K can be observed in Figure 3.16 where the plot of differences between experimental volumes and the volumes extrapolated from the HT structure is shown. Here, we fit a straight line $V = 0.0523T + 285.85$ (drawn as red line) to HT data taken at T ≥ 320 K. We then used the function to estimate the difference in cell volumes at LT compared to the extrapolated values. It is evident in Figure 3.16 that a considerable deviation from the high temperature extrapolated value occurs. The reason why unit cell parameters exhibit unusual behaviours will be discussed later based on strain modes.

The preceding analysis uses the unit cell of the *P*-1 child structure throughout. It is also possible to use the HT cell throughout. In this case the phase transition on cooling is *C*2/*m* → *C*-1. The corresponding cell parameters are plotted for completeness in Figure 3.17. We see different temperature dependences of the individual cell parameters as expected. The unit cell parameter *b* still exhibits a contraction over the temperature range of 240 K to 280 K, but the cell angle *γ* changes the most dramatically at the phase transition.

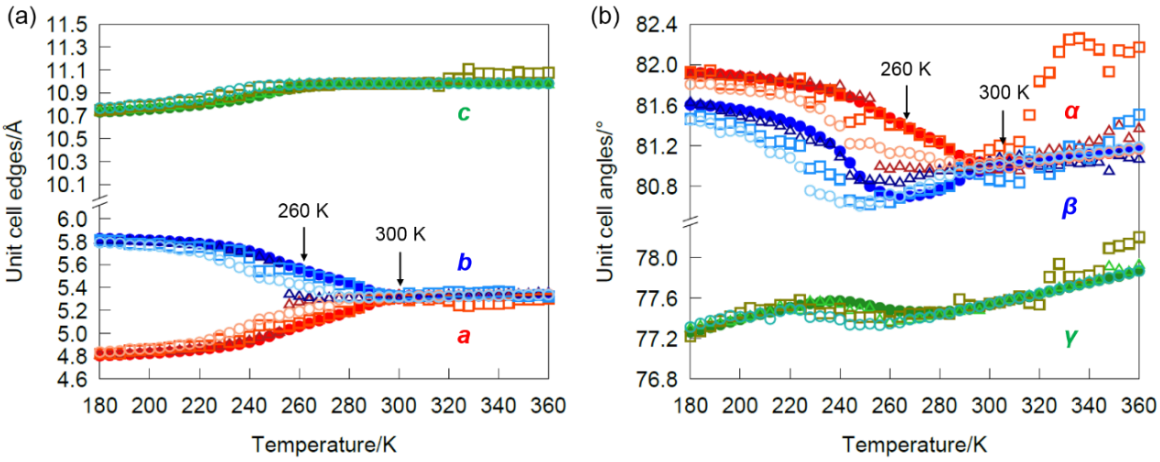

Figure 3.15: Unit cell parameters using *P*-1 cell setting extracted from powder data collected on warming (solid markers) and cooling (open markers). Data reveal some hysteresis and multiphase behaviour just below the phase transition temperature on cooling. (a) Unit cell

parameters *a* and *b*. (b) Unit cell parameter *c*. Note the very different *y*-axis scale of $\Delta l/l \approx 25\%$ and $\approx 5\%$ in (a) and (b).

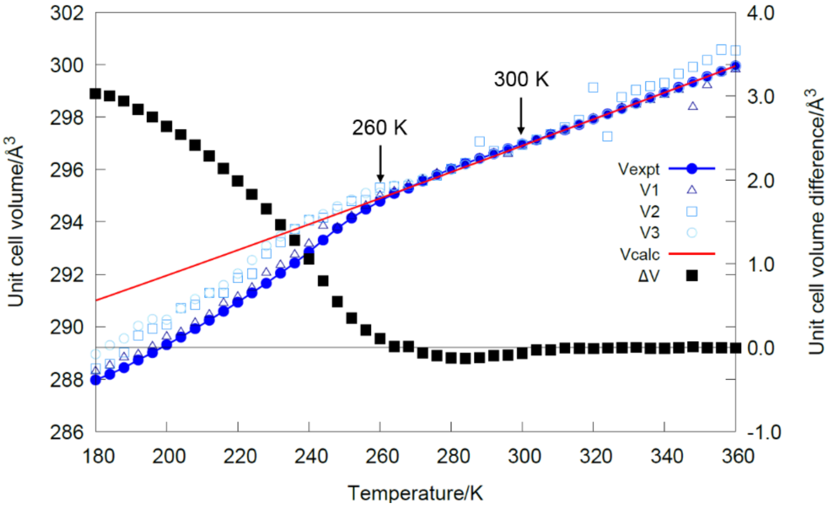

Figure 3.16: Unit cell volumes extracted from synchrotron X-ray diffraction data collected on warming (blue solid markers) and cooling (blue open makers) and volumetric strain (black solid squares) relative to values extrapolated from the high temperature cell.

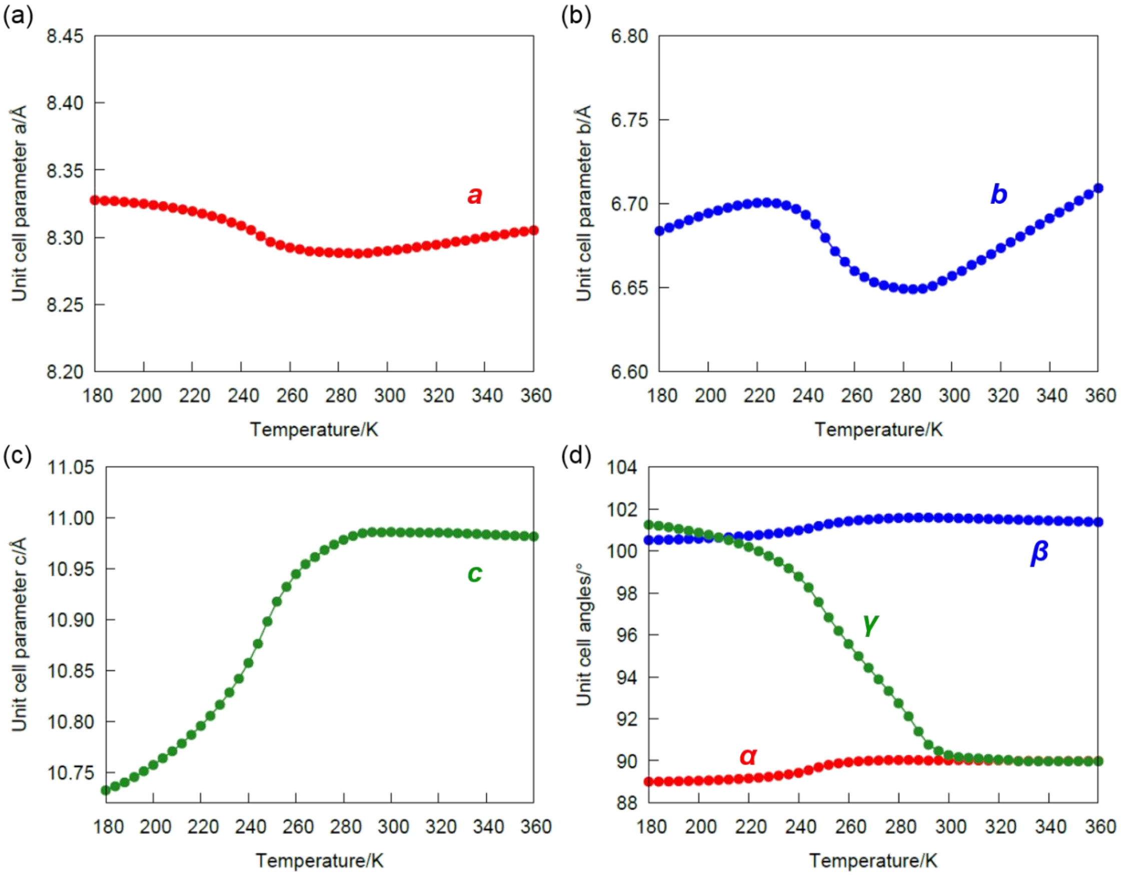

Figure 3.17: Unit cell parameters using *C*-1 cell setting from synchrotron warming data. (a) Cell parameter a, (b) cell parameter b, (c) cell parameter c and (d) cell angles *α*, *β* and *γ*.

3.8 Rotational symmetry mode description of the phase transition

The leading role of hydrogen bonds in the phase transition has already been excluded as the relevant bond lengths remain unchanged (Figure 3.5). We can, instead, understand the structural changes at the phase transition by considering rotational symmetry-adapted distortion modes (rotational symmetry mode for brevity) and seeing how the mode amplitudes belonging to different irreps change. The power of using symmetry-adapted distortion modes was introduced in section 2.9.

In essence the symmetry mode approach allows us to describe the LT structure in terms of the HT parent and the amplitude of symmetry-adapted distortion modes which describe molecular rotations and displacements. In the rotational symmetry mode description, six rotational modes (three for each unique molecule in the asymmetric unit) are generated in order to capture the structural changes in CA-Pyz. These rotational symmetry modes belong to two different irreps ($\Gamma_1^+$and Γ_2^+) of the parent symmetry group and are labelled as r_1-r_6. The *Γ* point is located at (0, 0, 0) in the first Brillioun zone of the reciprocal lattice. Figure 3.18 illustrates the direction of the axial vector corresponding to each unique rotational mode. Further information about the rotational modes are summarised in Table 3.7. The Γ_1^+*Ag*(*a*) modes on each molecule (labelled as r_3 and r_6), light green and dark green vectors in Figure 3.18 respectively) describe rotations around the parent *b* axis, and are allowed degrees of freedom in the parent; the rotation axes associated with these modes are perpendicular to the CA molecular plane and perpendicular to the N–N vector in the Pyz molecular plane, respectively. The symmetry-breaking Γ_2^+*Bg*_1(*a*) modes (r_1 and r_4), light red and dark red vectors in Figure 3.18 respectively) are rotations around the parent *c* axis and lie approximately parallel to the C=O bond of CA and the N–N vector of Pyz. The symmetry-breaking Γ_2^+*Bg*_2(*a*) modes (r_2 and r_5), light blue and dark blue vectors in Figure 3.18 respectively) are rotations around the parent *a* axis and are approximately perpendicular to the C=O axis of CA and to the Pyz plane.

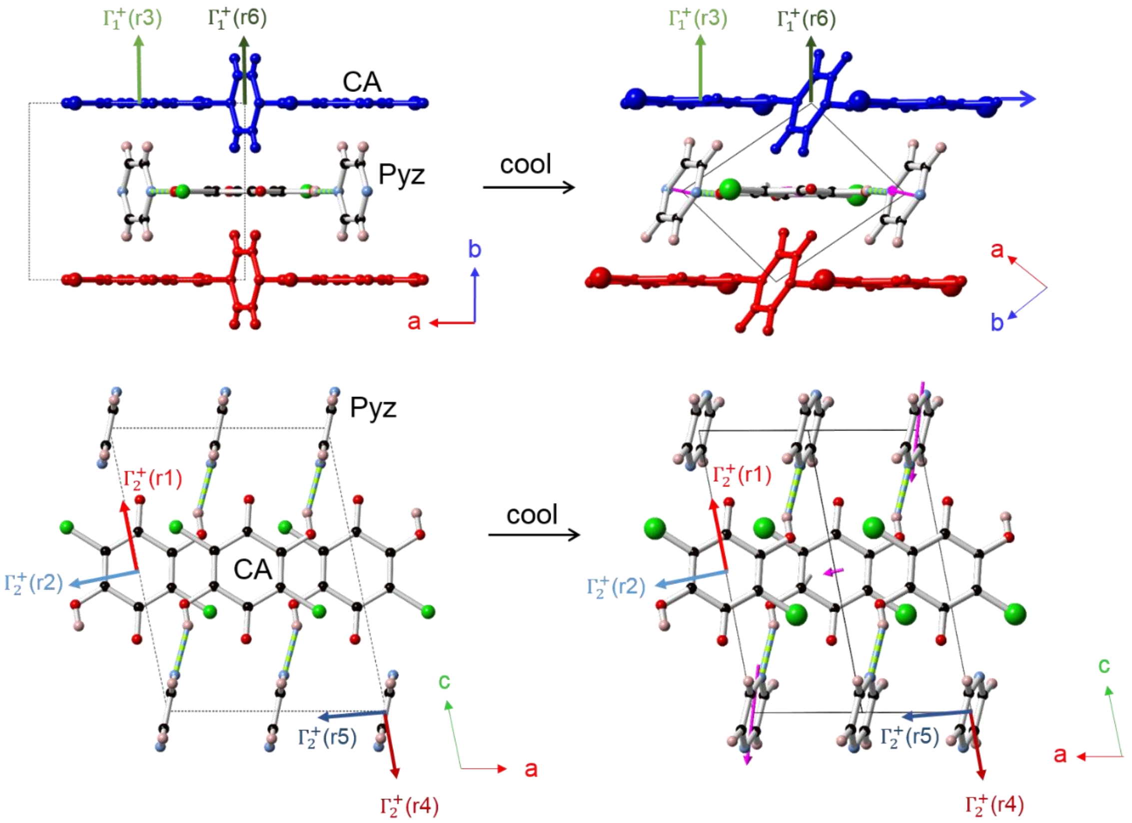

Figure 3.18: Illustration of each rotational symmetry mode and the resulting overall vectors (pink arrows) obtained by refinement.

Table 3.7 Information of each rotation axial-vector and its corresponding rotational symmetry mode.

Molecule	**Rotation mode**	**Mode label**	**Direction**
CA	r_1	$\Gamma_2^+ Bg\_1(a)$	around parent c-axis
	r_2	$\Gamma_2^+ Bg\_2(a)$	around parent a-axis
	r_3	$\Gamma_1^+ Ag(a)$	around parent b-axis
Pyz	r_4	$\Gamma_2^+ Bg\_1(a)$	around parent c-axis
	r_5	$\Gamma_2^+ Bg\_2(a)$	around parent a-axis
	r_6	$\Gamma_1^+ Ag(a)$	around parent b-axis

The crystal structure solved from 300 K single crystal X-ray diffraction data allows us to develop a straightforward description of the child LT phase of CA-Pyz. The TOPAS file containing the rotational symmetry mode description is shown in Appendix I. We extracted atomic coordinates for all atoms from structures determined by single crystal X-ray diffraction. Then we minimised the distances between every corresponding atoms from the low-temperature structure and the high-temperature structure by varying the amplitude of each rotational symmetry mode. The minimised distances were all extremely close to zero. Figure 3.19(a) and (b) shows the experimentally refined amplitude of each rotational symmetry mode at all temperatures. It is clear from the plots that the Pyz rotational mode r_4 belonging to Γ_2^+ irrep has by far the highest amplitudes (approximately 0.28 radian) at 150 K and other modes have extremely small amplitudes (the maximum ~0.07 radian) compared to r_4. Thus it is the most important in describing and understanding the phase transition. Moreover, the rotations of Pyz molecule (open markers) are much more important than those of the CA molecule (closed markers). Figure 3.21 (c) displays the amplitudes of the overall molecular rotations extracted from the single crystal diffraction data and (d) illustrates the rotation vectors resulting from the three axial-vectors for each molecule. For Pyz, we see that the large ~16° rotation is almost aligned with the N–N vector. For CA, the smaller ~4° rotation is approximately perpendicular to the C=O vector and slightly out of the molecular plane.

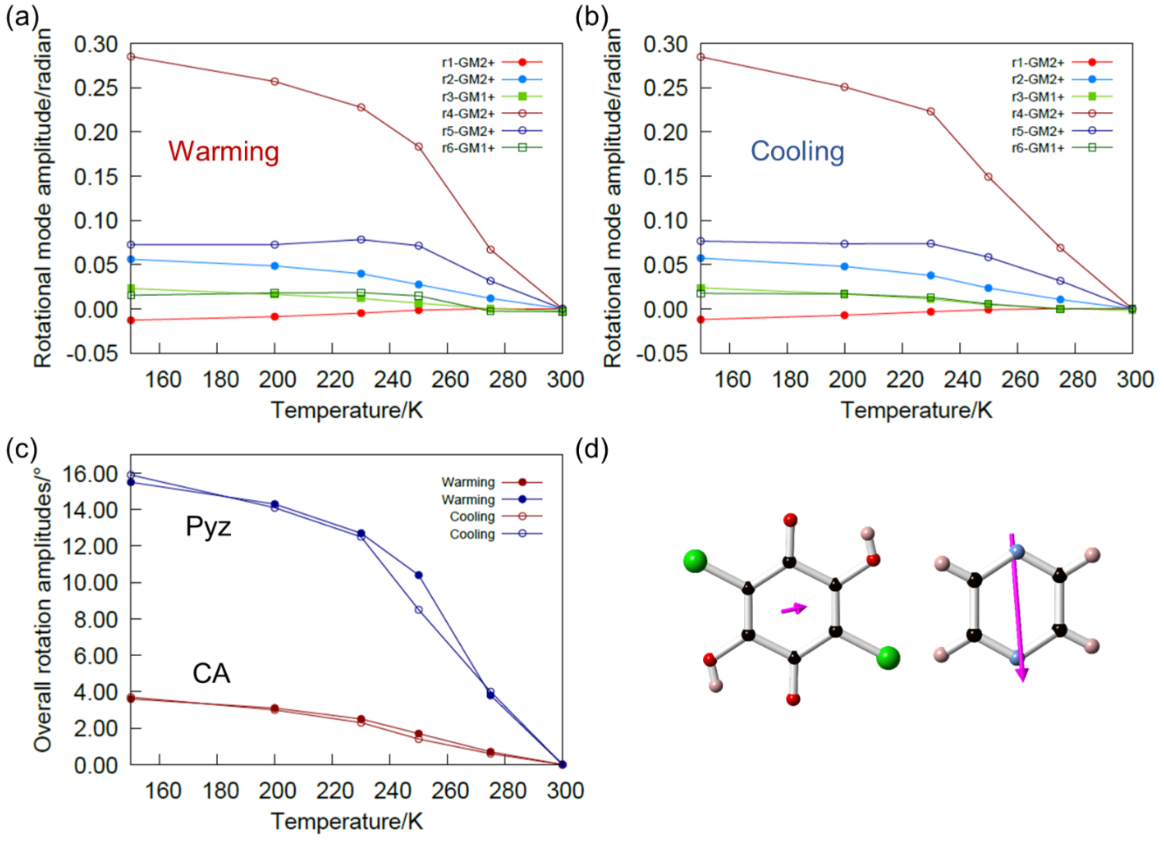

Figure 3.19: Results from the symmetry-adapted distortion mode analysis of single crystal diffraction data. (a) – (b) Rotational symmetry-mode amplitudes r1–r3 (CA, shaded markers) and r4–r6 (Pyz, open markers) in radian unit extracted from single crystal refinements on warming and cooling respectively. (c) Amplitudes for overall rotation vectors of each molecule. (d) Illustration of overall rotation vector for each molecule; vectors length displayed as 1 Å = 8°.

For small rotations of rigid molecules, these six rotational symmetry mode parameters should allow us to capture the key features of the phase transition. However, this is based on the assumption that the rigid molecules are hardly distorted. If additional distortions occur within the molecules, these additional distortion can be described by refining the internal displacive symmetry modes amplitudes. These internal modes can also be used to correct the distortions caused by large changes in cell metrics. In this work, internal symmetry modes belong to two parent point group irreps Γ_1^+ and Γ_2^+, 24 of which (the Γ_1^+ modes) describe structural degrees of freedom already present in the parent. To avoid over-parameterisation, we used soft restraints to keep the unnecessary internal mode amplitudes close to zero. The internal mode amplitudes therefore refined to zero unless they “have to be” non-zero. By doing so, we should be able to use rotational symmetry mode amplitudes to describe most of the changes in atomic coordinates. Figure 3.20(a) shows the internal mode amplitudes extracted at all temperatures with refining rotational symmetry mode amplitudes at the same time from single crystal data. As we can see, most of the internal mode amplitudes remain close to zero. Internal distortions due to the large changes in cell metrics only lead to atomic displacements of several atoms being up to 0.13 Å from true positions in the molecular rotation description at 150 K. To compare the rotational mode amplitudes, we plot the amplitudes extracted from 150 K single crystal data without and with refining all the internal modes as an example. As we can see in Figure 3.20(b), the values of rotational symmetry mode amplitudes are almost unchanged between these descriptions. The rotational rigid body model, therefore, captures most of the key structural changes in a small number of parameters.

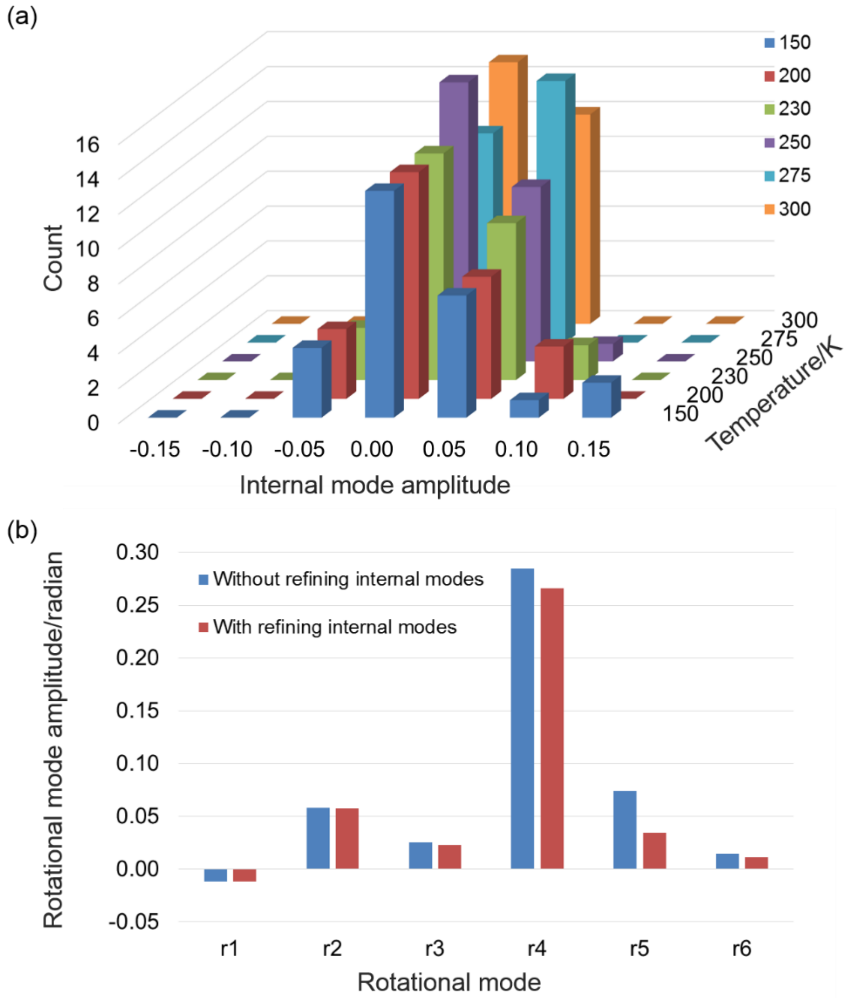

Figure 3.20: (a) Histograms of the amplitude of internal distortion symmetry modes extracted from data collected on warming. (b) The comparison of the rotational mode amplitudes extracted from 150 K single crystal data without and with refining the internal mode amplitudes.

We also tried the same method in the analysis of our laboratory powder diffraction data (experiment d6b_00803). Figure 3.21(a) and (b) show equivalent rotational mode amplitudes and overall molecular rotations refined directly from this relatively low-quality powder diffraction data, respectively. The good qualitative and quantitative agreement between Figures 3.21 and 3.19 shows that this restricted parameter set (in contrast to traditional *xyz* refinements) can be routinely and reliably extracted from low quality laboratory powder diffraction data.

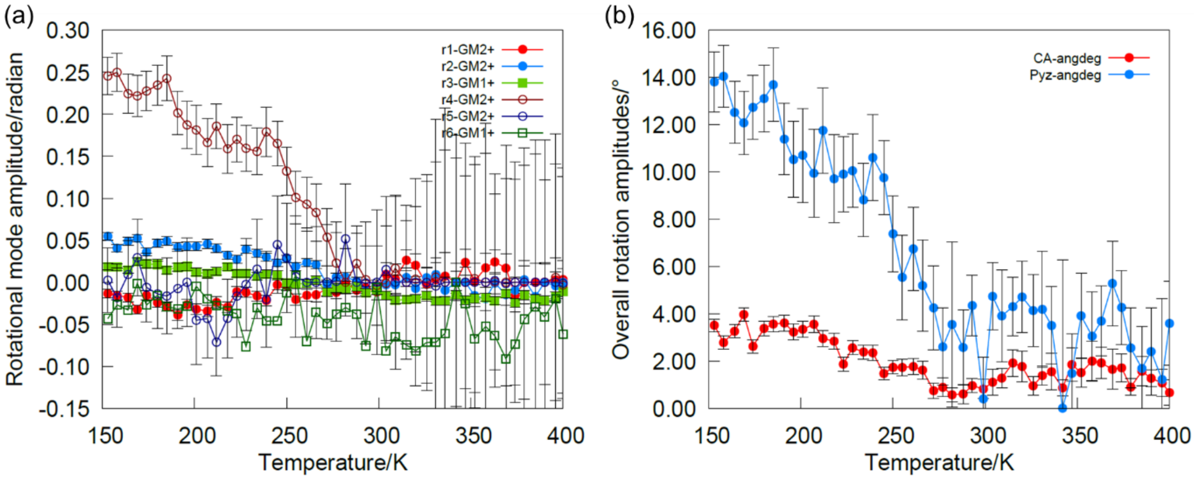

Figure 3.21: Results from symmetry-adapted distortion mode analysis of the laboratory powder diffraction data collected upon warming. (a) Rotational symmetry-mode amplitudes r1–r3 (CA, shaded markers) and r4–r6 (Pyz, open markers) in radians. (b) Amplitudes for overall rotation vectors of each molecule.

3.9 Super-colossal uniaxial negative thermal expansion

Even though CA-Pyz does not undergo a ferroelectric-type phase transition, it shows remarkable thermal expansion behaviour associated with the phase transition. In this section, we will focus on a comprehensive study of thermal expansion in CA-Pyz using a strain mode description. We will discuss the results from strain mode analysis in order to understand what structural features are responsible for the unusual thermal expansion behaviour observed in CA-Pyz.

Thermal expansion coefficients calculated for each unit cell axis and the volume are shown in Figure 3.22. Values are derived by fitting a smooth spline function to the data shown in Figure 3.15 followed by numerical differentiation. We can see an extreme negative thermal expansion (NTE), with the coefficient of thermal expansion (CTE) approaching -1500×10^{-6} K^{-1}, along the parent *b*-axis. Meanwhile, the maximum of CTE along the parent *a*-axis approaches $+1500 \times 10^{-6}$ K^{-1}, indicating an extremely large positive thermal expansion (PTE).

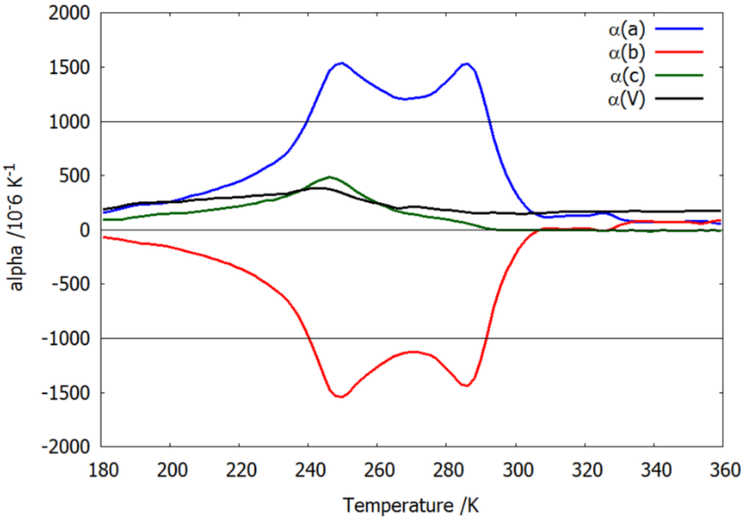

Figure 3.22: Thermal expansion coefficients for each unit cell axis.

Strain modes, which use a similar language to rotational modes, allow us to describe the cell parameter changes relative to the 300 K cell. A TOPAS script allowing us to extract the strain mode description is shown in Appendix II. The six degrees of freedom of the low temperature cell can be described by four strain modes (s_1–s_4) belonging to the Γ_1^+ irrep of the HT phase and two strain modes (s_5 and s_6) belonging to the Γ_2^+ irrep of the HT phase. Figure 3.23 shows the amplitude of each strain mode extracted from the unit cell parameters data shown in Figure 3.15. The symmetry-breaking strain modes Γ_2^+ refine to essentially zero values above T_c = 300 K for the monoclinic HT phase, but show significant changes in amplitudes below 300 K as anticipated. Noticeably, the Γ_2^+ s_5 strain mode reaches –0.14 (–14%) by 180 K. The effects of each strain mode on the cell metrics will be comprehensively discussed later. The amplitude of Γ_2^+ s_5 strain mode is significantly larger than other strain modes. This observation provides additional evidence (complementary to the rotational modes) that most of the structural changes in CA-Pyz at the phase transition can be described by using one mode belonging to Γ_2^+ irrep. The Γ_1^+ strain modes seem to show different temperature dependences from those of Γ_2^+ irrep. Their amplitudes show that marked deviations from their high temperature extrapolated behavior only appear below T ≈ 260 K.

The influence of the strain modes on individual cell parameters depends on the choice of cell setting used. If we use a non-standard $C\bar{1}$ setting for the child structure, we of course see the same temperature dependence of strain modes but they manifest in a different temperature dependence of cell parameters (Figure 3.18). In this alternative strain mode description, the large –14% amplitude of the s_5 Γ_2^+ mode predominantly influences the cell angle γ, which changes from 90 to ~101.6° between 300 and 150 K.

In order to properly decouple the physical changes of the crystal from the cell setting, we have calculated thermal expansion along three mutually orthogonal principal axes of the expansion tensor using the PAScal program[21]. The resulting expansivity indicatrix is a smooth surface used to visualize the thermal expansion tensor. The distance between the point on the surface and the origin represents the magnitude of the thermal expansion coefficient in a given direction. Red indicates positive thermal expansion and blue indicates negative We can see how the direction of the crystallographic unit cell axes relate to the principal axes by plotting them on the same figure. Figures 3.24 shows expansivity indicatrices representations for CA-Pyz considering just Γ_1^+, just Γ_2^+, and $\Gamma_1^+ + \Gamma_2^+$ combined strains along with their relationships to the parent cell axes. As anticipated from Figure 3.15, extremely large negative thermal expansion (blue) is close to the parent *b*-axis, extremely large positive expansion (red) close to the *a*-axis, and more normal (though still large) positive expansion close to the *c*-axis. We see that the extreme uniaxial contraction (−1500 K^{-1} at 250 K) is dominated by Γ_2^+ strains and that the dominant effect of Γ_1^+ is expansion of the interlayer *c*-axis. Thermal expansion coefficients along principal axes over a 50 and a 100 K temperature range are given in Table 3.9. The magnitudes of α_{X1} and α_{X3} correspond to a $\Delta l/l \sim -14\%$ and +15% respectively and are approximately 100 times bigger than the “colossal” definition introduced in the section 1.1.4 and bigger than most of the compounds listed in Table 1.1 in the introduction.

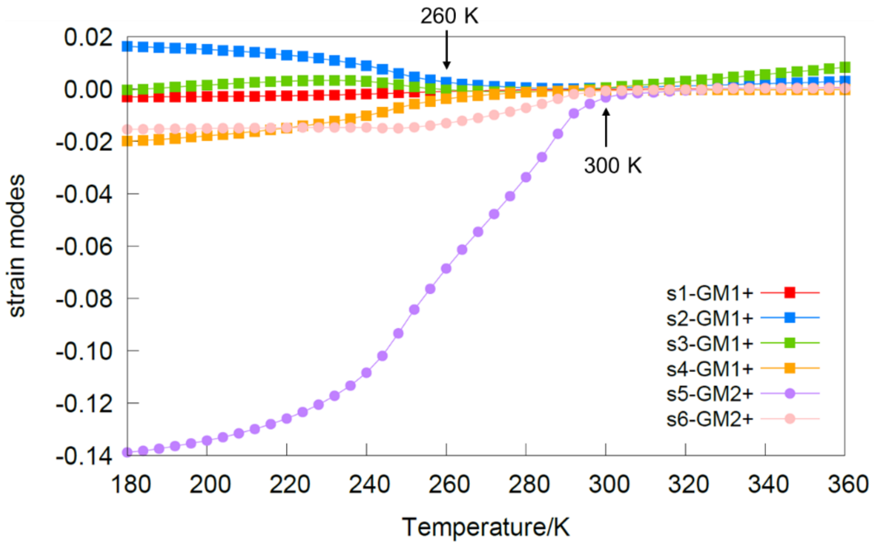

Figure3.23: Strain mode amplitudes s_1–s_6 relative to the 300 K cell.

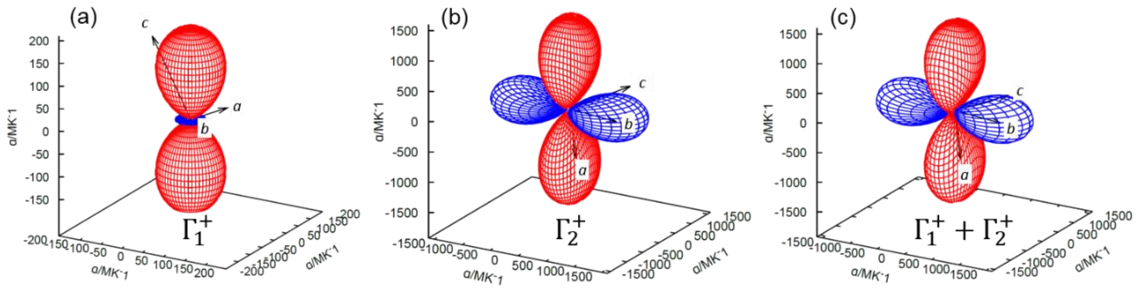

Figure 3.24: Thermal expansion indicatrices for (a) Γ_1^+only, (b) Γ_2^+ only and (c) Γ_1^++Γ_2^+ combined strains between 250 and 300 K. Note the much large axes scales in (b) and (c).

Table 3.9: Irrep-specific thermal expansions (left) over the 250–300 K range (200–300 K values given in parentheses for $\Gamma_1^+ + \Gamma_2^+$), along principal axes X_1–X_3, ordered from lowest (X1) to highest (X3) values, and overall volume expansion. Right hand columns show each principal-axis direction relative to crystallographic axes for the overall strain (i.e. components of Xn directions along *a*, *b* and *c* as shown in Figure 4c). Estimated uncertainties on expansion coefficients are ~30 × 10^{-6} K^{-1}.

Axes	**Thermal expansion (10^{-6} K−1) along principal axes**			**Principal axis components for overall $\Gamma_1^+ + \Gamma_2^+$ expansion**		
	Γ_1^+	Γ_2^+	$\Gamma_1^+ + \Gamma_2^+$	*a*	*b*	*c*
X_1	−34	−1345	−1375 (–893)	–0.10	0.99	–0.07
X_2	−33	−18	+196 (+188)	–0.17	0.01	0.99
X_3	+205	+1552	+1524 (+1065)	–0.99	0.10	0.03
Volume	+138	+88	+245 (+270)			

The influences of strain modes on each individual cell parameter are relatively complex. However, we can express the dependences of the individual child-cell (*P*-1 cell) parameters to first order, and then apply the observed 150 K strain-mode amplitudes to quantitatively determine which contributions are most important. These approximations will help to explain the extremely unusual behaviour of the cell parameters with changing temperature in Figure 3.15. Figure 3.25 shows the contributions of each strain mode to the changes of unit cell parameters graphically. Further information on these dependences are summarised in Table 3.10. As we can see in Figure 3.25(a), the changes in cell edges *a* and *b* are dominated by the mode s_5 and the change in cell edges *c* is largely affected by mode s_4 and slightly by s_2. As shown pictorially in Figure 3.25(b), the α and β cell angles vary in opposite directions with respect to either mode s_5 or s_6 of Γ_2^+. According to Table 3.10, the sensitivity of changes in the α and β values to s_5 is quite weak. However, since the s_5 mode has an extremely big amplitude it leads to −0.575° and 0.575° changes in α and β respectively. In contrast, the sensitivity to s_6 is strong but the amplitude of s_6 is small. As a result, s_6 makes comparable contributions to angle changes (0.811° to α and -0.811° to β) as to s_5. Therefore, the overall Γ_2^+contributions to both angles are $\Delta\alpha = 0.811^\circ - 0.575^\circ = 0.236^\circ$ and $\Delta\beta = -0.811 + 0.575 = -0.236^\circ$. Even though the amplitude of mode s_2 of Γ_1^+ is small, its eventual contributions to the changes in the α and β are significant due to the high sensitivity of both angles. Mode s_2 therefore needs to be considered as both angles are considerably sensitive to it. As a result, the total contributions of Γ_1^+ to the angles are $\Delta\alpha = \Delta\beta = 1.019^\circ - 0.199^\circ = 0.820^\circ$ at 150 K, which are ultimately larger than those of Γ_2^+. The $\Gamma_1^+ + \Gamma_2^+$ combined contributions are then $\Delta\alpha = 0.820^\circ + 0.236^\circ = 1.056^\circ$ and $\Delta\beta = 0.820^\circ - 0.236^\circ = 0.584^\circ$ at 150 K. However, because the Γ_1^+ modes only show significant amplitudes below ~260 K which is below the 300 K transition temperature (Figure 3.23), the decreases in β resulting from Γ_2^+ strains (i.e. $\Delta\beta$ is negative) with decreasing temperature is well underway before the increase in β arising from the Γ_1^+ strains (i.e. $\Delta\beta$ is positive) begins to evolve. This can explain the unusual temperature dependence (trend reversal) of the cell angle β observed in Figure 3.15(b).

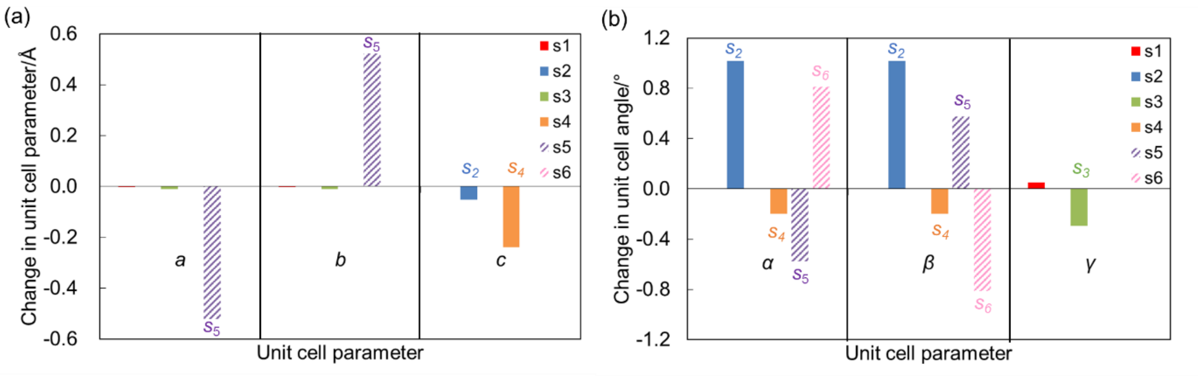

Figure 3.25: The contribution of each strain mode to the changes of (a) unit cell parameters *a*, *b* and *c*, and (b) unit cell angles *α*, *β* and *γ*.

Table 3.10: First-order terms in the expansion of each child-cell parameter in the unitless strain-mode amplitudes at 300 K, along with the resulting contributions at 150 K in parentheses. The values in a given column can be summed to determine the approximate total change in the corresponding cell parameter. For example, the pseudo-linear slope of the $\Delta c(s_2)$ curve is -3.061 Å, so that a value of $s_2 = +0.0107$ (at 150 K) results in a change of $\Delta c \approx (-3.061\ \text{Å})(0.0169) = -0.052\ \text{Å}$, in addition to $\Delta\alpha = \Delta\beta \approx (+1.050)(0.0107)(180°/\pi) = +1.019°$. Some of the smaller non-zero 150 K values were rounded to zero.

Irrep	**Mode**	***Δa*/Å**	***Δb*/Å**	***Δc*/Å**	***Δα*/°**	***Δβ*/°**	***Δγ*/°**
Γ_1^+	$s_1(-0.0009)$	3.234 s_1 (-0.003)	3.234 s_1 (-0.003)	0.444 s_1 (≈ 0)	-0.214 s_1 (≈ 0)	-0.214 s_1 (≈ 0)	-0.976 s_1 (0.049)
Γ_1^+	$s_2(\ \ 0.0169)$	0	0	-3.061 s_2 (-0.052)	1.050 s_2 (1.019)	1.050 s_2 (1.019)	0
Γ_1^+	$s_3(-0.0053)$	2.082 s_3 (-0.011)	2.082 s_3 (-0.011)	0	0.062 s_3 (≈ 0)	0.062 s_3 (≈ 0)	0.976 s_3 (-0.295)
Γ_1^+	$s_4(-0.0228)$	0	0	10.549 s_4 (-0.240)	0.152 s_4 (-0.199)	0.152 s_4 (-0.199)	0
Γ_2^+	$s_5(-0.1422)$	3.670 s_5 (-0.522)	-3.670 s_5 (0.522)	0	0.071 s_5 (-0.575)	-0.072 s_5 (0.575)	0
Γ_2^+	$s_6(-0.01612)$	0	0	0	-0.878 s_6 (0.811)	0.878 s_6 (-0.811)	0

Next, we will consider the cell volume changes shown in Figure 3.16. Unlike the individual cell parameters, the dependence of the cell volume on the strain amplitudes is expressed by a 3rd-order multi-variable polynomial:

$$\frac{\Delta V}{V} = s_1 + s_3 + s_4 + s_1 s_3 + s_1 s_4 + s_3 s_4 + s_1 s_3 s_4$$

$$-\frac{1}{2}\left(s_2^2 + s_5^2 + s_6^2 + s_3 s_2^2 + s_4 s_5^2 + s_1 s_6^2\right) + \frac{1}{\sqrt{2}} s_2 s_5 s_6$$

Considering only the lowest-order term in each strain ($s_1, s_3, s_4, s_2^2, s_5^2, s_6^2$), we see that the volume change is approximately linear in and very sensitive to strains s_1, s_3, s_4, which affect primarily the cell-edge lengths. In contrast, the volume change is merely quadratic in, and hence much less sensitive to, strains s_2, s_5, s_6, which tend to primarily change on the cell angles. As a result, although the Γ_2^+ strain s_5 dominates the structural (and presumably the energetic) changes, the much smaller Γ_1^+ strain s_4 makes the dominant contribution to the volume change. We therefore expect to see two different features in the cell volume evolution on cooling: a small change at ~300 K when the Γ_2^+ modes become active and a more significant change at lower temperature (260 K) when the Γ_1^+

strains become significant. The first change is expected to be negative $[-\frac{1}{2}(s_5^2 + s_6^2)]$ and the second change positive. This is clear in the ΔV plot (black squares) of Figure 3.16.

We still need to explain why the primary Γ_2^+ strain modes and the secondary Γ_1^+ strain modes show different temperature dependencies. In this context, the word "secondary" indicates the mathematical inability to generate the low-symmetry subgroup and hence the physical inability to break the parent symmetry and drive the transition. For example, the secondary Γ_1^+ modes do not break any parent symmetries at all since Γ_1^+ is also the identity irrep. One possible explanation is the occurance of a second phase transition near 260 K, which would necessarily be isosymmetric (space group $P\bar{1}$ is retained) and first order since its order parameter belongs to the identity irrep. We see no strong evidence to support such a phase transition in our data. In addition, a closer examination of Figure 3.23 reveals that the amplitude of the secondary Γ_1^+ modes are not precisely zero in the temperature range between 260 and 300 K. We therefore believe that the observed behaviour is caused by a coupling between the primary Γ_2^+ and secondary Γ_1^+ order parameters. In essence, for strains as large as those observed in CA-Pyz, cross-coupling terms in the Landau free-energy expansion become sufficiently large that they can no longer be ignored.

We also tried to understand why the Γ_2^+–Γ_1^+ strain coupling increases below ~260 K in terms of the molecular features of the CA-Pyz structure. The structural distortions in CA-Pyz are best understood with respect to the H-bonded chains which run along the child-cell's body diagonal ([101] of parent) and are emphasised by red and blue shading in Figure 3.18. Rotational symmetry-mode refinement shows the main structural change is a cooperative rotation of all Pyz molecules occuring around an axis close to the H···N(Pyz)N···H hydrogen bond direction. This is mainly affected by the r_4 Γ_2^+ rotation, with the smaller r_5 Γ_2^+ contribution bringing the rotation vector in line with the H-bonded chain. The rotations lead to the significant shift in Pyz positions together with a sliding of adjacent planes of CA molecules, with each layer moving laterally from its high-temperature position by ~1 Å between 300 and 250 K (as shown in Figure 3.7(a)). These structural changes are enabled by the relatively weak van der Waals interactions between CA planes and result in the significant expansion of the *b*-axis on cooling. In addition to the dominant Γ_2^+ rotations, we see a small r_6 Γ_1^+ rotation below 260 K (shown with open squares in Figure 3.19(a) and (b)). This corresponds to a rotation of Pyz around an axis perpendicular to the N-N direction and in the plane of the ring. The rotation direction is shown by the dark green arrow in the top left panel of Figure 3.18. This motion "buckles" the CA-Pyz chain, causing a reduction in the *c* axis (~0.2 Å) and a small expansion on cooling in the *ab* plane (~0.1 Å increase in $\sqrt{ab\,\sin(\gamma)}$ as an in-plane measure of dimension) as the Pyz plane becomes more closely aligned with it. It seems that this distortion is driven by the large r_4 rotation and provides the observed Γ_2^+ and Γ_1^+ strain-coupling that emerges with decreasing temperature.

3.10 Conclusions

The neutral 1:1 co-crystals of chloranilic acid pyrazine were successfully obtained by slow evaporation. We observed a reversible phase transition in CA-Pyz from our variable temperature single crystal and powder x-ray diffraction data. The phase transition, which happens close to room temperature, is associated with an extreme anisotropic thermal expansion behaviour with thermal expansion coefficients α_{X1} = −1375×10^{-6} K^{-1}, α_{X2} = +196 × 10^{-6} K^{-1} and α_{X3} = +1524 ×10^{-6} K^{-1} over a 100 K temperature range. This corresponds to a 14% contraction over a 100 K range and the magnitude of this change is 100 times the largest in phonon-driven ceramic materials. Our comprehensive structural studies revealed the phase transition is accompanied by the relatively large displacement of adjacent molecular layers resulting from the rotational motion of pyrazine molecule. In the HT form, anisotropic atomic displacement parameters derived from neutron diffraction data suggest significant (~22°) librational disorder of pyrazine molecules around an axis defined by the H⋯N(Pyz)N⋯H hydrogen bonds, which freeze out as a ~16° static rotation on cooling. The transition, which is presumably entropically driven, is enabled by the cooperative sliding of adjacent molecular layers ~1.34 Å (over the 150–300 K range) and leads to the high thermal anisotropy.

In this report, we also demonstrate the power of a symmetry-based description of the phase transition and how the symmetry-adapted rotational modes successfully capture all the important structural changes. We use a small number of parameters to describe the phase transition. This means that the important information can even be extracted from low-quality powder diffraction data. Additionally, we adopt the concept of symmetry-adapted strain modes to successfully describe the thermal expansion properties of the material. The use of strain modes allowed us to capture the unusual temperature dependence of cell parameters in this material in terms of coupling between primary and secondary order parameters.

These methods can be used for a wide range of molecular and hybrid materials undergoing phase transitions and can be readily applied using the ISODISTORT and TOPAS software suites, allowing useful information to be determined on such materials even using relatively low-quality powder diffraction data. We reapply molecular symmetry modes to different materials in chapters 4 and 5.

References

1. Horiuchi, S.; Kumai, R.; Tokura, Y., Hydrogen-bonded donor-acceptor compounds for organic ferroelectric materials. *Chemical Communications* **2007,** (23), 2321-2329.

2. Horiuchi, S.; Tokura, Y., Organic ferroelectrics. *Nature Materials* **2008,** *7* (5), 357-366.

3. Asaji, T.; Seliger, J.; Žagar, V.; Sekiguchi, M.; Watanabe, J.; Gotoh, K.; Ishida, H.; Vrtnik, S.; Dolinšek, J., Phase transition and temperature dependent electronic state of an organic ferroelectric, phenazine–chloranilic acid (1:1). *Journal of Physics: Condensed Matter* **2007,** *19* (22), 226203.

4. Horiuchi, S.; Kumai, R.; Tokura, Y., Proton-displacive ferroelectricity in neutral cocrystals of anilic acids with phenazine. *Journal of Materials Chemistry* **2009,** *19* (25), 4421-4434.

5. Lee, K.; Kolb, B.; Thonhauser, T.; Vanderbilt, D.; Langreth, D. C., Structure and energetics of a ferroelectric organic crystal of phenazine and chloranilic acid. *Physical Review B* **2012,** *86* (10), 104102.

6. Satio, K.; Amano, M.; Yamamura, Y.; Tojo, T.; Atake, T., Low-Temperature Phase Transitions of an Organic Ferroelectrics, Phenazine–Chloranilic Acid. *Journal of the Physical Society of Japan* **2006,** *75* (3), 033601.

7. Horiuchi, S.; Kumai, R.; Tokura, Y., Room-Temperature Ferroelectricity and Gigantic Dielectric Susceptibility on a Supramolecular Architecture of Phenazine and Deuterated Chloranilic Acid. *Journal of the American Chemical Society* **2005,** *127* (14), 5010-5011.

8. Groom, C. R.; Bruno, I. J.; Lightfoot, M. P.; Ward, S. C., The Cambridge Structural Database. *Acta Crystallographica Section B* **2016,** *72* (2), 171-179.

9. Ishida, H.; Kashino, S., 1:1 Complexes of chloranilic acid with pyrazine and morpholine: one- and two-dimensional hydrogen-bond networks. *Acta Crystallographica Section C* **1999,** *55* (11), 1923-1926.

10. Liu, H.; Gutmann, M. J.; Stokes, H. T.; Campbell, B. J.; Evans, I. R.; Evans, J. S. O., Supercolossal Uniaxial Negative Thermal Expansion in Chloranilic Acid Pyrazine, CA-Pyz. *Chemistry of Materials* **2019,** *31* (12), 4514-4523.

11. Altomare, A. C., G.; Giacovazzo, C.; Guagliardi, A.; Burla, M.C.; Polidori, G.; Camalli, M, SIR92. *Journal of Applied Crystallography* **1994,** *27*, 437.

12. Betteridge, P. W., Carruthers, J.R., Cooper, R.I., Prout, K., Watkin, D.J, CRYSTALS. *Journal of Applied Crystallography* **2003,** *36*, 1487.

13. Coelho, A. A.; Evans, J. S. O.; Evans, I. R.; Kern, A.; Parsons, S., The TOPAS symbolic computation system. *Powder Diffraction* **2011,** *26* (4), S22.

14. Dinnebier Robert, E.; Leineweber, A.; Evans John, S. O., *Rietveld Refinement, Practical Powder Diffraction Pattern Analysis using TOPAS*. 2018.

15. Coelho, A., TOPAS and TOPAS-Academic: an optimization program integrating computer algebra and crystallographic objects written in C++. *Journal of Applied Crystallography* **2018,** *51* (1), 210-218.

16. Campbell, B. J.; Stokes, H. T.; Tanner, D. E.; Hatch, D. M., ISODISPLACE: a web-based tool for exploring structural distortions. *Journal of Applied Crystallography* **2006,** *39* (4), 607-614.

17. Ford, S. J.; Delamore, O. J.; Evans, J. S. O.; McIntyre, G. J.; Johnson, M. R.; Radosavljević Evans, I., Giant Deuteron Migration During the Isosymmetric Phase Transition in Deuterated 3,5-Pyridinedicarboxylic Acid. *Chemistry – A European Journal* **2011,** *17* (52), 14942-14951.

18. Busing, W. R.; Levy, H. A., The effect of thermal motion on the estimation of bond lengths from diffraction measurements. *Acta Crystallographica* **1964,** *17* (2), 142-146.

19. Schomaker, V.; Trueblood, K. N., On the rigid-body motion of molecules in crystals. *Acta Crystallographica Section B* **1968,** *24* (1), 63-76.

20. Jarvinen, M., Application of symmetrized harmonics expansion to correction of the preferred orientation effect. *Journal of Applied Crystallography* **1993,** *26* (4), 525-531.

21. Cliffe, M. J.; Goodwin, A. L., PASCal: a principal axis strain calculator for thermal expansion and compressibility determination. *Journal of Applied Crystallography* **2012,** *45* (6), 1321-1329.

Chapter 4 Unusual symmetry properties of the phase transition in the molecular ferroelectric 5,6-dichloro-2-methylbenzimidazole (DC-MBI)

Overview

This chapter demonstrates a systematic and exhaustive symmetry-adapted distortion mode subgroup search for determining the crystal structure of a molecular material from powder X-ray diffraction data. We applied the method to the important molecular ferroelectric 5,6-dichloro-2-methylbenzimidazole (DC-MBI) which we found undergoes a phase transition at 400 K on warming (330 K on cooling). This is the first example of an organic molecular system whose structure has been solved by exhaustive symmetry search methods. We describe the unusual symmetry-lowering that occurs on heating in terms of rotational symmetry mode amplitudes.

4.1. Introduction

The single-component hydrogen-bonded material, 5,6-dichloro-2-methylbenzimidazole (DC-MBI), has been reported to exhibit ferroelectricity at room temperature.[1] The ferroelectricity is thermally robust to at least 373 K. A P-E hysteresis loop was obtained at 373 K, validating the ferroelectricity in DC-MBI. Above T~400 K a phase transition was reported based on DSC data, though no structural investigation was performed.

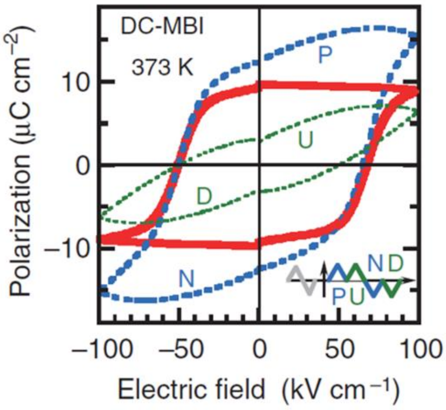

Figure 4.1: The *P-E* hysteresis loop obtained at 373 K by using the double-wave method reproduced directly from reference 1.[1] The 'non-hysteresis' polarization (green dashed curve) was obtained from the up (U) and down (D) runs and the total polarisation (blue dashed curve) from the positive (P) and negative (N) runs. The pure hysteresis component (red solid curve) was obtained by subtracting the 'non-hysteresis' polarization from the total.

The ferroelectric phase of DC-MBI adopts the polar orthorhombic space group $Pca2_1$ with unit cell parameters of a=14.238(3) Å, b=5.6866(12) Å, c=10.398(2) Å, V=841.9(3) Å^3 and Z=4 at 293 K. DC-MBI molecules play a dual role of proton donor and acceptor in the ferroelectric switching. As shown in Figure 4.2(a), DC-MBI molecules are connected by intermolecular hydrogen bonds (N-H3…N) which form a one-dimensional hydrogen-bonded chain running along the crystallographic *c*-axis. The donor-acceptor distance d(N···N) is 2.977(4) Å, and the N-H3···N angle is 145(3)°. The presence of pseudo-symmetry in the ferroelectric structure suggests the existence of a potential paraelectric high-temperature form. In the proposed high-temperature structure (Figure 4.2(d)), DC-MBI would adopt a centrosymmetric space group *Pbcm*. As illustrated in Figure 4.2(b), an additional mirror plane perpendicular to the molecular plane would be introduced by disordering the H3 protons in the N-H3…N hydrogen bond chain, increasing the symmetry of the structure. Thus, If DC-MBI undergoes a phase transition to the hypothetical *Pbcm* structure, the ferroelectric switching mechanism could be explained by the positional ordering of protons along the hydrogen-bonded chains.

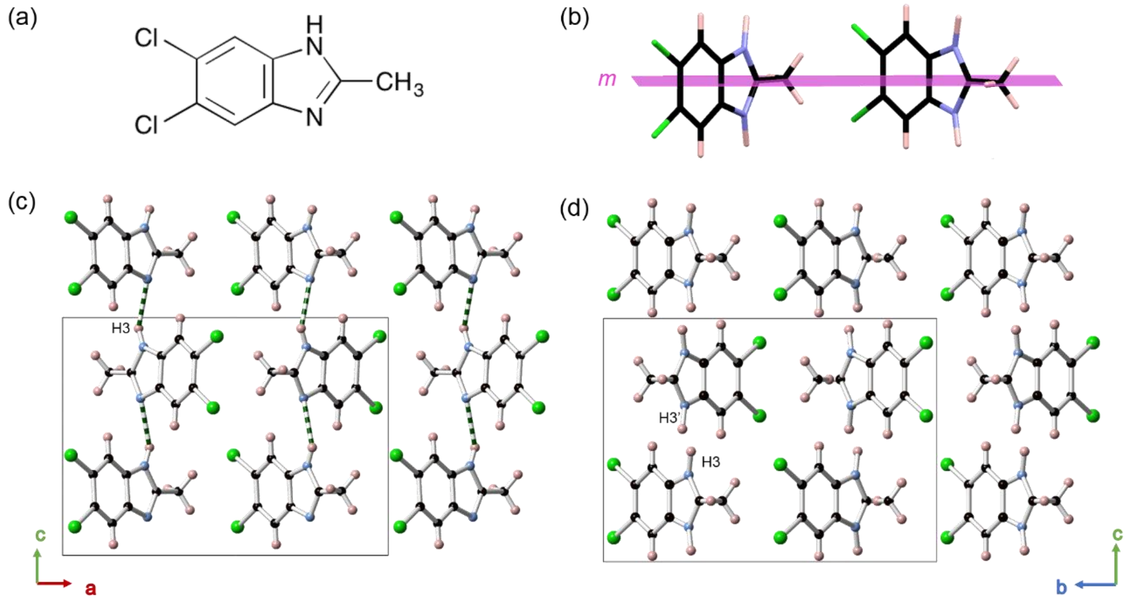

Figure 4.2: The molecular and crystal structure of DC-MBI. (a) Molecular structure of DC-MBI. (b) The additional mirror plane existing in the hypothetical *Pbcm* structure. (c) Room temperature $Pca2_1$ crystal structure. (b) Hypothetical *Pbcm* high temperature structure.

However, the structure of the high-temperature form of DC-MBI has not been identified experimentally. The objective of this work was to determine its crystal structure and carry out a comprehensive study of the phase transition. It was hoped that this would give insight into the ferroelectric switching mechanism. Although we confirmed that DC-MBI does undergo a phase transition, it surprisingly shows a symmetry-lowering at high temperature. We have used symmetry adapted distortion modes to explore all possible structures and test each candidate against powder X-ray diffraction data in order to determine the crystal structure of the high temperature phase systematically, exhaustively and automatically. We also report a study of phase transition and thermal expansion by using rotational modes and strain modes respectively. The work has been published in the Journal of American Chemical Society.[2]

4.2. Sample preparation and data collection

4.2.1 Sample preparation

5,6-dichloro-2-methylbenzimidazole (DC-MBI) was purchased from Sigma-Aldrich (99%). For powder diffraction experiments and second harmonic generation measurements, the material was used as purchased. Single crystals of DC-MBI (0.0201 g) were prepared by slow evaporation of an alcohol (methanol or ethanol) solution (typically 3 ml) at room temperature. Colourless needle-shaped crystals appeared after a week.

4.2.2 Laboratory and synchrotron X-ray diffraction

Variable temperature powder X-ray diffraction were carried out on two diffractometers, the “d6” and “d9”. Experimental details are summarised in Table 4.1. Experiments d6b_00839 and d6b_00840 were performed on pure DC-MBI, where a series of 15 mins PXRD patterns were recorded over the 2θ range of 2-30°using a step size of 0.02°. The sample was cooled from 450 K to 110 K at a rate of 20 Kh^{-1}, and was warmed from 110 K back to 450 K at the same rate. The results obtained from these two data sets will be discussed later in this work. Experiments d6b_01116 and d6b_01117 were performed to accurately calibrate the true sample temperature. A 1:4 by weight mixture of Si and DC-MBI powders was loaded into the capillary.

Table 4.1: Experimental details for variable temperature powder X-ray diffraction.

Experiment	Process	T range	Ramp rate	No. of runs	Total time
d6b_00839	cooling	450K-110K	20 K/hour	75	17 hours
d6b_00840	warming	110K-450K	20 K/hour	75	17 hours
d6b_01116	warming	100K-500K	10 K/hour	84	40.8 hours
d6b_01117	cooling	500K-100K	10 K/hour	84	40.8 hours

Synchrotron powder X-ray diffraction data were collected on beamline I11 of the Diamond Light Source. Samples were placed into a 0.7 mm quartz capillary attached to a brass holder which was spun during the measurement. Both low-temperature (100 K) and high-temperature (500 K) data were collected for 2h using λ = 0.8257653 Å (calibrated against silicon standard NIST 640c). All powder diffraction data were analysed using Topas Academic software.[3-4]

4.2.3 Temperature calibration for laboratory powder diffraction

Temperature was calibrated with a Si standard which has well determined low thermal expansion behaviour.[5] The Ideal value of the unit cell parameter was calculated at each temperature by an Einstein like expression (Equation 4.1).[6]

$$\ln\left({}^{a_i}/_{a_0}\right) = \sum_{j=1}^{n} \frac{X_j \theta_j}{\exp\left(\theta_j/T\right) - 1}$$

Equation 4.1

where a_i is the cell parameter at temperature T, a_0 is cell parameter at 0 K, X_j is an empirically derived coefficient and θ_j is an Einstein temperature. The magnitude of each coefficient used in the equation are summarised in Table 4.2.

Table 4.2: Coefficients used in the calculation of the unit cell parameters of Si using Equation 4.1.

Coefficients	Si
a_0/Å	5.42999
X_1/K^{-1}	-3.90610E-06
θ_1/K	321.79348
X_2/K^{-1}	7.34424E-06
θ_2/K	488.70035
X_3/K^{-1}	1.13321E-06
θ_4/K	1500

Unit cell parameters of Si were firstly fixed at their known values in the 300 K refinement and accurate zero point and instrumental peak shape parameters determined. In the variable temperature refinements, these were all fixed and the Si cell refined. Figure 4.3 shows the comparison between the experimental unit cell parameters (blue points) extracted from Rietveld refinement and the expected unit cell parameters (red points) calculated from Equation 4.1. The difference between the experimental and calculated values are scattered around 0 between 100 K and 400 K, which means the real experimental temperature is very close to the set temperature over this temperature range. The maximum deviation in the unit cell parameter is 0.0009 Å at 466 K in the warming experiment, indicating that the real experimental temperature is slightly lower than the set temperature at the highest temperature. Since Si has a relatively low thermal expansion a better calibration can be obtained using an Al internal standard. The temperature calibration based on Al is described in appendix III.

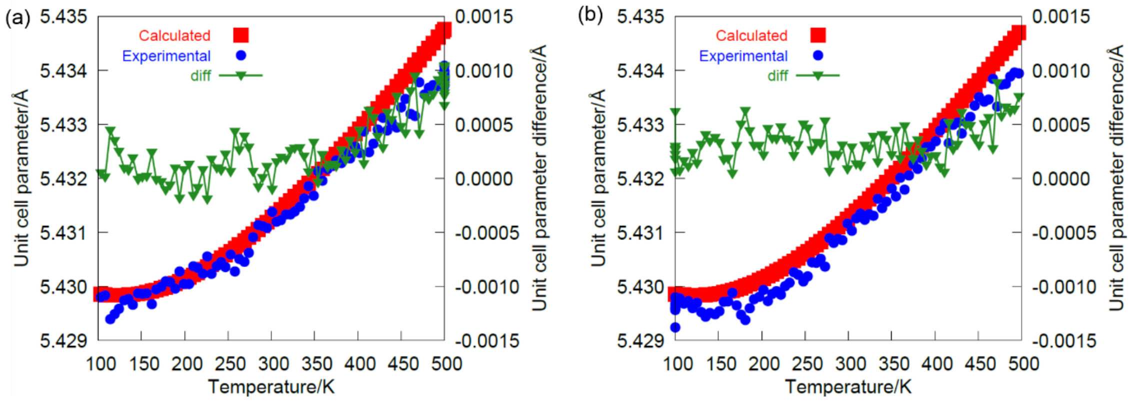

Figure 4.3: Temperature dependence of calculated and experimental unit cell parameters of Si obtained on “d6”. (a) Data collected on warming. (b) Data collected on cooling.

4.3. Variable temperature PXRD visual inspection

Figure 4.4 shows the laboratory variable temperature PXRD patterns over a 2θ range of 7-17° where the main changes occur. It is apparent that DC-MBI undergoes a reversible phase transition at high temperature. All peaks shift smoothly with changing temperature until the phase transition(T_c~400 K for warming and T_c~330 K for cooling) takes place. At high temperature, some peaks surprisingly appear to split, suggesting that the high-temperature (HT) phase has lower symmetry than to the low-temperature (LT) phase. Therefore the HT phase of DC-MBI cannot be the putative *Pbcm* structure with proton disordering previously proposed. The observation of a temperature hysteresis in the peak splitting, together with the temperature hysteresis in the DSC measurement reported in the literature[1], indicates a first-order phase transition.

Our attempts to determine the HT structure using single crystal X-ray diffraction did not succeed. Several single crystals of different sizes were tested on the “6K” diffractometer. Initially, they diffracted well at low temperature and also during heating, but shattered at ~450 K. This is presumably due to the abrupt volume change at the first-order phase transition. As a consequence, we were not able to determine the high-temperature structure using single crystal X-ray diffraction.

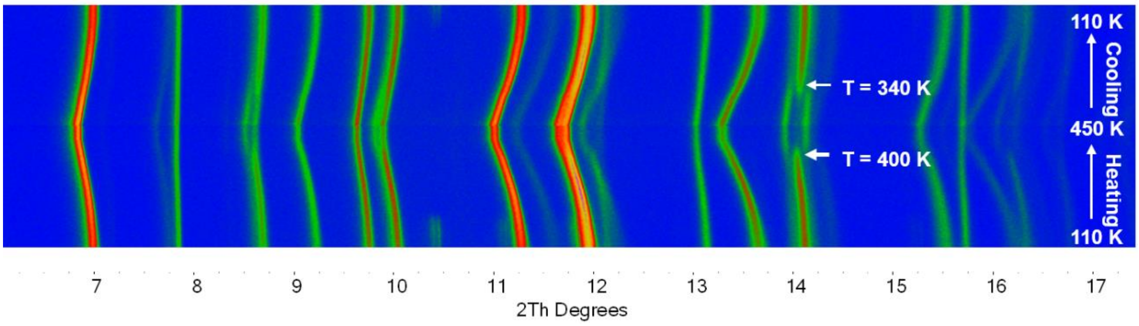

Figure 4.4: Variable temperature laboratory PXRD patterns collected on cooling and warming between 100 K and 450 K.

4.4. Exhaustive symmetry mode subgroup search: Structure solution of HT DC-MBI

4.6.1 Preliminary unit cell determination

We first attempted to solve the crystal structure from powder data in a conventional way. As described in section 2.4.4, extraction of peak positions from the 500 K synchrotron data followed by indexing for unit cell parameters determination was performed. The HT data can be successfully indexed using a monoclinic cell with a = 10.3812 Å, b = 14.487 Å, c =5.7383 Å and β = 90.950 Å. The orthorhombic to monoclinic change shows that there is an unusual symmetry lowering on warming. There are three possible space group types Pc, $P2_1$ and $P2_1/c$ suggested by the indexing. Figure 4.5 shows the Pawley fits using the unit cell parameters obtained from indexing using the different space group types. Pawley refinements confirm the correctness of the monoclinic unit cell; however, three space groups yield comparable fits. It is also hard to distinguish the candidate space group type for the HT phase only based on systematic absences. Visually, *hkl* ticks (as shown in Figure 4.5) yielded by these three space groups do not show much differences. One possible reason to explain this is the overlap of reflections, thus we could not differentiate individual reflections from the PXRD patterns. Another possible reason is the appearance of weak reflections that could not be distinguished from the background.

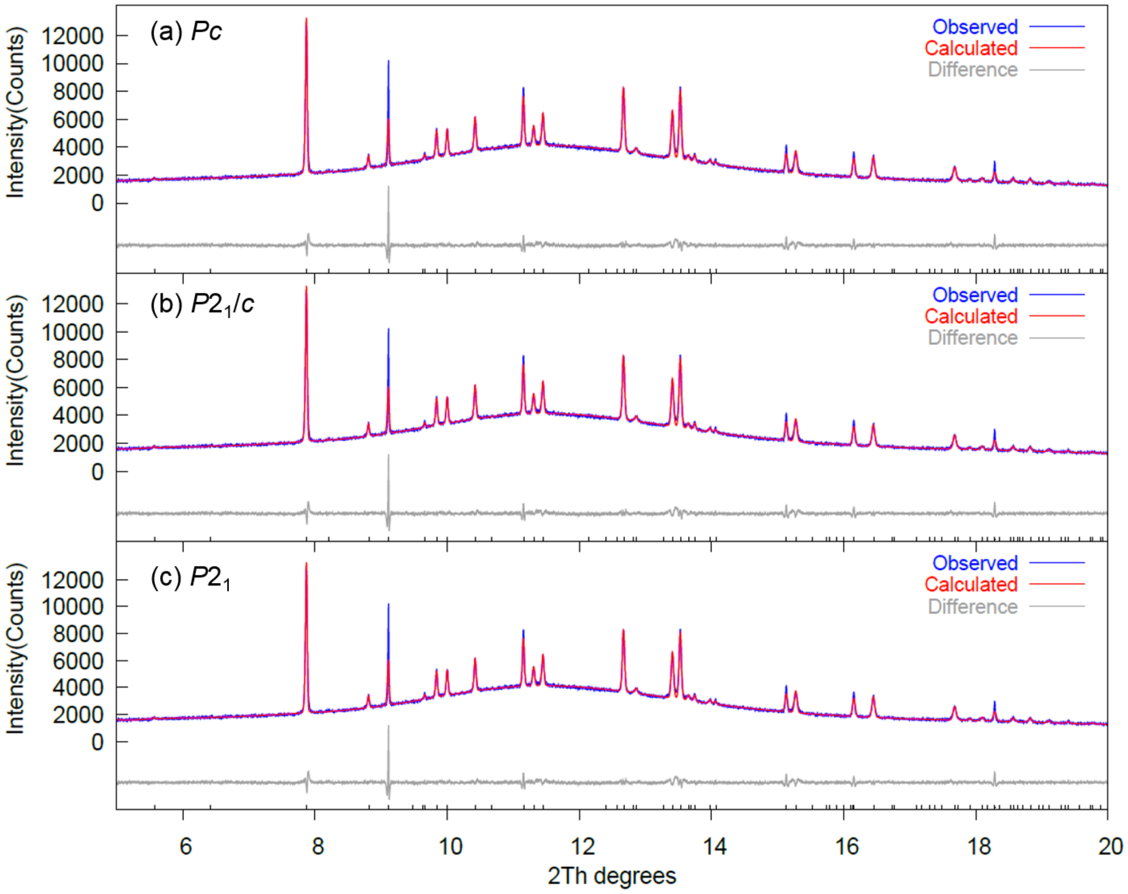

Figure 4.5 Examples of Pawley fits to HT PXRD data using a monoclinic cell. (a) Use of space group *Pc*. (b) Use of space group *P*2$_1$/*c*. (c) Use of space group *P*2$_1$. The systematic misfit in the ~9° peak is due to the *hkl*-dependent peak broadening and discussed in the text.

4.6.2 The advantages of using a symmetry mode subgroup search

Solving pseudosymmetry structures from powder diffraction data is a significant challenge, and there are numerous examples in the literature where structures have been revised multiple times due to incorrect unit cell or space group choices, particularly for functional inorganic materials. Recently, a variety of exhaustive methods for overcoming these problems have been described based on isotropy subgroups and symmetry-adapted distortion modes.[7] The first advantage of the new exhaustive symmetry search method comes from the use of the symmetry mode parameter set. As we discussed in section 2.5 and illustrated in chapter 3, the distortion modes approach is a powerful tool to understand the structure of a material using a small number of parameters. In the structural determination of DC-MBI, we combined the use of rotational and translational symmetry modes to describe the coherent movements of entire rigid body units. Instead of using the traditional parameter set of individual atomic shifts, the use of translational modes substantially simplifies the parameter set. The second advantage of using a symmetry mode subgroup search is that this method allows us to construct all possible intermediate subgroups between a high-symmetry parent structure and a lowest-possible-symmetry base structure and test each model against diffraction data systematically and automatically. This method will give a quantitative global view of the structure landscape. However, it should be noted that 1st order phase transitions may not necessarily produce crystal structures with group-subgroup relationships and symmetry mode subgroup search method works when group-subgroup relationships are valid at least between the model parent phase and child phase.

4.6.3 The choice of low symmetry child structure

The child structure should have low enough symmetry that it can model all peaks in the experimental PXRD pattern. Because the DC-MBI PXRD data does not give any evidence for any increase in the unit cell size, we could consider a *P*1-symmetry base structure as the lowest-possible child structure. In this *P*1 structure, no space group symmetry needs to be known or assumed. In the *P*1 description of symmetry modes, parent space group (*Pbcm*) symmetry gives rise to 12 rotational symmetry modes to describe the collective rotations of four DC-MBI molecules. 12 displacive symmetry modes are used to describe the translation of the DC-MBI molecules along parent cell axes, even though three of them are fixed at zero in order to fix the floating origin in the *P*1 cell. Parameters for instrumental peak shape (TCHZ peak shape) and axial divergence were fixed at the values obtained from silicon standard (640c NIST) refinement. 12 coefficients of a Chebyshev polynomical function were used to model the background. 15 terms of a 4th order spherical harmonics function were used to describe the anisotropic peak broadening. We can see from Figure 4.6 that the child *P*1-symmetry based structure yields an excellent Rietveld fit to the synchrotron X-ray diffraction data.

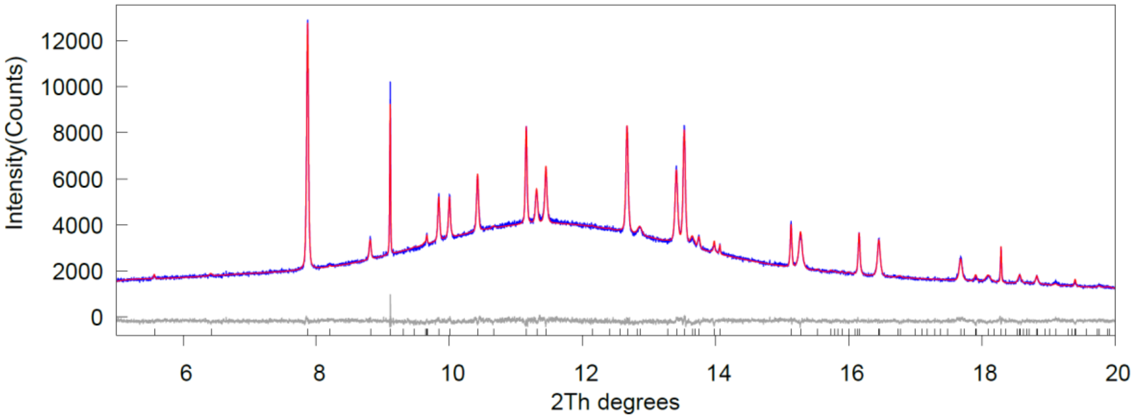

Figure 4.6: Rietveld fit to synchrotron PXRD pattern obtained at 450 K using the P1 child subgroup.

4.6.4 Subgroup tree

We can obtain a tree of all possible intermediate subgroups (Figure 4.7) that lie between the hypothetical *Pbcm* parent structure and the child *P*1-symmetry base structure by using ISODISTORT. ISODISTORT generates 16 subgroups including the parent structure. Some space group types appear twice with different origin choice relative to the parent resulting in distinct isotropy subgroups with inequivalent structural degree of freedom. The number of structural degrees of freedom ranged from 3 in space group *Pbcm* to 24 in space group *P*1. The active rotational and translational symmetry modes for each subgroup are summarised in Appendix IV. If we could detect which combination of symmetry modes is adequate to fully describe the PXRD pattern, we would be able to simultaneously determine the real space group of the HT phase of DC-MBI and its structural coordinates, that is to solve its structure.

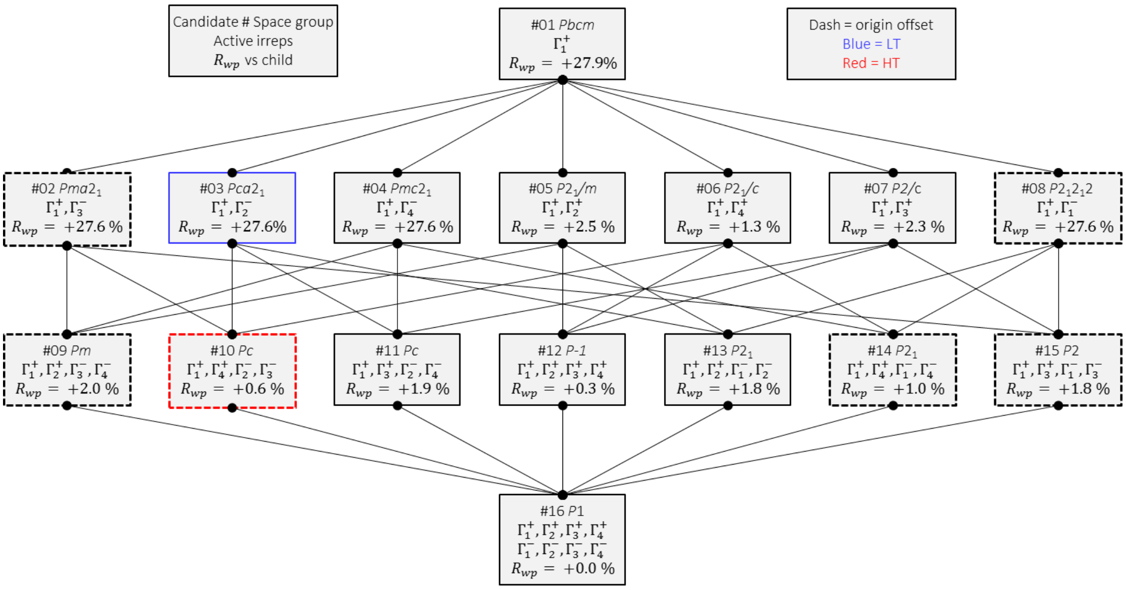

Figure 4.7: Tree of intermediate subgroups that lie between the symmetry groups of the hypothetical *Pbcm* parent structure (top) and the *P*1 base structure (bottom). The R_{wp} for refinement of each model relative to the *P*1 base structure is listed.

4.6.5 How to analyse a subgroup tree in TOPAS

Rietveld refinement was performed in order to test each subgroup candidate against the HT diffraction data. For each candidate, we repeated three sets of 1000 Rietveld iterations with values of parameters randomised after each convergence. At the end of all refinements, we assessed each subgroup candidate based on the visual evidence and the quality of the Rietveld fit as judged by different R-factors, and decide the most optimal candidate relative to the number of parameters needed.

We set up a single TOPAS script to enable the Rietveld refinement of multiple space group candidates to be performed in a single analysis. The “num_runs” macro inserted at the beginning of the script defines the number of runs that the TOPAS script performs and which space group type is used for each run. This macro allows us to test all subgroup candidates continuously and the relevant part of TOPAS script file is shown below:

```
'{{{ list of space groups
num_runs 48
         #list space_group_use sg_num {
         { #define sg01_pbcm  }   01
                  { #define sg01_pbcm  }   01
                  { #define sg01_pbcm  }   01
                  { #define sg01_pbcm  }   01
                  { #define sg02_pma2  }   02
                  { #define sg02_pma2  }   02
                  { #define sg02_pma2  }   02
                  { #define sg03_pca21 }   03
                  { #define sg03_pca21 }   03
                  { #define sg03_pca21 }   03
                           ...
                           etc
                           ...
                  { #define sg15_p2    }   15
                  { #define sg15_p2    }   15
                  { #define sg15_p2    }   15
                  { #define sg16_p1    }   16
                  { #define sg16_p1    }   16
                  { #define sg16_p1    }   16
         }
         space_group_use(Run_Number)
   out_file = Concat(String(INP_File), ".INP");
'}}}
```

In order for TOPAS to use the correct unit cell parameters and active symmetry distortion modes needed for each subgroup candidate, we include the refinement instructions below in the TOPAS script. The allowed irreps in each case are generated by ISODISTORT and are listed in Figure 4.7.

```
'{{{ define here which irreps to turn on/off for each space group and a flag for cell parameters free to refine
#ifdef sg01_pbcm   #define GM1+_on #define ortho #endif
#ifdef sg02_pma2   #define GM1+_on #define GM3-_on  #define ortho #endif
#ifdef sg03_pca21  #define GM1+_on #define GM2-_on  #define ortho #endif
#ifdef sg04_pmc21  #define GM1+_on #define GM4-_on  #define ortho #endif
#ifdef sg05_p21m   #define GM1+_on #define GM2+_on  #define mono  #endif
#ifdef sg06_p21c   #define GM1+_on #define GM4+_on  #define mono  #endif
#ifdef sg07_p2c    #define GM1+_on #define GM3+_on  #define mono  #endif
#ifdef sg08_p21212 #define GM1+_on #define GM1-_on  #define ortho #endif
#ifdef sg09_pm     #define GM1+_on #define GM2+_on  #define GM3-_on #define GM4-_on #define mono #endif
#ifdef sg10_pc     #define GM1+_on #define GM4+_on  #define GM2-_on #define GM3-_on #define mono #endif
#ifdef sg11_pc     #define GM1+_on #define GM3+_on  #define GM2-_on #define GM4-_on #define mono #endif
#ifdef sg12_pb1    #define GM1+_on #define GM2+_on  #define GM3+_on #define GM4+_on #define tric #endif
#ifdef sg13_p21    #define GM1+_on #define GM2+_on  #define GM1-_on #define GM2-_on #define mono #endif
#ifdef sg14_p21    #define GM1+_on #define GM4+_on  #define GM1-_on #define GM4-_on #define mono #endif
#ifdef sg15_p2     #define GM1+_on #define GM3+_on  #define GM1-_on #define GM3-_on #define mono #endif
#ifdef sg16_p1     #define GM1+_on #define GM2+_on  #define GM3+_on #define GM4+_on #define GM1-_on #define GM2-_on
#define GM3-_on #define GM4-_on #define tric #endif
```

```
'}}}

'cell parameters to refine depend on irreps active - i.e. space group
#ifdef ortho
a @  5.768694  c @  14.740271  b @  10.390251  al    90.00000 be    90.00000 ga    90.00000
#endif
#ifdef mono
a @  5.770275  c @  14.741435  b @  10.393210  al    90.00000 be    90.00000 ga  @  91.21605
#endif
#ifdef tric
a @  5.770667  c @  14.742132  b @  10.393593  al @   89.99329  be  @  89.99009  ga  @  91.21624
#endif

'{{{ mode definitions
macro vcr { val_on_continue = Rand(-0.01,0.01); }
#ifdef GM1+_on prm  r1   0.00245 min -20.00 max 20.00 vcr #endif 'Pbcm[0,0,0]GM1+(a)[He1:d:rot]A'(a)
#ifdef GM2+_on prm  r2  -0.06955 min -20.00 max 20.00 vcr #endif 'Pbcm[0,0,0]GM2+(a)[He1:d:rot]A'(a)
#ifdef GM3+_on prm  r3  -0.14473 min -20.00 max 20.00 vcr #endif 'Pbcm[0,0,0]GM3+(a)[He1:d:rot]A''_1(a)
#ifdef GM3+_on prm  r4   0.09435 min -20.00 max 20.00 vcr #endif 'Pbcm[0,0,0]GM3+(a)[He1:d:rot]A''_2(a)
#ifdef GM4+_on prm  r5   0.12188 min -20.00 max 20.00 vcr #endif 'Pbcm[0,0,0]GM4+(a)[He1:d:rot]A''_1(a)
#ifdef GM4+_on prm  r6  -0.07177 min -20.00 max 20.00 vcr #endif 'Pbcm[0,0,0]GM4+(a)[He1:d:rot]A''_2(a)
#ifdef GM1-_on prm  r7  -0.00434 min -20.00 max 20.00 vcr #endif 'Pbcm[0,0,0]GM1-(a)[He1:d:rot]A''_1(a)
#ifdef GM1-_on prm  r8  -0.00697 min -20.00 max 20.00 vcr #endif 'Pbcm[0,0,0]GM1-(a)[He1:d:rot]A''_2(a)
#ifdef GM2-_on prm  r9  -0.13402 min -20.00 max 20.00 vcr #endif 'Pbcm[0,0,0]GM2-(a)[He1:d:rot]A''_1(a)
#ifdef GM2-_on prm  r10  0.00961 min -20.00 max 20.00 vcr #endif 'Pbcm[0,0,0]GM2-(a)[He1:d:rot]A''_2(a)
#ifdef GM3-_on prm  r11 -0.07754 min -20.00 max 20.00 vcr #endif 'Pbcm[0,0,0]GM3-(a)[He1:d:rot]A'(a)
#ifdef GM4-_on prm  r12  0.01876 min -20.00 max 20.00 vcr #endif 'Pbcm[0,0,0]GM4-(a)[He1:d:rot]A'(a)
#ifdef GM1+_on prm  a1   2.03236 min -20.00 max 20.00 vcr #endif 'Pbcm[0,0,0]GM1+(a)[He1:d:dsp]A'_1(a)
#ifdef GM1+_on prm  a2  -2.59305 min -20.00 max 20.00 vcr #endif 'Pbcm[0,0,0]GM1+(a)[He1:d:dsp]A'_2(a)
#ifdef GM2+_on prm  a3  -1.84536 min -20.00 max 20.00 vcr #endif 'Pbcm[0,0,0]GM2+(a)[He1:d:dsp]A'_1(a)
#ifdef GM2+_on prm  a4  -0.15950 min -20.00 max 20.00 vcr #endif 'Pbcm[0,0,0]GM2+(a)[He1:d:dsp]A'_2(a)
#ifdef GM3+_on prm  a5  -1.13681 min -20.00 max 20.00 vcr #endif 'Pbcm[0,0,0]GM3+(a)[He1:d:dsp]A''(a)
#ifdef GM4+_on prm  a6   1.59862 min -20.00 max 20.00 vcr #endif 'Pbcm[0,0,0]GM4+(a)[He1:d:dsp]A''(a)
#ifdef GM1-_on prm  a7   3.27581 min -20.00 max 20.00 vcr #endif 'Pbcm[0,0,0]GM1-(a)[He1:d:dsp]A''(a)
#ifdef GM2-_on prm !a8   0.0000  min -20.00 max 20.00 vcr #endif 'Pbcm[0,0,0]GM2-(a)[He1:d:dsp]A''(a)
#ifdef GM3-_on prm !a9   0.0000  min -20.00 max 20.00 vcr #endif 'Pbcm[0,0,0]GM3-(a)[He1:d:dsp]A'_1(a)
#ifdef GM3-_on prm  a10  2.55372 min -20.00 max 20.00 vcr #endif 'Pbcm[0,0,0]GM3-(a)[He1:d:dsp]A'_2(a)
#ifdef GM4-_on prm  a11  4.77384 min -20.00 max 20.00 vcr #endif 'Pbcm[0,0,0]GM4-(a)[He1:d:dsp]A'_1(a)
#ifdef GM4-_on prm !a12  0.00000 min -20.00 max 20.00 vcr #endif 'Pbcm[0,0,0]GM4-(a)[He1:d:dsp]A'_2(a)
'}}}
```

The refinement instructions contains two parts: one defines the rotational and translational modes that belong to the active irreps and the other defines the cell parameters according to the crystal system type. For example, run number 1 will conduct Rietveld refinement using subgroup candidate #01 that is the parent space group *Pbcm*. As defined in the script, symmetry distortion modes belonging to the Γ_1^+ irrep are needed, which means rotational symmetry mode r_1 and translational modes a_1 and a_2 are refined. Since candidate #01 has an orthorhombic space group, only the unit cell edges (*a*, *b* and *c*) are refined and the unit cell angles are fixed at 90°. Run number 13 will test candidate #05 (*P*2$_1$/*m*) by refining symmetry distortion modes that belong to Γ_1^+ and Γ_2^+ irreps: r_1-r_2 for rotations and a_1-a_4 for translations. As candidate #05 has a monoclinic space group, the unit cell angle *γ* is refined in addition to the unit cell edges *a*, *b* and *c*. The complete TOPAS script for doing the exhaustive subgroup search is given in Appendix V. This TOPAS script allowed us to test all subgroup candidates automatically by conducting sequential equivalent refinements in a single script.

4.6.6 Results from exhaustive subgroup search

The quality of fit, indicated by R-factors, found in each space group candidate is shown graphically in Figure 4.8. We see identical trends with either R_{wp}, R_{Bragg} or a background-subtracted-R_{wp}' as the quality indicator. The minimum R_{wp} was found multiple times during the annealing process, suggesting that proper convergence was achieved in each subgroup. ΔR_{wp} is also included in Figure 4.7 where ΔR_{wp} is the increase in R_{wp} over the lowest R_{wp} found in any subgroup. The base candidate #16 (space group *P*1) yields the lowest R_{wp} (2.5%) as expected. This *P*1-symmetry based description possesses all the degrees of freedom of all its supergroups, with additional flexibility that its cell angles are slightly different from expected monoclinic values. We find from the structural refinement that cell angle α and β remained within ± 0.005° of 90° in the best solution with γ refining to 91.2°. The second-best fit is found for candidate #12 (*P*-1), though this candidate can be excluded since a positive SHG signal is observed up to DC-MBI's melting point.[2] Candidate #10 gives the next best fit among all the monoclinic candidates (#5–#7, #9–#11, #13–#15). We find that candidate #10 gives comparable fit to the *P*1 description with R_{wp} only marginally higher than that of #1 (*P*1), despite having far fewer degrees of freedom. We therefore select this candidate as having the optimum balance between giving an excellent fit to the data and having a low number of structural degrees of freedom.

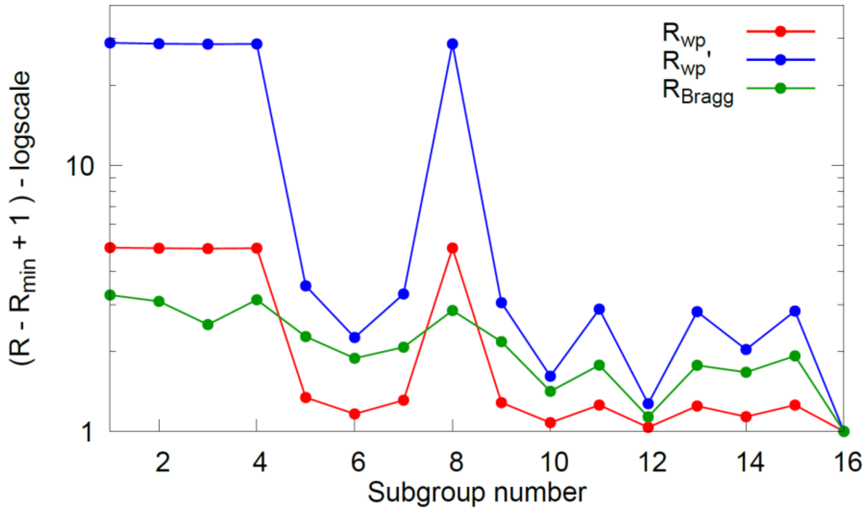

Figure 4.8: Three types of R-factor for each candidate subgroup from fits to the HT data.

The final fit for this candidate is shown in Figure 4.9(a), and the corresponding refined parameters are summarised in Table 4.6. The fit for another monoclinic *Pc* (candidate #11) with a different origin choice is significantly worse. As shown in Figure 4.9(b), this *Pc* description cannot model all the peaks in the PXRD pattern. We could have eliminated orthorhombic space groups (#1-#4 and #8) from our analysis due to the experimental observation of peak splitting in the high temperature PXRD patterns. However, in cases with more subtle splitting, they would need to be included, so we retained them for completeness. As a result, our process of the simultaneous annealing of cell parameters and internal coordinates effectively determines the true unit cell parameters during the process of structure solution.

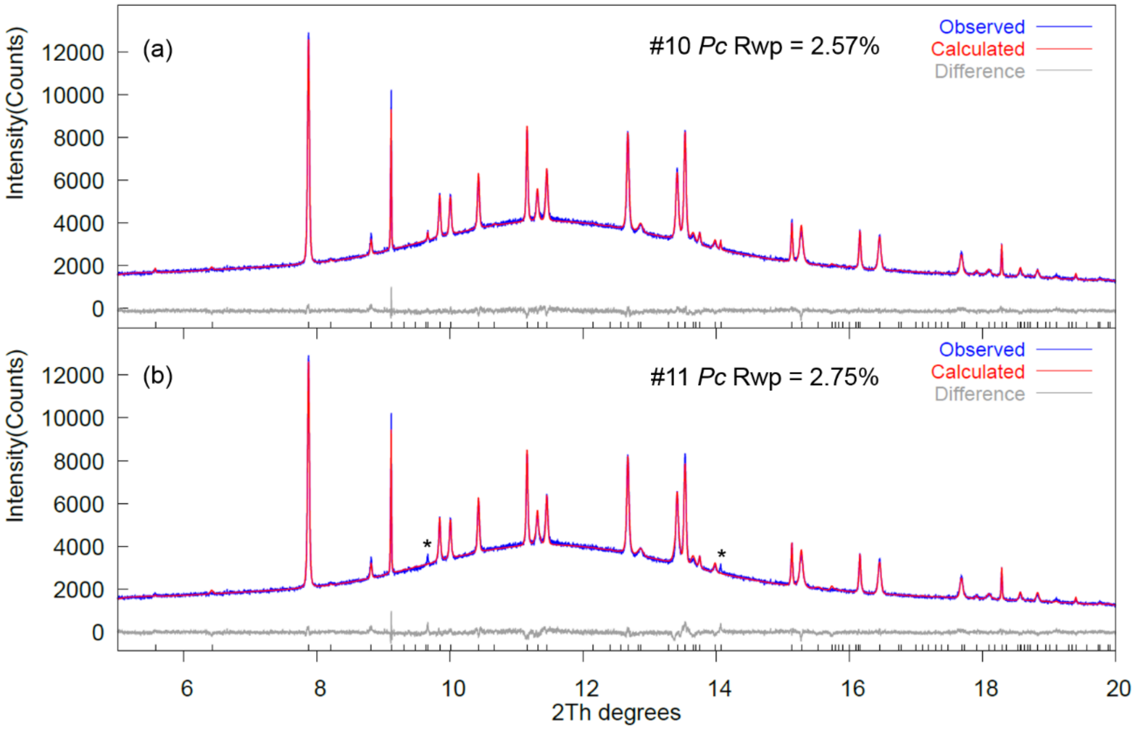

Figure 4.9: Fit of the (a) #10 *Pc* candidate and (b) #11 *Pc* candidate for the HT phase to 500 K synchrotron PXRD data. Peaks not modelled by candidate #11 are marked by stars.

Table 4.6: Refinement results for HT phase DC-MBI cell uses *P*11*b* non-standard setting of *Pc* to match other figures.

Chemical formula	$C_6H_8Cl_2N_2$
Crystal system	Monoclinic
Space group	*P11b* (No. 7)
***a*/Å**	5.7702(1)
***b*/Å**	10.3934(2)
***c*/Å**	14.7421(3)
***γ*/°**	91.2163(14)
V/Å³	884.01(3)
Z'	2
Temperature/K	500
Wavelength/Å	0.8257653

2θ range/°	5–30
Final $R_{wp}/R_p/R_{Bragg}$%	2.56/1.95/1.07

4.5. Crystal structure of the LT form of DC-MBI

The structure of the low-temperature (LT) phase of DC-MBI was re-determined in this work at 120 K via single crystal X-ray diffraction to allow comparison with the new high-temperature structure. An *R*-factor of 2.7% was obtained from the structure refinement. At 120 K, the material has cell parameters of a = 13.9343(3) Å, b = 5.64024(15) Å, c = 10.3593(3) Å, V = 814.16(2) Å with space group $Pca2_1$. This is the same as previously reported at room temperature. The hydrogen bonding pattern is shown in Figure 4.2(c). The bond distances involved in the N-H3····N hydrogen bond are d(N···N) = 2.962(3) Å and the N-H3···N angle is 150(2)°.

Even though the single crystal data give an unambiguous structure for the LT phase, we used powder data to further test our symmetry descent methodology. If the method works we should automatically identify candidate #03. As we see significant *hkl*-dependent peak broadening in synchrotron LT data collected at 100 K, we use the 15 terms of 4th order spherical harmonic function in order to correct the peak broadening arising solely from the anisotropic sample strain. The best fit to LT data is still found for the base candidate in space group $P1$ (Figure 4.10(a)). As shown in Figure 4.11, we find that in a $P1$ description the cell metric distorts slightly and the cell angle γ refines slightly away from 90°. This occurs due to the ability of a triclinic cell to model *hkl*-dependent peak shapes slightly better than monoclinic or orthorhombic cells and means that the fit quality of each candidate is dominated by the metric symmetry. This is easily determined in an initial symmetry descent process and we therefore performed a second run with an orthorhombic cell metric for all candidates, i.e. we fixed all cell angles at 90°. We find that candidates #2 and #3 give essentially equivalent fits to the data with R_{wp} ~0.15 % higher than the $P1$ description. If we take the other extreme description and allow a triclinic cell metric for each candidate, candidate #3 is the best choice (ΔR_{wp} = 0.15%). This is the expected $Pca2_1$ candidate for the LT phase. A Rietveld fit to the LT data is shown in Figure 4.10(b).

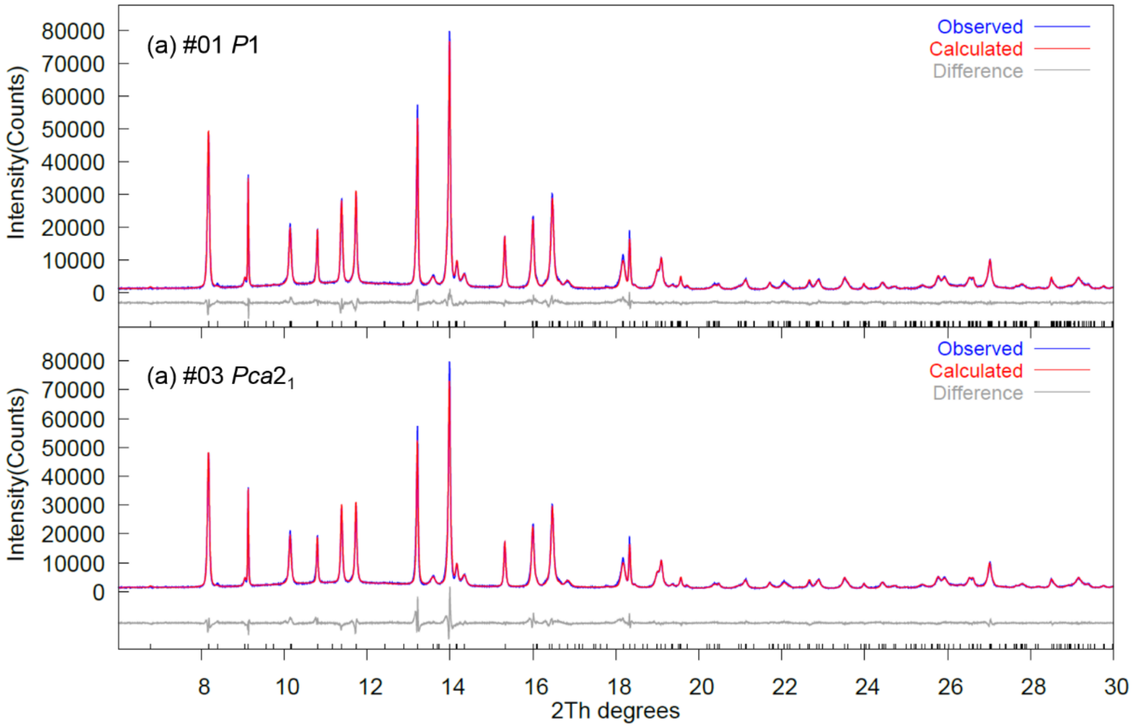

Figure 4.10: Rietveld fit of (a) the candidate #01 *P*1 with R_{wp} of 6.63% and (b) the candidate #03 *Pca*2$_1$ with R_{wp} of 8.36% for the LT phase to 100 K synchrotron PXRD data. Note the significant *hkl*-dependent strain broadening.

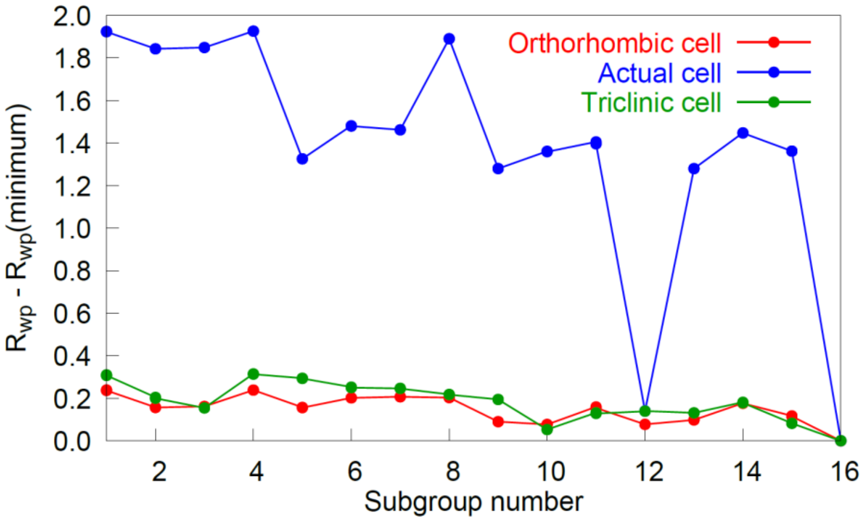

Figure 4.11: The increase in R_{wp} over the lowest R_{wp} found in any subgroup from fits to the LT data.

4.6. Understanding the cell distortion, thermal expansion and phase transition of DC-MBI

In this section, we focus on how the unit cell parameters of DC-MBI vary with temperature as extracted from the variable temperature laboratory PXRD data and how we can use strain modes and rotational modes to give more insight into the unit cell distortion, phase transition and its reversibility. The temperature dependence of unit cell parameters and cell volume of DC-MBI is shown in Figure 4.11. On warming, unit cell parameters increase smoothly with changing temperature below T_c ~400 K, showing normal positive thermal expansion. At the transition to the lower-symmetry HT phase, cell parameter *b* (Figure 4.12(b)) and *γ* (Figure 4.12(c)) change rapidly. On cooling, cell parameters exhibit similar behaviour but the phase transition occurs at a lower temperature (T_c~330 K). This hysteresis suggests a first-order transition, which is consistent with our observation in PXRD patterns. Thermal expansion coefficients calculated for each unit cell axis and cell volume are shown in Figure 4.13(a). Values are derived by fitting a smooth spline function to the data shown in Figure 4.12 followed by numerical differentiation. The maximum of CTE along the *c*-axis is approaching 150×10^{-6} K^{-1}; its magnitude falls into the “colossal” expansion category ($|\alpha|>100\times10^{-6}$ K^{-1}) observed in framework material such as $Ag_3[Co(CN)_6]$.[8]

Interestingly, a small contraction along the crystallographic *b*-axis is observed over a ~50 K interval close to the phase transition. This can be most clearly illustrated by the thermal expansion indicatrix calculated through the PASCal[9] program. The indicatrix from 400 K to 450 K calculated using data collected on warming is shown in Figure 4.13 and detailed information on the principal axes, as well as the calculated CTE along each principal axis, is summarised in Table 4.6. We see a uniaxial NTE along the principal axis X_1 which is close to *b*-axis and strong anisotropic PTE along X_2 and X_3.

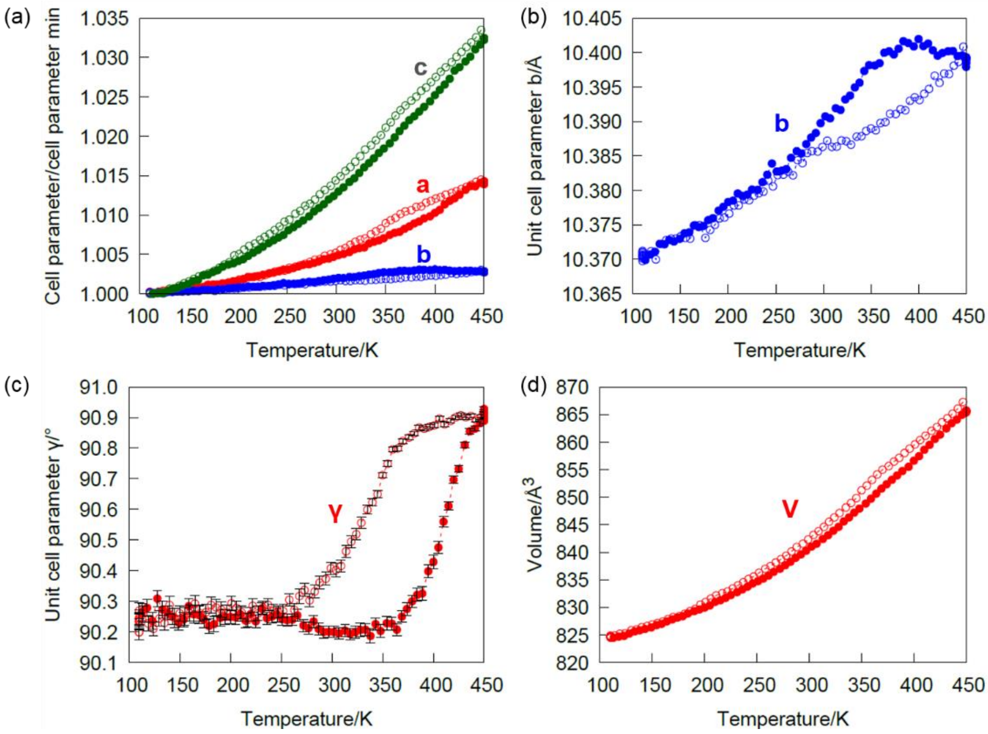

Figure 4.12: The temperature dependence of unit cell parameters and cell volume based on a *P*11*b* (non-standard setting of *Pc*) unit cell. Unit cell parameters and cell volume extracted from laboratory data.

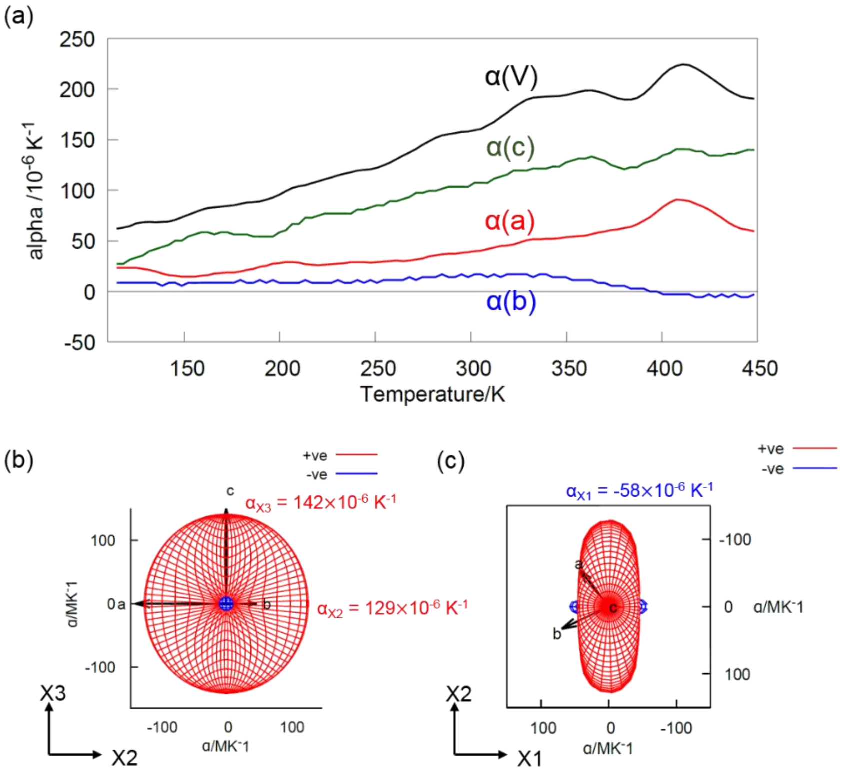

Figure 4.13: Thermal expansion coefficients and expansion indicatrix calculated from warming data between 400 K and 450 K.

Table 4.6: Thermal expansion along each principal axis on warming in the temperature range of 400 K-450 K.

Axes	**α/10^{-6} K^{-1}**	***a***	***b***	***c***
X_1	-58	0.74	0.66	0
X_2	128	-0.95	0.31	0
X_3	141	0	0.94	1
Volume	212			

We also used strain modes to describe the cell parameter variations relative to the LT cell as discussed in Chapter 3 for CA-Pyz. The four degrees of freedom of the HT cell appear as three parent-allowed Γ_1^+ strain modes (labelled as s_2-s_4) and one symmetry breaking Γ_4^+ strain mode (labelled as s_1). The amplitude of each mode extracted from laboratory variable temperature PXRD data is shown in Figure 4.14. Since in our *P*11*b* description the cell metric distorts slightly (cell angle *γ* are not exactly 90°) even in the LT orthorhombic phase, Γ_4^+ strain does not refine to exactly zero but shows a small amplitude at low temperature. As discussed above, this is caused by small *hkl*-dependent peak broadening. We see, however, that the amplitude of $\Gamma_4^+ s_1$ strain stays constant below the phase transition temperature (T_c ~400 K for warming and T_c ~330 K for cooling). Above the phase transition temperature, the $\Gamma_4^+ s_1$ mode deviates from the low temperature value and reaches 0.01% by 450 K. $\Gamma_4^+ s_1$strain affects the cell angle *γ* exclusively, which changes from 90.2° to 90.9° from 250 K to 450 K. $\Gamma_1^+ s_2$-s_4 modes change smoothly with temperature and influence the cell parameters *c*, *a* and *b* respectively.

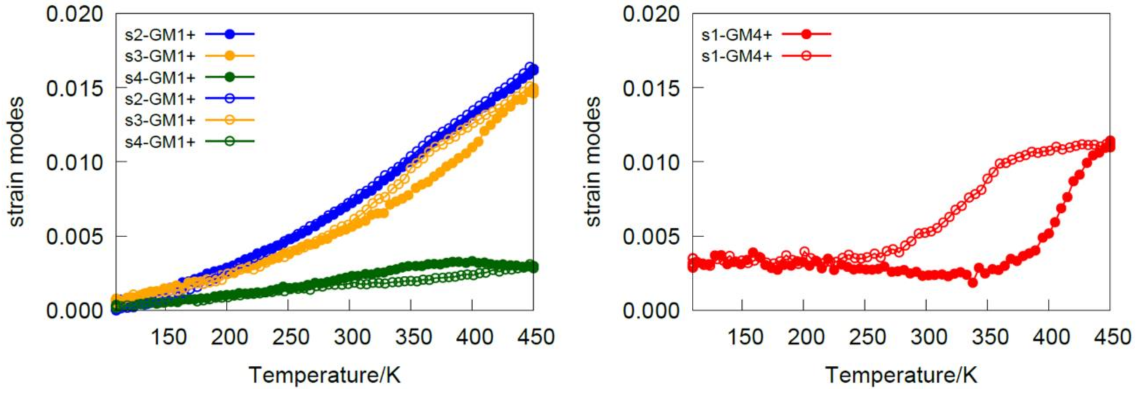

Figure 4.14: Strain mode amplitudes extracted from the laboratory variable temperature PXRD data.

Despite the relatively low information content of the laboratory VT-PXRD data, we can gain insight into the LT to HT transition from the temperature dependence of the rotational-mode amplitudes and corresponding molecular rotations discussed above. We use candidate #10 *Pc*, which has 6 allowed rotational modes (Γ_1^+, $2\Gamma_4^+$, $2\Gamma_2^-$, Γ_3^-) for this analysis. From our analysis of data collected on warming and cooling, we find that R_{wp} increases by an average of 0.12% and a maximum of 0.25% for all the data sets if the $2\Gamma_2^-$ and Γ_3^- mode amplitudes are fixed at zero. The small R_{wp} increase and the absence of any noticeable temperature dependence of important rotational modes suggest that these modes are not important and can be removed from the model. The temperature dependence of important rotational modes (Γ_1^+ and $2\Gamma_4^+$) is shown in Figure 4.15. We observe a clear increase in the Γ_4^+ amplitudes and a marked decrease in their standard uncertainty above the phase transition temperature. We also note that the R_{wp} difference between a model in which rotational mode amplitudes are fixed at zero (the high symmetry *Pca*2$_1$ phase) and a model in which they are allowed to refine grows significantly at the phase transition.

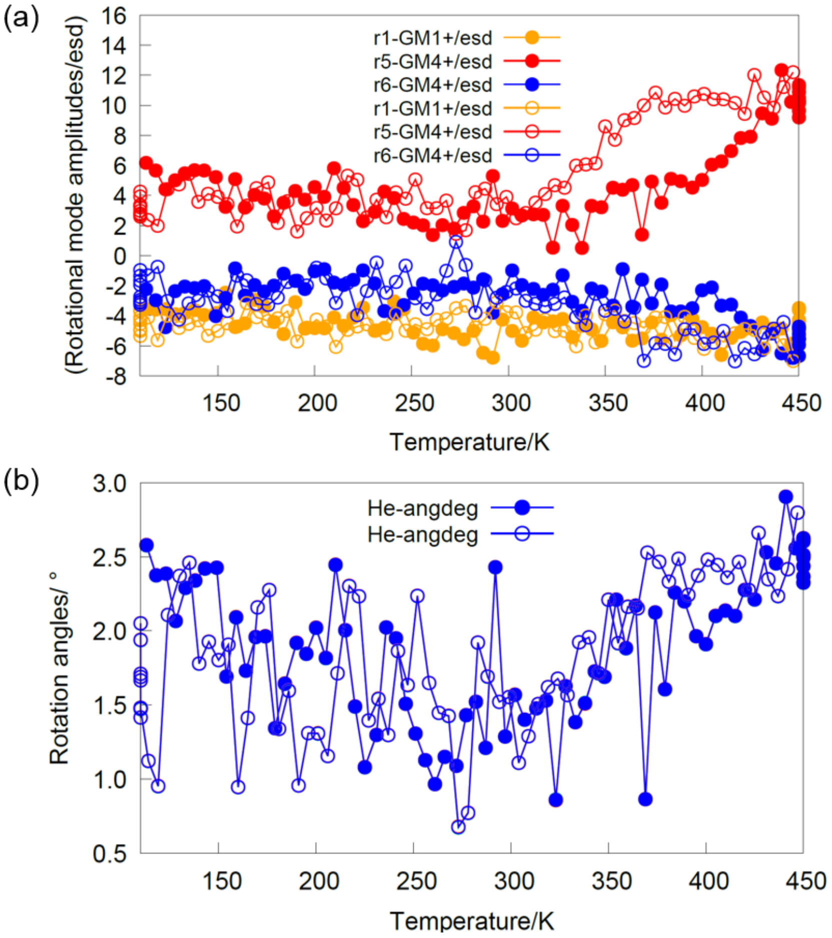

Figure 4.15: (a) Important rotational mode amplitudes/esd. (b) Overall molecular rotation angles for the two symmetry-unique molecules.

4.7. Unusual symmetry-loss phase transition of DC-MBI

Analysis of variable-temperature diffraction data, aided by the subgroup tree of Figure 4.7, gives a clear picture of the symmetry change that occurs at the LT-HT phase transition in DC-MBI. We first discuss the relationship between the hypothetical parent phase (*Pbcm*) and the known LT phase (*Pca*2$_1$). There is a small Γ_2^- rotational mode in the LT structure that breaks the symmetry of the parent, but only slightly. It is therefore best to consider the lower *Pca*2$_1$ symmetry as being derived principally from H3 ordering (Figure 4.2) rather than from rotations. The H3-disordered hypothetical *Pbcm* parent gives rise to 8 occupational symmetry modes (modes that change H site occupancy) that allow us to describe any pattern of H occupancies in the *P*1 base candidate #16. In fact, if the parent had the higher symmetry *Pbcm* structure, we would be able to explain the polar ordering observed in the LT phase by using the action of a single Γ_2^- occupancy mode.

The symmetry-lowering phase transition of DC-MBI on heating can be understood by rotaional symmetry modes. The low-symmetry HT phase is derived from the LT higher-symmetry phase by activating the primary Γ_4^+ modes. In our rotational symmetry mode description, six rotational modes are generated with the LT structure as parent; four of them belong to the Γ_1^+ irrep of the symmetry group of the LT structure (denoted by r_1-r_4) and two of them belong to Γ_4^+ (denoted as r_5 and r_6). Figure 4.16 illustrates the direction of the axial vectors related to important rotational modes. One of the symmetry-breaking Γ_4^+ modes (r_5) describes the rotation almost around the *a*-axis of the LT cell and the other Γ_4^+ mode (r_6) the rotation around the *c*-axis of the LT cell. If the amplitudes are related by $-r_5 = +r_6$, they describe equal rotations around the pseudo 2-fold axis of each molecule.The pink vectors shown on the right-hand side of the Figure 4.16 display the resulting overall axial vector by refining all rotational symmetry modes. The overall refined axial vector is close to the pseudo 2-fold axis of the molecule but slightly off the moleclar plane and results in alternate molecules along the H-bonded chains rotating in opposite directions. The length of the vector define the amplitude of the overall rotation, which is displayed as 1 Å = 0.5°. The other (secondary) modes allowed by the symmetry of the HT structure (2Γ_2^- and Γ_3^-) would rotate the molecule in the plane perpendicular to the chain direction and in the plane of the molecule, respectively. However, their observed magnitudes are small.

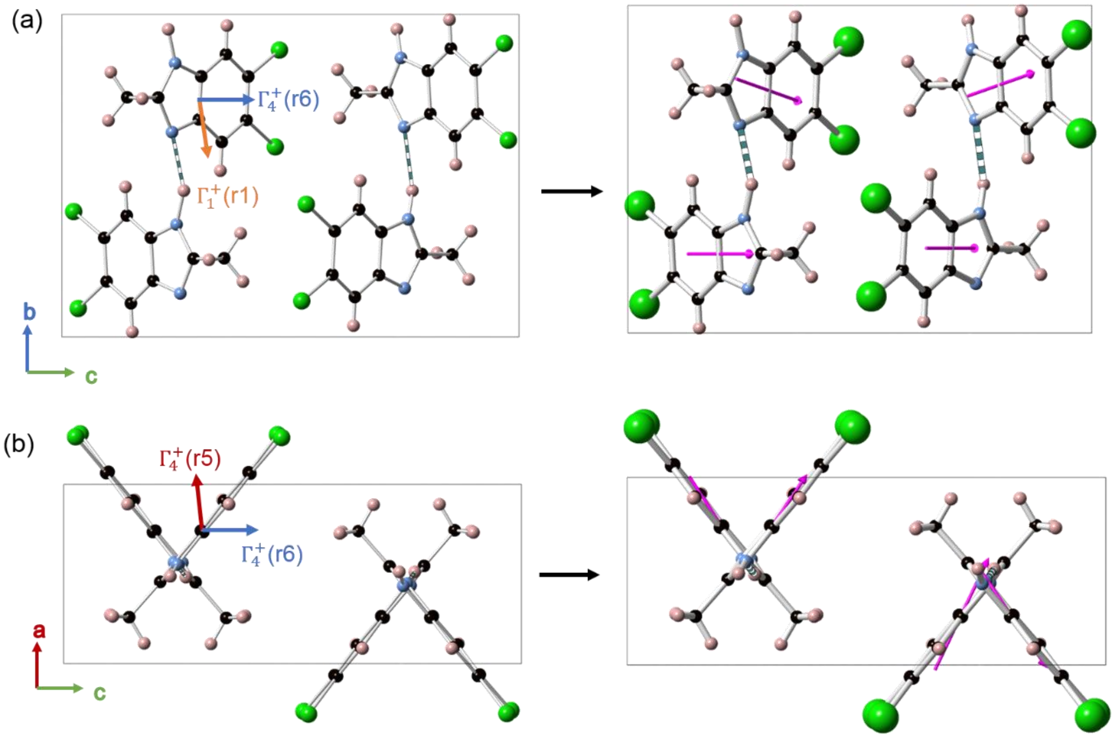

Figure 4.16: Examples of Axial vectors describing the symmetry adapted rotational modes

The most unusual feature of the phase transition in DC-MBI is that it transforms from a higher-symmetry LT ferroelectric phase (orthorhombic polar) to a lower-symmetry HT phase (monoclinic polar) on heating. It is not the conventional ferroelectric-paraelectric type phase transition expected. Nonreconstructive phase transitions are normally accompoined by an increase in symmetry on heating, even though it is not a thermodynamic requirement. In fact the prototype ferroelectric Rochelle salt[10-14] undergoes a so-called "re-entrant" phase transition on heating which involves a symmetry-lowering procedure. The space group sequence of the paraelectric-ferroelectric-paraelectric series of phase transitions is $P2_12_12$ (T < 255 K), $P2_111$ (255 K < T < 297 K) and $P2_12_12$ (T > 297 K). There is a possibility that DC-MBI would transit back to the $Pca2_1$ phase (or a *Pbcm* phase) at higher temperature, but it melts first. We see strong evidence from the hysteresis in the unit cell parameters and from the phase co-existence close to T_c that the LT ↔ HT transition in DC-MBI is discontinuous. It is associated with significant increases in *a* and *c* and a slight contraction in *b*.

The observation that DC-MBI transforms from polar space group $Pca2_1$ to polar space group *Pc* means that we cannot explain the polarity switching mechanism by the H3-ordering as proposed earlier. This is supported by SHG measurements which show the material remains non-centrosymmetric up to its melting point. The switching mechanism is therefore likely to involve nucleation and growth of chains with different H-bonding directions. The lack of proton disorder in the HT phase also helps rationalize why the coercive field of DC-MBI was too high to measure a ferroelectric hysteresis loop at room temperature[1] and that switching could only be observed at elevated temperature.

4.8. Conclusion

In this chapter we reported a symmetry-reducing phase transition on heating DC-MBI and carried out a comprehensive study to understand the unusual behaviour associated with the phase transition. We successfully solved the HT structure from powder data by using a novel symmetry-inspired methodology, based on rotational molecular symmetry modes. This is the first time that a combined use of rotational and translational symmetry mode parameters and systematic and exhaustive subgroup searching has been used to solve a molecular crystal structure. We also successfully employed a “single .INP file” approach in order to test multiple space group candidates automatically. We found that the HT structure adopts monoclinic *Pc* symmetry rather than the anticipated centrosymmetric orthorhombic *Pbcm* expected from simple structural considerations. This is supported by the retention of SHG activity all the way up to the material's melting point. The observation that DC-MBI undergoes a symmetry-reducing transition on warming is unusual. The phase transition appears to be first order and displays a ~70 K hysteresis. We observe a contraction of the b-axis close to the phase transition leading to uniaxial negative thermal expansion over a ~50 K range. The strain modes and rotational modes analysis suggests predominant influences of Γ_4^+ modes on the cell metric and coherent molecular rotations around their two fold axes.

References

1. Horiuchi, S.; Kagawa, F.; Hatahara, K.; Kobayashi, K.; Kumai, R.; Murakami, Y.; Tokura, Y., Above-room-temperature ferroelectricity and antiferroelectricity in benzimidazoles. *Nature Communications* **2012,** *3*, 1308.
2. Liu, H.; Zhang, W.; Halasyamani, P. S.; Stokes, H. T.; Campbell, B. J.; Evans, J. S. O.; Evans, I. R., Understanding the Behavior of the Above-Room-Temperature Molecular Ferroelectric 5,6-Dichloro-2-methylbenzimidazole Using Symmetry Adapted Distortion Mode Analysis. *Journal of the American Chemical Society* **2018,** *140* (41), 13441-13448.
3. Coelho, A. A.; Evans, J. S. O.; Evans, I. R.; Kern, A.; Parsons, S., The TOPAS symbolic computation system. *Powder Diffraction* **2011,** *26* (4), S22.

4. Coelho, A., TOPAS and TOPAS-Academic: an optimization program integrating computer algebra and crystallographic objects written in C++. *Journal of Applied Crystallography* **2018,** *51* (1), 210-218.
5. Swenson, C. A., Recommended Values for the Thermal Expansivity of Silicon from 0 to 1000 K. *Journal of Physical and Chemical Reference Data* **1983,** *12* (2), 179-182.
6. Stinton, G. W.; Evans, J. S. O., Parametric Rietveld refinement. *Journal of Applied Crystallography* **2007,** *40* (1), 87-95.
7. Lewis, J. W.; Payne, J. L.; Evans, I. R.; Stokes, H. T.; Campbell, B. J.; Evans, J. S. O., An Exhaustive Symmetry Approach to Structure Determination: Phase Transitions in $Bi_2Sn_2O_7$. *Journal of the American Chemical Society* **2016,** *138* (25), 8031-8042.
8. Goodwin, A. L.; Calleja, M.; Conterio, M. J.; Dove, M. T.; Evans, J. S. O.; Keen, D. A.; Peters, L.; Tucker, M. G., Colossal Positive and Negative Thermal Expansion in the Framework Material $Ag_3[Co(CN)_6]$. *Science* **2008,** *319* (5864), 794-797.
9. Cliffe, M. J.; Goodwin, A. L., PASCal: a principal axis strain calculator for thermal expansion and compressibility determination. *Journal of Applied Crystallography* **2012,** *45* (6), 1321-1329.
10. Beevers, C. A.; Hughes, W., The Crystal Structure of Rochelle Salt (Sodium Potassium Tartrate Tetrahydrate $NaKC_4H_4O_6$. $4H_2O$). *Proceedings of the Royal Society of London. Series A, Mathematical and Physical Sciences* **1941,** *177* (969), 251-259.
11. Solans, X.; Gonzalez-Silgo, C.; Ruiz-Pérez, C., A Structural Study on the Rochelle Salt. *Journal of Solid State Chemistry* **1997,** *131* (2), 350-357.
12. Gorbitz, C. H.; Sagstuen, E., Potassium sodium (2R,3R)-tartrate tetrahydrate: the paraelectric phase of Rochelle salt at 105 K. *Acta Crystallographica Section E* **2008,** *64* (4), m507-m508.
13. Uddin, M. J.; Middya, T. R.; Chaudhuri, B. K., Room temperature ferroelectric effect and enhanced dielectric permittivity in Rochelle salt/PVA percolative composite films. *Current Applied Physics* **2013,** *13* (3), 461-466.
14. Mo, F.; Mathiesen, R. H.; Beukes, J. A.; Vu, K. M., Rochelle salt – a structural reinvestigation with improved tools. I. The high-temperature para-electric phase at 308 K. *IUCrJ* **2015,** *2* (Pt 1), 19-28.

Chapter 5 Structural investigations of 2:1 cocrystal of benzoic acid and ethylenediamine, 2BA-ETD

Overview

This chapter describes the structure determination from powder X-ray diffraction of the 2:1 cocrystal of benzoic acid and ethylenediamine (2BA-ETD) in various forms. The molecular structure of 2BA-ETD is shown in Figure 5.1. We report two new polymorphic forms of 2BA-ETD (*β*- and *γ*-2BA-ETD). We demonstrate the use of our symmetry descent subgroup approach in solving the structure of *β*-form and describe the challenges we met in the structure determination of both forms.

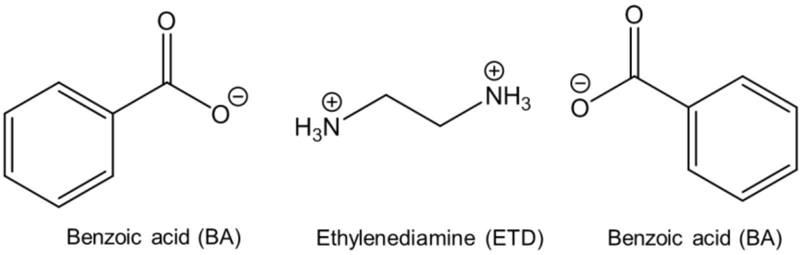

Figure 5.1: The molecular structure of the 2:1 cocrystal of benzoic acid and ethylenediamine (2BA-ETD).

5.1 Introduction

The possible ferroelectricity of a material can be identified by detecting the pseudocentricity of its polar structure. To find potential new molecular ferroelectrics in this way, two procedures are required: (1) searching for polar crystal structures in the Cambridge Structural Database (CSD) and (2) performing a pseudosymmetry test on the polar structures. Several software suites, such as ISODISTORT and Bilbao Crystallographic Server, incorporate programs for pseudosymmetry detection. A number of new ferroelectrics[1-2] have been reported by following these procedures.

Organic bases, such as alkyl diamines, that contain a N-C-C-N unit are able to form cocrystals with acids through hydrogen-bonding interactions. Several cocrystals of this type have been reported to show ferroelectricity.[3-4] We searched for organic structures that contain this unit in the CSD and a 2:1 cocrystal of benzoic acid and ethylenediamine (CSD refcode RIBLET) was found. The room-temperature structure of this cocrystal has been reported by Adam *et al.*[5] Their structural study using single crystal neutron diffraction shows that at room temperature 2BA-ETD adopts orthorhombic space group

Pca2_1 with unit cell of *a* = 8.425(3) Å, *b* = 9.144(3) Å, *c* = 21.000(5) Å and V = 1617.8 Å^3. This previously-reported structure is labelled as the *α*-form in this chapter. The protons from the carboxyl groups of the benzoic acids are transferred to the nitrogen atoms of the ethylenediamine molecules, resulting in the formation of positively charged amines and negatively charged acids. As shown in Figure 5.2(a), *α*-2BA-ETD contains parallel planes of three layers of molecules: each charged amine layer being sandwiched by a pair of benzoate layers. The layers are perpendicular to the crystallographic *c*-axis. By segregating into planes, the hydrophobic and hydrophilic portions of the molecules are separated.

We performed pseudosymmetry detection on *α*-2BA-ETD using the pseudosymmetry search program[6] at the Bilbao Crystallographic Server. The pseudosymmetry detection suggested that an additional mirror plane could form between the two adjacent benzoate planes if the benzoate molecules underwent a small cooperative movement. This process implied the existence of a potential higher symmetry structure at high temperature. The high symmetry 2BA-ETD would adopt centrosymmetric orthorhombic space group *Pbca* and its origin would be at (0.25, 0, 0) relative to the *Pca*2_1 structure. This putative high-symmetry structure can be obtained by applying a transformation matric of (0 1 0, -1 0 0, 0 0 1) to the *Pca*2_1 structure and is shown in Figure 5.2(b). The two distinct benzoate molecules in the asymmetric unit of *α*-2BA-ETD would become symmetry equivalent in this high symmetry *Pbca* structure. Therefore, if 2BA-ETD undergoes a phase transition to this proposed *Pbca* structure, it would be a potential route for the ferroelectric switching, making 2BA-ETD an attractive candidate for further study.

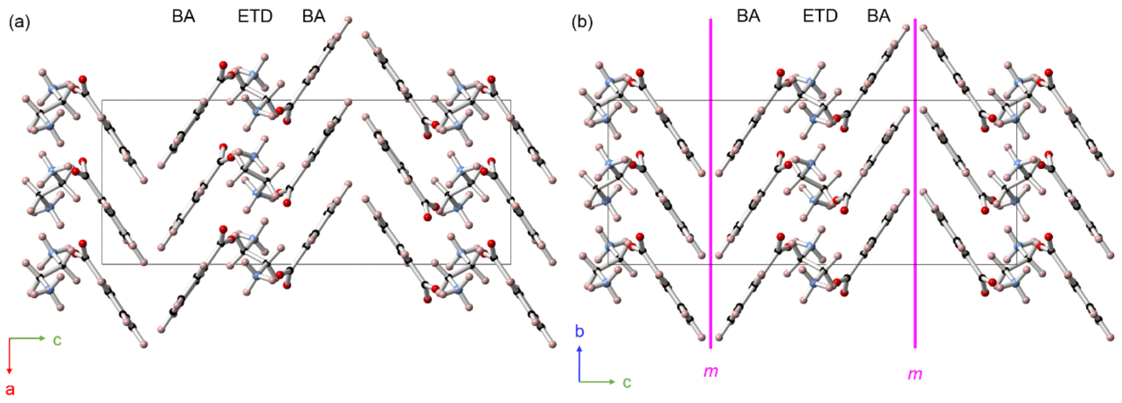

Figure 5.2: Crystal structures of (a) the reported RT phase and (b) the putative HT *Pbca* phase of 2BA-ETD. The predicted additional mirror planes are drawn in pink in (b).

No phase transition at high temperature had been identified experimentally before our study. Our work aimed to determine if this proposed transition occurs, which would help discover a new molecular ferroelectric with a clear switching mechanism. Although the anticipated phase transition was not observed, our X-ray diffraction studies revealed two previously unreported structures of 2BA-ETD (we call these the β- and γ-forms). We have used the symmetry-inspired subgroup search method of chapter 4 to help determine the crystal structure of β-form from powder X-ray diffraction data. The structure of the γ-form was determined *ab-initio* from powder diffraction data using simulated annealing.

5.2 Sample preparation and data collection

5.2.1 Sample preparation

Single crystals of 2BA-ETD were obtained by slow evaporation from a methanol solution of ethylenediamine (Aldrich, ≥99.5%) and benzoic acid (Aldrich, ≥99.5%) with molar ratio 2:1. Benzoic acid (0.7327 g, 6 mmol) was dissolved in 8 mL methanol in an 18 mL sample vial. Ethylenediamine (0.2 mL, 3 mmol) was added to the methanol solution. The sample vial was loosely capped and left at room temperature for crystallisation. Large colourless rhombus-shaped single crystals appeared after eight days. Polycrystalline samples of β-2BA-ETD were produced by gentle grinding of the single crystals.

Polycrystalline samples of the high-temperature γ-2BA-ETD formed by heating the room-temperature polycrystalline β-2BA-ETD samples in the furnace at 110°C for 2 hours. HT samples were finely ground before use.

5.2.2 Laboratory powder X-ray diffraction (PXRD)

In order to solve the structures of β- and γ-2BA-ETD, room temperature powder X-ray diffraction data were collected on several different diffractometers. The experimental details of each measurement are summarised in Table 5.1. The experiment “d6b_01486” was the best data collection performed on β-2BA-ETD: a 65-hour scan was collected on the “d6” in capillary mode over the 2θ range of 2-35° using a step size of 0.01°. The experiment “d6b_01462” was the best data collection for γ-2BA-ETD: a 16.5-hour PXRD pattern was collected over the 2θ range of 2-30° using a step size of 0.01° on the “d6”. The structure of γ-2BA-ETD was solved *ab-initio* from this data set.

Variable temperature PXRD measurements were carried out on the “d7” in capillary mode. Experimental details are summarised in Table 5.2. The sample was heated from

300 K to 400 K and then cooled down to 280 K at a ramping rate of 10 K/hr. A series of 1 hour scans were recorded over the 2θ range of 5-80° using a step size of 0.02° on heating and a series of 25 mins scans were recorded over the 2θ range of 5-60° on cooling.

PXRD patterns for Si standard were recorded before the RT and VT measurement to calibrate the zero point and provide information for the instrumental peak shape model.

Table 5.1: Experimental details for room temperature powder X-ray diffraction.

Experiment	**Diffractometer**	**Mode**	**Sample**	**Total time**
d6b_01486	d6	Capillary	*β*-2BA-ETD	65 hrs
d7_14576	d7	Capillary	*β*-2BA-ETD	15 hrs
d6b_01462	d6	Capillary	*γ*-2BA-ETD	16.5 hrs
d7_14574	d7	Capillary	*γ*-2BA-ETD	8 hrs
d7_15717	d7	Flat-plate	*γ*-2BA-ETD	8 hrs

Table 5.2: Experimental details for variable temperature powder X-ray diffraction collected on the diffractometer “d7”.

Experiment	**Process**	**T range**	**Ramp rate**	**No. of runs**	**Total time**
d7_14572	warming	300-400 K	10 K/hr	10	10 hrs
d7_14573	cooling	400-280 K	10 K/hr	30	12 hrs

5.2.3 Solid state NMR and computational methods

^{13}C solid state NMR spectra were recorded on both *β*-2BA-ETD and *γ* -2BA-ETD at room temperature with an 8 kHz spinning rate using neat tetramethylsilane as reference on a Bruker Advance III HD spectrometer.

Two structural models (*Pc β*-2BA-ETD and $P2_1/c$ *γ*-2BA-ETD) were used to calculate the ^{13}C solid state NMR spectra. All the simulations were performed within the density functional theory (DFT) using the CASTEP[7] programme by Prof. Paul Hodgkinson from Durham University.

5.3 PXRD inspection and attempts at single crystal diffraction

Figure 5.3 shows laboratory variable temperature powder X-ray diffraction patterns collected upon heating a sample of polycrystalline 2BA-ETD from 300 K to 400 K. We only show a 2θ range of 5-45° where the main changes occur. 2BA-ETD undergoes an irreversible phase transition on heating through ~363 K. The marked PXRD changes observed suggest there is no close relationship between the RT phase and the HT phase. 2BA-ETD stays in its HT phase even when it is cooled back to 300 K.

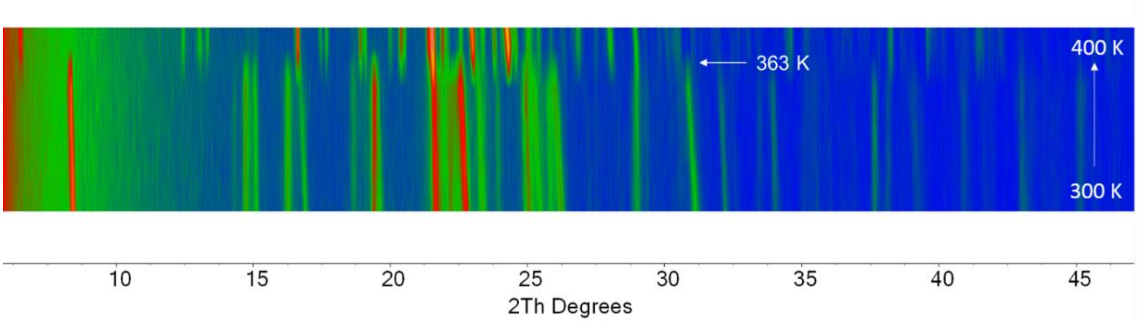

Figure 5.3: Variable temperature PXRD patterns collected on heating using the diffractometer “d7” in capillary mode.

Variable temperature single crystal X-ray diffraction measurements were attempted to gain insight into the phase transition of *α*-2BA-ETD upon heating. The crystal structure of 2BA-ETD was re-determined at 120 K. This LT structure retains the same space group (*Pca*2_1) as the previously reported *α*-BA-ETD structure[5] with unit cell parameters of *a* = 8.4399(4) Å, *b* = 9.1423(3) Å, *c* = 20.5595(12) Å, *α* = *β* = *γ* = 90° and V = 1586.38(9) Å^3. Crystallographic information and crystal structures of this LT 2BA-ETD are shown in Appendix VII. We attempted to collect single crystal diffraction data at 295 K and higher; however, the 295 K and 340 K refinements against data collected on different crystals give negative atomic displacement parameters on several carbon atoms. The crystals shattered on heating through ~380 K. As a result, we could not determine the HT structure using the laboratory single crystal X-ray diffraction.

5.4 Determination of the new *β*-2BA-ETD structure

5.4.1 Revealing the existence of *β*-2BA-ETD

A close inspection of the RT PXRD patterns of ground crystals suggests that the formation of a new 2BA-ETD structure is induced by grinding. Even gentle grinding showed this structural transformation. Figure 5.4 shows a comparison of the experimental PXRD pattern (black) collected on *β*-2BA-ETD and the simulated PXRD pattern (red) from the published orthorhombic *α*-2BA-ETD structure. The difference in these patterns is clear evidence for a phase transition. We ground one of the large single crystals (space group *Pca*2_1, 0.5×0.5×0.2 cm) very gently with the hope of finding single crystals with the new structure for single crystal X-ray diffraction experiments. Several single crystals were screened on the diffractometer “OD”. However, they all diffracted extremely weakly and were not suitable for data collections. Therefore, we were not able to determine the structure of *β*-2BA-ETD structure using single crystal X-ray diffraction.

The comparison of PXRD patterns in Figure 5.4 suggests a close relationship between the new *β*-form and the previously reported *α*-form. For example, the peaks at ~ 15, 17, 19 and 22° 2θ in the simulated pattern seem to "split" and give several peaks separated by several 2θ degrees in the experimental pattern. This is reminiscent of the peak splitting behaviour observed in the PXRD patterns of CA-PYZ and DC-MBI in previous chapters and suggests that the new *β*-2BA-ETD could have a subgroup symmetry of the previously reported *α*-2BA-ETD. Thus, we used a similar method as developed for DC-MBI to solve the structure. That is, we applied a symmetry-descending subgroup search to solve the new *β*-2BA-ETD structure.

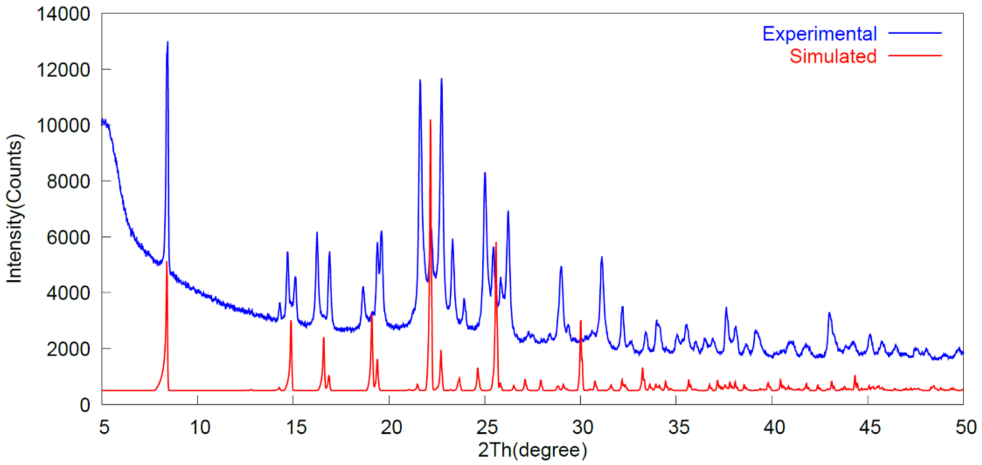

Figure 5.4: Comparison between the experimental PXRD pattern and simulated PXRD pattern from previously reported 2BA-ETD structure (*Pca*2_1).

5.4.2 Symmetry-inspired subgroup search

Two powder diffraction data sets were collected on the "d6" and "d7" respectively. The "d6" data set is high quality in terms of the peak intensities whereas the d7 data have incorrect low angle intensities. Symmetry decent subgroup searches were carried out using both data sets to demonstrate the consistency of the results and to test the reliability of our structure solution method.

Initial by-hand distortions of the 2BA-ETD structure suggested that all the observed peaks could be explained by a triclinic unit cell with the same volume as that of *α*-2BA-ETD. We, therefore, chose a *P*1 base structure to consider as the lowest-symmetry child structure. If we assume that the amine and acid molecules can be treated as rigid bodies, there are 36 rotational modes (r_1-r_{36}) to describe the rotations of the 12 rigid molecules and 36 translational modes (a_1-a_{36}) to define their translations along the parent cell axes in the *P*1 description. These symmetry modes belong to four different irreps, Γ_1^+, Γ_2^+, Γ_3^+ and Γ_4^+, of the parent symmetry group. Three translational modes were fixed at zero in order to fix the floating origin; other modes were freely refined in the *P*1 refinement. Parameters for zero point, axial divergence and instrument TCHZ peak shape were all fixed at values obtained from refinement of a Si standard. In the refinement against the "d6" data, we needed an *hkl*-dependent peak shape to model the anisotropic peak broadening observed. For this, we used fifteen terms of a 4th order spherical harmonic function. The result from the Rietveld refinement using the *P*1 description against the "d6" data is shown in Figure 5.5(a). The *P*1 base structure gives a good fit with R_{wp} = 6.2%. In the refinement against the "d7" data, fifteen terms of a 4th order spherical harmonic function were used to model preferred orientation. Two TOPAS parameters, CS_G and Strain_G, were used to describe isotropic peak broadening arising from crystallite size and microstrain respectively. Comparison between different experimental data sets suggested that the intensity of the first peak (~ 8° 2θ) in the "d7" PXRD pattern is unreliable, presumably due to a systematic error of the diffractometer. As a result, we put a zero weighting on the contribution of the first peak to the refinement, which leads to its overcalculation as shown in Figure 5.5(b). We can see from Figure 5.5(b) that, with the exception of this first peak, the *P*1 base structure gives a good Rietveld fit to the "worse" powder diffraction data with R_{wp} = 5.4%. This gives confidence that the true structure of β-2BA-ETD lies somewhere on the subgroup tree between the $Pca2_1$ parent and this *P*1 child.

We, therefore, used ISODISTORT to calculate a tree of all intermediate subgroups that lie between the parent $Pca2_1$ structure and the child *P*1 base structure. As shown in Figure 5.6, ISODISTORT generates 5 subgroups, including the parent structure. Space group *Pc* appears twice with different origin choices.

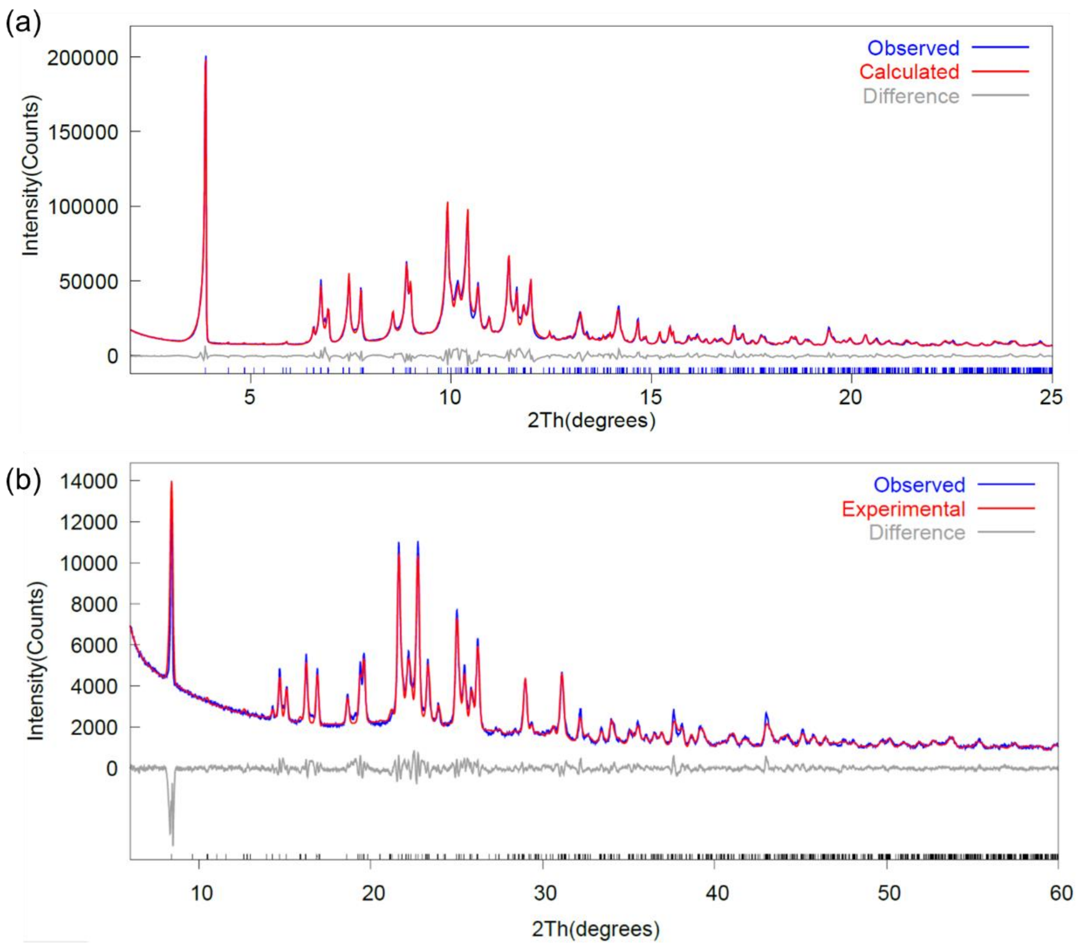

Figure 5.5: Rietveld refinement of *P*1 base structure against (a) “d6” data and (b) “d7” data.

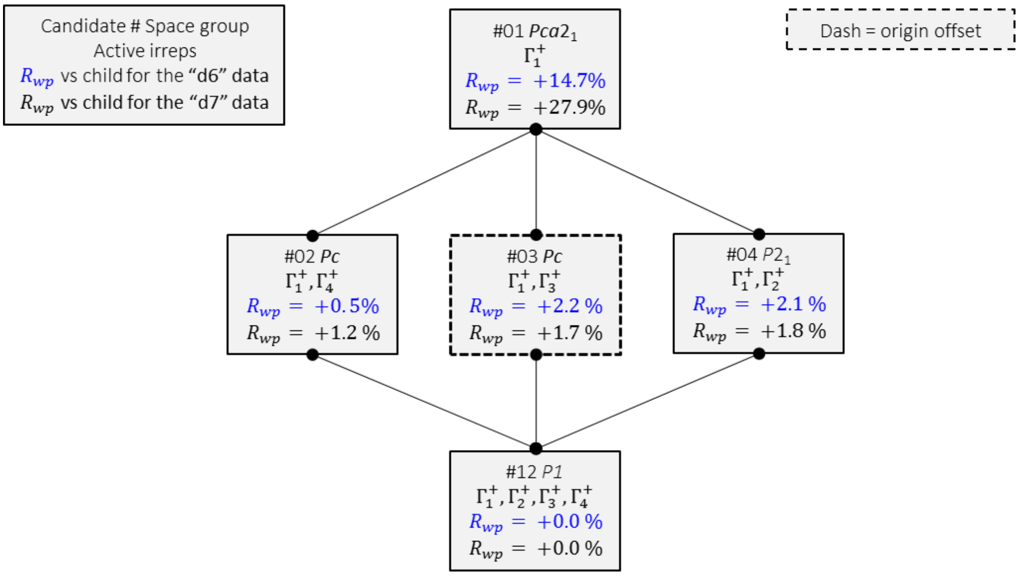

Figure 5.6: The tree of intermediate subgroups that lie between the previously reported *Pca*2₁ parent structure (top) and *P*1 base structure (bottom). The R_{wp} is the increase in R_{wp} over the lowest R_{wp} found in any subgroup. Blue for the “d6” data set and black for the “d7” data set.

A single TOPAS script was used to test all subgroup candidates by performing successive equivalent refinements. For each candidate, we repeated six sets of 500 Rietveld iterations using the “d6” data (three sets of 1000 Rietveld iterations using the “d7” data) with the value of each parameter randomised after convergence. As shown in Figure 5.7, the magnitudes of three R-factors (R_{wp}, R_{wp}' and R_{Bragg}) obtained from two data sets indicate the quality of each fit. The best fit was found for base structure candidate #1 *P*1 since it has all the degrees of freedom of each of its supergroup plus the additional flexibility in the cell metrics. The candidate #2 *Pc* has far fewer degrees of freedom and gives the second-best fit with R_{wp} only 0.5% (1.2% for the “d7” data) higher than the lowest R_{wp}. Thus, we selected this candidate as the best structural model for *β*-2BA-ETD. We note that the *hkl*-dependent peak shape description will be over-parameterised in the intermediate space groups. We, therefore, performed an equivalent search with an isotropic peak shape. This gave equivalent results.

The Rietveld fit for this *Pc* candidate using the “d6” data is shown in Figure 5.8(a). Nine terms of 4th order spherical harmonics in the *Pc* symmetry were used to correct the *hkl*-dependent peak broadening. The Rietveld fit can be further improved by introducing *α*-2BA-ETD as a minor second phase (Figure 5.8(b)). The refinement results from the “d6” data set are summarised in Table 5.3.

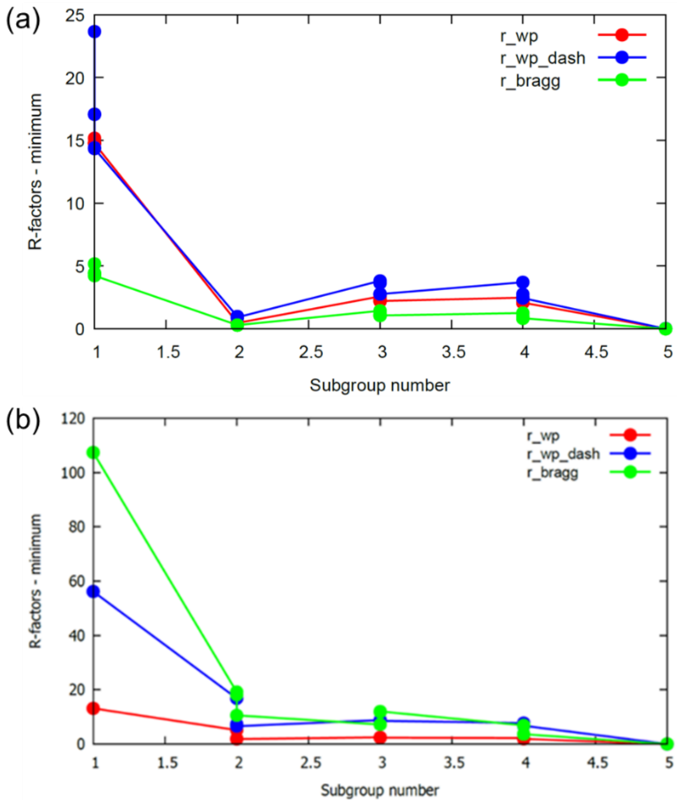

Figure 5.7: R-factors for each space group candidate (a) from the “d6” data and (b) from the “d7” data.

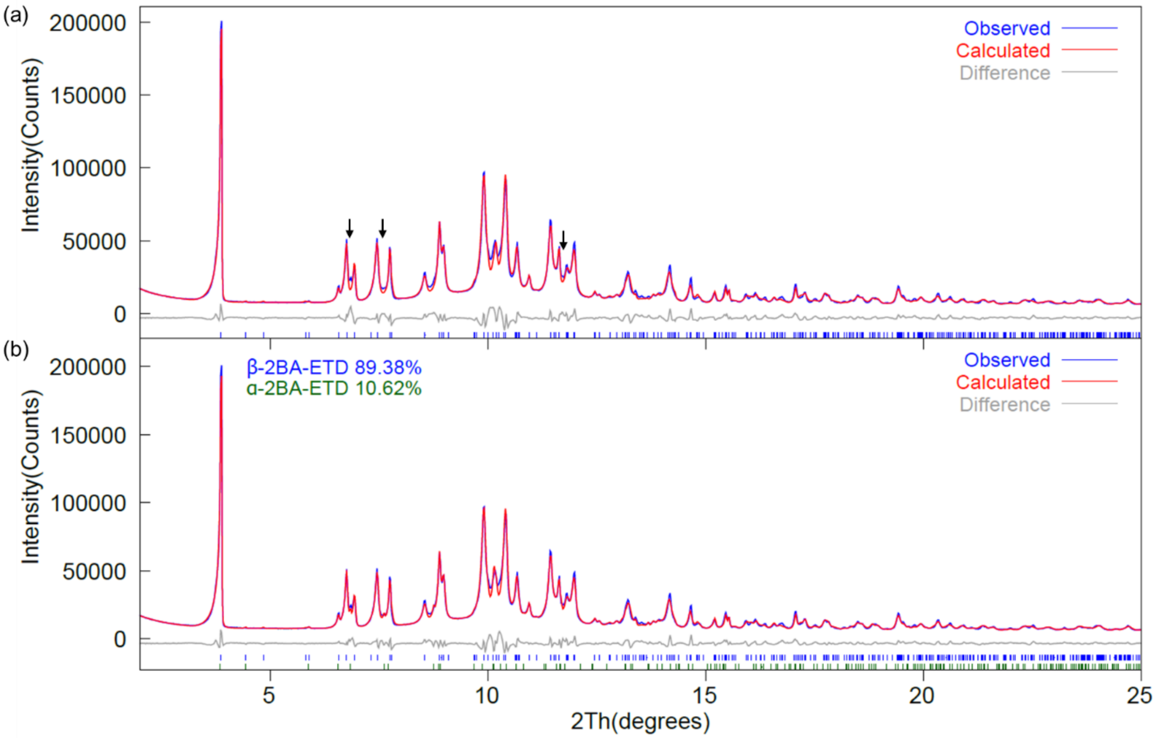

Figure 5.8: Results from the Rietveld refinements using *Pc* structure model (a) without *α*-BA-ETD as the second phase (R_{wp} = 7.3%) and (b) with *α*-BA-ETD as the second phase (R_{wp} = 6.2%).

Table 5.3: Rietveld results for new *β*-2BA-ETD.

Chemical formula	$C_{16}H_{20}N_2O_4$
Crystal system	Monoclinic
Space group	*P*1*c*1
Z	4
***a*/Å**	8.4322(7)
***b*/Å**	9.164(1)
***c*/Å**	21.059(1)
***α*/°**	90
***β*/°**	93.891(5)
***γ*/°**	90
Volume/$Å^3$	1623.6(3)
Wavelength/Å	1.5418
2θ range/°	6-60
Final R_{wp}, R_p, R_{bragg}/%	6.2, 4.6, 1.6

5.4.3 Structural discussion

Figure 5.9 shows the crystal structure of *β*-2BA-ETD in the *Pc* description and how the molecules are shifted relative to *α*-2BA-ETD. The acids and amines in *β*-2BA-ETD structure (Figure 5.9(b)) show the same connectivity as in the previously reported $Pca2_1$ structure (Figure 5.9(c)). The overall rotation vector for each molecule is depicted using a pink arrow where 0.1 Å length represents a 1° rotation in Figure 5.2(a). The rotation vectors of all acids are in their molecular planes and that of amines nearly parallel to the C-N bonds. Our symmetry distortion mode analysis captures the subtle structural changes in 2BA-ETD. All the molecules rotate differently in the asymmetric unit of *β*-2BA-ETD. The maximum rotation of ~15.5° is observed on a benzoate molecule.

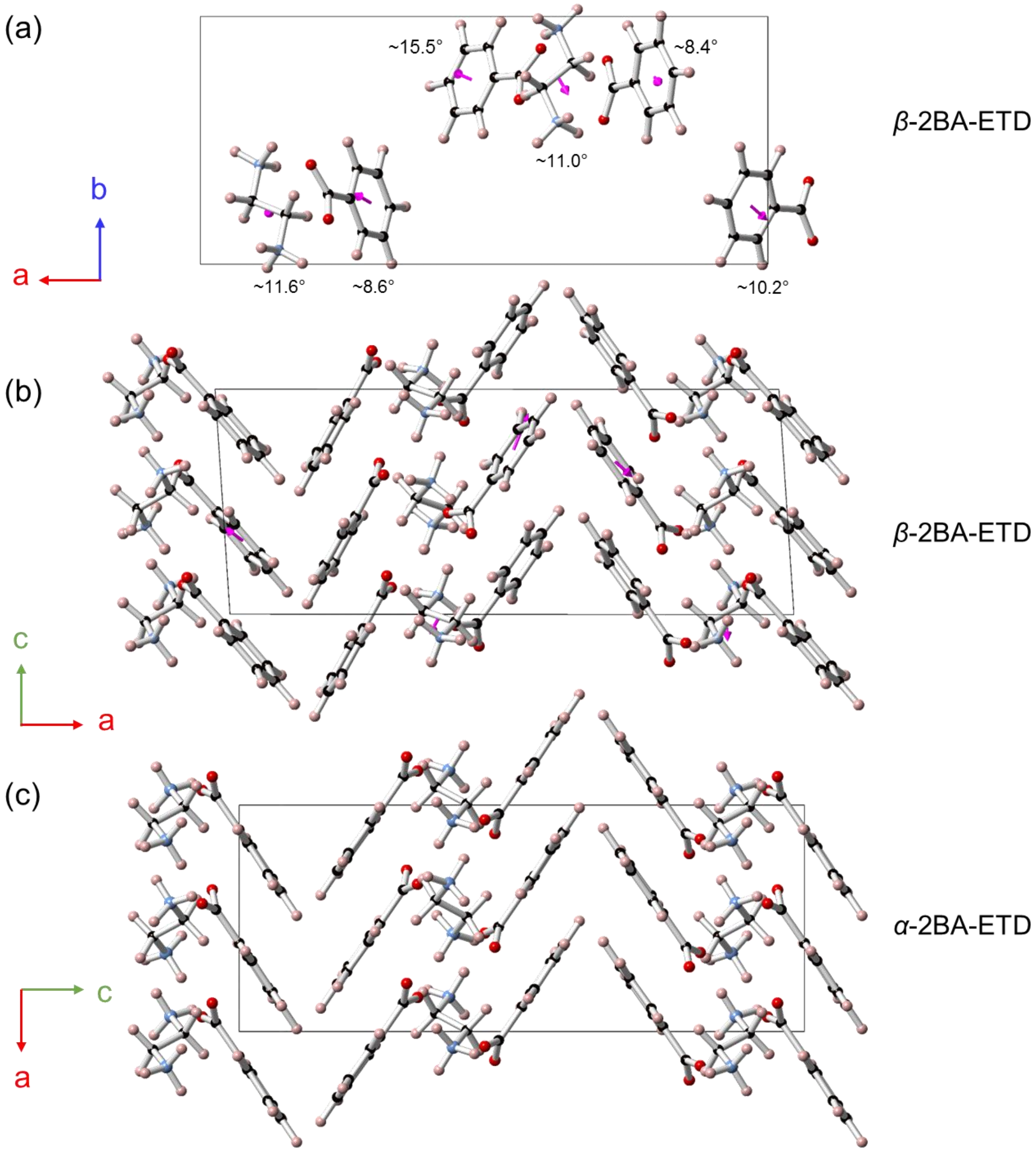

Figure 5.9: (a) The asymmetric unit of new *β*-2BA-ETD with overall rotation vector for each molecule shown as a pink arrow. (b) Crystal structure of monoclinic *β*-2BA-ETD viewed down *b*-axis. (c) Crystal structure of orthorhombic *α*-2BA-ETD viewed down *b*-axis. Rotation amplitude for each molecule is shown in (a).

5.5 Determination of the new *γ*-2BA-ETD structure

5.5.1 Preliminary characterisation and unit cell determination

As discussed in section 5.3, a phase transition takes place on heating *β*-2BA-ETD through ~363 K, and the HT form is stable on cooling. We do not see any obvious close relationship between the *β*-form (space group *Pc*) and the HT form from the peak positions and intensities in the PXRD patterns. This suggests either a major reconstructive phase transition or, perhaps, a change in the molecular composition. We first carried out CHN microanalysis to determine whether the composition of the HT form is the same as that of RT *β*-form. The measured weight percentages of carbon, hydrogen and nitrogen in the HT form show good agreements to the expected values. This confirms that the composition of the HT form remains 2BA-ETD ($C_{16}H_{20}N_2O_4$).

Table 5.4: Results from the CHN microanalysis for HT phase. The theoretical values are calculated by assuming the HT form retains the same composition as *β*-2BA-ETD.

	%C	**%H**	**%N**
Measured	63.10	6.59	9.18
Theoretical	63.14	6.62	9.20
Deviation	-0.04	-0.03	-0.02

The structure of the HT 2BA-ETD (*γ*-form) has not been reported before. Since single crystals of *γ*-2BA-ETD were not available, we attempted to solve the structure *ab-initio* from the powder diffraction data. Peak position extraction from the room temperature diffraction data (measurement d6b_01461) followed by indexing[8] was performed to determine the unit cell parameters for *γ*-2BA-ETD. The diffraction data can be successfully indexed using a monoclinic cell with a = 13.4170 Å, b = 20.0109 Å, c = 8.8597 Å, β = 93.881° and V = 2373 Å^3. Three possible space groups are suggested by indexing: $P2_1/c$, Pc and $P2_1$. However, we are not able to distinguish these space groups from the systematic absences mainly due to the reflection overlaps. A Pawley fit using this cell successfully fitted all observed peaks, giving confidence that it was correct.

5.5.2 Structure solution using DASH

Structure solution was attempted using all three space groups. We describe the structure solution using the space group $P2_1/c$ in the DASH program in this section. Similar structural models were obtained in the other space groups (all subgroups of $P2_1/c$) using

DASH and within TOPAS. The structure models in these space groups are compared using symmetry descent in a later section.

Building the molecules

The estimated number of molecules per unit cell for γ-2BA-ETD is eighteen as suggested by the cell volume (ρ_{calc} = 1.27 gcm^{-3}), which requires 3 benzoate molecules and 1.5 ethylenediamine molecules in the asymmetric unit of a $P2_1/c$ description. Each molecule was expressed as a rigid body in z-matrix format. Internal coordinates such as bond lengths, bond angles and torsion angles for constructing the rigid body were obtained from the previously reported α-2BA-ETD structure (space group $Pca2_1$). Examples of the z-matrix rigid body in DASH language are shown below:

```
#zmatrix rigid body for benzoate molecule
1.0 1.0 1.0 90.0 90.0 90.0
14  0
C  0.0000000  0    0.000000  0    0.000000  0   0   0   0  3.0  1.0   1 C51
C  1.5163709  0    0.000000  0    0.000000  0   1   0   0  3.0  1.0   2 C52 C51
C  1.3873498  0  121.030325  0    0.000000  0   1   2   0  3.0  1.0   5 C55 C51 C52
C  1.3900476  0  119.773591  0  179.746350  0   1   2   3  3.0  1.0   9 C59 C51 C52 C55
O  1.2652215  0  116.988257  0  175.966922  1   2   1   3  3.0  1.0   3 O53 C52 C51 C55
O  1.2302968  0  119.204397  0  179.051966  0   2   1   5  3.0  1.0   4 O54 C52 C51 O53
C  1.3897877  0  120.090288  0  178.601046  0   3   1   2  3.0  1.0   6 C56 C55 C51 C52
H  1.0709055  0  120.845341  0 -178.431621  0   3   1   7  6.0  1.0  10 H60 C55 C51 C56
C  1.3830278  0  120.526366  0 -178.001457  0   4   1   2  3.0  1.0   8 C58 C59 C51 C52
H  1.0774114  0  120.309357  0  178.042995  0   4   1   9  6.0  1.0  14 H64 C59 C51 C58
C  1.3723730  0  119.754784  0    1.170246  0   7   3   1  3.0  1.0   7 C57 C56 C55 C51
H  1.1110935  0  118.575531  0 -179.772144  0   7   3  11  6.0  1.0  11 H61 C56 C55 C57
H  1.0892655  0  119.760042  0  177.053751  0   9   4   1  6.0  1.0  13 H63 C58 C59 C51
H  1.1146679  0  124.993820  0  179.338326  0  11   7   3  6.0  1.0  12 H62 C57 C56 C55

#zmatrix rigid body for half amine
1.0 1.0 1.0 90.0 90.0 90.0
8   0
He 0.0000000  0    0.000000  0    0.000000  0   0   0   0  4.0  0.0   1 He1
C  0.7546117  0    0.000000  0    0.000000  0   1   0   0  4.0  1.0   2 C2 He1
H  1.0540239  0  109.100910  0    0.000000  0   2   1   0  4.0  1.0   6 H6 C2 He1
H  1.1136320  0  110.017088  0  120.108342  0   2   1   3  4.0  1.0   7 H7 C2 He1 H6
N  1.4743574  0  109.463322  0 -121.440795  0   2   1   3  4.0  1.0   8 N8 C2 He1 H6
H  1.0269236  0  111.176554  0   50.821427  0   5   2   1  4.0  1.0   3 H3 N8 C2 He1
H  1.0873960  0  114.970141  0 -137.097157  0   5   2   6  4.0  1.0   4 H4 N8 C2 H3
H  1.0358266  0   90.540331  0  113.557346  0   5   2   6  4.0  1.0   5 H5 N8 C2 H3
```

Figure 5.10 shows the benzoate and ethylenediamine molecules generated by the z-matrices. All coordinates are expressed relative to the first atom defined in the z-matrix. For example, to construct the half amine, we introduced a dummy atom He1 at the midpoint of the C-C bond and designated it as the first atom at the origin. The second atom C2 is defined only by the bond length to atom He1 and always placed on the positive z-axis. The third atom H6 is described by the bond length to C2 and the H6-C2-He1 bond angle. The fourth and remaining atoms are defined by a bond length, a bond angle and a torsion angle.

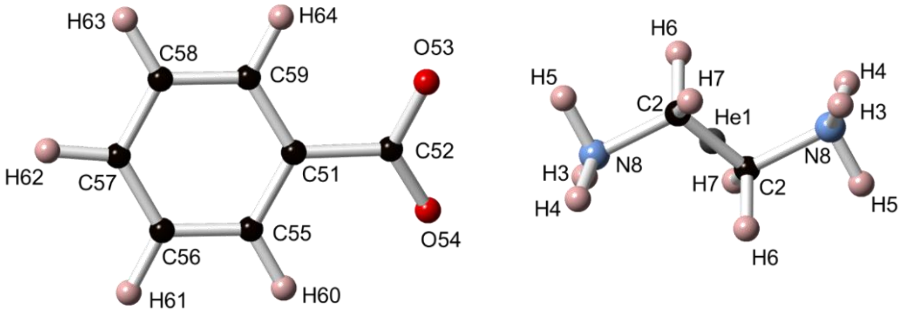

Figure 5.10: Atom numbering in rigid bodies generated by z-matrices.

Solving the structure by simulated annealing

Once the z-matrix description for all molecules was complete, we carried out simulated annealing structure solution using DASH. The unit cell parameters were started at the values obtained from indexing and Pawley refinement performed in DASH to extract integrated peak intensities and their correlations. For simulated annealing, the half amine molecule was fixed at the origin and allowed to rotate about the atom He1. Other molecules were moved and rotated freely in the unit cell. Parameters specifying the rotations, translations and the internal degrees of freedom (torsions) were randomly assigned for each trial structure. DASH then calculates the diffraction data for each trial structures and assesses the agreement between the calculated and observed intensities through the χ^2 value. As we discussed in section 2.4.4, the simulated annealing algorithm adjusts each parameter in the model and accepts those that give a downhill move in χ^2 space. Moves that are uphill are accepted according to a Boltzmann probability to prevent the model getting stuck in false minima. The “best” solution was found several times after several hundred million moves.

5.5.3 Structure refinements

Our final structure refinement using the structure model from DASH (space group $P2_1/c$) was performed in TOPAS Academic. In the refinement, each molecule was expressed as a z-matrix rigid body. The half amine only has three structural degrees of freedom (rotations only) since it was fixed at the origin. Other molecules all have seven structural degrees of freedom, three for rotations, three for translations and one for an internal molecular torsion. The parameters describing the background, zero point and unit cell parameters were freely refined. Other parameters that specify the TCHZ peak shape and axial divergence model were fixed at the values obtained from the refinement of a Si standard. In addition, we used one TOPAS parameter, Strain_G, to describe the isotropic strain broadening and one term of a March-Dollase function to model the preferred orientation observed in (100).

We then used ISODISTORT to create structure descriptions in the subgroups of $P2_1/c$ based on this $P2_1/c$ parent *(i.e. Pc* and $P2_1$ models expressed in terms of the molecular symmetry distortion modes). In each refinement, the molecular rotational and translational mode amplitudes were freely refined. All the mode amplitudes refined to essentially zero in the $P2_1/c$ refinement as expected and refined to small numbers in the *Pc* and $P2_1$ refinements. Figure 5.11 shows the final results of Rietveld refinements using the three possible space groups against the powder diffraction data.

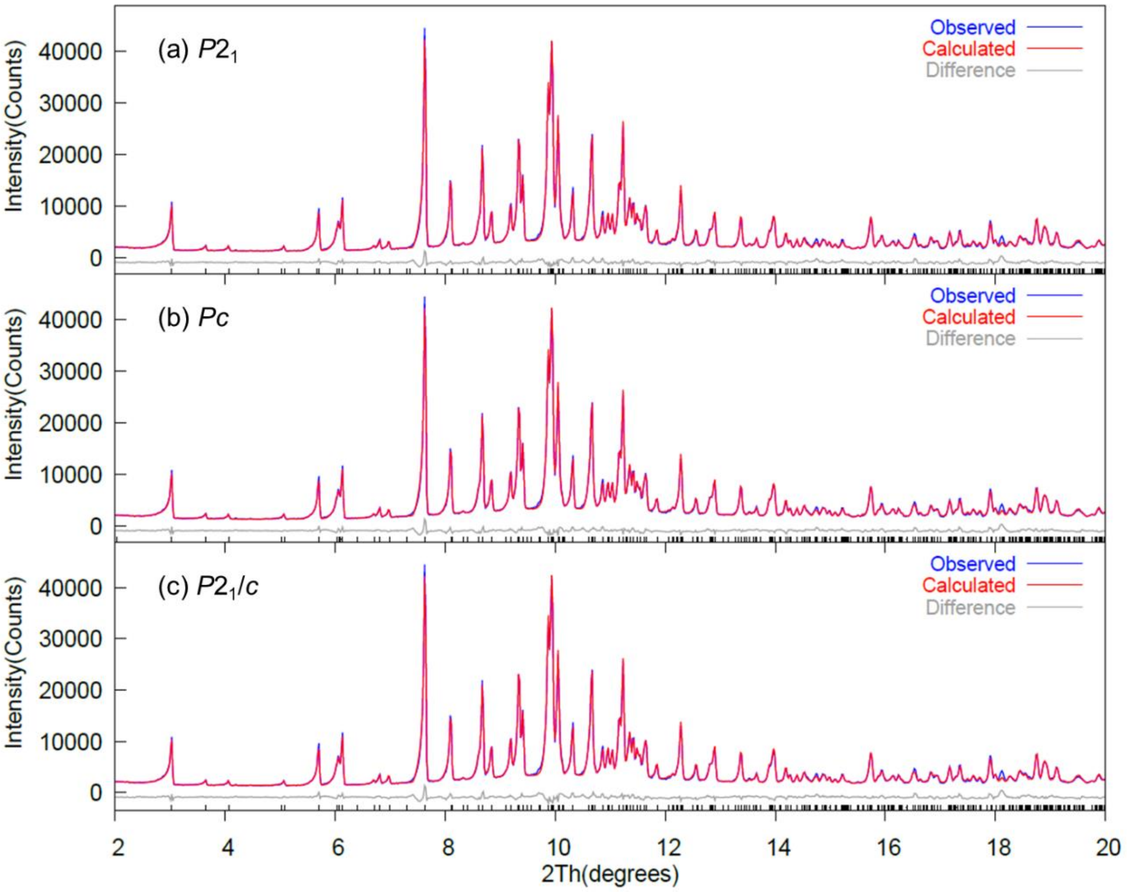

Figure 5.11: Rietveld fits to powder diffraction data of γ-2BA-ETD using three different space group types. (a) Space group $P2_1$ with R_{wp} = 4.937%, (b) space group *Pc* with R_{wp} = 5.023% and (c) space group $P2_1/c$ with R_{wp} = 5.279%.

As with other examples in this thesis, we are left with a choice of three different space groups. In this case, the R_{wp} differences between $P2_1/c$ (R_{wp} = 5.279%, 31 structural degrees of freedom), $P2_1$ (R_{wp} = 4.937%, 63 structural degrees of freedom) and Pc (R_{wp} = 5.023%, 63 structural degrees of freedom) are sufficiently small that $P2_1/c$ appears the best choice. In addition, the three structures are extremely similar in terms of molecular positions and refined values for the internal degrees of freedom of each molecule. For example, Table 5.5 compares O-C-C-O torsion angles of the benzoic acid molecules and N-C-C-N torsion angles of the ethylenediamine molecules in our structures. The results of a CSD search to find expected values of O-C-C-C and N-C-C-N torsion angles are shown in Figure 5.12. As evidenced by the histogram, all torsion angles in the molecules of our structures fall within the most likely range.

We have, however, performed an SHG test on γ-2BA-ETD and found a positive response (approximately 40% of quartz) which suggests a non-centrosymmetric structure. This is clearly incompatible with the $P2_1/c$ structural model. It may be that the inversion symmetry of γ-2BA-ETD is broken solely by hydrogen positions or small structural distortion to which PXRD is not very sensitive. Therefore, we discuss the $P2_1/c$ model in the rest of this chapter.

Table 5.5: Torsion angles obtained from different structure models.

Torsion angle	**Molecule**	***P*2₁/*c***	***P*2₁**	***Pc***
O-C-C-C	Acid 1	23.4(14)°	25(8)°	23(7)°
	Acid 2	17.6(12)°	23(8)°	23(6)°
	Acid 3	3.7(14)°	21(9)°	22(7)°
	Acid 4		16(9)°	17(5)°
	Acid 5		13(6)°	7(20)°
	Acid 6		4(7)°	2(9)°
N-C-C-N	Amine 1	179(7)°	180(10)°	180(8)°
	Amine 2		178(9)°	178(5)°
	Amine 3		173(6)°	175(5)°

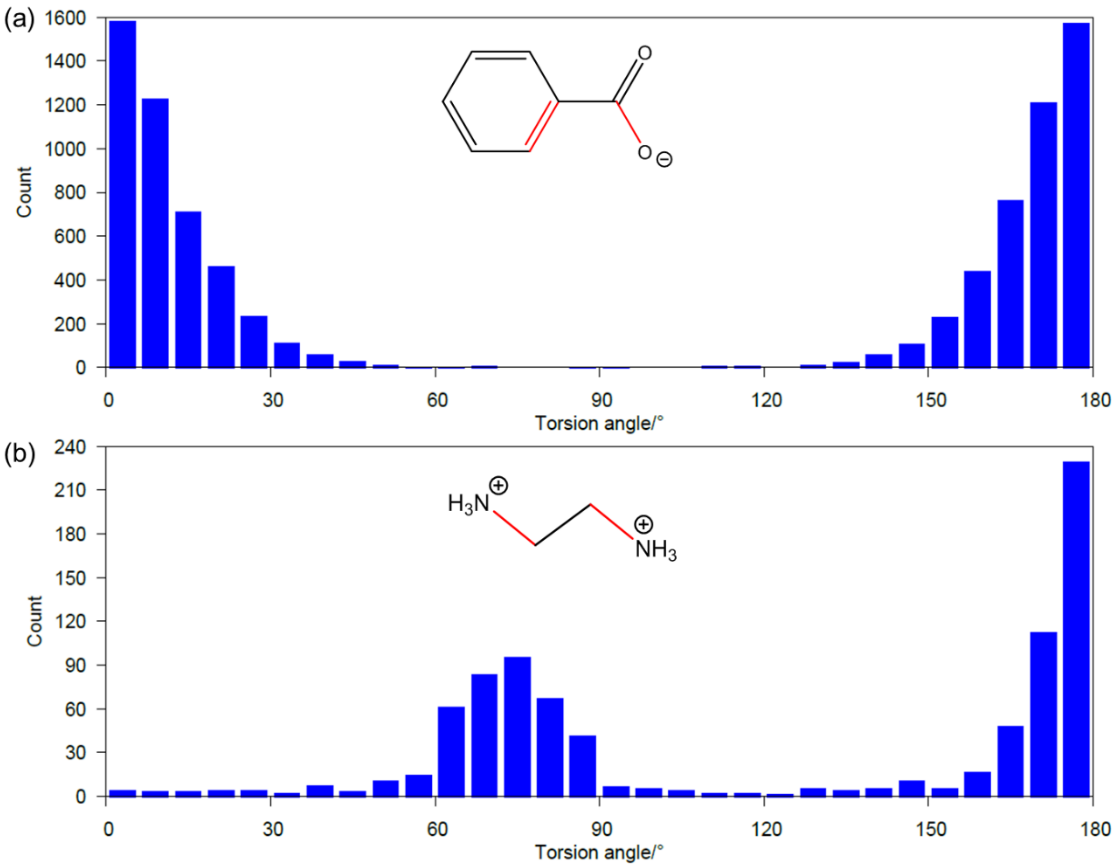

Figure 5.12: Histograms of torsion angles between (a) O-C and C-C bonds in the benzoic acid and (b) N-C and C-N in the ethylenediamine based on the search of organic and organometallic structures in the CSD.

5.5.4 Discussion of structure

From the powder diffraction study, we obtained three structure models (space groups $P2_1/c$, $P2_1$ and Pc) for *γ*-2BA-ETD. The differences between these models are extremely small, which means the real symmetry of the *γ*-2BA-ETD structure is very close to $P2_1/c$ symmetry. Figure 5.13 shows the crystal structures of previously reported *α*-2BA-ETD ($Pca2_1$) and our *γ*-2BA-ETD ($P2_1/c$). As shown in Figure 5.13(a), the molecular arrangement in *α*-2BA-ETD can be expressed as BAB'···BAB'···where A represents the amine layer and B and B' represent the two crystallographically distinct benzoate layers. The distance between nearest ethylenediamine layers is approximately 10.5 Å. A single BAB' layer (highlighted using the green solid box in Figure 5.13(a)) is shown in Figure 5.13(b). Ethylenediamine molecules have a herringbone arrangement in the RT structure. As shown in Figure 5.13(c), the *γ*-2BA-ETD again contains BAB' layers. The distance between the adjacent amine layers is larger at approximately 13.4 Å. One key difference is that benzoate molecules no longer stack side-by-side in *γ*-2BA-ETD, but are interdigitated. There are also two distinct ethylenediamine molecules in the *γ*-2BA-ETD structure, labelled as I and II in Figure 5.13(c). Figure 5.13(d) displays a single BAB' layer from the *γ*-2BA-ETD structure (the plane highlighted using green solid line in Figure 5.13(c)). The centre of amine I is at the inversion centre. Rows of amine I and II stack alternatively along the crystallographic *b*-axis. The different density of amine molecules in adjacent rows perpendicular to *b*-axis in panels (b) and (d) exemplifies the strong structural differences between *β*- and *γ*-2BA-ETD.

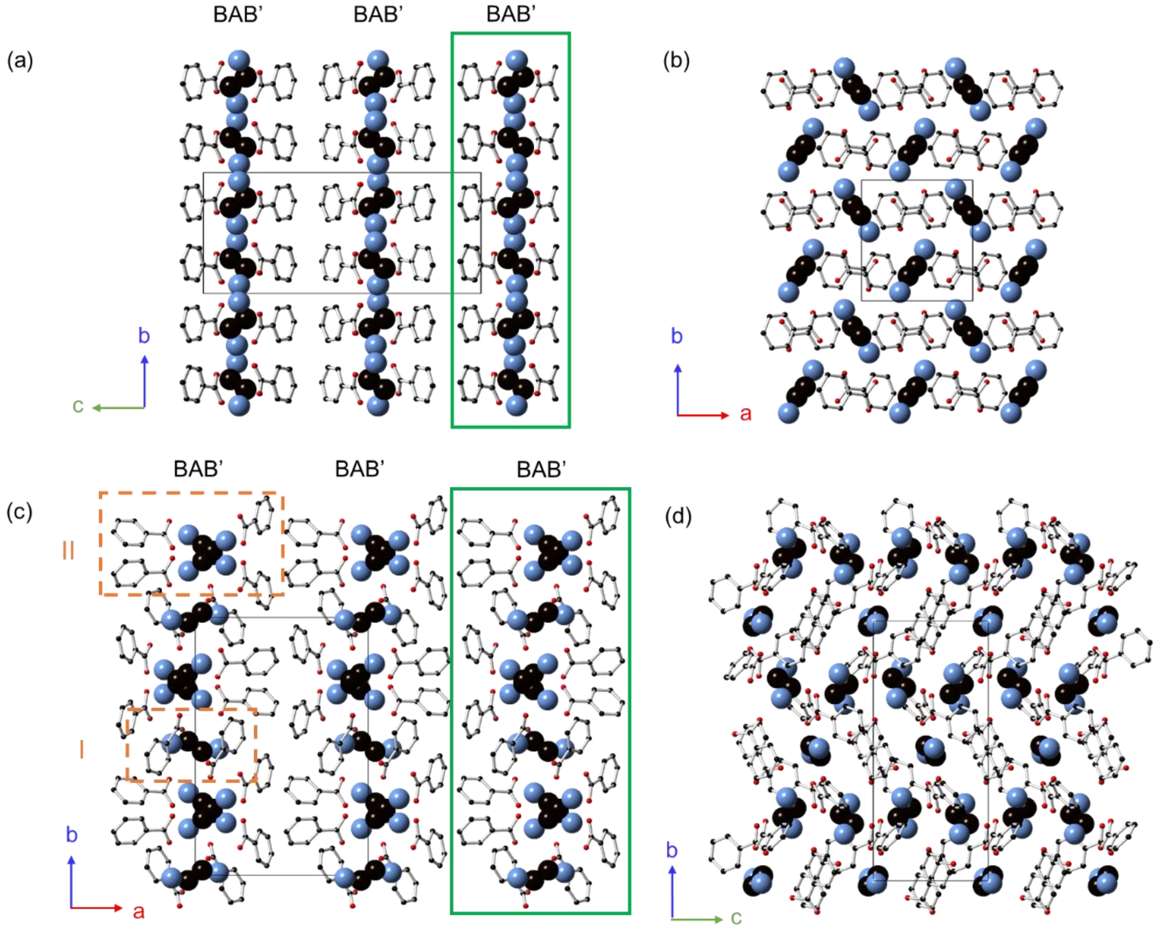

Figure 5.13: Crystal structures of 2BA-ETD. The previously reported *α*-2BA-ETD structure (*Pca*2_1) view down (a) *a*- and (b) *c*-axis. The *γ*-2BA-ETD structure (*P*2_1/*c*) view down (c) *c*- and (d) *a*-axis.

Figure 5.14 illustrates the hydrogen bond interactions in which each symmetry inequivalent ethylenediamine is involved. The donor-acceptor distances are summarised in Table 5.6. In the RT structure, the amine takes part in six hydrogen bonds; these hydrogen bonds have similar bond lengths in the range of 2.727(5)–2.764(6)°.[5] In the *γ*-2BA-ETD structure, amine I (Figure 5.14(b)) is involved in six hydrogen bonds (N4-H···O40, N4-H···O25 and N4-H···O39). Amine II participates in five hydrogen bonds where atom N12 connects to benzoate molecules through three hydrogen bonds and atom N9 through two hydrogen bonds.

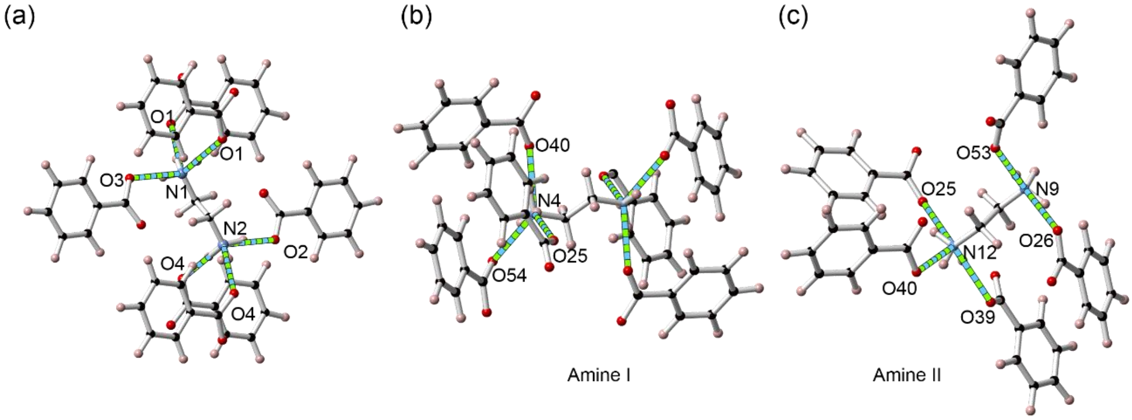

Figure 5.14: The hydrogen bond geometry for (a) amines in *α*-2BA-ETD, (b) amine I and (c) amine II in *γ*-2BA-ETD.

Table 5.6: Donor-acceptor distances of hydrogen bonds for *α*-2BA-ETD (space group *Pca*21) and *γ*-2BA-ETD (space group $P2_1/c$).

Form	**D···A**	**Bond length/Å**
α-2BA-ETD	N1···O1	2.7266(8)
	N1···O1	2.7562(6)
	N1···O3	2.7586(7)
	N2···O4	2.7277(8)
	N2···O4	2.7616(6)
	N2···O2	2.7641(7)
γ-2BA-ETD	N4-O40 (amine I)	2.79(7) (×2)
	N4-O25 (amine I)	2.71(5) (×2)
	N4-O54 (amine I)	2.70(5) (×2)
	N12-O25 (amine II)	2.81(10)
	N12-O40 (amine II)	2.81(14)
	N12-O39 (amine II)	2.69(11)
	N9-O53 (amine II)	2.72(8)
	N9-O26 (amine II)	2.71(8)

5.6 DFT and solid state NMR studies of *β*- and *γ*-2BA-ETD

5.6.1 Structure optimisations

Geometry optimisations of each *γ*-2BA-ETD structural model were performed using DFT to see if there were significant energy differences. The optimisation was also required prior to calculation of their ^{13}C SSNMR spectra.[9] The energy of each structure was minimised by allowing the positions of atoms in the molecules to vary according to their space group symmetry. Unit cell parameters were fixed at the values obtained from powder diffraction data. The overall energy converged to essentially identical values for each model, suggesting each had converged to the same minimum. This was confirmed by superimposing the $P2_1$ structure and Pc structure separately onto the $P2_1/c$ structure as shown in Figure 5.15. This also suggests the $P2_1/c$ structure is the best structure model for γ-2BA-ETD, even though it is incompatible with the positive SHG signal. Rietveld refinement was also performed using the optimised $P2_1/c$ structure with fixed coordinates to compare to the structure refined freely against the powder diffraction data. The Rietveld fit is visually almost as good as the fits shown in Figure 5.11 with a similar R_{wp} value (7.05%).

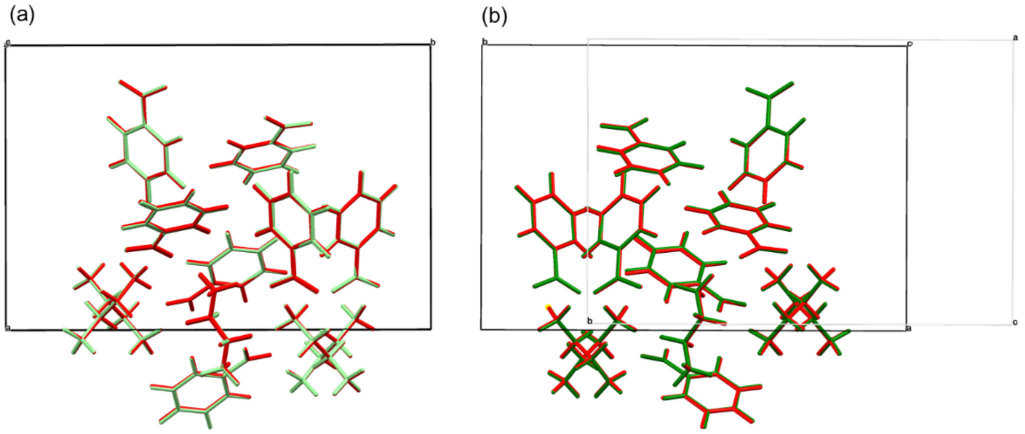

Figure 5.15: Comparisons of three optimised crystal strutcures. (a) Superimposed $P2_1/c$ and $P2_1$ structures. (b) Superimposed $P2_1/c$ and Pc structures. Red molecules: $P2_1/c$ structure, light green molecules: $P2_1$ structure and dark green molecules: Pc structure.

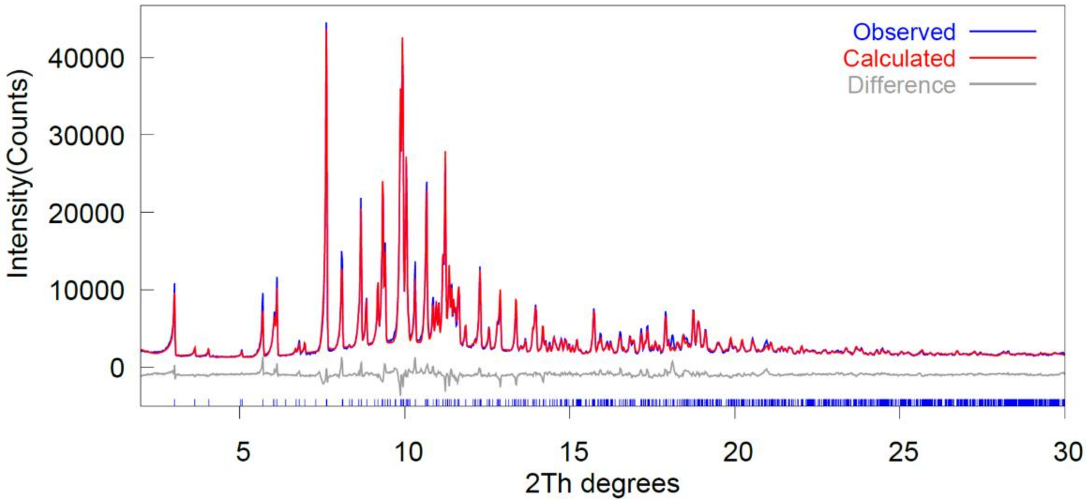

Figure 5.16: Result of Rietveld refinement using the optimised $P2_1/c$ structure with R_{wp} = 7.05%.

5.6.2 ^{13}C structures NMR: experimental and simulated spectra

Since ^{13}C solid state NMR spectra contain information on different environments of carbon, we recorded ^{13}C spectra for both *β*-and *γ*-2BA-ETD. We expected to see differences between these two spectra to provide further evidence for the reconstructive phase transition. We also tried to distinguish the three structural models ($P2_1/c$, Pc and $P2_1$) reported for *γ*-2BA-ETD in the previous section by comparing their simulated ^{13}C spectra to the experimental ^{13}C spectrum collected on *γ*-2BA-ETD. Even though the differences in chemical shifts will be small, we hoped that the predicted ^{13}C spectra for these structural models might be distinguishable.

Figure 5.17 shows comparisons of the experimental and predicted ^{13}C solid state NMR spectra for *β*- and *γ*-2BA-ETD. The assignments for each signal are presented in Table 5.7. The lowest frequency signal is assigned to the carbon atoms in ethylenediamine. The highest frequency signal is assigned to the carbon atoms in the carboxyl group and the signals that fall in the 100-150 ppm region are all assigned to the carbon atoms of the aromatic rings. We see good agreement between simulated and observed spectra, though the precise chemical shifts of the ring carbon atoms lead to slight discrepancies in the overlapped peak shape around 130 ppm.

As shown in Figure 5.17(b), the simulated ^{13}C spectrum for *γ*-2BA-ETD is also consistent with the experimental one in terms of the positions of the different carbon signals. However, there are several small differences between the two spectra. For example, the simulated ^{13}C spectrum shows three lowest-frequency signals with ratio 1:1:1 according to the types of carbons (labelled as 6a, 6b and 6c in Table 5.7) in the ethylenediamines. On the other hand, we only observed two signals with ratio ~2:1 at the lowest frequency in the experimental spectrum, which might be explained by two signals accidentally overlapping. Given the level of uncertainty in predicted peak positions and the fact that DFT optimisations all converged to equivalent models, we cannot distinguish between the $P2_1/c$, Pc and $P2_1$ structural models for *γ*-2BA-ETD by comparing the simulated and experimental ^{13}C spectra.

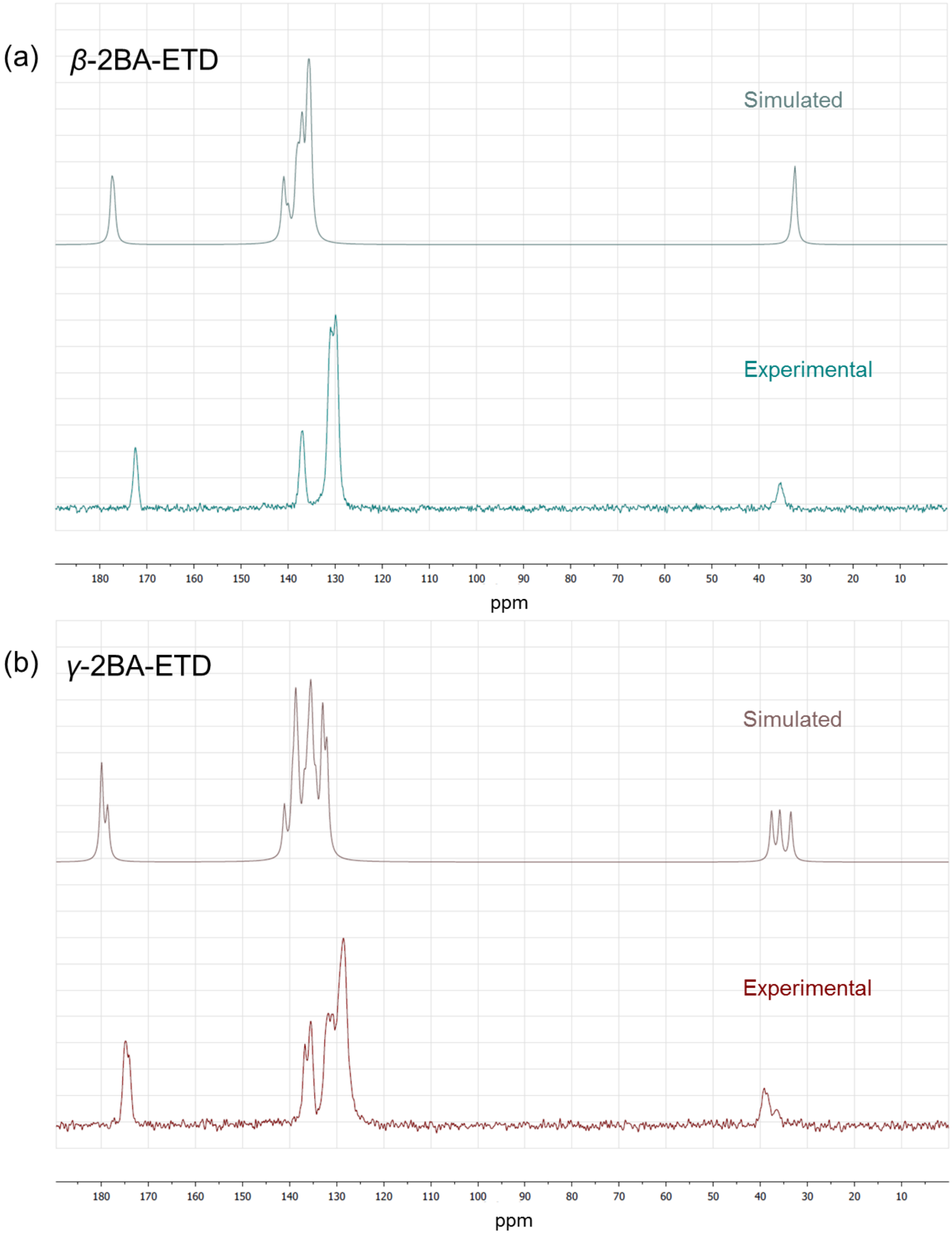

Figure 5.17: Simulated and experimental ^{13}C solid state NMR spectra for 2BA-ETD. (a) Comparison of the calculated and experimental ^{13}C spectra for *β*-2BA-ETD. (b) Comparison of the calculated $P2_1/c$ description and experimental spectra for *γ*-2BA-ETD.

Table 5.7: Chemical shift assignments for *β*-2BA-ETD and *γ*-2BA-ETD (space group *P*2$_1$/*c)* in the experimental ^{13}C solid state NMR spectra.

<table>
<tr><th colspan="2"><i>β</i>-2BA-ETD (<i>Pc</i> structure)</th><th colspan="2"><i>γ</i>-2BA-ETD (<i>P</i>2$_1$/<i>c</i> structure)</th></tr>
<tr><td colspan="2">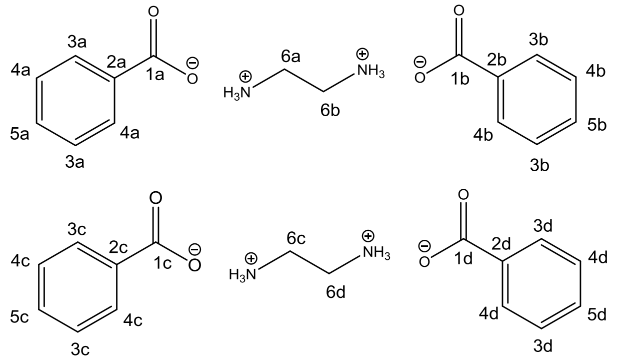
</td><td colspan="2">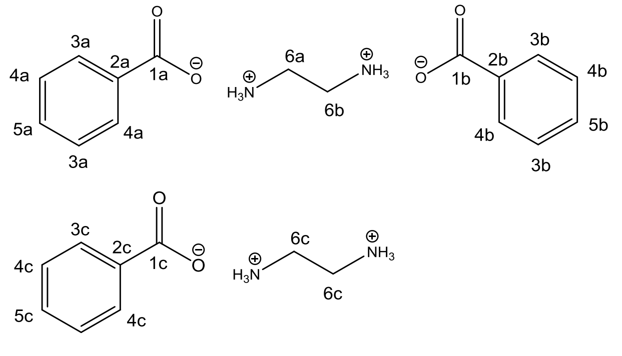
</td></tr>
<tr><td>Assignment</td><td>Experimental ppm</td><td>Assignment</td><td>Experimental ppm</td></tr>
<tr><td>6a,6b,6c,6d</td><td>35.5</td><td>6a,6b,6c</td><td>39.1, 36.5</td></tr>
<tr><td>2a,3a,4a,2b,3b,4b
2c,3c,4c,2d,3d,4d</td><td>129.8, 131.0</td><td>2a,3a,4a,2b,3b,4b
2c,3c,4c</td><td>131.8, 131.0, 130.8, 128.6</td></tr>
<tr><td>5a,5b,5c,5d</td><td>137.1</td><td>5a,5b,5c</td><td>136.8, 135.5</td></tr>
<tr><td>1a,1b,1c</td><td>172.5</td><td>1a,1b,1c</td><td>174.9, 174.1</td></tr>
</table>

5.7 Conclusions and future work

The 2:1 cocrystals of benzoic acid and ethylenediamine (2BA-ETD) were successfully obtained by slow evaporation. Figure 5.18 summarises the structural transitions between the *α*-, *β*- and *γ*-2BA-ETD. Powder diffraction studies give clear evidence that 2BA-ETD undergoes a structural change upon even light grinding of single crystals. A structure solution from powder X-ray diffraction data using the symmetry-adapted subgroup search method suggests that the new RT *β*-form adopts space group *Pc*. The subtle changes in the structure result from the anisotropic rotations of molecules. The new *β*-2BA-ETD undergoes an irreversible phase transition at ~363 K to *γ*-2BA-ETD; this *γ*-form is stable upon cooling. We obtained three possible structure models (space groups *P*2$_1$/*c*, *P*2$_1$ and *Pc*) from powder X-ray diffraction data using DASH followed by structural refinement in TOPAS Academic. We would suggest *P*2$_1$/*c* structure as the best structural model for *γ*-2BA-ETD according to the results from Rietveld refinements, structural optimisations and predicted ^{13}C SSNMR spectra. However, this conclusion is surprisingly inconsistent with the observation of a significant SHG activity for *γ*-2BA-ETD. We suggest this could be related to the subtlety of the hydrogen bonds in the real structure, which cannot be investigated by the laboratory powder X-ray diffraction data. As a result, high-resolution data such as neutron diffraction might be needed in order to gain insight into the subtlety of the hydrogen bonds.

Figure 5.18: Summary of the phase transitions between different forms of 2BA-ETD.

References

1. Horiuchi, S.; Kumai, R.; Tokura, Y., Hydrogen-Bonding Molecular Chains for High-Temperature Ferroelectricity. *Advanced Materials* **2011,** *23* (18), 2098-2103.
2. Horiuchi, S.; Kagawa, F.; Hatahara, K.; Kobayashi, K.; Kumai, R.; Murakami, Y.; Tokura, Y., Above-room-temperature ferroelectricity and antiferroelectricity in benzimidazoles. *Nature Communications* **2012,** *3* (1), 1308.
3. Horiuchi, S.; Kumai, R.; Tokura, Y., A Supramolecular Ferroelectric Realized by Collective Proton Transfer. *Angewandte Chemie International Edition* **2007,** *46* (19), 3497-3501.
4. Horiuchi, S.; Kumai, R.; Tokura, Y., High-Temperature and Pressure-Induced Ferroelectricity in Hydrogen-Bonded Supramolecular Crystals of Anilic Acids and 2,3-Di(2-pyridinyl)pyrazine. *Journal of the American Chemical Society* **2013,** *135* (11), 4492-4500.
5. R. Adam, K.; M. Atkinson, I.; Lindsay Davis, R.; F. Lindoy, L.; S. Mahinay, M.; J. McCool, B.; W. Skelton, B.; H. White, A., Self-assembly directed by NH···O hydrogen bonding: a neutron study of a trilayered supramolecular array formed between 1,2-diaminoethane and benzoic acid. *Chemical Communications* **1997,** (5), 467-468.
6. Capillas, C.; Tasci Emre, S.; de la Flor, G.; Orobengoa, D.; Perez-Mato Juan, M.; Aroyo Mois, I., A new computer tool at the Bilbao Crystallographic Server to detect and characterize pseudosymmetry. In *Zeitschrift für Kristallographie Crystalline Materials*, 2011; Vol. 226, p 186.
7. Clark, S. J.; Segall, M. D.; Pickard, C. J.; Hasnip, P. J.; Probert, M. J.; Refson, K.; Payne, M. C., First principles methods using CASTEP. *Zeitschrift für Kristallographie* **2005,** *220* (5-6), 567-570.
8. Coelho, A. A.; Evans, J. S. O.; Evans, I. R.; Kern, A.; Parsons, S., The TOPAS symbolic computation system. *Powder Diffraction* **2011,** *26* (4), S22.

9. Bonhomme, C.; Gervais, C.; Babonneau, F.; Coelho, C.; Pourpoint, F.; Azaïs, T.; Ashbrook, S. E.; Griffin, J. M.; Yates, J. R.; Mauri, F.; Pickard, C. J., First-Principles Calculation of NMR Parameters Using the Gauge Including Projector Augmented Wave Method: A Chemist's Point of View. *Chemical Reviews* **2012,** *112* (11), 5733-5779.

Chapter 6 Cocrystals of chloranilic acid with pyrazole and benzimidazole

Overview

This chapter describes our attempts to grow cocrystals of chloranilic acid with pyrazole and benzimidazole as potential hydrogen-bonded ferroelectric materials. We report the structure determinations of two previously unknown cocrystals, pyrazolium chloranilate (CA-PYR) monohydrate and bis(benzimidazolium) dichloranilate (CA-2BEN) by using single crystal or powder X-ray diffraction. The structures of the molecules used are given in Figure 6.1.

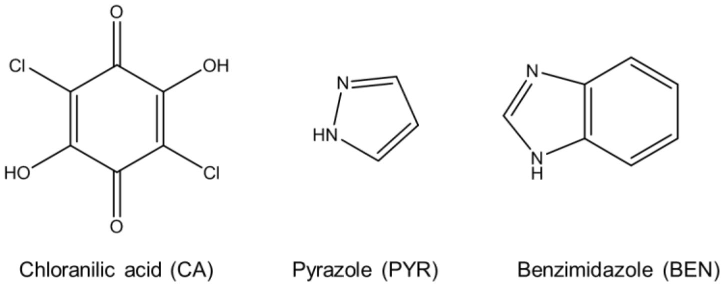

Figure 6.1: The molecular structures of cocrystals components.

6.1 Introduction

Chloranilic acid, as a good acidic component, shows attractive potential to form cocrystals with heterocyclic aromatic compounds via hydrogen-bonding interactions. A variety of cocrystals of this type have been reported and the hydrogen bond in the systems can play a key role in physical properties as demonstrated, for example, in the ferroelectric chloranilic acid phenazine[1-5]. The crystal structure of bis(pyrazolium) chloroanilate (CA-2PYR) has been reported by Ishida and Kashino.[6] CA-2PYR crystallised in a centrosymmetric space group $P2_1/c$, and strong hydrogen-bonding interactions were observed. The structure of a 1:1 chloranilic acid pyrazole co-crystal (CA-PYR) has not been reported and there is a possibility that chloranilic acid will form a cocrystal with pyrazole in molar ratio 1:1. We also extend our study to cocrystals of chloranilic acid and another heterocyclic system benzimidazole (BEN) with stoichiometry 1:1 and 1:2, since the formation of cocrystals can be expected based on the hydrogen bonding between the functional groups of the two molecules[7]. The molecular structures of crystals components are shown in Figure 6.1. The aim of this work was to grow cocrystals CA-PYR, CA-BEN and CA-2BEN, determine the crystal structures and identify possible phase transitions by X-ray diffraction in order to know whether any of the cocrystals are potential ferroelectric materials. However, the cocrystals do not show ferroelectricity as they all crystallise in centrosymmetric space groups. Herein, we record our attempts to produce those cocrystals and report the structures of two new cocrystals, pyrazolium chloranilate (CA-PYR) monohydrate and bis(benzimidazolium) dichloranilate (CA-2BEN), determined by using single crystal and powder X-ray diffraction respectively.

6.2 Sample preparation and structure determination of chloranilic acid : pyrazole cocrystals

6.2.1 Sample preparation

We used three methods to produce CA-PYR cocrystals; however, none of our attempts was successful:

1) *Slow evaporation*. Single crystal growth of CA-PYR was attempted from the slow evaporation of four different solutions: water, acetonitrile, ethanol and dry methanol. Chloranilic acid (0.0627g, 0.03mmol) and pyrazole (0.0204g, 0.3mmol) were dissolved separately in a minimum volume of each solvent. The solutions were combined in an 18 mL sample vial and left to crystallise at room temperature.
2) *Co-grinding*. Polycrystalline samples of CA-PYR were targeted by both solvent assisted co-grinding and neat co-grinding (without the assistance of solvents) of the two components with molar ratio 1:1 using the ball mill.
3) *Dehydration of monohydrate sample*. The monohydrate sample was gradually heated up to 400 K in order to remove the water molecule.

6.2.2 Attempts on synthesis of anhydrous CA-PYR

Our attempts to grow single crystals from slow evaporation only gave crystals that incorporate a water molecule. Transparent dark-red needle-like single crystals of monohydrated CA-PYR appeared after five days in the sample vials. The crystal structure of monohydrated CA-PYR is reported in the section 6.2.3.

Neat grinding without the assistance of solvents was attempted to produce the anhydrous polycrystalline CA-PYR samples. The PXRD patterns recorded after 20-, 40- and 60-min grinding in a ball mill are shown in Figure 6.2. Several peaks that do not belong to either the starting materials or CA-2PYR appear after 20-min of neat grinding.

The presence of the high background suggests the formation of poorly crystalline materials or amorphous components. Further grinding slightly helps the formation of cocrystals; however, indexing of the PXRD data was attempted but not successful. Co-grinding with the assistance of different solvents were also tested:

1) Co-grinding with the assistance of ethanol yielded polycrystalline CA-PYR monohydrate.
2) Co-grinding with the assistance of dry methanol gave the same results as neat grinding. Indexing of the PXRD data was not successful.

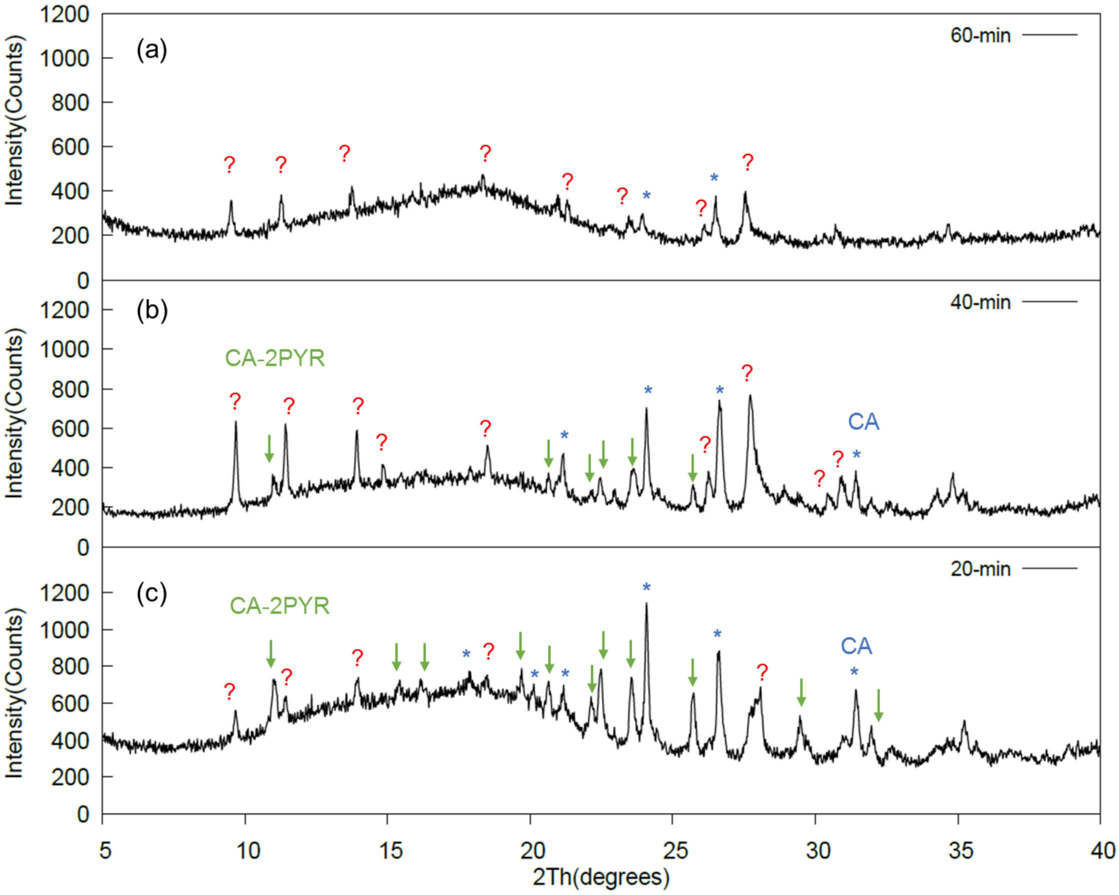

Figure 6.2: PXRD patterns collected after (a) 20 mins, (b) 40 mins and (c) 60 mins neat grinding using ball mill. Each PXRD pattern was collected in 30 mins over a 2θ range of 5-40° using a step size of 0.02° on the diffractometer “d7”.

We also tried to produce anhydrous sample by removing water from the monohydrate sample by gradual heating. VT PXRD patterns were collected for 30 mins every 5 K over 2θ range of 5-50° from 308 K to 393 K on the diffractometer “d9” fitted with a HTK1200 furnace. However, as shown in Figure 6.3(a), the monohydrate sample partially decomposes at 363 K to form chloranilic acid. The Rietveld fitting (Figure 6.3(b)) against 363 K diffraction data confirms the formation of chloranilic acid. This is consistent with the results obtained from TGA analysis (Appendix VIII). The mass loss in the TGA curve starting at ~376 K indicates the loss of water molecule and pyrazole molecules. Therefore, we are not able to isolate the anhydrous CA-PYR by removing the water molecule from the monohydrate product by controlled heating.

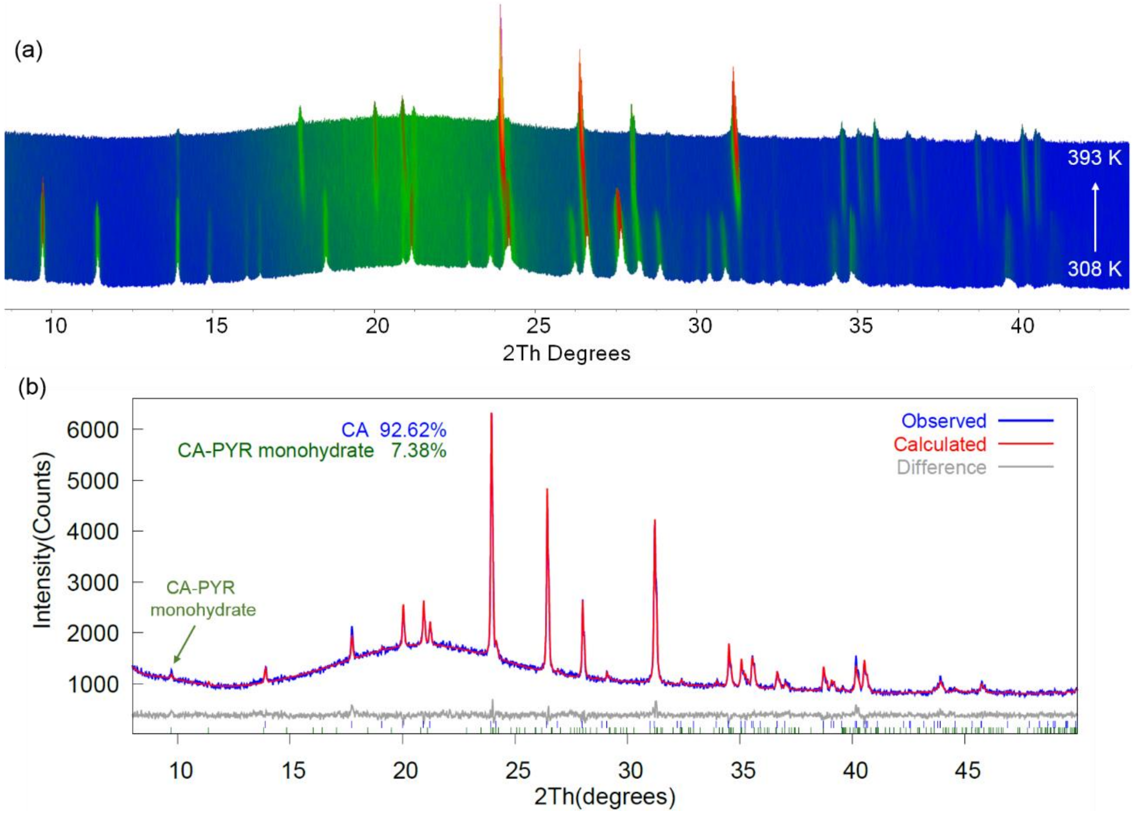

Figure 6.3: (a) Variable temperature PXRD patterns collected for 15 mins every 5 K over 2θ range of 5-50°. (b) Rietveld refinement against 363 K diffraction data showing presence of chloranilic acid.

6.2.3 Structure solution of monohydrate CA-PYR from single crystal X-ray diffraction

The crystal structure of the monohydrate CA-PYR has not been reported. In this section, we report the structure solution by using single crystal X-ray diffraction. Single crystal X-ray diffraction was performed at 120 K on the diffractometers “D8V” using Cu radiation and the structure solved by direct methods. All hydrogens were found in a difference Fourier maps. Hydrogen atoms involved in hydrogen-bonding interaction were refined isotropically without restraints. The remaining hydrogen atoms were placed geometrically and refined with riding mode. The crystallographic information is summarised in Table 6.1. The monohydrate CA-PYR adopts centrosymmetric space group *C*2/*c* and therefore does not show the possibility to exhibit ferroelectricity.

Table 6.1: Crystallographic data for the co-crystal of chloranilic acid and pyrazole with the stoichiometry of 1:1 from single crystal X-ray diffraction.

Chemical formula	$C_9H_6N_2O_4Cl_2 \cdot H_2O$
M_r/g·mol^{-1}	295.08
Experimental temperature/K	120
Crystal system	Monoclinic
Space group	*C*2/*c*
Z	2
***a*/Å**	31.231(2)
***b*/Å**	3.7524(3)
***c*/Å**	22.3085(14)
***α*/°**	90
***β*/°**	125.217(4)
***γ*/°**	90
Volume/Å^3	2135.88(13)
No. of measured reflections	13642
No. of observed reflections	1328
No. of parameters	161
R, R_w	0.0612, 0.1186
I/Sigma cutoff	2

As shown in Figure 6.4, chloranilic acid plays a dual role of proton donor and acceptor in the formation of one-dimensional molecular chains running along the crystallographic *a*-axis. There are no remarkable interactions between the molecular chains. The bond distances and angles involved in each hydrogen-bond interaction are summarised in Table 6.2. Atom O4 in CA retains its proton and participates in the moderate[8] O4-H3···O6 interaction to form CA dimers. Two pyrazolium ions are linked together through a water molecule by hydrogen bond N13-H1···O1 to form Pyz/H_2O units. Alternating CA dimer and Pyz/H_2O unit are connected by N14-H2···O11, N13-H1···O10 and O1-H8···O11 interactions. The proton originally attached to O11 in CA has transferred to the nitrogen atom N14 in pyrazole, resulting in the strong hydrogen-bond interaction[8] (N14-H2···O11) between the pyrazolium ions and chloranilate ions. Atom O10 in CA acting as the proton acceptor takes part in the moderate hydrogen bond N13-H1···O10 and atom O1 from the water molecule is involved in the hydrogen bond O1-H8···O11. Removal of water molecules breaks up the molecular chain, which presumably explain why water loss and pyrazole loss happen together when heating the monohydrate CA-PYR.

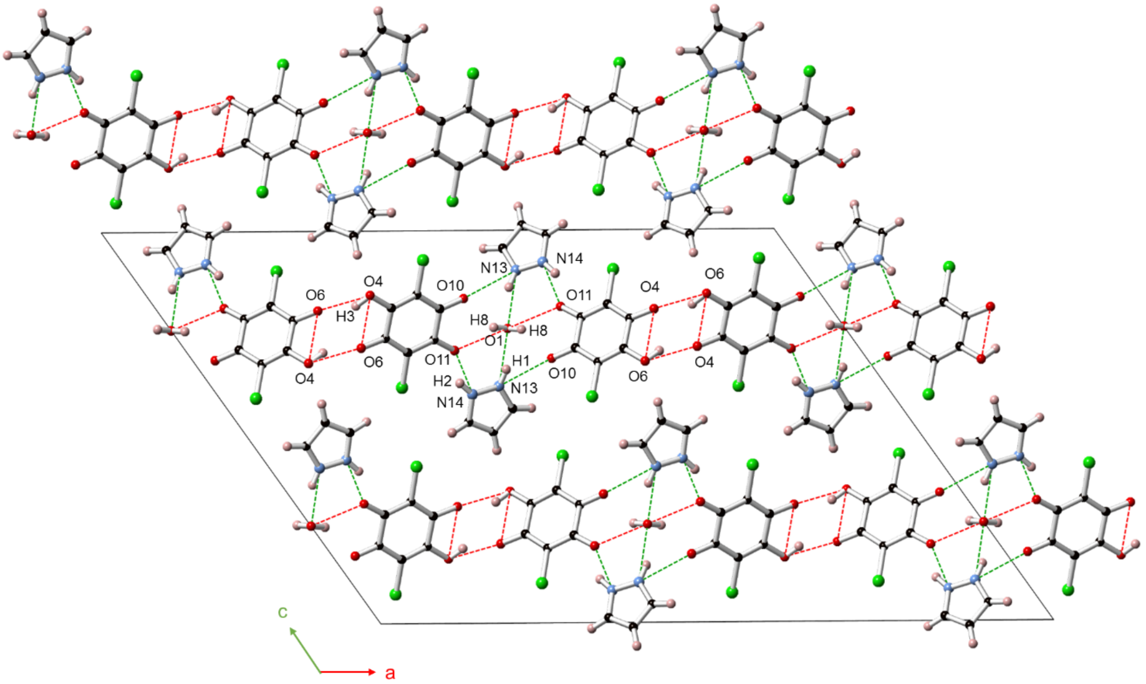

Figure 6.4: The crystal structure of monohydrate CA-PYR with atomic numbering scheme. Hydrogen bonds N-H···O are drawn with a green dashed line and O-H···O with a red dashed line.

Table 6.2: Hydrogen-bonding geometry for monohydrate CA-PYR.

D-H···A	D-H/Å	D···A/Å	D-H···A angle/°
N14-H2···O11	0.855	2.595(9)	144.87(19)
N13-H1···O10	0.865	2.953(6)	116.82(13)
N13-H1···O1	0.865	2.843(9)	156.73(15)
O1-H8···O11	0.828	2.807(9)	137.70(16)
O4-H3···O6	0.832	2.696(9)	134.28(16)

6.3 Sample preparation and structure determination of chloranilic acid : benzimidazole cocrystals

6.3.1 Sample preparation and data collection

Single crystals of CA-2BEN were targeted by slow evaporation from three different solutions: water, ethanol and dry methanol. Polycrystalline samples of CA-2BEN were obtained from slow evaporation of solutions of chloranilic acid (0.0627g, 0.03mmol) and benzimidazole (0.0708g, 0.6mmol). X-ray powder diffraction data were acquired on the diffractometer “d6” at room temperature for 16 hours over a 2θ range of 2-30° in order to solve the structure.

The growth of cocrystals of chloranilic acid and benzimidazole with molar ratio 1:1 was also attempted by solvent assisted co-grinding and neat co-grinding but was not successful. By co-grinding, only CA-2BEN was produced.

6.3.2 Structure solution from powder X-ray diffraction data

Preliminary unit cell determination

Extraction of peak positions and indexing of the RT data were performed to determine the unit cell parameters. The RT data can be successfully indexed using a monoclinic cell with a = 10.2482 Å, b = 5.1764 Å, c = 17.2665 Å, β = 95.574° and V = 911.628 Å^3. The indexing suggests three possible space group: $P2_1/c$, Pc *and* $P2_1$ (as shown in Figure 6.5). We eliminated space group $P2_1$ since it has a number of additional *hkl* reflections compared to other space group candidates. However, we could not distinguish candidate space group $P2_1/c$ and Pc by Pawley fits and systematic absence.

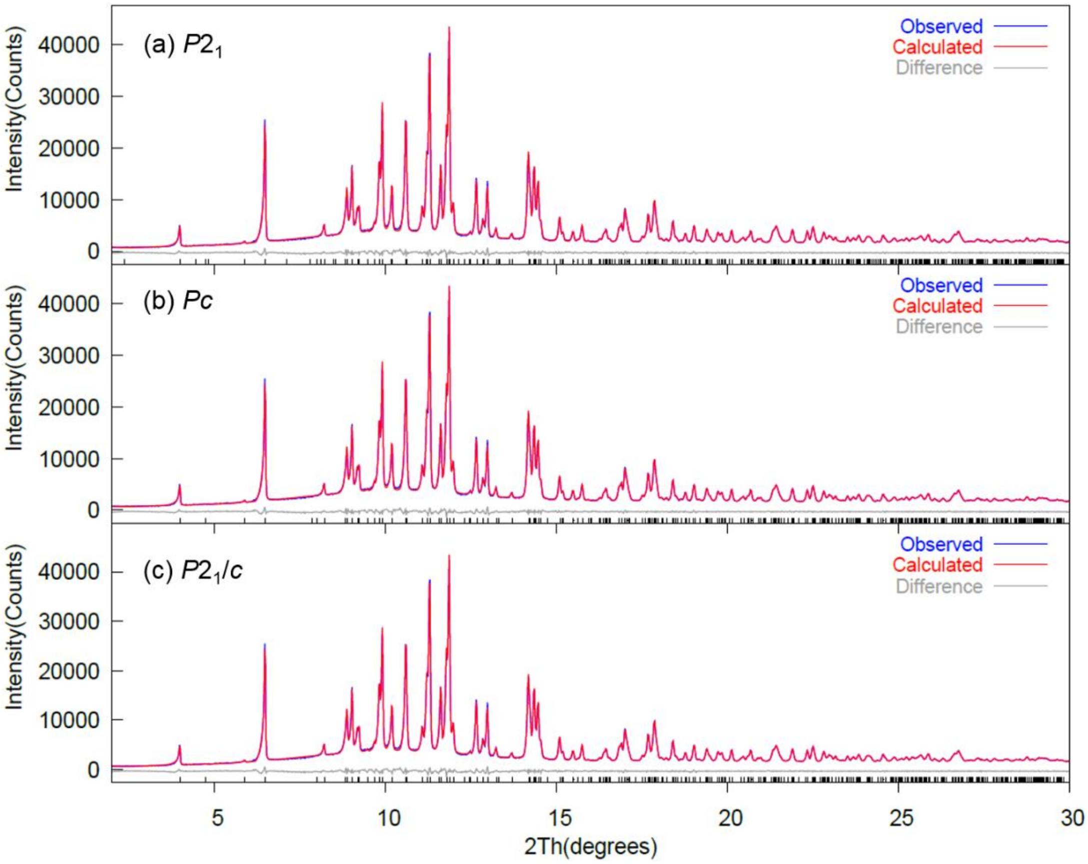

Figure 6.5: Pawley fits to PXRD data using monoclinic cell. (a) Use of space group $P2_1$. (b) Use of space group Pc. (c) Use of space group $P2_1/c$.

Structure solution using a rigid body approach

Structure solution of CA-2BEN was attempted using space group $P2_1/c$. The atomic arrangement for each molecular unit was obtained from the known structures of chloranilic acid and benzimidazole in the Cambridge Structural Database (CSD). Each was expressed as a rigid body in terms of Cartesian coordinates. Since the cell volume suggests half a chloranilic acid and one benzimidazole in the asymmetric unit, we fixed the centre of chloranilic acid at the inversion centre (0,0,0.5) to allow the whole molecule to be generated by symmetry, and allowed benzimidazole to rotate and translate freely. As a result, the rigid body describing chloranilic acid has three structural degrees of freedom while the benzimidazole unit has six degrees of freedom (three for rotations and three for translations). Rietveld refinement based on rigid bodies was performed for different random trial structures using TOPAS academic software for several hundred thousand iterations. For each Rietveld refinement, we allowed the parameters describing molecular rotations and translations to refine. These parameters were randomised after each convergence. Other parameters specifying the unit cell parameters, zero point, background and TCHZ peak shape were initially fixed at the values obtained from the Pawley refinement. The “best” solution was found several times with R_{wp} ~ 15.46%. As shown in Figure 6.6(a), the Rietveld fit using the initial “best” model is slightly improved (R_{wp} = 14.71%) by refining the parameters for unit cell, zero point, background and TCHZ peak shape.

A closer visual inspection of our Rietveld fit in Figure 6.6(a) shows some misfits in several peaks which are probably due to preferred orientation. We tested 15 terms of a 4th order spherical harmonic function in $P2_1/c$ symmetry for preferred orientation correction and this improves the Rietveld fit significantly to R_{wp} of 8.78%. The Rietveld fit including the preferred orientation correction is shown in Figure 6.5(b).

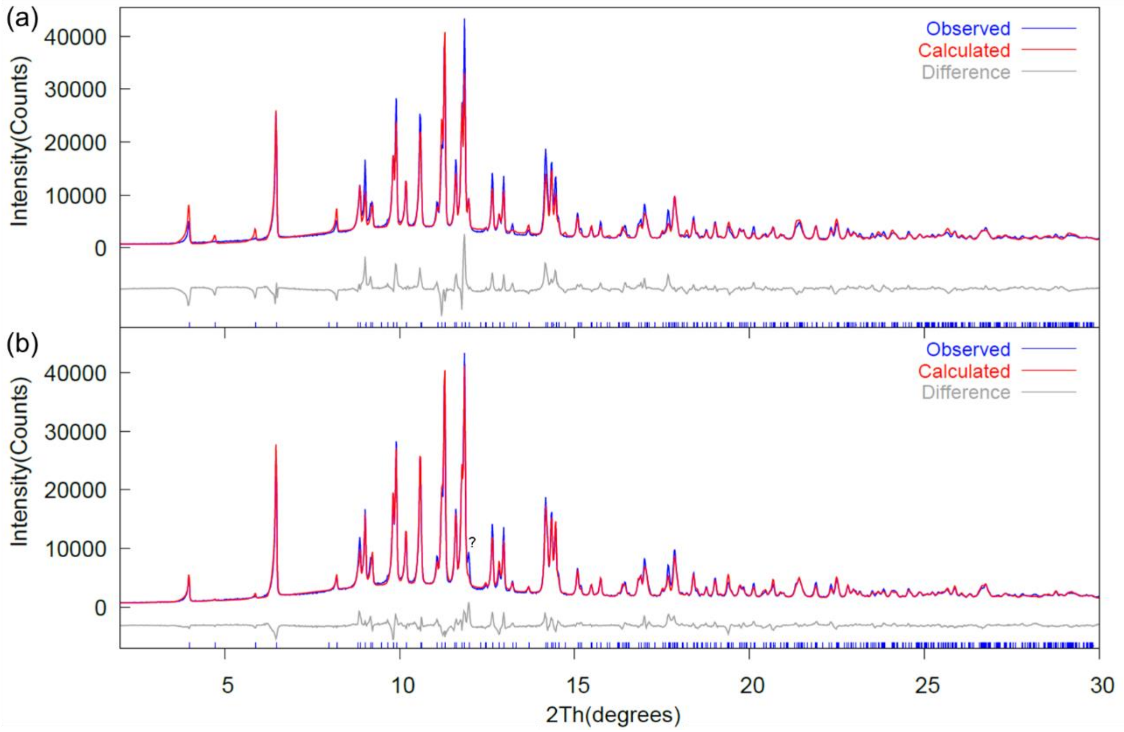

Figure 6.6: Results from Rietveld refinements based on rigid bodies (a) without preferred orientation (R_{wp} = 14.71%) and (b) with preferred orientation (R_{wp} = 8.78%).

All observed peaks are well estimated by our model however a small number of weak peaks (e.g at ~12° 2θ) suggest a minor impurity phase (~5%) might be present. One possible impurity is chloranilic acid. We tried a two-phase Rietveld refinement using chloranilic acid as the second phase. As shown in Figure 6.7(a), the Rietveld fit is slightly better by introducing the chloranilic acid phase and gives a lower R_{wp} = 7.61%. The Rietveld fit can be further improved by freely refining the coordinates of Cl atom. This leads to a small distortion of the CA molecule but decreases the value for R_{wp} to 6.28%. Figure 6.7(b) shows the final result of the two-phase Rietveld refinement based on rigid bodies including the refinement of preferred orientation coefficients and internal coordinates of Cl atoms. The slight distortion of CA molecules is also shown as an inset.

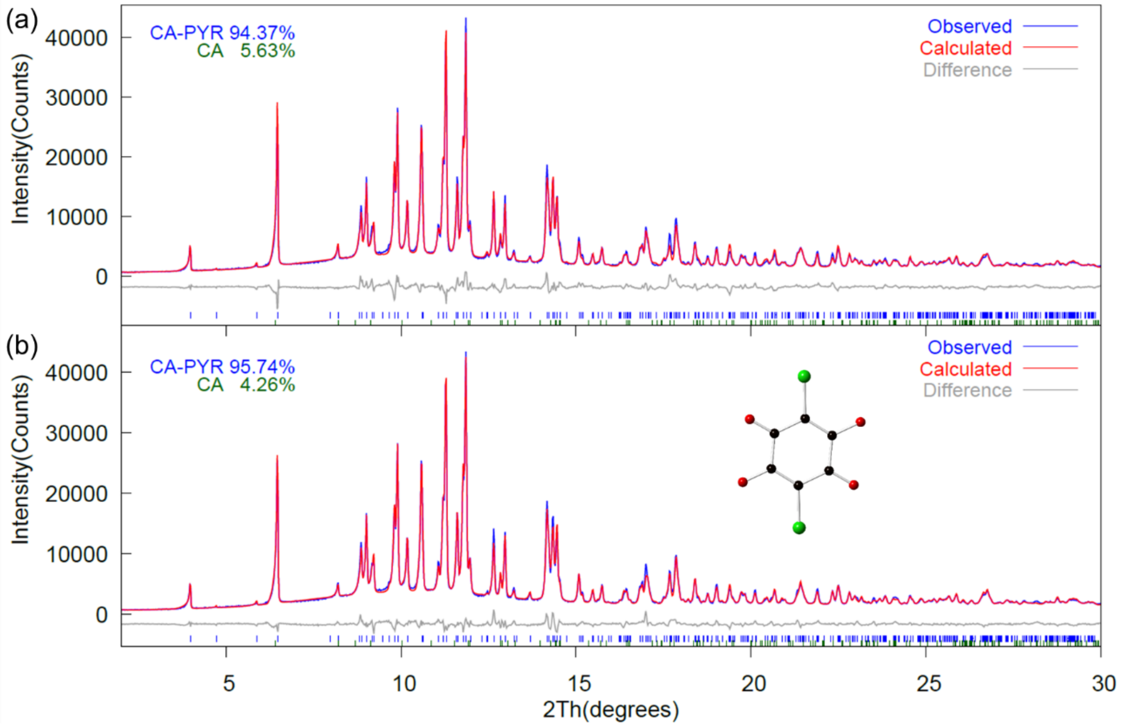

Figure 6.7: Results from two-phase Rietveld refinements based on rigid bodies (a) without refining Cl coordinates (R_{wp} = 7.61%) and (b) with refining Cl coordinates (R_{wp} = 6.28%).

Structure refinement using a restrained approach

We also tried an equivalent refinement but using bond distance and angle restraints to describe the molecules instead of the rigid body language. The molecules were also restrained to be planar using the “flatten” restraint in TOPAS. All the bond lengths and bond angles are restrained to the ideal values based on the previously reported single crystal structures of CA and BEN found in CSD. As shown in Figure 6.8, a restrained refinement gives a slightly better fit and a lower R_{wp} of 5.24%. Similarly, Cl atoms in the CA ring distort relative to the carbon atoms but not markedly.

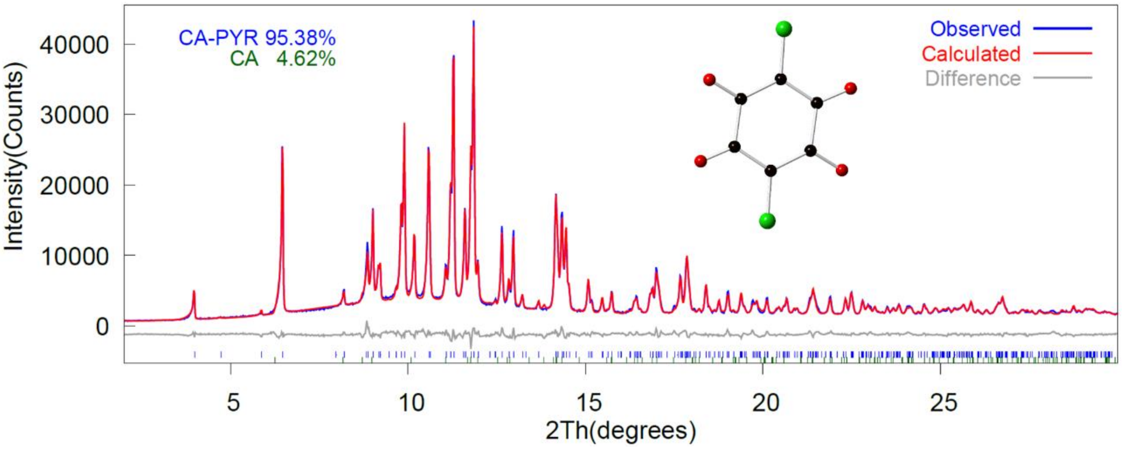

Figure 6.8: Final result of Rietveld refinement using bond distance and angle restraints (R_{wp} = 5.24%).

Test of space group Pc

We carried out the same Rietveld refinement based on rigid bodies but using space group *Pc*. The only difference in the *Pc* structural model is that there are two different benzimidazole molecules and one chloranilic acid molecule in the asymmetric unit. As a result, we need more parameters to describe the extra degrees of freedom. Figure 6.9 shows the results from the Rietveld refinements using the *Pc* description. The *Pc* description gives a comparable Rietveld fit with R_{wp} = 7.58% to the $P2_1/c$ description (R_{wp} = 7.61%) without refining the Cl coordinates. When refining the internal coordinates of Cl atoms, it gives a marginally better fit but CA molecules are more distorted. The distorted CA molecule is shown in Figure 6.9(b) as an insert. The $P2_1/c$ structural model has fewer parameters than the *Pc* description and gives an excellent fit with molecules less distorted. We would suggest the $P2_1/c$ structural model as the optimal structural model for CA-2BEN.

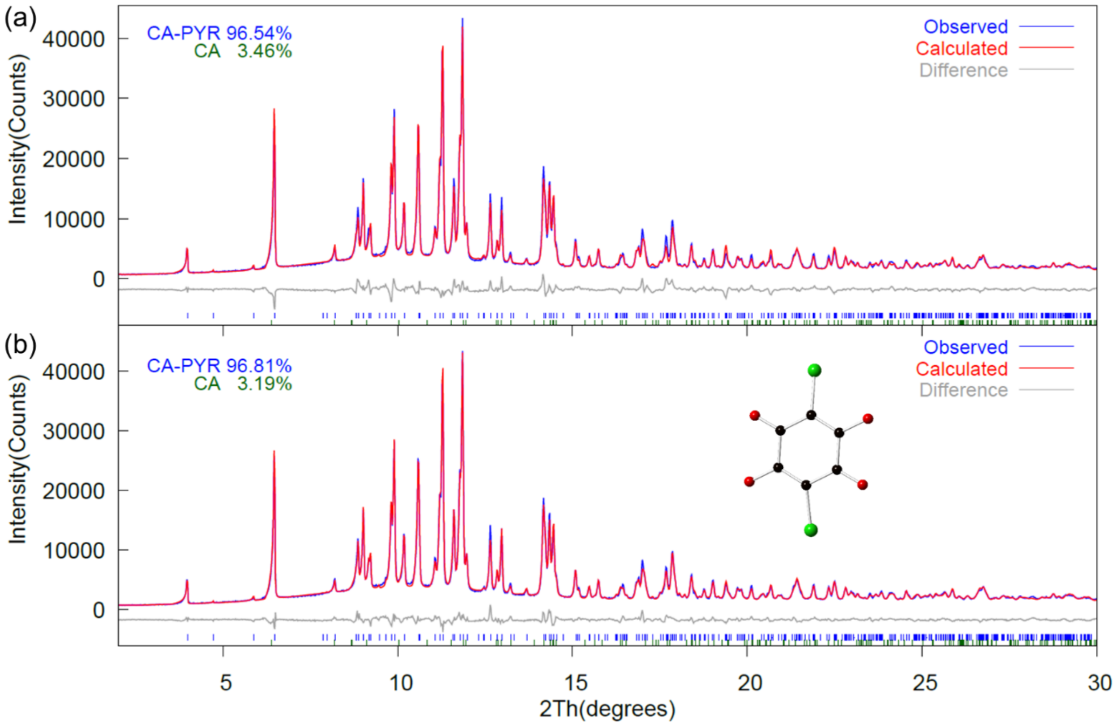

Figure 6.9: Results of the Rietveld refinements based on rigid bodies using space group *Pc* (a) without refining Cl coordinates (R_{wp} = 7.58%) and (b) with refining Cl coordinates (R_{wp} = 5.78%).

6.3.3 Structure solution from single crystal X-ray diffraction data

After the powder diffraction study of section 6.3.2 was completed, we surprisingly identified single crystals of CA-2BEN from an experiment targeting growth of the CA-BEN 1:1 cocrystals. A small amount of rectangular dark-red single crystals of CA-2BEN were grown surprisingly from the dry methanol solution of chloranilic acid and benzimidazole with molar ratio 1:1. A single crystal diffraction experiment was performed on the diffractometer “OD” at 120 K. The crystallographic information is summarised in Table 6.3. Rietveld refinement against PXRD data using the structure determined from single crystal diffraction gave an R_{wp} of 5.24%, as shown in Figure 6.10. Our structure solution from powder diffraction data gives comparable result to that from single crystal diffraction. Single crystal diffraction proves that the structure model from the powder diffraction data is correct, although the CA molecule does not distort in the structure model from single crystal diffraction data. The superimposition of two structures is shown in Figure 6.11. Two structures are almost identical despite the benzimidazole molecules (highlighted using a blue dashed box) are not perfectly superimposed.

Table 6.3: Crystallographic data for the co-crystal of chloranilic acid and benzimidazole with stoichiometry of 1:2 from the single crystal X-ray diffraction.

Chemical formula	$C_{10}H_7C_{11}N_2O_2$
M_r	222.63
Experimental temperature/K	120
Crystal system	Monoclinic
Space group	$P2_1/c$
Z	2
***a*/Å**	10.0608(9)
***b*/Å**	5.2007(2)
***c*/Å**	17.1919(10)
***α*/°**	90
***β*/°**	94.570(7)
***γ*/°**	90
Volume/Å^3	896.67(5)
No. of measured reflections	6585
No. of observed reflections	1134
No. of parameters	136
R, R_w	0.0552, 0.0783
I/Sigma cutoff	2

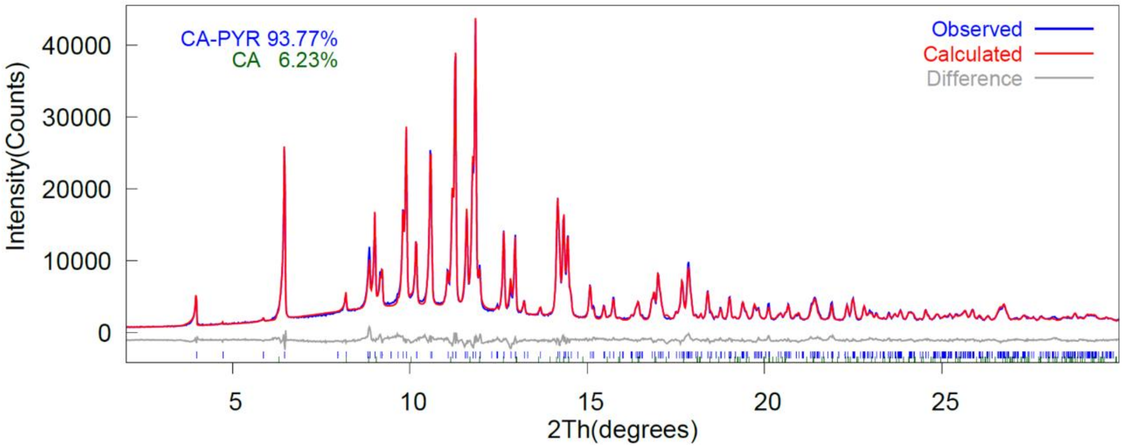

Figure 6.10: Rietveld refinement using the structure model from single crystal X-ray diffraction.

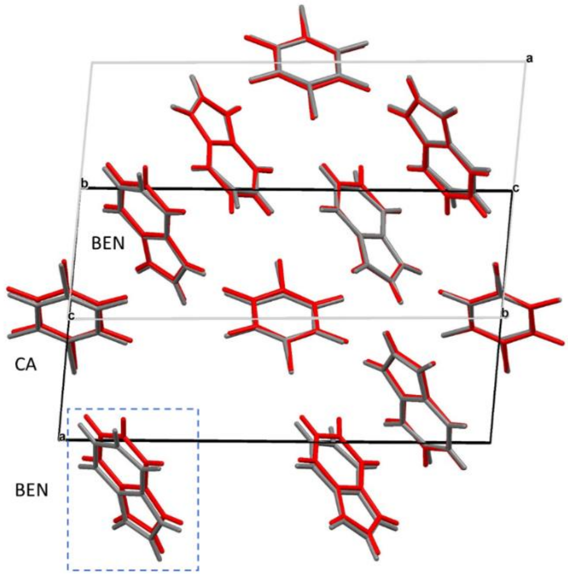

Figure 6.11: Comparison of crystal structures determined from powder and single crystal X-ray diffraction. Molecules in the powder diffraction structural model all shown in grey and molecules in the single crystal structural model all shown in red.

Figure 6.12 displays the crystal structure of CA-2BEN determined by single crystal X-ray diffraction. The protons attached to CA oxygen atoms O5 have transferred onto nitrogen atoms N9 in pyrazole molecules, resulting in the formation of divalent dichloranilate ions and pyrazolium ions. Atoms O1 and O5 participate in the intermolecular hydrogen bonds N7-H71···O1 and N9-H91···O5 respectively. The donor-acceptor distance is 2.712 Å for N7 ···O1 and 2.758 Å for and N9 ···O5. The cations and anions are connected via these strong hydrogen bonds[8], forming one-dimensional molecular chains along the crystallographic *c*-axis.

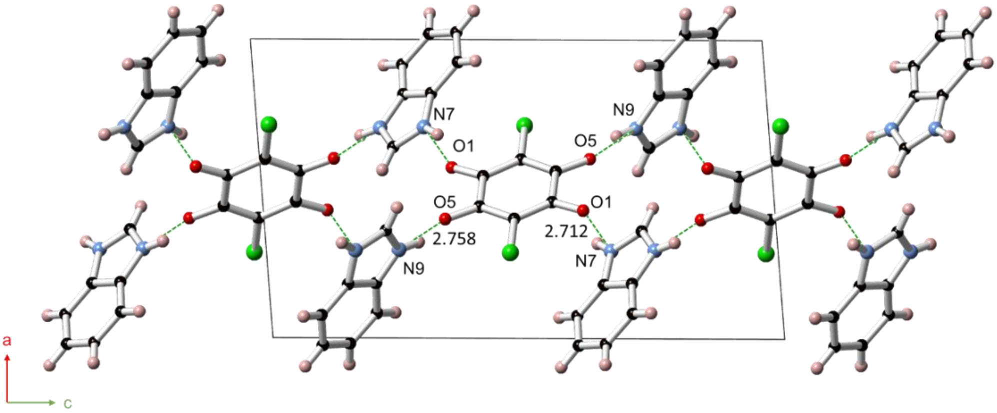

Figure 6.12: Crystal structure of CA-2BEN with atomic numbering scheme viewed down the crystallographic *b*-axis. N-H···O hydrogen bonds drawn as green dash line.

6.4 Conclusions

We attempted to grow cocrystals between CA and PYR or BEN. Only the monohydrate CA-PYR and CA-2BEN cocrystals were successfully prepared. The single crystal X-ray diffraction study on monohydrate CA-PYR indicates that the crystal adopts centrosymmetric space group *C*2/*c* with unit cell *a* = 31.231(2) Å, *b* = 3.7524(3) Å, *c* = 22.3085(14) Å, *β* = 125.217(4)° and V = 2135.88(13) $Å^3$. The structural model helps rationalise why a dehydrated sample cannot be formed. Its centrosymmetric nature precludes ferroelectricity. We also demonstrated the structure solution of CA-2BEN from powder data. Reassuringly for the work in other chapters of the thesis, we find that our powder diffraction based solution is very similar to a later single crystal study. This gave a useful blind confidence test on the methods we have used. Our structural study on CA-2BEN shows that the crystal adopts a centrosymmetric space group $P2_1/c$ with *a* = 10.0608(9) Å, *b* = 5.2007(2) Å, *c* = 17.1919(10) Å, *β* = 94.570(7)° and V = 896.67(5) $Å^3$. CA-2BEN therefore does not show ferroelectricity due to its centrosymmetric nature.

References

1. Horiuchi, S.; Kumai, R.; Tokura, Y., Room-Temperature Ferroelectricity and Gigantic Dielectric Susceptibility on a Supramolecular Architecture of Phenazine and Deuterated Chloranilic Acid. *Journal of the American Chemical Society* **2005,** *127* (14), 5010-5011.
2. Low-Temperature Phase Transitions of an Organic Ferroelectrics, Phenazine–Chloranilic Acid. *Journal of the Physical Society of Japan* **2006,** *75* (3), 033601.
3. Asaji, T.; Seliger, J.; Žagar, V.; Sekiguchi, M.; Watanabe, J.; Gotoh, K.; Ishida, H.; Vrtnik, S.; Dolinšek, J., Phase transition and temperature dependent electronic state of an organic ferroelectric, phenazine–chloranilic acid (1:1). *Journal of Physics: Condensed Matter* **2007,** *19* (22), 226203.
4. Lee, K.; Kolb, B.; Thonhauser, T.; Vanderbilt, D.; Langreth, D. C., Structure and energetics of a ferroelectric organic crystal of phenazine and chloranilic acid. *Physical Review B* **2012,** *86* (10), 104102.
5. Noohinejad, L.; Mondal, S.; Wölfel, A.; Ali, S. I.; Schönleber, A.; van Smaalen, S., Ferroelectricity of Phenazine–Chloranilic Acid at T = 100 K. *Journal of Chemical Crystallography* **2014,** *44* (8), 387-393.
6. Ishida, H.; Kashino, S., 1:2 Complexes of chloranilic acid with pyrazole and imidazole, and the acetonitrile solvate of a 1:1 complex with imidazole. *Acta Crystallographica Section C* **2001,** *57* (4), 476-479.

7. Yang, D.-J.; Qu, S.-H., Benzimidazolium chloranilate monohydrate. *Acta Crystallographica Section E* **2006,** *62* (10), o4720-o4722.

8. Steiner, T., The Hydrogen Bond in the Solid State. *Angewandte Chemie International Edition* **2002,** *41* (1), 48-76.

Appendix I TOPAS file containing the symmetry distortion mode description

The TOPAS file containing the symmetry distortion mode description allows to extract the amplitude of each rotational symmetry modes for CA-Pyz (see section 3.8).

```
r_wp  21.2411736 r_exp  18.1603939 r_p  16.8563402 r_wp_dash  48.0132183 r_p_dash  45.8518803
r_exp_dash  41.0494718 weighted_Durbin_Watson  1.60817238 gof  1.16964278

iters 1000000
chi2_convergence_criteria 0.0001
continue_after_convergence
do_errors

xdd d6b_00803_400K.raw
x_calculation_step = Yobs_dx_at(Xo); convolution_step 4
bkg  @  18.8551688 -1.68069449 -4.28930188  2.46111373  2.66462091 -3.64804513   -0.206494593
1.22990098 -0.446353014 -1.16873301  1.03846091  -0.319246381
LP_Factor(!th2_monochromator, 12.46)
   lam ymin_on_ymax 0.0001
   Lam_recs {1.0  0.709300  0.2695 }
   Zero_Error(zero, 0.00684`_0.00094)

'-----------------------------------------------------------------------------------------------
-------------------------------------------
'Topas .str file generated by ISODISTORT
'-----------------------------------------------------------------------------------------------
-------------------------------------------

'Structure information
str
  space_group P-1
  a  @  4.756179
  b  @  5.833794
  c  @ 10.669387
  al @  82.00990
  be @  81.60171
  ga @  76.83881
  volume @  283.44
  r_bragg  8.04325342
  Phase_Density_g_on_cm3( 1.74038)
  scale  @  1.09823131e-005
  weight_percent  @  72.479

'{{{peak shape spherical harmonic
spherical_harmonics_hkl shpk
sh_order 4
load sh_Cij_prm {
  y00    shpk_c00     0.17354 vcsh
  y20    shpk_c20    -0.13632 vcsh
  y21p   !shpk_c21p   0.000 vcsh
  y21m   !shpk_c21m   0.000 vcsh
  y22p   !shpk_c22p   0.000 vcsh
  y22m   !shpk_c22m   0.000 vcsh
  y40    !shpk_c40    0.000 vcsh
  y41p   !shpk_c41p   0.000 vcsh
  y41m   !shpk_c41m   0.000 vcsh
  y42p   !shpk_c42p   0.000 vcsh
  y42m   !shpk_c42m   0.000 vcsh
  y43p   !shpk_c43p   0.000 vcsh
  y43m   !shpk_c43m   0.000 vcsh
  y44p   shpk_c44p   -0.12480 vcsh
  y44m   shpk_c44m    0.03536 vcsh
}
prm  !eta_sh 1
lor_fwhm = eta_sh*(Max(0.00001,shpk * Tan(Th)));
gauss_fwhm = (1-eta_sh)*(Max(0.00001,shpk * Tan(Th)));
macro vcsh {val_on_continue = Rand(-0.1,0.1); min -1 max 1}
'}}}

'{{{mode definitions
```

```
  prm   !a1     0.000 min  -1.41 max  1.41 'C2/m[0,0,0]GM2+(a)[Cl1:i:dsp] A''(a)
  prm   !a2     0.000 min  -1.41 max  1.41 'C2/m[0,0,0]GM1+(a)[Cl1:i:dsp] A'_1(a)
  prm   !a3     0.000 min  -1.41 max  1.41 'C2/m[0,0,0]GM1+(a)[Cl1:i:dsp] A'_2(a)
  prm   !a4     0.000 min  -1.41 max  1.41 'C2/m[0,0,0]GM2+(a)[C2:i:dsp] A''(a)
  prm   !a5     0.000 min  -1.41 max  1.41 'C2/m[0,0,0]GM1+(a)[C2:i:dsp] A'_1(a)
  prm   !a6     0.000 min  -1.41 max  1.41 'C2/m[0,0,0]GM1+(a)[C2:i:dsp] A'_2(a)
  prm   !a7     0.000 min  -1.41 max  1.41 'C2/m[0,0,0]GM2+(a)[C3:i:dsp] A''(a)
  prm   !a8     0.000 min  -1.41 max  1.41 'C2/m[0,0,0]GM1+(a)[C3:i:dsp] A'_1(a)
  prm   !a9     0.000 min  -1.41 max  1.41 'C2/m[0,0,0]GM1+(a)[C3:i:dsp] A'_2(a)
  prm   !a10    0.000 min  -1.41 max  1.41 'C2/m[0,0,0]GM2+(a)[C4:i:dsp] A''(a)
  prm   !a11    0.000 min  -1.41 max  1.41 'C2/m[0,0,0]GM1+(a)[C4:i:dsp] A'_1(a)
  prm   !a12    0.000 min  -1.41 max  1.41 'C2/m[0,0,0]GM1+(a)[C4:i:dsp] A'_2(a)
  prm   !a13    0.000 min  -1.41 max  1.41 'C2/m[0,0,0]GM2+(a)[O5:i:dsp] A''(a)
  prm   !a14    0.000 min  -1.41 max  1.41 'C2/m[0,0,0]GM1+(a)[O5:i:dsp] A'_1(a)
  prm   !a15    0.000 min  -1.41 max  1.41 'C2/m[0,0,0]GM1+(a)[O5:i:dsp] A'_2(a)
  prm   !a16    0.000 min  -1.41 max  1.41 'C2/m[0,0,0]GM2+(a)[O6:i:dsp] A''(a)
  prm   !a17    0.000 min  -1.41 max  1.41 'C2/m[0,0,0]GM1+(a)[O6:i:dsp] A'_1(a)
  prm   !a18    0.000 min  -1.41 max  1.41 'C2/m[0,0,0]GM1+(a)[O6:i:dsp] A'_2(a)
  prm   !a19    0.000 min  -1.41 max  1.41 'C2/m[0,0,0]GM2+(a)[N7:i:dsp] A''(a)
  prm   !a20    0.000 min  -1.41 max  1.41 'C2/m[0,0,0]GM1+(a)[N7:i:dsp] A'_1(a)
  prm   !a21    0.000 min  -1.41 max  1.41 'C2/m[0,0,0]GM1+(a)[N7:i:dsp] A'_2(a)
  prm   !a22    0.000 min  -2.00 max  2.00 'C2/m[0,0,0]GM2+(a)[C8:j:dsp] A_1(a)
  prm   !a23    0.000 min  -2.00 max  2.00 'C2/m[0,0,0]GM2+(a)[C8:j:dsp] A_2(a)
  prm   !a24    0.000 min  -2.00 max  2.00 'C2/m[0,0,0]GM2+(a)[C8:j:dsp] A_3(a)
  prm   !a25    0.000 min  -2.00 max  2.00 'C2/m[0,0,0]GM1+(a)[C8:j:dsp] A_1(a)
  prm   !a26    0.000 min  -2.00 max  2.00 'C2/m[0,0,0]GM1+(a)[C8:j:dsp] A_2(a)
  prm   !a27    0.000 min  -2.00 max  2.00 'C2/m[0,0,0]GM1+(a)[C8:j:dsp] A_3(a)
  prm   !a28    0.000 min  -2.00 max  2.00 'C2/m[0,0,0]GM2+(a)[H81:j:dsp] A_1(a)
  prm   !a29    0.000 min  -2.00 max  2.00 'C2/m[0,0,0]GM2+(a)[H81:j:dsp] A_2(a)
  prm   !a30    0.000 min  -2.00 max  2.00 'C2/m[0,0,0]GM2+(a)[H81:j:dsp] A_3(a)
  prm   !a31    0.000 min  -2.00 max  2.00 'C2/m[0,0,0]GM1+(a)[H81:j:dsp] A_1(a)
  prm   !a32    0.000 min  -2.00 max  2.00 'C2/m[0,0,0]GM1+(a)[H81:j:dsp] A_2(a)
  prm   !a33    0.000 min  -2.00 max  2.00 'C2/m[0,0,0]GM1+(a)[H81:j:dsp] A_3(a)
  prm   !a34    0.000 min  -1.41 max  1.41 'C2/m[0,0,0]GM2+(a)[H51:i:dsp] A''(a)
  prm   !a35    0.000 min  -1.41 max  1.41 'C2/m[0,0,0]GM1+(a)[H51:i:dsp] A'_1(a)
  prm   !a36    0.000 min  -1.41 max  1.41 'C2/m[0,0,0]GM1+(a)[H51:i:dsp] A'_2(a)

  prm    r1 -0.01790 min  -4.00 max  4.00 vcr 'C2/m[0,0,0]GM2+(a)[He1:d:rot]Bg_1(a)
  prm    r2  0.04848 min  -4.00 max  4.00 vcr 'C2/m[0,0,0]GM2+(a)[He1:d:rot]Bg_2(a)
  prm    r3  0.03232 min  -4.00 max  4.00 vcr 'C2/m[0,0,0]GM1+(a)[He1:d:rot]Ag(a)
  prm    r4  0.22173 min  -4.00 max  4.00 vcr 'C2/m[0,0,0]GM2+(a)[He2:a:rot]Bg_1(a)
  prm    r5 -0.00001 min  -4.00 max  4.00 vcr 'C2/m[0,0,0]GM2+(a)[He2:a:rot]Bg_2(a)
  prm    r6 -0.03804 min  -4.00 max  4.00 vcr 'C2/m[0,0,0]GM1+(a)[He2:a:rot]Ag(a)
macro vcr {val_on_continue = Rand(-0.0001,0.0001);}

penalties_weighting_K1 1
macro aP(a) { penalty = 1 * Ln(Abs(a)+1); }
  aP(a1)
  aP(a2)
  aP(a3)
'}}}

'{{{mode-amplitude to delta transformation
  prm  Cl1_1_dx     = +  0.10627*a1 +  0.08701*a3;:  0.00000
  prm  Cl1_1_dy     = -  0.10627*a1 +  0.08701*a3;:  0.00000
  prm  Cl1_1_dz     = -  0.06432*a2 -  0.01320*a3;: -0.00000
  prm  C2_1_dx      = +  0.10627*a4 +  0.08701*a6;:  0.00000
  prm  C2_1_dy      = -  0.10627*a4 +  0.08701*a6;:  0.00000
  prm  C2_1_dz      = -  0.06432*a5 -  0.01320*a6;: -0.00000
  prm  C3_1_dx      = +  0.10627*a7 +  0.08701*a9;:  0.00000
  prm  C3_1_dy      = -  0.10627*a7 +  0.08701*a9;:  0.00000
  prm  C3_1_dz      = -  0.06432*a8 -  0.01320*a9;: -0.00000
  prm  C4_1_dx      = +  0.10627*a10 +  0.08701*a12;:  0.00000
  prm  C4_1_dy      = -  0.10627*a10 +  0.08701*a12;:  0.00000
  prm  C4_1_dz      = -  0.06432*a11 -  0.01320*a12;: -0.00000
  prm  O5_1_dx      = +  0.10627*a13 +  0.08701*a15;:  0.00000
  prm  O5_1_dy      = -  0.10627*a13 +  0.08701*a15;:  0.00000
  prm  O5_1_dz      = -  0.06432*a14 -  0.01320*a15;: -0.00000
  prm  O6_1_dx      = +  0.10627*a16 +  0.08701*a18;:  0.00000
  prm  O6_1_dy      = -  0.10627*a16 +  0.08701*a18;:  0.00000
  prm  O6_1_dz      = -  0.06432*a17 -  0.01320*a18;: -0.00000
  prm  N7_1_dx      = +  0.10627*a19 +  0.08701*a21;:  0.00000
  prm  N7_1_dy      = -  0.10627*a19 +  0.08701*a21;:  0.00000
  prm  N7_1_dz      = -  0.06432*a20 -  0.01320*a21;: -0.00000
  prm  C8_1_dx      = +  0.06153*a23 +  0.07514*a24 +  0.06153*a26 +  0.07514*a27;:  0.00000
  prm  C8_1_dy      = +  0.06153*a23 -  0.07514*a24 +  0.06153*a26 -  0.07514*a27;:  0.00000
```

```
  prm  C8_1_dz      = -  0.04548*a22 -  0.00934*a23 -  0.04548*a25 -  0.00934*a26;: -0.00000
  prm  C8_2_dx      = +  0.06153*a23 -  0.07514*a24 -  0.06153*a26 +  0.07514*a27;:  0.00000
  prm  C8_2_dy      = +  0.06153*a23 +  0.07514*a24 -  0.06153*a26 -  0.07514*a27;:  0.00000
  prm  C8_2_dz      = -  0.04548*a22 -  0.00934*a23 +  0.04548*a25 +  0.00934*a26;:  0.00000
  prm  H81_1_dx     = +  0.06153*a29 +  0.07514*a30 +  0.06153*a32 +  0.07514*a33;:  0.00000
  prm  H81_1_dy     = +  0.06153*a29 -  0.07514*a30 +  0.06153*a32 -  0.07514*a33;:  0.00000
  prm  H81_1_dz     = -  0.04548*a28 -  0.00934*a29 -  0.04548*a31 -  0.00934*a32;: -0.00000
  prm  H81_2_dx     = +  0.06153*a29 -  0.07514*a30 -  0.06153*a32 +  0.07514*a33;:  0.00000
  prm  H81_2_dy     = +  0.06153*a29 +  0.07514*a30 -  0.06153*a32 -  0.07514*a33;:  0.00000
  prm  H81_2_dz     = -  0.04548*a28 -  0.00934*a29 +  0.04548*a31 +  0.00934*a32;:  0.00000
  prm  H51_1_dx     = +  0.10627*a34 +  0.08701*a36;:  0.00000
  prm  H51_1_dy     = -  0.10627*a34 +  0.08701*a36;:  0.00000
  prm  H51_1_dz     = -  0.06432*a35 -  0.01320*a36;: -0.00000

  prm  He1_1_drlx   = +  0.12305*r2 +  0.15029*r3;: 0.01082
  prm  He1_1_drly   = +  0.12305*r2 -  0.15029*r3;: 0.00111
  prm  He1_1_drlz   = -  0.09097*r1 -  0.01867*r2;: 0.00072
  prm  He2_1_drlx   = +  0.12305*r5 +  0.15029*r6;: -0.00572
  prm  He2_1_drly   = +  0.12305*r5 -  0.15029*r6;: 0.00572
  prm  He2_1_drlz   = -  0.09097*r4 -  0.01867*r5;: -0.02017
'}}}

'{{{distorted parameters
  prm !He1_1_x      = 1/2;:  0.50000
  prm !He1_1_y      = 1/2;:  0.50000
  prm !He1_1_z      = 1/2;:  0.50000
  prm  Cl1_1_x      =    0.21180 + Cl1_1_dx;:  0.21180
  prm  Cl1_1_y      =    0.21180 + Cl1_1_dy;:  0.21180
  prm  Cl1_1_z      =    0.35068 + Cl1_1_dz;:  0.35068
  prm  C2_1_x       =    0.36860 + C2_1_dx;:  0.36860
  prm  C2_1_y       =    0.36860 + C2_1_dy;:  0.36860
  prm  C2_1_z       =    0.43410 + C2_1_dz;:  0.43410
  prm  C3_1_x       =    0.53340 + C3_1_dx;:  0.53340
  prm  C3_1_y       =    0.53340 + C3_1_dy;:  0.53340
  prm  C3_1_z       =    0.36810 + C3_1_dz;:  0.36810
  prm  C4_1_x       =    0.67060 + C4_1_dx;:  0.67060
  prm  C4_1_y       =    0.67060 + C4_1_dy;:  0.67060
  prm  C4_1_z       =    0.43930 + C4_1_dz;:  0.43930
  prm  O5_1_x       =    0.82320 + O5_1_dx;:  0.82320
  prm  O5_1_y       =    0.82320 + O5_1_dy;:  0.82320
  prm  O5_1_z       =    0.37690 + O5_1_dz;:  0.37690
  prm  O6_1_x       =    0.57310 + O6_1_dx;:  0.57310
  prm  O6_1_y       =    0.57310 + O6_1_dy;:  0.57310
  prm  O6_1_z       =    0.25480 + O6_1_dz;:  0.25480
  prm !He2_1_x      = 0;:  0.00000
  prm !He2_1_y      = 0;:  0.00000
  prm !He2_1_z      = 0;:  0.00000
  prm  N7_1_x       =   -0.06510 + N7_1_dx;: -0.06510
  prm  N7_1_y       =   -0.06510 + N7_1_dy;: -0.06510
  prm  N7_1_z       =    0.12450 + N7_1_dz;:  0.12450
  prm  C8_1_x       =   -0.19670 + C8_1_dx;: -0.19670
  prm  C8_1_y       =    0.12810 + C8_1_dy;:  0.12810
  prm  C8_1_z       =    0.06370 + C8_1_dz;:  0.06370
  prm  C8_2_x       =   -0.12810 + C8_2_dx;: -0.12810
  prm  C8_2_y       =    0.19670 + C8_2_dy;:  0.19670
  prm  C8_2_z       =   -0.06370 + C8_2_dz;: -0.06370
  prm  H81_1_x      =   -0.34710 + H81_1_dx;: -0.34710
  prm  H81_1_y      =    0.22530 + H81_1_dy;:  0.22530
  prm  H81_1_z      =    0.10600 + H81_1_dz;:  0.10600
  prm  H81_2_x      =   -0.22530 + H81_2_dx;: -0.22530
  prm  H81_2_y      =    0.34710 + H81_2_dy;:  0.34710
  prm  H81_2_z      =   -0.10600 + H81_2_dz;: -0.10600
  prm  H51_1_x      =    0.82600 + H51_1_dx;:  0.82600
  prm  H51_1_y      =    0.82600 + H51_1_dy;:  0.82600
  prm  H51_1_z      =    0.30500 + H51_1_dz;:  0.30500

  prm  He1_1_rlx    = 0  + He1_1_drlx;:  0.01082
  prm  He1_1_rly    = 0  + He1_1_drly;:  0.00111
  prm  He1_1_rlz    = 0  + He1_1_drlz;:  0.00072
  prm  He2_1_rlx    = 0  + He2_1_drlx;: -0.00572
  prm  He2_1_rly    = 0  + He2_1_drly;:  0.00572
  prm  He2_1_rlz    = 0  + He2_1_drlz;: -0.02017

'occupancy of each atom
  prm !He1_1_occ    = 1;:  1.00000
  prm !Cl1_1_occ    = 1;:  1.00000
```

```
  prm !C2_1_occ     = 1;:  1.00000
  prm !C3_1_occ     = 1;:  1.00000
  prm !C4_1_occ     = 1;:  1.00000
  prm !O5_1_occ     = 1;:  1.00000
  prm !O6_1_occ     = 1;:  1.00000
  prm !He2_1_occ    = 1;:  1.00000
  prm !N7_1_occ     = 1;:  1.00000
  prm !C8_1_occ     = 1;:  1.00000
  prm !C8_2_occ     = 1;:  1.00000
  prm !H81_1_occ    = 1;:  1.00000
  prm !H81_2_occ    = 1;:  1.00000
  prm !H51_1_occ    = 1;:  1.00000
'}}}

'{{{rigid body info
        'rotation angles in radians and degrees
        metrictensor()
        prm  He1_1_angrad = vectorlength(He1_1_rlx, He1_1_rly, He1_1_rlz);:  0.06115
        prm  He1_1_angdeg = He1_1_angrad*radian;:  3.50347
        prm  He2_1_angrad = vectorlength(He2_1_rlx, He2_1_rly, He2_1_rlz);:  0.21706
        prm  He2_1_angdeg = He2_1_angrad*radian;:  12.43640

        'dummy atom positions relative to rigid-body centers
        prm  Q_He1_1_na = He1_1_rlx/He1_1_angrad;: 0.17699
        prm  Q_He1_1_nb = He1_1_rly/He1_1_angrad;: 0.01811
        prm  Q_He1_1_nc = He1_1_rlz/He1_1_angrad;: 0.01183
        prm  Q_He2_1_na = He2_1_rlx/He2_1_angrad;: -0.02635
        prm  Q_He2_1_nb = He2_1_rly/He2_1_angrad;: 0.02633
        prm  Q_He2_1_nc = He2_1_rlz/He2_1_angrad;: -0.09293

        rigid
        point_for_site He1_1   ua = He1_1_x;   ub = He1_1_y;    uc = He1_1_z;
        point_for_site Q_He1_1 ua = Q_He1_1_na+He1_1_x; ub = Q_He1_1_nb+He1_1_y; uc =
Q_He1_1_nc+He1_1_z;
        point_for_site Cl1_1   ua = Cl1_1_x;   ub = Cl1_1_y;    uc = Cl1_1_z;
        point_for_site C2_1    ua = C2_1_x;    ub = C2_1_y;     uc = C2_1_z;
        point_for_site C3_1    ua = C3_1_x;    ub = C3_1_y;     uc = C3_1_z;
        point_for_site C4_1    ua = C4_1_x;    ub = C4_1_y;     uc = C4_1_z;
        point_for_site O5_1    ua = O5_1_x;    ub = O5_1_y;     uc = O5_1_z;
        point_for_site O6_1    ua = O6_1_x;    ub = O6_1_y;     uc = O6_1_z;
        point_for_site H51_1   ua = H51_1_x;    ub = H51_1_y;    uc = H51_1_z;
        Rotate_about_points( =He1_1_angdeg;:3.50347, He1_1, Q_He1_1)

        rigid
        point_for_site He2_1 ua = He2_1_x; ub = He2_1_y; uc = He2_1_z;
        point_for_site Q_He2_1 ua = Q_He2_1_na+He2_1_x; ub = Q_He2_1_nb+He2_1_y; uc =
Q_He2_1_nc+He2_1_z;
        point_for_site N7_1    ua = N7_1_x;     ub = N7_1_y;     uc = N7_1_z;
        point_for_site C8_1    ua = C8_1_x;     ub = C8_1_y;     uc = C8_1_z;
        point_for_site C8_2    ua = C8_2_x;     ub = C8_2_y;     uc = C8_2_z;
        point_for_site H81_1   ua = H81_1_x;    ub = H81_1_y;    uc = H81_1_z;
        point_for_site H81_2   ua = H81_2_x;    ub = H81_2_y;    uc = H81_2_z;
        Rotate_about_points( =He2_1_angdeg;:12.43640, He2_1, Q_He2_1)
'}}}

'{{{mode-dependent sites
        site He1_1    x  0.50000 y  0.50000 z  0.50000 occ He = He1_1_occ;  beq  bval1  5.35148
        site Q_He1_1  x  0.67699 y  0.51811 z  0.51183 occ H   0            beq  bval1  5.35148
        site Cl1_1    x  0.21065 y  0.22766 z  0.34204 occ Cl = Cl1_1_occ;  beq  bval1  5.35148
        site C2_1     x  0.36818 y  0.37559 z  0.43017 occ C  = C2_1_occ;   beq  bval1  5.35148
        site C3_1     x  0.52676 y  0.54790 z  0.36855 occ C  = C3_1_occ;   beq  bval1  5.35148
        site C4_1     x  0.66451 y  0.67754 z  0.44387 occ C  = C4_1_occ;   beq  bval1  5.35148
        site O5_1     x  0.81130 y  0.83723 z  0.38552 occ O  = O5_1_occ;   beq  bval1  5.35148
        site O6_1     x  0.56055 y  0.60008 z  0.25595 occ O  = O6_1_occ;   beq  bval1  5.35148
        site He2_1    x  0.00000 y  0.00000 z  0.00000 occ He = He2_1_occ;  beq  bval1  5.12242
        site Q_He2_1  x -0.02635 y  0.02633 z -0.09293 occ H   0            beq  bval2  5.12242
        site N7_1     x -0.07592 y -0.04554 z  0.12551 occ N  = N7_1_occ;   beq  bval2  5.12242
        site C8_1     x -0.16291 y  0.15594 z  0.05992 occ C  = C8_1_occ;   beq  bval2  5.12242
        site C8_2     x -0.08264 y  0.20405 z -0.06857 occ C  = C8_2_occ;   beq  bval2  5.12242
        site H81_1    x -0.28812 y  0.27429 z  0.09940 occ H  = H81_1_occ;  beq  bval2  5.12242
        site H81_2    x -0.14462 y  0.36014 z -0.11465 occ H  = H81_2_occ;  beq  bval2  5.12242
        site H51_1    x  0.81078 y  0.84791 z  0.31344 occ H  = H51_1_occ;  beq  bval2  5.12242
'}}}

'{{{macros for calculations involving the lattice parameters
        macro straincell(pa0, pb0, pc0, pal0, pbe0, pga0)
```

```
        {
                prm  !radian  57.2957795
                prm  palpha0 = pal0/radian;
                prm  pbeta0  = pbe0/radian;
                prm  pgamma0 = pga0/radian;
                'parent-lattice basis vectors in cartesian coords
                prm  zzz  = (Cos(palpha0)- Cos(pbeta0)*Cos(pgamma0))/Sin(pgamma0);
                prm  a0x = pa0;
                prm  b0x = pb0*Cos(pgamma0);
                prm  b0y = pb0*Sin(pgamma0);
                prm  c0x = pc0*Cos(pbeta0);
                prm  c0y = pc0*zzz;
                prm  c0z = pc0*Sqrt(1 - Cos(pbeta0)^2 - zzz^2);
        }
'Use basis-transformation matrix to transform from parent-cell to supercell parameters
        macro celltransform(t11, t12, t13, t21, t22, t23, t31, t32, t33)
        {
                prm  !radian  57.2957795

                'parent-lattice basis vectors in cartesian coords
                prm  pv11 = a0x*(pe1 + 1);
                prm  pv21 = a0x*(pe6/2);
                prm  pv31 = a0x*(pe5/2);
                prm  pv12 = b0x*(pe1 + 1) + b0y*(pe6/2);
                prm  pv22 = b0x*(pe6/2)   + b0y*(pe2 + 1);
                prm  pv32 = b0x*(pe5/2)   + b0y*(pe4/2);
                prm  pv13 = c0x*(pe1 + 1) + c0y*(pe6/2) + c0z*(pe5/2);
                prm  pv23 = c0x*(pe6/2)+ c0y*(pe2 + 1) + c0z*(pe4/2);
                prm  pv33 = c0x*(pe5/2)   + c0y*(pe4/2) + c0z*(pe3 + 1);

                'supercell basis vectors in cartesian coords
                prm  sv11 = (t11)*pv11 + (t12)*pv12 + (t13)*pv13;
                prm  sv21 = (t11)*pv21 + (t12)*pv22 + (t13)*pv23;
                prm  sv31 = (t11)*pv31 + (t12)*pv32 + (t13)*pv33;
                prm  sv12 = (t21)*pv11 + (t22)*pv12 + (t23)*pv13;
                prm  sv22 = (t21)*pv21 + (t22)*pv22 + (t23)*pv23;
                prm  sv32 = (t21)*pv31 + (t22)*pv32 + (t23)*pv33;
                prm  sv13 = (t31)*pv11 + (t32)*pv12 + (t33)*pv13;
                prm  sv23 = (t31)*pv21 + (t32)*pv22 + (t33)*pv23;
                prm  sv33 = (t31)*pv31 + (t32)*pv32 + (t33)*pv33;

                'distorted supercell parameters
                prm  sa = Sqrt(sv11^2+sv21^2+sv31^2);
                prm  sb = Sqrt(sv12^2+sv22^2+sv32^2);
                prm  sc = Sqrt(sv13^2+sv23^2+sv33^2);
                prm  salpha = ArcCos((sv12*sv13+sv22*sv23+sv32*sv33)/(sb*sc));
                prm  sbeta  = ArcCos((sv11*sv13+sv21*sv23+sv31*sv33)/(sa*sc));
                prm  sgamma = ArcCos((sv11*sv12+sv21*sv22+sv31*sv32)/(sa*sb));
                prm  sal = salpha*radian;
                prm  sbe = sbeta*radian;
                prm  sga = sgamma*radian;
        }

        macro metrictensor()
        {
                prm  !radian  57.2957795
                prm   ra = Get(a);
                prm   rb = Get(b);
                prm   rc = Get(c);
                prm   ralpha = Get(al)/radian;
                prm   rbeta  = Get(be)/radian;
                prm   rgamma = Get(ga)/radian;
                prm   rrr  = (Cos(ralpha) - Cos(rbeta)*Cos(rgamma))/Sin(rgamma);

                prm   basis11 = ra;
                prm  !basis21  0
                prm  !basis31  0
                prm   basis12 = rb*Cos(rgamma);
                prm   basis22 = rb*Sin(rgamma);
                prm  !basis32  0
                prm   basis13 = rc*Cos(rbeta);
                prm   basis23 = rc*rrr;
                prm   basis33 = rc*Sqrt(1 - Cos(rbeta)^2 - rrr^2);

                prm  g11 = basis11*basis11 + basis12*basis12 + basis13*basis13;
                prm  g21 = basis21*basis11 + basis22*basis12 + basis23*basis13;
```

```
                prm  g31 = basis31*basis11 + basis32*basis12 + basis33*basis13;
                prm  g12 = basis11*basis21 + basis12*basis22 + basis13*basis23;
                prm  g22 = basis21*basis21 + basis22*basis22 + basis23*basis23;
                prm  g32 = basis31*basis21 + basis32*basis22 + basis33*basis23;
                prm  g13 = basis11*basis31 + basis12*basis32 + basis13*basis33;
                prm  g23 = basis21*basis31 + basis22*basis32 + basis23*basis33;
                prm  g33 = basis31*basis31 + basis32*basis32 + basis33*basis33;
        }

        macro vectorlength(vlx, vly, vlz)
        {
                Max(Sqrt(g11*vlx^2 + g12*vlx*vly + g21*vlx*vly + g22*vly^2 + g13*vlx*vlz +
g31*vlx*vlz + g23*vly*vlz + g32*vly*vlz + g33*vlz^2), 0.000001)
        }
'}}}

'{{{impurity structure
str
  phase_name "Ice 1h"
  a @ 4.496761 min 4.40 max 4.55
  b @ 4.496761 min 4.40 max 4.55
  c @ 7.324512 min 7.20 max 7.40
  al 90.
  be 90.
  ga 120.
  volume  128.265
  space_group "P63/mmc"
  site O1 x =1/3; y =2/3; z 0.0618 occ O 1. beq  !bvali  2.00000 min 0 max 20
  site H1 x =1/3; y =2/3; z 0.1980 occ H 0.5 beq !bvali  2.00000 min 0 max 20
  site H2 x 0.437 y 0.874 z 0.028  occ H 0.5 beq !bvali  2.00000 min 0 max 20
  scale  scal_ice  3.41187753e-005`_1.336e-006
  r_bragg  5.10745452
  Phase_Density_g_on_cm3( 0.93291)
  weight_percent !perc_ice  24.716
  Strain_L(!strain_ice, 0.76)
'}}}

'{{{common structural information
for strs {
TCHZ_Peak_Type(pku, -0.02133, pkv, 0.00237, pkw, 0.00053, !pkz, 0.000, pky, 0.00010, !pkx,
0.000)
Simple_Axial_Model(axial, 6.65146)
}
'}}}
```

Appendix II Strain mode description and thermal expansion indicatrices

TOPAS file containing the strain mode description

The TOPAS file allows to extract the strain mode description for CA-Pyz (see section 3.9) in order to describe the cell parameter changes relative to the 300 K cell.

```
only_penalties
chi2_convergence_criteria 0.00000000001
num_runs 46

#list Temperature aval bval cval alval beval gaval {
'{{{cells from Diamond 4K data sets
  180.00000     4.80386     5.82532     10.73207   81.92427    81.60365    77.26423
  184.00000     4.80676     5.82369     10.73606   81.91890    81.59809    77.28604
  188.00000     4.81063     5.82167     10.73986   81.91142    81.59179    77.30866
  192.00000     4.81506     5.81888     10.74518   81.90502    81.58418    77.33650
  196.00000     4.81960     5.81574     10.75088   81.89710    81.56738    77.36238
  200.00000     4.82436     5.81253     10.75704   81.88676    81.55456    77.38817
  204.00000     4.82954     5.80843     10.76364   81.87485    81.53762    77.41274
  208.00000     4.83570     5.80359     10.77048   81.86346    81.51624    77.43814
  212.00000     4.84217     5.79814     10.77810   81.85224    81.49370    77.46195
  216.00000     4.84968     5.79153     10.78660   81.83734    81.46142    77.48397
  220.00000     4.85782     5.78411     10.79545   81.82169    81.42898    77.50543
  224.00000     4.86709     5.77517     10.80529   81.80231    81.39183    77.52659
  228.00000     4.87754     5.76474     10.81623   81.78224    81.34410    77.54318
  232.00000     4.88988     5.75212     10.82832   81.76110    81.28655    77.55612
  236.00000     4.90369     5.73713     10.84189   81.73637    81.22230    77.56840
  240.00000     4.92111     5.71832     10.85737   81.70377    81.14526    77.56829
  244.00000     4.94355     5.69335     10.87616   81.67998    81.03158    77.55999
  248.00000     4.97311     5.65944     10.89802   81.63370    80.89830    77.54223
  252.00000     5.00443     5.62379     10.91765   81.57991    80.80147    77.52323
  256.00000     5.03237     5.59336     10.93214   81.52914    80.74805    77.50139
  260.00000     5.05987     5.56377     10.94467   81.47398    80.71492    77.48165
  264.00000     5.08591     5.53691     10.95447   81.42340    80.69709    77.47164
  268.00000     5.11034     5.51137     10.96140   81.37521    80.70141    77.46482
  272.00000     5.13549     5.48654     10.96835   81.32563    80.71396    77.46048
  276.00000     5.16074     5.46163     10.97369   81.27959    80.73241    77.46108
  280.00000     5.18765     5.43537     10.97837   81.22258    80.76315    77.46249
  284.00000     5.21626     5.40765     10.98217   81.16800    80.80154    77.46642
  288.00000     5.24944     5.37534     10.98489   81.10519    80.86099    77.47723
  292.00000     5.27886     5.34772     10.98598   81.04913    80.92183    77.48993
  296.00000     5.29385     5.33567     10.98574   81.03941    80.94824    77.50825
  300.00000     5.30393     5.32795     10.98612   81.02954    80.97363    77.53056
  304.00000     5.30949     5.32483     10.98569   81.04205    80.98461    77.55011
  308.00000     5.31246     5.32477     10.98563   81.04700    80.99825    77.57420
  312.00000     5.31490     5.32502     10.98558   81.04706    81.01656    77.59111
  316.00000     5.31792     5.32499     10.98548   81.05263    81.03351    77.61386
  320.00000     5.32072     5.32514     10.98552   81.06548    81.04261    77.63962
  324.00000     5.32287     5.32593     10.98523   81.07662    81.05441    77.66104
  328.00000     5.32715     5.32476     10.98486   81.06860    81.08436    77.68149
  332.00000     5.32883     5.32604     10.98448   81.08262    81.09562    77.70646
  336.00000     5.33040     5.32771     10.98417   81.09149    81.10876    77.72821
  340.00000     5.33202     5.32935     10.98358   81.10112    81.12178    77.74889
  344.00000     5.33346     5.33088     10.98325   81.11340    81.13423    77.77212
  348.00000     5.33514     5.33220     10.98282   81.12594    81.14394    77.79281
  352.00000     5.33653     5.33411     10.98239   81.13587    81.15706    77.81461
  356.00000     5.33864     5.33492     10.98208   81.15179    81.17247    77.84009
  360.00000     5.33970     5.33700     10.98169   81.16563    81.18536    77.86543
  }
'}}}

      prm !a_expt  =aval(Run_Number);:4.80386
      prm !b_expt  =bval(Run_Number);:5.82532
      prm !c_expt  =cval(Run_Number);:10.73207
      prm !al_expt =alval(Run_Number);:81.94000
      prm !be_expt =beval(Run_Number);:81.60000
      prm !ga_expt =gaval(Run_Number);:77.25000

      'refine strain mode
```

```
                prm s1 -0.13617 min -0.9 max 0.90 'C2/m[0,0,0]GM2+(a)strain_1(a)
                prm s2 -0.01541 min -0.9 max 0.90 'C2/m[0,0,0]GM2+(a)strain_2(a)
                prm s3 -0.00364 min -0.9 max 0.90 'C2/m[0,0,0]GM1+(a)strain_1(a)
                prm s4  0.01629 min -0.9 max 0.90 'C2/m[0,0,0]GM1+(a)strain_2(a)
                prm s5 -0.00339 min -0.9 max 0.90 'C2/m[0,0,0]GM1+(a)strain_3(a)
                prm s6 -0.02012 min -0.9 max 0.90 'C2/m[0,0,0]GM1+(a)strain_4(a)

                'unitless parent cell strains (in lattice rather than orthogonal coords)
                prm  pe1 = +  1.00000*s3;: -0.00364`
                prm  pe2 = +  1.00000*s5;: -0.00339`
                prm  pe3 = +  1.00000*s6;: -0.02012`
                prm  pe4 = +  1.41421*s2;: -0.02179`
                prm  pe5 = +  1.41421*s4;:  0.02304`
                prm  pe6 = +  1.41421*s1;: -0.19258`

                straincell(8.30522,6.70931,10.98169,90.00000,101.37400,90.00000)
                celltransform(0.5,0.5,0,0.5,-0.5,0,0,0,-1)

                penalty = (a_expt  - sa )^2;: 2.59175161e-013`
                penalty = (b_expt  - sb )^2;: 4.60204234e-015`
                penalty = (c_expt  - sc )^2;: 1.23121232e-012`
                penalty = (al_expt - sal)^2;: 3.10642799e-013`
                penalty = (be_expt - sbe)^2;: 1.71760298e-013`
                penalty = (ga_expt - sga)^2;: 3.21786969e-014`

                prm     cell_a  = sa;:    4.80000
                prm     cell_b  = sb;:    5.80000
                prm     cell_c  = sc;:   10.73000
                prm     cell_al = sal;:  81.94000
                prm     cell_be = sbe;:  81.60000
                prm     cell_ga = sga;:  77.25000

'{{{macros for calculations involving the lattice parameters

        'Takes non-refinable undistorted cell parameters, and variable strains as input.
        'Returns strained cell parameters
        macro straincell(pa0, pb0, pc0, pal0, pbe0, pga0)
        {
                prm  !radian  57.2957795
                prm  palpha0 = pal0/radian;
                prm  pbeta0  = pbe0/radian;
                prm  pgamma0 = pga0/radian;
                'parent-lattice basis vectors in cartesian coords
                prm  zzz  = (Cos(palpha0)- Cos(pbeta0)*Cos(pgamma0))/Sin(pgamma0);
                prm  a0x = pa0;
                prm  b0x = pb0*Cos(pgamma0);
                prm  b0y = pb0*Sin(pgamma0);
                prm  c0x = pc0*Cos(pbeta0);
                prm  c0y = pc0*zzz;
                prm  c0z = pc0*Sqrt(1 - Cos(pbeta0)^2 - zzz^2);
        }

        'Use basis-transformation matrix to transform from parent-cell to supercell parameters
        macro celltransform(t11, t12, t13, t21, t22, t23, t31, t32, t33)
        {
                prm  !radian  57.2957795

                'parent-lattice basis vectors in cartesian coords
                prm  pv11 = a0x*(pe1 + 1);
                prm  pv21 = a0x*(pe6/2);
                prm  pv31 = a0x*(pe5/2);
                prm  pv12 = b0x*(pe1 + 1) + b0y*(pe6/2);
                prm  pv22 = b0x*(pe6/2)   + b0y*(pe2 + 1);
                prm  pv32 = b0x*(pe5/2)   + b0y*(pe4/2);
                prm  pv13 = c0x*(pe1 + 1) + c0y*(pe6/2) + c0z*(pe5/2);
                prm  pv23 = c0x*(pe6/2)+ c0y*(pe2 + 1) + c0z*(pe4/2);
                prm  pv33 = c0x*(pe5/2)   + c0y*(pe4/2) + c0z*(pe3 + 1);

                'supercell basis vectors in cartesian coords
                prm  sv11 = (t11)*pv11 + (t12)*pv12 + (t13)*pv13;
                prm  sv21 = (t11)*pv21 + (t12)*pv22 + (t13)*pv23;
                prm  sv31 = (t11)*pv31 + (t12)*pv32 + (t13)*pv33;
                prm  sv12 = (t21)*pv11 + (t22)*pv12 + (t23)*pv13;
                prm  sv22 = (t21)*pv21 + (t22)*pv22 + (t23)*pv23;
                prm  sv32 = (t21)*pv31 + (t22)*pv32 + (t23)*pv33;
                prm  sv13 = (t31)*pv11 + (t32)*pv12 + (t33)*pv13;
```

```
                prm  sv23 = (t31)*pv21 + (t32)*pv22 + (t33)*pv23;
                prm  sv33 = (t31)*pv31 + (t32)*pv32 + (t33)*pv33;

                'distorted supercell parameters
                prm  sa = Sqrt(sv11^2+sv21^2+sv31^2);
                prm  sb = Sqrt(sv12^2+sv22^2+sv32^2);
                prm  sc = Sqrt(sv13^2+sv23^2+sv33^2);
                prm  salpha = ArcCos((sv12*sv13+sv22*sv23+sv32*sv33)/(sb*sc));
                prm  sbeta  = ArcCos((sv11*sv13+sv21*sv23+sv31*sv33)/(sa*sc));
                prm  sgamma = ArcCos((sv11*sv12+sv21*sv22+sv31*sv32)/(sa*sb));
                prm  sal = salpha*radian;
                prm  sbe = sbeta*radian;
                prm  sga = sgamma*radian;
        }

        macro metrictensor()
        {
                prm  !radian  57.2957795
                prm   ra = Get(a);
                prm   rb = Get(b);
                prm   rc = Get(c);
                prm   ralpha = Get(al)/radian;
                prm   rbeta  = Get(be)/radian;
                prm   rgamma = Get(ga)/radian;
                prm   rrr  = (Cos(ralpha) - Cos(rbeta)*Cos(rgamma))/Sin(rgamma);

                prm   basis11 = ra;
                prm  !basis21  0
                prm  !basis31  0
                prm   basis12 = rb*Cos(rgamma);
                prm   basis22 = rb*Sin(rgamma);
                prm  !basis32  0
                prm   basis13 = rc*Cos(rbeta);
                prm   basis23 = rc*rrr;
                prm   basis33 = rc*Sqrt(1 - Cos(rbeta)^2 - rrr^2);

                prm  g11 = basis11*basis11 + basis12*basis12 + basis13*basis13;
                prm  g21 = basis21*basis11 + basis22*basis12 + basis23*basis13;
                prm  g31 = basis31*basis11 + basis32*basis12 + basis33*basis13;
                prm  g12 = basis11*basis21 + basis12*basis22 + basis13*basis23;
                prm  g22 = basis21*basis21 + basis22*basis22 + basis23*basis23;
                prm  g32 = basis31*basis21 + basis32*basis22 + basis33*basis23;
                prm  g13 = basis11*basis31 + basis12*basis32 + basis13*basis33;
                prm  g23 = basis21*basis31 + basis22*basis32 + basis23*basis33;
                prm  g33 = basis31*basis31 + basis32*basis32 + basis33*basis33;
        }

        macro vectorlength(vlx, vly, vlz)
        {
                Max(Sqrt(g11*vlx^2 + g12*vlx*vly + g21*vlx*vly + g22*vly^2 + g13*vlx*vlz +
g31*vlx*vlz + g23*vly*vlz + g32*vly*vlz + g33*vlz^2), 0.000001)
        }
'}}}
```

Thermal expansion indicatrices for Γ_1^+ only and Γ_2^+ only.

Table 3.9: Irrep-specific thermal expansions (left) over the 250–300 K range, along principal axes X_1–X_3, ordered from lowest (X1) to highest (X3) values, and overall volume expansion.

Axes	**Thermal expansion (10^{-6} K−1) along principal axes**		**Principal axis components for Γ_1^+ only expansion**			**Principal axis components Γ_2^+ only expansion**		
	Γ_1^+	Γ_2^+	*a*	*b*	*c*	*a*	*b*	*c*
X_1	−34	−1345	0.69	0.68	-0.26	–0.09	0.99	–0.05
X_2	−33	−18	0.70	-0.71	0.00	-0.07	-0.07	1.00
X_3	+205	+1552	0.38	0.38	0.84	-0.99	0.10	0.05
Volume	+138	+88						

Appendix III Temperature calibration for powder X-ray diffraction

A 1:4 by weight mixture of Al and DC-MBI powders was loaded into the capillary. Variable temperature PXRD patterns were collected over the temperature range of 100 – 300 K on the diffractometer "d9" configured with an Oxford cryosystems PheniX cryostat in order to accurately calibrate the true sample temperature.

Experiment	**Process**	**T range**	**Ramp rate**	**No. of runs**	**Total time**
d9_07767	warming	100K-500K	10 K/hour	84	40.8 hours
d9_07768	cooling	500K-100K	10 K/hour	84	40.8 hours

The Ideal value of the unit cell parameter was calculated at each temperature by an Einstein-like expression[6]:

$$\ln\left(\frac{a_i}{a_0}\right) = \sum_{j=1}^{n} \frac{X_j \theta_j}{\exp\left(\theta_j / T\right) - 1}$$

where a_i is cell parameter at temperature T, a_0 is cell parameter at 0 K, X_j is an empirically derived coefficient and θ_j is an Einstein temperature. The magnitude of each coefficient used in the equation are summarised in the following table:

Coefficients	**Al**
a_0/Å	4.03257
X_1/K^{-1}	2.19967E-06
θ_1/K	200
X_2/K^{-1}	7.97758E-06
θ_2/K	1100

Figure 1 shows the difference between the experimental and the calculated unit cell parameter of Al. The difference between the experimental and calculated values stays almost constant (~ 0.0005 Å) at between 150 K and 300 K, which means the real experimental temperature is very close to the set temperature over this temperature range. We therefore compare the unit cell parameters of DC-MBI extracted from "d9" data to that from "d6" data. Over the temperature range of 100 – 300 K, unit cell parameters from both data sets show good agreements. This suggests that the unit cell parameters showed in the main context are reliable.

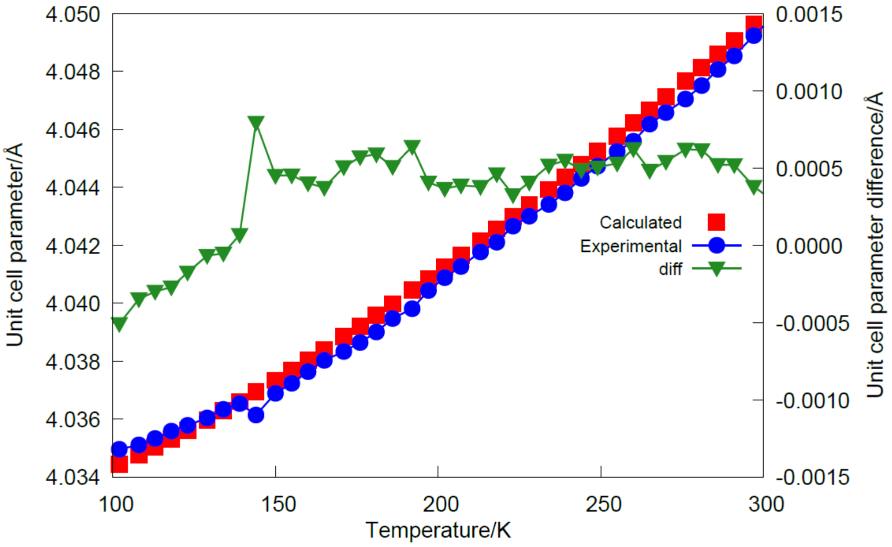

Figure 1: Temperature dependence of calculated and experimental unit cell parameters of Al obtained on the "d9".

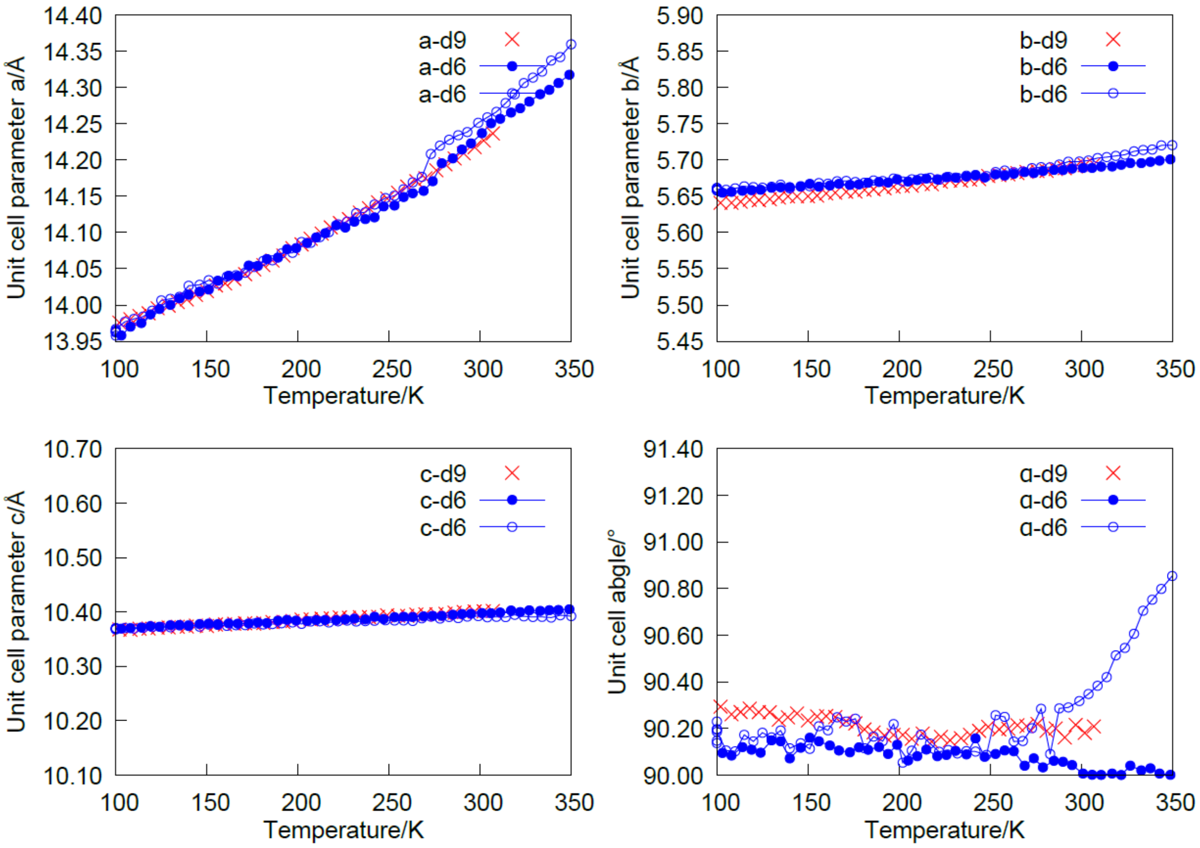

Figure 2: Comparisons of unit cell parameters obtained from the "d6" data and the "d9" data.

Appendix IV Active rotational and translational symmetry modes for each subgroup candidate

ISODISTORT was used to calculate a tree of all possible intermediate subgroups that lie between the hypothetical *Pbcm* parent and the child *P*1 base structure for DC-MBI. The active rotational and translational symmetry modes for each subgroup are summarised in the following table.

Table 1: Active rotational symmetry modes for each subgroup candidate

Space group No.	**Rotational symmetry modes needed**
#1 *Pbcm*	r1-GM1+
#2 $Pma2_1$	r1-GM1+, r11-GM3-
#3 $Pca2_1$	r1-GM1+, r9-GM2-, r10-GM2-
#4 $Pmc2_1$	r1-GM1+, r12-GM4-
#5 $P2_1/m$	r1-GM1+, r2-GM2+
#6 $P2_1/c$	r1-GM1+, r5-GM4+, r6-GM4+
#7 *P*2/*c*	r1-GM1+, r3-GM3+, r4-GM3+
#8 $P2_12_12$	r1-GM1+, r7-GM1-, r8-GM1-
#9 *Pm*	r1-GM1+, r2-GM2+, r11-GM3-, r12-GM4-
#10 *Pc*	r1-GM1+, r5-GM4+, r6-GM4+, r9-GM2-, r10-GM2-, r11-GM3-
#11 *Pc*	r1-GM1+, r3-GM3+, r4-GM3+, r9-GM2-, r10-GM2-, r12-GM4-
#12 *P*-1	r1-GM1+, r2-GM2+, r3-GM3+, r4-GM3+, r5-GM4+, r6-GM4+
#13 $P2_1$	r1-GM1+, r2-GM2+, r7-GM1-, r8-GM1-, r9-GM2-, r10-GM2-
#14 $P2_1$	r1-GM1+, r4-GM3+, r5-GM4+, r7-GM1-, r8-GM1-, r12-GM4-
#15 *P*2	r1-GM1+, r4-GM3+, r7-GM1-, r8-GM1-, r11-GM3-
#16 *P*1	r1-GM1+, r2-GM2+, r3-GM3+, r4-GM3+, r5-GM4+, r6-GM4+ r7-GM1-, r8-GM1-, r9-GM2-, r10-GM2-, r11-GM3-, r12-GM4-

Table 1: Active translational symmetry modes for each subgroup candidate

Space group No.	**Rotational symmetry modes needed**
#1 *Pbcm*	a1-GM1+, a2-GM1+
#2 *Pma*2$_1$	a1-GM1+, a2-GM1+, a9-GM3-, a10-GM3-
#3 *Pca*2$_1$	a1-GM1+, a2-GM1+, a8-GM2-
#4 *Pmc*2$_1$	a1-GM1+, a2-GM1+, a11-GM4-
#5 *P*2$_1$/*m*	a1-GM1+, a2-GM1+, a3-GM2+, a4-GM2+
#6 *P*2$_1$/*c*	a1-GM1+, a2-GM1+, a6-GM4+
#7 *P*2/*c*	a1-GM1+, a2-GM1+, a5-GM3+
#8 *P*2$_1$2$_1$2	a1-GM1+, a2-GM1+, a7-GM1-
#9 *Pm*	a1-GM1+, a2-GM1+, a9-GM3-, a10-GM3-, a11-GM4-, a12-GM4-
#10 *Pc*	a1-GM1+, a2-GM1+, a6-GM4+, a8-GM2-, a11-GM4-, a12-GM4-
#11 *Pc*	a1-GM1+, a2-GM1+, a5-GM3+, a8-GM2-, a11-GM4-, a12-GM4-
#12 *P*-1	a1-GM1+, a2-GM1+, a3-GM2+, a4-GM2+, a5-GM3+, a6-GM4+
#13 *P*2$_1$	a1-GM1+, a2-GM1+, a7-GM1-, a8-GM2-
#14 *P*2$_1$	a1-GM1+, a2-GM1+, a6-GM4+, a7-GM1-
#15 *P*2	a1-GM1+, a2-GM1+, a5-GM3+, a7-GM1-, a9-GM3-, a10-GM3-
#16 *P*1	a1-GM1+, a2-GM1+, a3-GM2+, a4-GM2+, a5-GM3+, a6-GM4+ a7-GM1-, a8-GM2-, a9-GM3-, a10-GM3-, a11-GM4-, a12-GM4-

*a9, a8 and a12 are set to zero in order to fixing the floating origin in *P*1.

Appendix V TOPAS script containing the rotational and translational symmetry modes for structure determination of DC-MBI by using exhaustive subgroup search

The HT structure of DC-MBI was determined from powder X-ray diffraction using the exhaustive symmetry search methods. A single TOPAS script contains the rotational and translational symmetry modes is shown below. This TOPAS script allows to test all the subgroup candidates automatically.

```
r_wp   2.49925222 r_exp   1.62956269 r_p   1.93059348 r_wp_dash   17.7150602 r_p_dash   29.1229474
r_exp_dash  11.5505754 weighted_Durbin_Watson  1.44225021 gof  1.53369504

iters 1000
continue_after_convergence
chi2_convergence_criteria 0.00001
do_errors
no_LIMIT_warnings
line_min
use_extrapolation

'{{{ list of space groups
num_runs 48
        #list space_group_use sg_num {
                { #define sg01_pbcm  }   01
                { #define sg01_pbcm  }   01
                { #define sg01_pbcm  }   01
                { #define sg02_pma2  }   02
                { #define sg02_pma2  }   02
                { #define sg02_pma2  }   02
                { #define sg03_pca21 }   03
                { #define sg03_pca21 }   03
                { #define sg03_pca21 }   03
                { #define sg04_pmc21 }   04
                { #define sg04_pmc21 }   04
                { #define sg04_pmc21 }   04
                        ...
                        etc
                        ...
                { #define sg13_p21   }   13
                { #define sg13_p21   }   13
                { #define sg13_p21   }   13
                { #define sg14_p21   }   14
                { #define sg14_p21   }   14
                { #define sg14_p21   }   14
                { #define sg15_p2    }   15
                { #define sg15_p2    }   15
                { #define sg15_p2    }   15
                { #define sg16_p1    }   16
                { #define sg16_p1    }   16
                { #define sg16_p1    }   16
                }
        space_group_use(Run_Number)
   out_file = Concat(String(INP_File), ".INP");
'}}}

xdd 576457-mac-001_reb_0003.xye
        start_X 5
        finish_X 30
        x_calculation_step = Yobs_dx_at(Xo);
        'lam taken from calibration of 503416 with TCHz symmetric function
```

```
        lam ymin_on_ymax 0.00001 la 1.0 lo 0.8257653 lh 0.1
        LP_Factor(90) 'change the LP correction  or lh value if required
   prm !zero    -1.43981 val_on_continue = 0; th2_offset = (zero/1000);
   'use 12 background terms to fit background humps
   bkg    1759.43082  -692.314322  -388.15422   692.993438  -239.261119  -274.893993   331.425032  -
69.2383629  -136.257731   170.008849  -53.8038534  -76.5129471   82.9724235  -6.27429566  -33.9620647
27.051865  -5.51048912  -0.832029124

        str
                'P1
                space_group   1
                scale @  0.000109072562

'{{{ define here which irreps to turn on/off for each space group and a flag for cell parameters
free to refine
#ifdef sg01_pbcm     #define GM1+_on                  #define ortho #endif
#ifdef sg02_pma2    #define GM1+_on  #define GM3-_on  #define ortho #endif
#ifdef sg03_pca21   #define GM1+_on  #define GM2-_on  #define ortho #endif
#ifdef sg04_pmc21   #define GM1+_on  #define GM4-_on  #define ortho #endif
#ifdef sg05_p21m    #define GM1+_on  #define GM2+_on  #define mono  #endif
#ifdef sg06_p21c    #define GM1+_on  #define GM4+_on  #define mono  #endif
#ifdef sg07_p2c     #define GM1+_on  #define GM3+_on  #define mono  #endif
#ifdef sg08_p21212  #define GM1+_on  #define GM1-_on  #define ortho #endif
#ifdef sg09_pm #define GM1+_on  #define GM2+_on  #define GM3-_on  #define GM4-_on  #define mono  #endif
#ifdef sg10_pc #define GM1+_on  #define GM4+_on  #define GM2-_on  #define GM3-_on  #define mono  #endif
#ifdef sg11_pc #define GM1+_on  #define GM3+_on  #define GM2-_on  #define GM4-_on  #define mono  #endif
#ifdef sg12_pb1  #define GM1+_on  #define GM2+_on  #define GM3+_on  #define GM4+_on  #define tric  #endif
#ifdef sg13_p21  #define GM1+_on  #define GM2+_on  #define GM1-_on  #define GM2-_on  #define mono  #endif
#ifdef sg14_p21  #define GM1+_on  #define GM4+_on  #define GM1-_on  #define GM4-_on  #define mono  #endif
#ifdef sg15_p2   #define GM1+_on  #define GM3+_on  #define GM1-_on  #define GM3-_on  #define mono  #endif
#ifdef sg16_p1   #define GM1+_on  #define GM2+_on  #define GM3+_on  #define GM4+_on  #define GM1-_on
#define GM2-_on  #define GM3-_on  #define GM4-_on  #define tric  #endif
 '}}}

   'cell parameters to refine depend on irreps active - i.e. space group
   #ifdef ortho
   a @  5.768694 c @  14.740271 b @  10.390251 al    90.00000 be    90.00000 ga    90.00000
   #endif
   #ifdef mono
   a @  5.770275 c @  14.741435 b @  10.393210 al    90.00000 be    90.00000 ga  @  91.21605
   #endif
   #ifdef tric
   a @  5.770667 c @  14.742132 b @  10.393593 al @   89.99329 be  @  89.99009 ga  @  91.21624
   #endif


'{{{ mode definitions
'fix a8, a9 and a12 to fix the floating origin in P1

  macro vcr { val_on_continue = Rand(-0.01,0.01); }
  #ifdef GM1+_on prm   r1   0.00245 min  -20.00 max  20.00 vcr 'Pbcm[0,0,0]GM1+(a)[He1:d:rot]A'(a)
  #ifdef GM2+_on prm   r2  -0.06955 min  -20.00 max  20.00 vcr 'Pbcm[0,0,0]GM2+(a)[He1:d:rot]A'(a)
  #ifdef    GM3+_on    prm          r3       -0.14473    min       -20.00    max       20.00    vcr
'Pbcm[0,0,0]GM3+(a)[He1:d:rot]A''_1(a)
  #ifdef    GM3+_on    prm          r4         0.09435    min       -20.00    max       20.00    vcr
'Pbcm[0,0,0]GM3+(a)[He1:d:rot]A''_2(a)
  #ifdef    GM4+_on    prm          r5         0.12188    min       -20.00    max       20.00    vcr
'Pbcm[0,0,0]GM4+(a)[He1:d:rot]A''_1(a)
  #ifdef    GM4+_on    prm          r6       -0.07177    min       -20.00    max       20.00    vcr
'Pbcm[0,0,0]GM4+(a)[He1:d:rot]A''_2(a)
  #ifdef   GM1-_on   prm       r7     -0.00434   min     -20.00   max     20.00   vcr   'Pbcm[0,0,0]GM1-
(a)[He1:d:rot]A''_1(a)
  #ifdef   GM1-_on   prm       r8     -0.00697   min     -20.00   max     20.00   vcr   'Pbcm[0,0,0]GM1-
(a)[He1:d:rot]A''_2(a)
  #ifdef   GM2-_on   prm       r9     -0.13402   min     -20.00   max     20.00   vcr   'Pbcm[0,0,0]GM2-
(a)[He1:d:rot]A''_1(a)
```

```
  #ifdef   GM2-_on   prm       r10     0.00961   min     -20.00   max     20.00   vcr   'Pbcm[0,0,0]GM2-
(a)[He1:d:rot]A''_2(a)
  #ifdef GM3-_on prm   r11 -0.07754 min  -20.00 max  20.00 vcr 'Pbcm[0,0,0]GM3-(a)[He1:d:rot]A'(a)
  #ifdef GM4-_on prm   r12  0.01876 min  -20.00 max  20.00 vcr 'Pbcm[0,0,0]GM4-(a)[He1:d:rot]A'(a)
  #ifdef GM1+_on prm   a1   2.03236 min  -20.00 max  20.00 vcr 'Pbcm[0,0,0]GM1+(a)[He1:d:dsp]A'_1(a)
  #ifdef GM1+_on prm   a2  -2.59305 min  -20.00 max  20.00 vcr 'Pbcm[0,0,0]GM1+(a)[He1:d:dsp]A'_2(a)
  #ifdef GM2+_on prm   a3  -1.84536 min  -20.00 max  20.00 vcr 'Pbcm[0,0,0]GM2+(a)[He1:d:dsp]A'_1(a)
  #ifdef GM2+_on prm   a4  -0.15950 min  -20.00 max  20.00 vcr 'Pbcm[0,0,0]GM2+(a)[He1:d:dsp]A'_2(a)
  #ifdef GM3+_on prm   a5  -1.13681 min  -20.00 max  20.00 vcr 'Pbcm[0,0,0]GM3+(a)[He1:d:dsp]A''(a)
  #ifdef GM4+_on prm   a6   1.59862 min  -20.00 max  20.00 vcr 'Pbcm[0,0,0]GM4+(a)[He1:d:dsp]A''(a)
  #ifdef GM1-_on prm   a7   3.27581 min  -20.00 max  20.00 vcr 'Pbcm[0,0,0]GM1-(a)[He1:d:dsp]A''(a)
  #ifdef GM2-_on prm  !a8   0.0000  min  -20.00 max  20.00 vcr 'Pbcm[0,0,0]GM2-(a)[He1:d:dsp]A''(a)
  #ifdef GM3-_on prm  !a9   0.0000  min  -20.00 max  20.00 vcr 'Pbcm[0,0,0]GM3-(a)[He1:d:dsp]A'_1(a)
  #ifdef GM3-_on prm   a10  2.55372 min  -20.00 max  20.00 vcr 'Pbcm[0,0,0]GM3-(a)[He1:d:dsp]A'_2(a)
  #ifdef GM4-_on prm   a11  4.77384 min  -20.00 max  20.00 vcr 'Pbcm[0,0,0]GM4-(a)[He1:d:dsp]A'_1(a)
  #ifdef GM4-_on prm  !a12  0.00000 min  -20.00 max  20.00 vcr 'Pbcm[0,0,0]GM4-(a)[He1:d:dsp]A'_2(a)
  '}}}

                 prm  !a13      0.00000 min  -2.83 max  2.83 'Pbcm[0,0,0]GM1+(a)[Cl1:e:dsp] A_1(a)
                 prm  !a14      0.00000 min  -2.83 max  2.83 'Pbcm[0,0,0]GM1+(a)[Cl1:e:dsp] A_2(a)
                 prm  !a15      0.00000 min  -2.83 max  2.83 'Pbcm[0,0,0]GM1+(a)[Cl1:e:dsp] A_3(a)
                         ...
                         etc
                         ...
                 prm  !a215     0.00000 min  -2.00 max  2.00 'Pbcm[0,0,0]GM4-(a)[H3:d:dsp] A'_1(a)
                 prm  !a216     0.00000 min  -2.00 max  2.00 'Pbcm[0,0,0]GM4-(a)[H3:d:dsp] A'_2(a)
'}}}

'{{{ mode-amplitude to delta transformation
                 prm !He1_dx = He1_1_dx + He1_2_dx + He1_3_dx + He1_4_dx;:        0.00000`_0.00000
                 prm !He1_dy = He1_1_dy + He1_2_dy + He1_3_dy + He1_4_dy;:        0.00000`_0.00000
                 prm !He1_dz = He1_1_dz + He1_2_dz + He1_3_dz + He1_4_dz;:       -0.00000`_0.00000
'                penalty = 0.00 * (He1_dx + He1_dy + He1_dz)^2;

        prm  He1_1_dx = +  0.08793*a1 +  0.08793*a3 +  0.08793*a9 +  0.08793*a11;:  -0.29831
        prm  He1_1_dy  = +  0.04809*a5 +  0.04809*a6 +  0.04809*a7 +  0.04809*a8;: -0.09737
        prm  He1_1_dz     = -  0.03512*a2 -  0.03512*a4 -  0.03512*a10 -  0.03512*a12;: 0.04314
        prm  He1_2_dx     = +  0.08793*a1 -  0.08793*a3 +  0.08793*a9 -  0.08793*a11;   -0.27174
        prm  He1_2_dy    = -  0.04809*a5 +  0.04809*a6 -  0.04809*a7 +  0.04809*a8;:        0.29742
        prm  He1_2_dz     = +  0.03512*a2 -  0.03512*a4 +  0.03512*a10 -  0.03512*a12;:   -0.08071
        prm  He1_3_dx    = -  0.08793*a1 +  0.08793*a3 +  0.08793*a9 -  0.08793*a11;:       0.57742
        prm  He1_3_dy    = +  0.04809*a5 -  0.04809*a6 -  0.04809*a7 +  0.04809*a8;:        0.09364
        prm  He1_3_dz     = -  0.03512*a2 +  0.03512*a4 +  0.03512*a10 -  0.03512*a12;:   -0.06273
        prm  He1_4_dx     = -  0.08793*a1 -  0.08793*a3 +  0.08793*a9 +  0.08793*a11;:    -0.00737
        prm  He1_4_dy     = -  0.04809*a5 -  0.04809*a6 +  0.04809*a7 +  0.04809*a8;:     -0.29369
        prm  He1_4_dz    = +  0.03512*a2 +  0.03512*a4 -  0.03512*a10 -  0.03512*a12;:      0.10030
                         ...
                         etc
                         ...
        prm   He1_4_drly    = +   0.04809*r1  +   0.04809*r2  -   0.04809*r11  -   0.04809*r12;:   -
0.00094`_0.00059
        prm   He1_4_drlz    = -   0.03512*r4  -   0.03512*r6  +   0.03512*r8  +   0.03512*r10;:    -
0.00230`_0.00061
'}}}

'{{{ distorted parameters
        rm  He1_1_x      =    0.25920 + He1_1_dx;:          -0.03911`_0.16930
        prm  He1_1_y      = 1/4 + He1_1_dy;:  0.15263`_0.13362
        prm  He1_1_z      =    0.69845 + He1_1_dz;:    0.74159`_0.04595
                 ...
                 etc
                 ...
        prm  H3_4_y       = 3/4 + H3_4_dy;:  0.75000
        prm  H3_4_z       =    0.17730 + H3_4_dz;:  0.17730

        prm !He1_1_occ    = 0;:  0.00000
        prm !He1_2_occ    = 0;:  0.00000
```

```
        prm !He1_3_occ    = 0;:  0.00000
        prm !He1_4_occ    = 0;:  0.00000
                ...
                etc
                ...
        prm !H3_2_occ     = 1;:  1.00000
        prm !H3_3_occ     = 1;:  1.00000
        prm !H3_4_occ     = 1;:  1.00000
'}}}

'{{{ 'rotation angles in radians and degrees
'added P atoms so that 1 degree is 0.1 A in crystalmaker

        metrictensor()
        prm  He1_1_angrad = vectorlength(He1_1_rlx, He1_1_rly, He1_1_rlz);:  0.09131`_0.00647
        prm  He1_1_angdeg = He1_1_angrad*radian;:  5.23149`_0.37060
        prm  He1_2_angrad = vectorlength(He1_2_rlx, He1_2_rly, He1_2_rlz);:  0.07798`_0.00909
        prm  He1_2_angdeg = He1_2_angrad*radian;:  4.46801`_0.52105
        prm  He1_3_angrad = vectorlength(He1_3_rlx, He1_3_rly, He1_3_rlz);:  0.22904`_0.00909
        prm  He1_3_angdeg = He1_3_angrad*radian;:  13.12275`_0.52096
        prm  He1_4_angrad = vectorlength(He1_4_rlx, He1_4_rly, He1_4_rlz);:  0.03589`_0.00882
        prm  He1_4_angdeg = He1_4_angrad*radian;:  2.05611`_0.50538

        'dummy atom positions relative to rigid-body centers
        prm  Q_He1_1_na = He1_1_rlx/He1_1_angrad;:               -0.00986`_0.01827
        prm  Q_He1_1_nb = He1_1_rly/He1_1_angrad;:                 -0.09062`_0.00310
                        ...
                        etc
                        ...
        prm  P_He1_4_na = He1_4_rlx*radian*0.333;:                0.02028`_0.03184
        prm  P_He1_4_nb = He1_4_rly*radian*0.333;:                 -0.01791`_0.01116
        prm  P_He1_4_nc = He1_4_rlz*radian*0.333;:                   -0.04390`_0.01161


        rigid
                point_for_site He1_1 ua = He1_1_x; ub = He1_1_y; uc = He1_1_z;
                point_for_site  Q_He1_1  ua  =  Q_He1_1_na+He1_1_x;  ub  =  Q_He1_1_nb+He1_1_y;  uc  =
Q_He1_1_nc+He1_1_z;
                point_for_site  P_He1_1  ua  =  P_He1_1_na+He1_1_x;  ub  =  P_He1_1_nb+He1_1_y;  uc  =
P_He1_1_nc+He1_1_z;
                point_for_site Cl1_1    ua = Cl1_1_x;    ub = Cl1_1_y;    uc = Cl1_1_z;
                point_for_site Cl1_8    ua = Cl1_8_x;    ub = Cl1_8_y;    uc = Cl1_8_z;
                point_for_site N1_1     ua = N1_1_x;     ub = N1_1_y;     uc = N1_1_z;
                point_for_site N1_8     ua = N1_8_x;     ub = N1_8_y;     uc = N1_8_z;
                point_for_site C1_1     ua = C1_1_x;     ub = C1_1_y;     uc = C1_1_z;
                point_for_site C2_1     ua = C2_1_x;     ub = C2_1_y;     uc = C2_1_z;
                point_for_site C3_1     ua = C3_1_x;     ub = C3_1_y;     uc = C3_1_z;
                point_for_site C3_8     ua = C3_8_x;     ub = C3_8_y;     uc = C3_8_z;
                point_for_site C4_1     ua = C4_1_x;     ub = C4_1_y;     uc = C4_1_z;
                point_for_site C4_8     ua = C4_8_x;     ub = C4_8_y;     uc = C4_8_z;
                point_for_site C5_1     ua = C5_1_x;     ub = C5_1_y;     uc = C5_1_z;
                point_for_site C5_8     ua = C5_8_x;     ub = C5_8_y;     uc = C5_8_z;
                point_for_site H1_1     ua = H1_1_x;     ub = H1_1_y;     uc = H1_1_z;
                point_for_site H1_8     ua = H1_8_x;     ub = H1_8_y;     uc = H1_8_z;
                point_for_site H2_1     ua = H2_1_x;     ub = H2_1_y;     uc = H2_1_z;
                point_for_site H2_8     ua = H2_8_x;     ub = H2_8_y;     uc = H2_8_z;
                point_for_site H3_1     ua = H3_1_x;     ub = H3_1_y;     uc = H3_1_z;
'               translate tx = He1_1_dx;:  0.00295_0.00102 ty = He1_1_dy;:  0.00000 tz = He1_1_dz;:
0.00116_0.00035 operate_on_points "* !He1_1" in_FC  '"* !He_1"
                Rotate_about_points( =He1_1_angdeg;, He1_1, Q_He1_1)
        rigid
                point_for_site He1_2 ua = He1_2_x; ub = He1_2_y; uc = He1_2_z;
                point_for_site  Q_He1_2  ua  =  Q_He1_2_na+He1_2_x;  ub  =  Q_He1_2_nb+He1_2_y;  uc  =
Q_He1_2_nc+He1_2_z;
                point_for_site  P_He1_2  ua  =  P_He1_2_na+He1_2_x;  ub  =  P_He1_2_nb+He1_2_y;  uc  =
P_He1_2_nc+He1_2_z;
                point_for_site Cl1_2    ua = Cl1_2_x;    ub = Cl1_2_y;    uc = Cl1_2_z;
```

```
                point_for_site Cl1_7    ua = Cl1_7_x;    ub = Cl1_7_y;    uc = Cl1_7_z;
                point_for_site N1_2     ua = N1_2_x;     ub = N1_2_y;     uc = N1_2_z;
                point_for_site N1_7     ua = N1_7_x;     ub = N1_7_y;     uc = N1_7_z;
                point_for_site C1_2     ua = C1_2_x;     ub = C1_2_y;     uc = C1_2_z;
                point_for_site C2_2     ua = C2_2_x;     ub = C2_2_y;     uc = C2_2_z;
                point_for_site C3_2     ua = C3_2_x;     ub = C3_2_y;     uc = C3_2_z;
                point_for_site C3_7     ua = C3_7_x;     ub = C3_7_y;     uc = C3_7_z;
                point_for_site C4_2     ua = C4_2_x;     ub = C4_2_y;     uc = C4_2_z;
                point_for_site C4_7     ua = C4_7_x;     ub = C4_7_y;     uc = C4_7_z;
                point_for_site C5_2     ua = C5_2_x;     ub = C5_2_y;     uc = C5_2_z;
                point_for_site C5_7     ua = C5_7_x;     ub = C5_7_y;     uc = C5_7_z;
                point_for_site H1_2     ua = H1_2_x;     ub = H1_2_y;     uc = H1_2_z;
                point_for_site H1_7     ua = H1_7_x;     ub = H1_7_y;     uc = H1_7_z;
                point_for_site H2_2     ua = H2_2_x;     ub = H2_2_y;     uc = H2_2_z;
                point_for_site H2_7     ua = H2_7_x;     ub = H2_7_y;     uc = H2_7_z;
                point_for_site H3_2     ua = H3_2_x;     ub = H3_2_y;     uc = H3_2_z;
 '              translate tx = He1_2_dx;:  0.00295_0.00102 ty = He1_2_dy;:  0.00000 tz = He1_2_dz;:
-0.00116_0.00035 operate_on_points "* !He1_2" in_FC  '"* !He_1"
                Rotate_about_points( =He1_2_angdeg;, He1_2, Q_He1_2)
        rigid
                point_for_site He1_3 ua = He1_3_x; ub = He1_3_y; uc = He1_3_z;
                point_for_site Q_He1_3 ua = Q_He1_3_na+He1_3_x; ub = Q_He1_3_nb+He1_3_y; uc =
Q_He1_3_nc+He1_3_z;
                point_for_site P_He1_3 ua = P_He1_3_na+He1_3_x; ub = P_He1_3_nb+He1_3_y; uc =
P_He1_3_nc+He1_3_z;
                point_for_site Cl1_3    ua = Cl1_3_x;    ub = Cl1_3_y;    uc = Cl1_3_z;
                point_for_site Cl1_6    ua = Cl1_6_x;    ub = Cl1_6_y;    uc = Cl1_6_z;
                point_for_site N1_3     ua = N1_3_x;     ub = N1_3_y;     uc = N1_3_z;
                point_for_site N1_6     ua = N1_6_x;     ub = N1_6_y;     uc = N1_6_z;
                point_for_site C1_3     ua = C1_3_x;     ub = C1_3_y;     uc = C1_3_z;
                point_for_site C2_3     ua = C2_3_x;     ub = C2_3_y;     uc = C2_3_z;
                point_for_site C3_3     ua = C3_3_x;     ub = C3_3_y;     uc = C3_3_z;
                point_for_site C3_6     ua = C3_6_x;     ub = C3_6_y;     uc = C3_6_z;
                point_for_site C4_3     ua = C4_3_x;     ub = C4_3_y;     uc = C4_3_z;
                point_for_site C4_6     ua = C4_6_x;     ub = C4_6_y;     uc = C4_6_z;
                point_for_site C5_3     ua = C5_3_x;     ub = C5_3_y;     uc = C5_3_z;
                point_for_site C5_6     ua = C5_6_x;     ub = C5_6_y;     uc = C5_6_z;
                point_for_site H1_3     ua = H1_3_x;     ub = H1_3_y;     uc = H1_3_z;
                point_for_site H1_6     ua = H1_6_x;     ub = H1_6_y;     uc = H1_6_z;
                point_for_site H2_3     ua = H2_3_x;     ub = H2_3_y;     uc = H2_3_z;
                point_for_site H2_6     ua = H2_6_x;     ub = H2_6_y;     uc = H2_6_z;
                point_for_site H3_3     ua = H3_3_x;     ub = H3_3_y;     uc = H3_3_z;
 '              translate tx = He1_3_dx;: -0.00295_0.00102 ty = He1_3_dy;:  0.00000 tz = He1_3_dz;:
0.00116_0.00035 operate_on_points "* !He1_3" in_FC  '"* !He_1"
                Rotate_about_points( =He1_3_angdeg;, He1_3, Q_He1_3)
        rigid
                point_for_site He1_4 ua = He1_4_x; ub = He1_4_y; uc = He1_4_z;
                point_for_site Q_He1_4 ua = Q_He1_4_na+He1_4_x; ub = Q_He1_4_nb+He1_4_y; uc =
Q_He1_4_nc+He1_4_z;
                point_for_site P_He1_4 ua = P_He1_4_na+He1_4_x; ub = P_He1_4_nb+He1_4_y; uc =
P_He1_4_nc+He1_4_z;
                point_for_site Cl1_4    ua = Cl1_4_x;    ub = Cl1_4_y;    uc = Cl1_4_z;
                point_for_site Cl1_5    ua = Cl1_5_x;    ub = Cl1_5_y;    uc = Cl1_5_z;
                point_for_site N1_4     ua = N1_4_x;     ub = N1_4_y;     uc = N1_4_z;
                point_for_site N1_5     ua = N1_5_x;     ub = N1_5_y;     uc = N1_5_z;
                point_for_site C1_4     ua = C1_4_x;     ub = C1_4_y;     uc = C1_4_z;
                point_for_site C2_4     ua = C2_4_x;     ub = C2_4_y;     uc = C2_4_z;
                point_for_site C3_4     ua = C3_4_x;     ub = C3_4_y;     uc = C3_4_z;
                point_for_site C3_5     ua = C3_5_x;     ub = C3_5_y;     uc = C3_5_z;
                point_for_site C4_4     ua = C4_4_x;     ub = C4_4_y;     uc = C4_4_z;
                point_for_site C4_5     ua = C4_5_x;     ub = C4_5_y;     uc = C4_5_z;
                point_for_site C5_4     ua = C5_4_x;     ub = C5_4_y;     uc = C5_4_z;
                point_for_site C5_5     ua = C5_5_x;     ub = C5_5_y;     uc = C5_5_z;
                point_for_site H1_4     ua = H1_4_x;     ub = H1_4_y;     uc = H1_4_z;
                point_for_site H1_5     ua = H1_5_x;     ub = H1_5_y;     uc = H1_5_z;
                point_for_site H2_4     ua = H2_4_x;     ub = H2_4_y;     uc = H2_4_z;
```

```
                point_for_site H2_5     ua = H2_5_x;     ub = H2_5_y;     uc = H2_5_z;
                point_for_site H3_4     ua = H3_4_x;     ub = H3_4_y;     uc = H3_4_z;

'               translate tx = He1_4_dx;: -0.00295_0.00102 ty = He1_4_dy;:  0.00000 tz = He1_4_dz;:
-0.00116_0.00035 operate_on_points "* !He1_4" in_FC  '"* !He_1"
                Rotate_about_points( =He1_4_angdeg;, He1_4, Q_He1_4)
 '}}}

'{{{ mode-dependent sites
        site He1_1    x   -0.03911   y  0.15263    z  0.74159  occ He = He1_1_occ;    beq 0
        site Q_He1_1  x   -0.04898   y  0.06201    z  0.76451  occ D   0              beq 0
        site P_He1_1  x   -0.05630   y -0.00524    z  0.78152  occ P   0              beq 0
        site He1_2    x   -0.01254   y  1.04742    z  0.72084  occ He = He1_2_occ;    beq 0
        site Q_He1_2  x   -0.10857   y  1.03120    z  0.77642  occ D   0              beq 0
        site P_He1_2  x   -0.15542   y  1.02328    z  0.80353  occ P   0              beq 0
        site He1_3    x    1.31822   y  0.34364    z  0.13572  occ He = He1_3_occ;    beq 0
        site Q_He1_3  x    1.16286   y  0.30638    z  0.15390  occ D   0              beq 0
        site P_He1_3  x    0.63929   y  0.18083    z  0.21516  occ P   0              beq 0
        site He1_4    x    0.73343   y  0.45631    z  0.40185  occ He = He1_4_occ;    beq 0
        site Q_He1_4  x    0.76305   y  0.43015    z  0.33774  occ D   0              beq 0
        site P_He1_4  x    0.75371   y  0.43840    z  0.35795  occ P   0              beq 0

'molecule 1
        site Cl1_1   x -0.22611 y  0.09498 z  0.52441 occ Cl = Cl1_1_occ;:1.00000 beq bcl  15.86450
        site Cl1_8   x -0.24266 y  0.39546 z  0.52303 occ Cl = Cl1_8_occ;:1.00000 beq bcl  15.86450
        site N1_1    x  0.43548 y  0.15117 z  0.77190 occ N  = N1_1_occ;:1.00000  beq bca  13.89824
        site N1_8    x  0.42369 y  0.36513 z  0.77092 occ N  = N1_8_occ;:1.00000  beq bca  13.89824
        site C1_1    x  0.52554 y  0.26002 z  0.80776 occ C  = C1_1_occ;:1.00000  beq bca  13.89824
        site C2_1    x  0.70867 y  0.26363 z  0.88163 occ C  = C2_1_occ;:1.00000  beq bca  13.89824
        site C3_1    x  0.26594 y  0.18796 z  0.70848 occ C  = C3_1_occ;:1.00000  beq bca  13.89824
        site C3_8    x  0.25856 y  0.32181 z  0.70786 occ C  = C3_8_occ;:1.00000  beq bca  13.89824
        site C4_1    x  0.10212 y  0.38786 z  0.65094 occ C  = C4_1_occ;:1.00000  beq bca  13.89824
        site C4_8    x  0.11710 y  0.11597 z  0.65219 occ C  = C4_8_occ;:1.00000  beq bca  13.89824
        site C5_1    x -0.04614 y  0.31648 z  0.59488 occ C  = C5_1_occ;:1.00000  beq bca  13.89824
        site C5_8    x -0.03870 y  0.18143 z  0.59550 occ C  = C5_8_occ;:1.00000  beq bca  13.89824
        site H1_1    x  0.12216 y  0.02682 z  0.65263 occ H  = H1_1_occ;:1.00000  beq bca  13.89824
        site H1_8    x  0.09735 y  0.47701 z  0.65056 occ H  = H1_8_occ;:1.00000  beq bca  13.89824
        site H2_1    x  0.68774 y  0.33841 z  0.91957 occ H  = H2_1_occ;:1.00000  beq bca  13.89824
        site H2_8    x  0.69599 y  0.18878 z  0.92025 occ H  = H2_8_occ;:1.00000  beq bca  13.89824
        site H3_1    x  0.86072 y  0.26602 z  0.85303 occ H  = H3_1_occ;:1.00000  beq bca  13.89824

'molecule 2
        site Cl1_2   x -0.26752 y  0.90659 z  0.97171 occ Cl = Cl1_2_occ;:1.00000 beq bcl  15.86450
        site Cl1_7   x -0.23312 y  0.60707 z  0.98093 occ Cl = Cl1_7_occ;:1.00000 beq bcl  15.86450
        site N1_2    x  0.46036 y  0.87540 z  0.75205 occ N  = N1_2_occ;:1.00000  beq bca  13.89824
        site N1_7    x  0.48486 y  0.66213 z  0.75862 occ N  = N1_7_occ;:1.00000  beq bca  13.89824
        site C1_2    x  0.57723 y  0.77046 z  0.72284 occ C  = C1_2_occ;:1.00000  beq bca  13.89824
        site C2_2    x  0.77801 y  0.77346 z  0.65636 occ C  = C2_2_occ;:1.00000  beq bca  13.89824
        site C3_2    x  0.28254 y  0.83251 z  0.80978 occ C  = C3_2_occ;:1.00000  beq bca  13.89824
        site C3_7    x  0.29787 y  0.69909 z  0.81389 occ C  = C3_7_occ;:1.00000  beq bca  13.89824
        site C4_2    x  0.13966 y  0.62752 z  0.86648 occ C  = C4_2_occ;:1.00000  beq bca  13.89824
        site C4_7    x  0.10854 y  0.89855 z  0.85814 occ C  = C4_7_occ;:1.00000  beq bca  13.89824
        site C5_2    x -0.03362 y  0.69298 z  0.91465 occ C  = C5_2_occ;:1.00000  beq bca  13.89824
        site C5_7    x -0.04908 y  0.82760 z  0.91050 occ C  = C5_7_occ;:1.00000  beq bca  13.89824
        site H1_2    x  0.09848 y  0.98742 z  0.85537 occ H  = H1_2_occ;:1.00000  beq bca  13.89824
        site H1_7    x  0.15002 y  0.53866 z  0.86919 occ H  = H1_7_occ;:1.00000  beq bca  13.89824
        site H2_2    x  0.77958 y  0.69626 z  0.61996 occ H  = H2_2_occ;:1.00000  beq bca  13.89824
        site H2_7    x  0.76245 y  0.84541 z  0.61537 occ H  = H2_7_occ;:1.00000  beq bca  13.89824
        site H3_2    x  0.92194 y  0.78065 z  0.69060 occ H  = H3_2_occ;:1.00000  beq bca  13.89824

'molecule 3
        site Cl1_3   x  1.29463 y  0.36812 z  0.02432 occ Cl = Cl1_3_occ;:1.00000 beq bcl  15.86450
        site Cl1_6   x  1.32280 y  0.07443 z  0.06779 occ Cl = Cl1_6_occ;:1.00000 beq bcl  15.86450
        site N1_3    x  0.53479 y  0.36130 z  0.22687 occ N  = N1_3_occ;:1.00000  beq bca  13.89824
        site N1_6    x  0.55485 y  0.15218 z  0.25782 occ N  = N1_6_occ;:1.00000  beq bca  13.89824
        site C1_3    x  0.43418 y  0.26201 z  0.27125 occ C  = C1_3_occ;:1.00000  beq bca  13.89824
```

```
        site C2_3     x  0.22102 y  0.27330 z  0.33075 occ C  = C2_3_occ;:1.00000  beq bca  13.89824
        site C3_3     x  0.73143 y  0.31299 z  0.18241 occ C  = C3_3_occ;:1.00000  beq bca  13.89824
        site C3_6     x  0.74398 y  0.18217 z  0.20177 occ C  = C3_6_occ;:1.00000  beq bca  13.89824
        site C4_3     x  0.92591 y  0.10665 z  0.16695 occ C  = C4_3_occ;:1.00000  beq bca  13.89824
        site C4_6     x  0.90042 y  0.37239 z  0.12762 occ C  = C4_6_occ;:1.00000  beq bca  13.89824
        site C5_3     x  1.09426 y  0.16549 z  0.11243 occ C  = C5_3_occ;:1.00000  beq bca  13.89824
        site C5_6     x  1.08160 y  0.29749 z  0.09290 occ C  = C5_6_occ;:1.00000  beq bca  13.89824
        site H1_3     x  0.89190 y  0.45953 z  0.11475 occ H  = H1_3_occ;:1.00000  beq bca  13.89824
        site H1_6     x  0.93411 y  0.01951 z  0.17987 occ H  = H1_6_occ;:1.00000  beq bca  13.89824
        site H2_3     x  0.22751 y  0.21137 z  0.37960 occ H  = H2_3_occ;:1.00000  beq bca  13.89824
        site H2_6     x  0.21348 y  0.35762 z  0.35796 occ H  = H2_6_occ;:1.00000  beq bca  13.89824
        site H3_3     x  0.08411 y  0.25827 z  0.29335 occ H  = H3_3_occ;:1.00000  beq bca  13.89824

'molecule 4
        site Cl1_4    x  1.28225 y  0.58879 z  0.47134 occ Cl = Cl1_4_occ;:1.00000 beq bcl  15.86450
        site Cl1_5    x  1.30062 y  0.88965 z  0.47268 occ Cl = Cl1_5_occ;:1.00000 beq bcl  15.86450
        site N1_4     x  0.57591 y  0.64757 z  0.24435 occ N  = N1_4_occ;:1.00000  beq bca  13.89824
        site N1_5     x  0.58899 y  0.86180 z  0.24530 occ N  = N1_5_occ;:1.00000  beq bca  13.89824
        site C1_4     x  0.47988 y  0.75693 z  0.21143 occ C  = C1_4_occ;:1.00000  beq bca  13.89824
        site C2_4     x  0.28327 y  0.76127 z  0.14323 occ C  = C2_4_occ;:1.00000  beq bca  13.89824
        site C3_4     x  0.75720 y  0.68377 z  0.30259 occ C  = C3_4_occ;:1.00000  beq bca  13.89824
        site C3_5     x  0.76538 y  0.81779 z  0.30319 occ C  = C3_5_occ;:1.00000  beq bca  13.89824
        site C4_4     x  0.93252 y  0.88334 z  0.35539 occ C  = C4_4_occ;:1.00000  beq bca  13.89824
        site C4_5     x  0.91590 y  0.61111 z  0.35418 occ C  = C4_5_occ;:1.00000  beq bca  13.89824
        site C5_4     x  1.09062 y  0.81130 z  0.40677 occ C  = C5_4_occ;:1.00000  beq bca  13.89824
        site C5_5     x  1.08236 y  0.67608 z  0.40617 occ C  = C5_5_occ;:1.00000  beq bca  13.89824
        site H1_4     x  0.91030 y  0.52185 z  0.35376 occ H  = H1_4_occ;:1.00000  beq bca  13.89824
        site H1_5     x  0.93783 y  0.97261 z  0.35576 occ H  = H1_5_occ;:1.00000  beq bca  13.89824
        site H2_4     x  0.29718 y  0.83636 z  0.10489 occ H  = H2_4_occ;:1.00000  beq bca  13.89824
        site H2_5     x  0.28803 y  0.68654 z  0.10423 occ H  = H2_5_occ;:1.00000  beq bca  13.89824
        site H3_4     x  0.13741 y  0.76371 z  0.17628 occ H  = H3_4_occ;:1.00000  beq bca  13.89824
'}}}

'{{{ macros for calculations involving the lattice parameters

        macro metrictensor()
        {
                prm  !radian  57.2957795
'               prm   ra = Get(a);
'               prm   rb = Get(b);
'               prm   rc = Get(c);
'               prm   ralpha = Get(al)/radian;
'               prm   rbeta  = Get(be)/radian;
'               prm   rgamma = Get(ga)/radian;
                prm   !ra = Constant(Get(a));
                prm   !rb = Constant(Get(b));
                prm   !rc = Constant(Get(c));
                prm   !ralpha = Constant(Get(al)/radian);
                prm   !rbeta  = Constant(Get(be)/radian);
                prm   !rgamma = Constant(Get(ga)/radian);
                prm   rrr  = (Cos(ralpha) - Cos(rbeta)*Cos(rgamma))/Sin(rgamma);

                prm   basis11 = ra;
                prm  !basis21  0
                prm  !basis31  0
                prm   basis12 = rb*Cos(rgamma);
                prm   basis22 = rb*Sin(rgamma);
                prm  !basis32  0
                prm   basis13 = rc*Cos(rbeta);
                prm   basis23 = rc*rrr;
                prm   basis33 = rc*Sqrt(1 - Cos(rbeta)^2 - rrr^2);

                prm  g11 = basis11*basis11 + basis12*basis12 + basis13*basis13;
                prm  g21 = basis21*basis11 + basis22*basis12 + basis23*basis13;
                prm  g31 = basis31*basis11 + basis32*basis12 + basis33*basis13;
                prm  g12 = basis11*basis21 + basis12*basis22 + basis13*basis23;
```

```
                prm  g22 = basis21*basis21 + basis22*basis22 + basis23*basis23;
                prm  g32 = basis31*basis21 + basis32*basis22 + basis33*basis23;
                prm  g13 = basis11*basis31 + basis12*basis32 + basis13*basis33;
                prm  g23 = basis21*basis31 + basis22*basis32 + basis23*basis33;
                prm  g33 = basis31*basis31 + basis32*basis32 + basis33*basis33;
        }

        macro vectorlength(vlx, vly, vlz)
        {
                Max(Sqrt(g11*vlx^2  +  g12*vlx*vly  +  g21*vlx*vly  +  g22*vly^2  +  g13*vlx*vlz  +
g31*vlx*vlz + g23*vly*vlz + g32*vly*vlz + g33*vlz^2), 0.000001)
        }
'}}}

'{{{ instrumental and sample peak shape etc
'Si standard peak shape
                TCHZ_Peak_Type(!pku,-0.00072,!pkv,  -0.00008,!pkw,  -0.00080,!pkz,  0.00087,!pky,
0.01490,!pkx, 0.00175)
      Simple_Axial_Model(!axial, 1.86652)
        local  !individual_b  0 min -4 max 20 'single bvalue for all phases
        scale_pks = (Exp(-2*individual_b/(2 D_spacing)^2)); 'bvalue for all phases in each dataset
  spherical_harmonics_hkl sh sh_order  4 load sh_Cij_prm {
                        y00   sh_c00    0.39745
                        y20   sh_c20    0.23684 vcsh
                        y21p  sh_c21p  -0.13323 vcsh
                        y21m  sh_c21m  -0.02971 vcsh
                        y22p  sh_c22p   0.05049 vcsh
                        y22m  sh_c22m   0.09667 vcsh
                        y40   sh_c40    0.08579 vcsh
                        y41p  sh_c41p  -0.06884 vcsh
                        y41m  sh_c41m   0.19337 vcsh
                        y42p  sh_c42p  -0.07365 vcsh
                        y42m  sh_c42m  -0.05547 vcsh
                        y43p  sh_c43p  -0.03794 vcsh
                        y43m  sh_c43m   0.07862 vcsh
                        y44p  sh_c44p   0.00234 vcsh
                        y44m  sh_c44m  -0.09766 vcsh
                        }
                        macro vcsh {val_on_continue = Rand(-0.05,0.05);}
                        prm zeta  0.24396`_0.01071 min 0 max 1
                        lor_fwhm = zeta * Max(0.0001, sh * Tan(Th));
                        gauss_fwhm = (1-zeta) * Max(0.0001, sh * Tan(Th));
'}}}
```

Appendix VI Results from the pseudosymmetry detection using the pseudosymmetry search program at the Bilbao Crystallographic Server

The Crystallographic Information File (CIF) of the proposed high symmetry 2BA-ETD structure derived from CSD entry RIBLET obtained from the Bilbao Crystallographic Server is shown below:

```
data_generated_by_bilbao_crystallographic_server

_cell_length_a                    9.1440
_cell_length_b                    8.4250
_cell_length_c                    21.0000
_cell_angle_alpha                 90.00
_cell_angle_beta                  90.00
_cell_angle_gamma                 90.00
_symmetry_space_group_name_H-M   'Pbca'
_symmetry_Int_Tables_number       61

loop_
_symmetry_equiv_pos_site_id
_symmetry_equiv_pos_as_xyz
1    'x,y,z'
2    '-x+1/2,-y,z+1/2'
3    '-x,y+1/2,-z+1/2'
4    'x+1/2,-y+1/2,-z'
5    '-x,-y,-z'
6    'x+1/2,y,-z+1/2'
7    'x,-y+1/2,z+1/2'
8    '-x+1/2,y+1/2,z'

loop_
_atom_site_label
_atom_site_type_symbol
_atom_site_symmetry_multiplicity
_atom_site_Wyckoff_symbol
_atom_site_fract_x
_atom_site_fract_y
_atom_site_fract_z
C1    C   0.01462  0.56526  0.62521
C2    C   0.02890  0.41790  0.58442
O1    O   0.15248  0.39190  0.55951
O2    O   0.92144  0.33039  0.57791
H1    H   0.24550  0.60250  0.63530
H2    H   0.22050  0.84450  0.70040
H3    H   0.97550  0.94250  0.72885
H4    H   0.75400  0.80100  0.68830
H5    H   0.78200  0.55850  0.62475
C10   C   0.12298  0.37826  0.35852
C11   C   0.13801  0.24238  0.32164
C12   C   0.01537  0.16529  0.30030
C13   C   0.87806  0.21992  0.31592
C14   C   0.86236  0.35498  0.35325
N1    N   0.17741  0.11101  0.49589
C15   C   0.04068  0.03702  0.47247
H11   H   0.23700  0.03100  0.52425
H12   H   0.15700  0.21550  0.52195
H13   H   0.24850  0.14050  0.45880
H14   H   0.06600  0.94650  0.43805
H15   H   0.97600  0.12950  0.45045
```

The maximum atomic displacements (0.9392 Å) between the two structures are given by nitrogen atoms.

Appendix VII Crystallographic information and crystal structure of *α*-2BA-ETD at 120 K

The structure of *α*-2BA-ETD was re-determined at 120 K (see section 5.3). All hydrogen atoms were located using Fourier difference maps. Hydrogens involved in the -NH···O hydrogen bonding were refined isotropically without restraints while remaining hydrogens were refined using riding mode. The crystallographic information is summarised in Table 1. Figure 1 shows the crystal structure of the LT *α*-2BA-ETD. This structure is the same as the previously-reported *α*-2BA-ETD at room temperature.

Table 1: Crystallographic information of *α*-2BA-ETD.

Temperature	120 K
Chemical formula	$C_{16}H_{20}N_2O_4$
M_r	304.34
Crystal system	Orthorhombic
Space group	$Pca2_1$
Z	4
***a* (Å)**	8.4399(4)
***b* (Å)**	9.1423(3)
***c* (Å)**	20.5595(12)
***α* (°)**	90
***β* (°)**	90
***γ* (°)**	90
Volume ($Å^3$)	1586.38(9)
No. of measured reflections	27247
I/Sigma cutoff	2
No. of observed reflections	1435
No. of parameters	199
R, Rw	0.0822, 0.1601

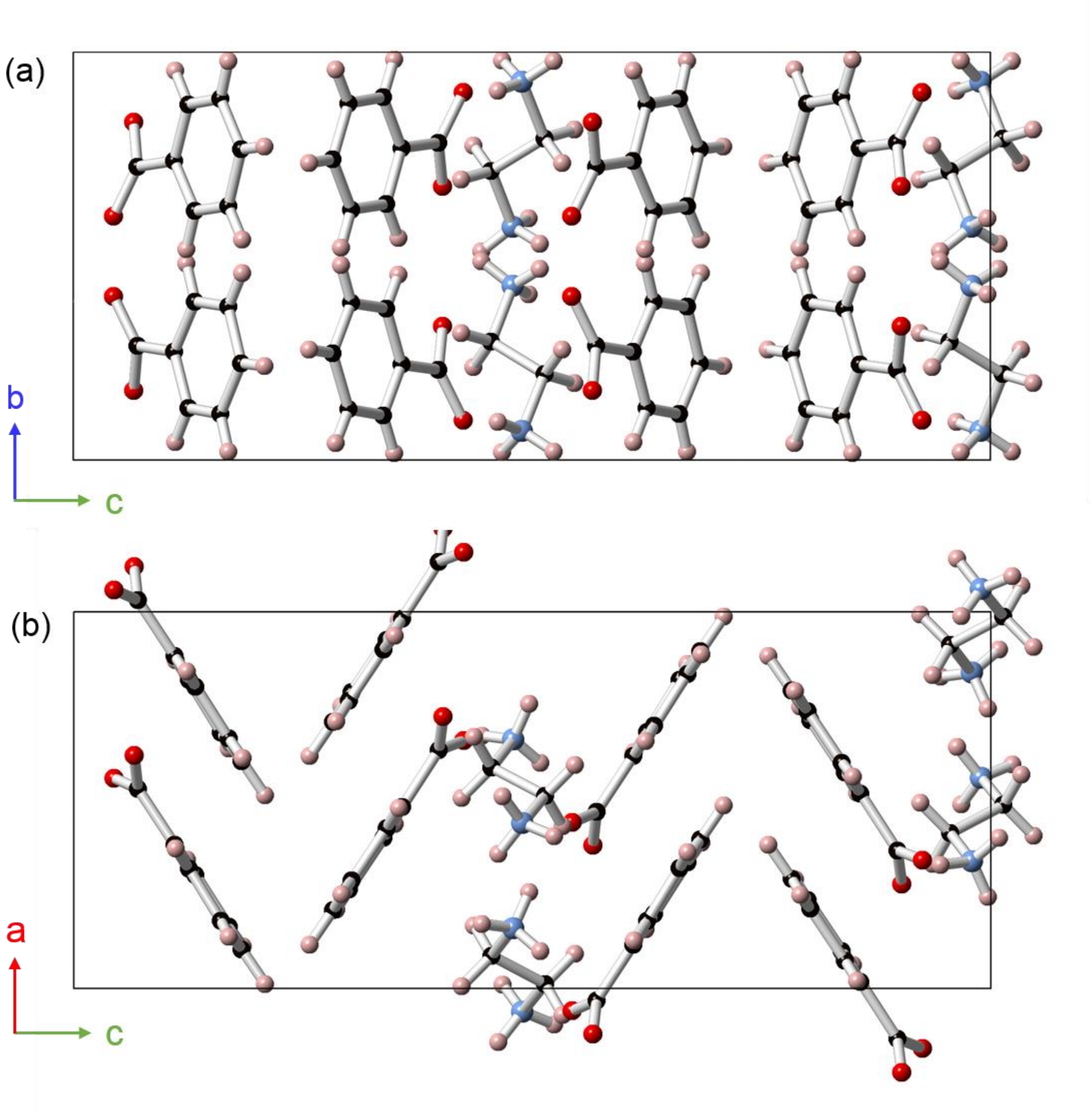

Figure 1: The crystal structure of 120 K *α*-2BA-ETD structure (a) viewed down *a*-axis and (b) viewed down *b*-axis.

Appendix VIII TGA curve collected on CA-PYR monohydrate

The TGA measurement was performed on 2.853 mg monohydrated CA-PYR sample heating from 30°C to 500°C at 10°C/min under nitrogen.

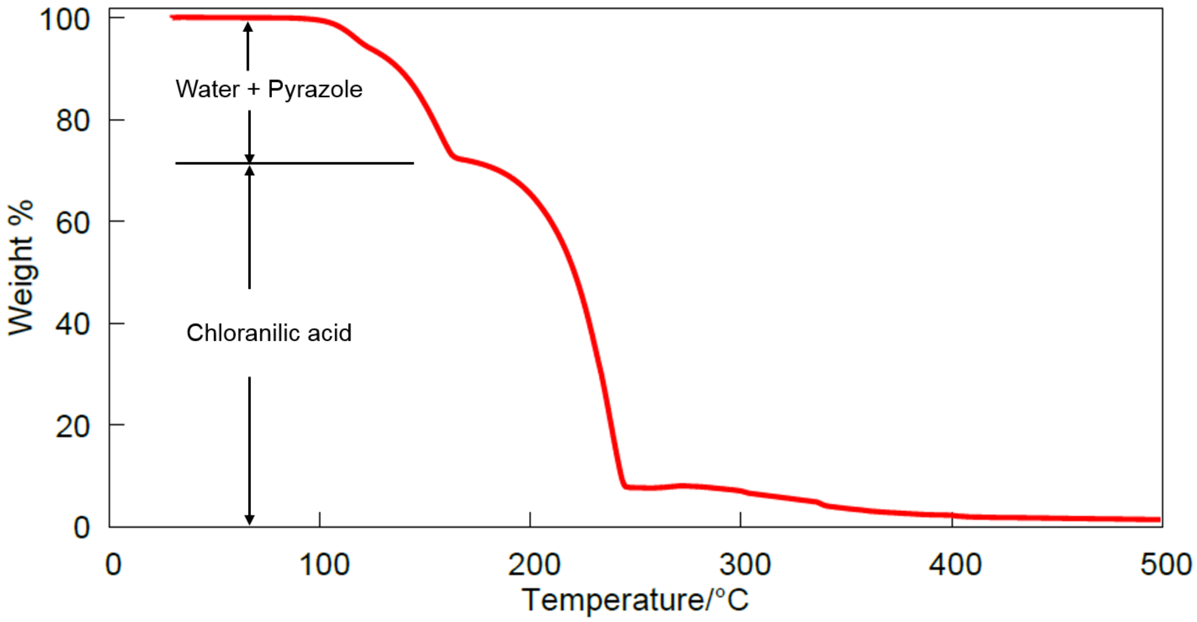

Appendix IX Spherical harmonic functions

Spherical harmonics are functions that defined on the surface of a sphere in mathematics. The distance between a given point on the surface and the origin is dependent on two coordinates, θ and φ. The expressions of a specific set of 4th order spherical harmonics, denoted as $Y_{ijp}(\theta,\varphi)$, are shown in the Table 1. The overall spherical harmonic function is determined by refining a coefficient C_{ij} for each function. It can be used for corrections of both preferred orientation and *hkl*-dependent peak broadening.

Table 1: The spherical harmonic functions $Y_{ijp}(\theta,\varphi)$

ij	$Y_{ij}(\theta,\varphi)$
00	1
20	$0.5(3\cos^2\theta\ -1)$
21+	$2\cos\theta\sin\theta\cos\varphi$
21-	$2\cos\theta\sin\theta\sin\varphi$
22+	$\sin^2\theta\cos 2\varphi$
22-	$\sin^2\theta\sin 2\varphi$
40	$0.12500(35\cos^4\theta\ -30\cos^2\theta+3)$
41+	$0.94695(7\cos^2\theta\ -3)\cos\theta\sin\theta\cos\varphi$
41-	$0.94695(7\cos^2\theta\ -3)\cos\theta\sin\theta\sin\varphi$
42+	$0.77778(7\cos^2\theta\ -1)\ \sin^2\theta\cos 2\varphi$
42-	$0.77778(7\cos^2\theta\ -1)\ \sin^2\theta\sin 2\varphi$
43+	$3.07920\cos\theta\sin^3\theta\cos 3\varphi$
43-	$3.07920\cos\theta\sin^3\theta\sin 3\varphi$
44+	$\sin^4\theta\cos 4\varphi$
44-	$\sin^4\theta\sin 4\varphi$